RESEARCH ONLINE

University of Wollongong
Research Online

University of Wollongong Thesis Collection

University of Wollongong Thesis Collections

2011

Luminescence investigations into the time of final deposition of Toba volcanic ash and artefact-bearing alluvial sediments in the Middle Son Valley, Madhya Pradesh, India

Christina Neudorf
University of Wollongong

Recommended Citation

Neudorf, Christina, Luminescence investigations into the time of final deposition of Toba volcanic ash and artefact-bearing alluvial sediments in the Middle Son Valley, Madhya Pradesh, India, Doctor of Philosophy thesis, School of Earth and Environmental Sciences, University of Wollongong, 2011. http://ro.uow.edu.au/theses/3663

Research Online is the open access institutional repository for the University of Wollongong. For further information contact the UOW Library: research-pubs@uow.edu.au

RESEARCH ONLINE

UNIVERSITY OF WOLLONGONG

COPYRIGHT WARNING

You may print or download ONE copy of this document for the purpose of your own research or study. The University does not authorise you to copy, communicate or otherwise make available electronically to any other person any copyright material contained on this site. You are reminded of the following:

Copyright owners are entitled to take legal action against persons who infringe their copyright. A reproduction of material that is protected by copyright may be a copyright infringement. A court may impose penalties and award damages in relation to offences and infringements relating to copyright material. Higher penalties may apply, and higher damages may be awarded, for offences and infringements involving the conversion of material into digital or electronic form.

Luminescence investigations into the time of final deposition of Toba volcanic ash and artefact-bearing alluvial sediments in the Middle Son Valley, Madhya Pradesh, India

A thesis submitted in fulfilment of the requirements for the award of the degree

Doctor of Philosophy

from

University of Wollongong

By

Christina M. Neudorf

MSc Simon Fraser University

Centre for Archaeological Science
School of Earth and Environmental Sciences

2011

Certification

I, Christina M. Neudorf, declare that this thesis, submitted in fulfilment of the requirements for the award of degree of Doctor of Philosophy, in the School of Earth and Environmental Sciences, University of Wollongong, is wholly my work unless otherwise referenced or acknowledged. This document has not been submitted for qualifications at any other academic institution.

Christina M. Neudorf

March 28, 2012

ABSTRACT

Terraced alluvial deposits in the Middle Son Valley, Madhya Pradesh, India contain Youngest Toba Tuff (YTT) deposits and an archaeological record that spans the Acheulean to the Neolithic. For the past three decades, this region has been the focus of geological and archaeological investigations that aim to understand the impact of the ~74 thousand year (ka) Toba volcanic super-eruption on the environment and human populations in India. The research presented in this study is focussed on two main themes: 1) developing and applying luminescence dating techniques to alluvial sediments in the Middle Son Valley to assess the reliability of the YTT ash as a reliable chronostratigraphic marker in palaeoenvironmental investigations; and 2) to test a previously published model of alluvial deposition for the Middle Son Valley near the confluence of the Rehi and Son Rivers.

The luminescence dating potential of potassium feldspar (KF) was explored at both the single aliquot and the single grain level for sediments in the Middle Son Valley. In this study, KF grains are shown to be suited to single-aliquot regenerative-dose measurement procedures and individual KF grains exhibit fading rates ranging from 0 to more than 20 %/decade. Post-infrared infrared signals (pIRIR) are shown to be less susceptible to anomalous fading, as expected, but evidence presented here suggests that pIRIR ages for alluvial sediments in the Middle Son Valley are less reliable than IRSL ages, because the source traps for these signals are less likely to be completely emptied by sun exposure during transport and deposition in the Son River.

IRSL ages from KF and OSL ages from quartz presented in this study suggest that the final deposition of the sediments above and below the YTT ash deposits in the Middle Son Valley occurred sometime (possibly up to a few tens of thousands of years) after the Toba volcanic super-eruption. This chronology suggests that: 1) the YTT ash has been reworked by fluvial processes and cannot be considered a reliable chronostratigraphic marker as was previously thought; or 2) the YTT ash was deposited soon after the volcanic event ~74 ka ago, but the underlying sediments have since been eroded and replaced by younger, inset fluvial sediments. In both cases, the temporal framework presented here calls into question the validity of previous palaeoenvironmental interpretations and hypotheses that were based on pedogenic carbonates sampled above, below and within the YTT ash.

A previously published model of alluvial deposition for the Middle Son Valley subdivides the preserved alluvium within the valley system into five stratigraphic formations. These formations include (from oldest to youngest) the Sihawal, Khunteli, Patpara, Baghor and Khetaunhi Formations. The accuracy of this model was tested near the Rehi-Son confluence using cross-valley topographic profiles, field observations, and IRSL age estimates from terraced alluvial sediments. IRSL age estimates for the highest terrace

mark the beginning of incision of the Middle Son Valley alluvium at ~16 ka (as predicted by the model) and the termination of deposition of the Baghor Formation fine member silts between ~16 and ~21 ka ago. Maximum IRSL age estimates of ~1.9–2.7 ka, ~10 m above river level, mark the termination of deposition of the Khetaunhi Formation silts and the sands on the lowest terrace. These ages are only slightly younger than previously reported radiocarbon age estimates of ~3–5 ka for this formation. The age estimates for coarse sands and gravels that lie at intermediate elevations (~20 m above river level) between these two terraces contradict what is predicted by the model. According to the model, these sediments should be between ~40 and 58 ka in age and form part of the Patpara Formation, which has been exposed by fluvial erosion of the overlying Baghor Formation. By contrast, maximum IRSL age estimates presented here suggest that these deposits are only up to ~5–7 ka in age and form inset sediments that were deposited during a brief aggradational phase, sometime after incision of the highest alluvial surface ~16 ka ago. Incision of the Middle Son Valley alluvium across from the Rehi-Son confluence began shortly after ~16–21 ka, probably as a result of SW monsoon intensification. The inset coarse sand and gravel at ~20 m above river level likely aggraded under wet conditions in the early Holocene, and the lowest (~10 m high) inset terrace probably aggraded under more arid conditions during the late Holocene. Both the Middle Son Valley, and its neighbour, the Belan Valley, record major phases in regional climate and human occupation of northern India. Improved chronological control on the stratigraphies of these valleys therefore has implications for enhancing our understanding the history of climate change and human occupation in India.

Acknowledgements

I am eternally grateful to my supervisors, Prof Richard Roberts and Dr. Zenobia Jacobs, for giving me the opportunity to pursue this project and providing invaluable support and guidance along the way. Special thanks to Profs Michael Petraglia and J. N. Pal for introducing me to the field sites in India and to the wonderful world of Indian archaeology. Thanks to Michael Haslam, Adam Durant, Emma Gatti, Jimbob Blinkhorn, Janardhana Bora, Jinu Koshy, Kathryn Price, Clair Davey, Ceri Shipton, Kate Connell, Kevin Cunningham, Manas Mishra, Metin Eren, Harindra Prasad and the local villagers from the Middle Son Valley for an amazing time in the field that I will never forget. Special thanks to Brent Peterson for help with the ETS and to Heidi Brown and Michael Stevens for help with my GPS, DGPS and mapping enquiries. Thanks to Penny Williamson for courageously lending me the field camera for fieldwork in India—I wish I could have brought it back in better condition.... Thanks to Terry Lachlan for help in the lab. Thanks to José Abrantes for help with sample preparation for the microprobe and to Kevin Grant and Norman Pearson for advice and assistance with my microprobe measurements. Thanks to Mike Meyer for the OSL discussions, earth science seminars, and for providing me a place to stay between conferences. Thanks to Andrew Murray, Geoff Duller, Sebastian Huot, Christina Thomsen, Olav Lian, Dave Huntley, Mayank Jain and Jan-Pieter Buylaert for providing feedback on my work and answering my questions on luminescence dating. Thanks to Henne May for constructive feedback on a chapter.

Thanks to my office mates, Nathan Jankowski, Stephanie Kermode, Luke Gilganic, and the rest for the coffees, OSL meetings, enlightening conversations, hilarious youtube videos, constructive criticisms and moral support! I wish you guys the best for the future.

Thanks to all my friends in the Gong and back home for the parties, music, sports, laughs and the moral support. I'm indebted to you for helping me maintain my sanity throughout this PhD. I love you all and hope we meet again! And last, but not least, thanks to my family for your inspiration and support. Without you, I never would have made it this far!

Table of Contents

CERTIFICATION ..... **I**

ABSTRACT ..... **III**

ACKNOWLEDGEMENTS ..... **V**

TABLE OF CONTENTS ..... **VII**

LIST OF FIGURES ..... **XIII**

LIST OF TABLES ..... **XXII**

CHAPTER 1 – INTRODUCTION AND PROJECT AIMS **1**

1.1 Introduction 1

1.2 The Middle Son Valley 2

1.2.1 Alluvial deposition in the Middle Son Valley *4*

1.2.2 Sihawal Formation *5*

1.2.3 Patpara Formation *9*

1.2.4 Baghor Formation *10*

1.2.5 Khunteli Formation *10*

1.2.6 Khetaunhi Formation *11*

1.2.7. The need for better chronological control *11*

1.3 YTT ash – a reliable chronostratigraphic marker? 11

1.4 Constraining the time of final deposition of alluvial deposits and their artefacts – methods used previously 14

1.4.1 Radiocarbon dating *14*

1.4.2 Thermoluminescence dating *14*

1.4.3 OSL dating *15*

1.4.4 IRSL dating *15*

1.5 The aims of this research and structure of the thesis 16

CHAPTER 2 – LUMINESCENCE DATING **19**

2.1 Luminescence dating principles 19

2.2 Quartz or feldspar? 20

2.3 The luminescence process in quartz 21

2.4 OSL measurement protocols 23

2.5 The luminescence process in feldspar 25

2.6 Anomalous fading 27

2.6.1 Causes and geological control *27*

2.6.2 Toward a non-fading signal *28*

2.6.3 Fading rate measurements and corrections.....*29*
2.7 LUMINESCENCE MEASUREMENTS ON SINGLE KF GRAINS.....29
2.8 INTERNAL DOSE RATES OF KF GRAINS.....34
2.9 EXTERNAL DOSE RATES.....37
2.9.1 Alpha particles.....*37*
2.9.2 Beta particles and gamma rays.....*38*
2.9.3 Cosmic rays.....*38*
2.9.4 Adjustments for water content, organic matter and calcium carbonate.....*38*
2.10 SUMMARY.....39

CHAPTER 3 – LUMINESCENCE DATING METHODOLOGY AND SAMPLES 41

3.1 SAMPLES AND SAMPLE COLLECTION.....41
3.2 SAMPLE PREPARATION AND MEASUREMENT.....41
3.3 ALIQUOT PREPARATION METHODS USING CRYSTALBOND 509.....42
3.4 D_E DETERMINATION.....43
3.5 INTERNAL DOSE RATES TO KF AND QUARTZ GRAINS.....44
3.6 EXTERNAL DOSE RATE DETERMINATION.....45
3.7 ADJUSTMENTS FOR WATER CONTENT, ORGANIC MATTER AND CALCIUM CARBONATE.....46
3.8 SUMMARY.....46

CHAPTER 4 – ELEMENTAL ANALYSES.....47

4.1 INTRODUCTION.....47
4.2 HEAVY LIQUID SEPARATION AND LUMINESCENCE MEASUREMENTS.....48
4.3 D_E DETERMINATION AND REJECTION CRITERIA.....49
4.4 ANOMALOUS FADING MEASUREMENTS.....50
4.5 FADING RATE AND FADING-CORRECTED AGE CALCULATIONS.....51
4.6 EDS ANALYSIS.....52
4.6.1 Measurements.....*52*
4.6.2 EDS results.....*55*
4.6.3 Luminescence intensity versus feldspar type.....*57*
4.7 WDS ANALYSIS.....58
4.7.1 WDS measurements.....*58*
4.7.2 WDS results.....*61*
4.7.3 Major element content and IRSL.....*63*
4.7.4 Feldspar elemental composition, D_e and fading rate.....*66*
4.8 LIMITATIONS OF WDS AND EDS MEASUREMENTS.....71
4.9 SUMMARY AND IMPLICATIONS FOR SINGLE-GRAIN DATING.....71

CHAPTER 5 – PRELIMINARY SINGLE-GRAIN IRSL MEASUREMENTS 73

5.1 INTRODUCTION 73

5.2 ASSESSING LASER POWER, STIMULATION DURATION, AND THE PROPORTION OF GRAINS THAT CONTRIBUTE TO THE TOTAL IRSL SIGNAL 73

5.3 TESTING FOR GRAIN HEATING BY THE IR LASER 74

5.4 DOSE RECOVERY TESTS 78

5.4.1 Laboratory-bleached and heated grains 80

5.4.2 Sun-bleached grains 81

5.4.3 L_n and L_x residual signals 82

5.5 SUMMARY 86

CHAPTER 6 – SOURCES OF OVERDISPERSION IN A K-RICH FELDSPAR SAMPLE FROM NORTH-CENTRAL INDIA: INSIGHTS FROM D_E, K CONTENT AND IRSL AGE DISTRIBUTIONS FOR INDIVIDUAL GRAINS 87

ABSTRACT 88

6.1 INTRODUCTION 89

6.2 SAMPLES 89

6.3 TESTING A SAR PROTOCOL 90

6.3.1 Natural IRSL signals 90

6.3.2 The SAR procedure and data rejection criteria 90

6.3.3 Dose recovery test 91

6.4 D_E DETERMINATION AND SOURCES OF OVERDISPERSION 91

6.5 ANOMALOUS FADING TESTS 92

6.5.1 Fading measurement procedures 92

6.5.2 Fading test results 93

6.6 KF GRAIN AGE DISTRIBUTIONS 93

6.6.1 Single-grain and multi-grain KF ages 93

6.6.2 Single-grain quartz ages 94

6.6.3 Isolating zero-fading grains 94

6.6.4 The influence of K content on single-grain age distributions 94

6.7 DISCUSSION AND CONCLUSIONS 95

ACKNOWLEDGEMENTS 96

REFERENCES 97

FIGURES 99

SUPPLEMENTARY MATERIAL 103

Sample preparation procedures and equipment 103

g-value calculations 103

Aliquot preparation methods using Crystalbond 509 ..... *105*

Environmental dose rate calculations *105*

Wavelength-dispersive spectrometry (WDS) methods *106*

CHAPTER 7 – ASSESSING THE TIME OF FINAL DEPOSITION OF YOUNGEST TOBA TUFF DEPOSITS IN THE MIDDLE SON VALLEY, INDIA—A LUMINESCENCE APPROACH USING MULTIPLE METHODS 111

7.1 INTRODUCTION 111

7.2 YTT ASH DEPOSITS AND SAMPLES 111

7.2.1 Ghoghara main section *111*

7.2.2 Khunteli Formation type-section *117*

7.3 $IRSL_{50}$ AND $pIRIR_{225}$ SIGNAL CHARACTERISTICS OF SMALL KF ALIQUOTS 117

7.3.1 The $IRSL_{50}$ and $pIRIR_{225}$ signals *117*

7.3.2 Preheat plateau tests *118*

7.3.3 Dose recovery tests *121*

7.3.4 Fading rates *121*

7.3.5 Signal resetting *124*

7.4 $IRSL_{50}$ AND $pIRIR_{225}$ KF ALIQUOT AGE DISTRIBUTIONS 126

7.4.1 Recycling ratios, OD, and aliquot ages *126*

7.5 SINGLE-GRAIN AGE DISTRIBUTIONS OF QUARTZ AND KF AND EVIDENCE FOR SEDIMENT MIXING 129

7.5.1 Quartz *129*

7.5.2 KF grains *132*

7.6 IMPLICATIONS OF SINGLE-GRAIN DATA FOR KF ALIQUOTS 133

7.6.1 Using the MAM to calculate a maximum $IRSL_{50}$ age *133*

7.6.2 Comparisons between quartz and KF single-grain age distributions and KF multi-grain aliquot age distributions *133*

7.7 ENVIRONMENTAL DOSE RATES 135

7.7.1 Assessing the potential of radioactive disequilibrium in U and Th decay chains *135*

7.7.2 Causes of sample-to-sample variations in ^{40}K content *136*

7.7.3 A comparison between external dose rates measured using HRGS and low-level beta counting plus in situ gamma spectrometry *137*

7.7.4 Age calculations using water contents approaching saturation *139*

7.8 IMPLICATIONS FOR THE TIME OF FINAL DEPOSITION OF THE YTT ASH AND PALAEOENVIRONMENTAL RECONSTRUCTIONS OF TOBA'S IMPACT 139

7.9 SUMMARY 142

CHAPTER 8 – TESTING A MODEL OF ALLUVIAL DEPOSITION IN THE MIDDLE SON VALLEY, INDIA USING IRSL AGES OF TERRACED ALLUVIAL SEDIMENTS 144

8.1 Introduction 144
8.2 Study area 144
8.3 Methods 148
8.3.1 Topographic surveys 148
8.3.2 Sampling and IRSL measurements 148
8.3.3 Environmental dose rate determination 149
8.4 Results 149
8.4.1 Alluvial terraces and sediments south of the Son River 149
8.4.2 IRSL age determination 152
8.5 Discussion 158
8.5.1 Consistencies with previously reported age estimates 158
8.5.2 Inconsistencies with the Williams et al. (2006) model 158
8.5.3 Chronological evidence for northward migration of the Son River 159
8.5.4 Modifications to the Williams et al. (2006) model 159
8.5.5 The palaeo-Son River response to past changes in SW Indian monsoon intensity – multiproxy records spanning the last 150,000 years 161
8.5.6 Lacustrine records of monsoon intensity in north India during the Holocene 163
8.5.7 Fluvial sequences – The Gangetic Plains, the Belan River valley, and the southern margin of the Thar Desert 165
8.6 Conclusions 168

CHAPTER 9 – SUMMARY, CONCLUSIONS AND RECOMMENDATIONS FOR FUTURE RESEARCH 169

9.1 The luminescence dating potential of KF grains using SAR dating techniques, fading measurements and corrections 169
9.1.1 Main findings 169
9.1.2 Implications and future research directions 170
9.2 Assessing the time of final deposition of YTT ash-bearing deposits at the Ghoghara main section and the Khunteli type-section using luminescence dating techniques 170
9.2.1 Main findings 170
9.2.2 Implications and future research directions 171
9.3 Testing and refining a model of alluvial deposition in the Middle Son Valley 172
9.3.1 Main findings 172
9.3.2 Implications and future research directions 173

REFERENCES 174

List of Figures

Figure 1-1. a) The Middle Son Valley (MSV) and the locations of archaeological sites and preserved YTT ash along the banks of the Son River after Sharma and Clark (1983). B) View south across the Son River from Dhaba sites 2 and 3 of Haslam *et al.* (2012). **3**

Figure 1-2. Schematic cross-section of the Middle Son Valley looking east from the Rehi-Son confluence, modified after Williams and Royce (1983) to include the new Khunteli Formation introduced by Williams et al. (2006). Formation ages are estimated from reports from Williams and Royce (1982), Pal *et al.* (2005), and Williams et al. (2006). The ages of the Patpara and Khunteli formations include a question mark as these are debated (see Section 1.2 for details). **8**

Figure 1-3. a) Study area. b) Ghoghara main section containing YTT ash. The lower 4 cm of this ash unit is thought to be primary ash. c) Khunteli Formation type-section containing YTT ash-rich sandy silt (photo courtesy of R.G. Roberts). This ash unit is thought to be re-worked (Gatti *et al.* 2011). **12**

Figure 2-1. The luminescence process in quartz. (i) Ionization due to exposure of the crystal to nuclear radiation, with trapping of electrons and holes at defects L and T, respectively. (ii) Storage during antiquity. (iii) Electron eviction from T and subsequent recombination at L in response to optical stimulation. Alternatively, electrons may recombine at non-luminescence centres, be recaptured by a trap of the same type, or be captured by another type of trap. From Aitken (1998). **22**

Figure 2-2. The effect of bleaching (with a green laser beam for 10 s) on the TL glow-curve of quartz grains (from Aitken 1998, based on Rhodes (1990)). **22**

Figure 2-3. An OSL decay curve from a single quartz grain. The OSL signal intensity is reported in photon counts (cts) per 0.02 s of green (532 nm) laser stimulation. From Duller *et al.* (2003). **23**

Figure 2-4. The luminescence process in feldspar, involving an electron trap and a hole trap (Poolton *et al.* 2002a). (a) Low energy optical excitation (~1.4 eV) raises the electron to deep-lying band-tail states, and thermal energy from the lattice allows thermal ionization, followed by recombination. (b) If the defects are close, recombination via tunnelling is possible from the excited state with no thermal activation. (c) If the electron and hole traps are very close, recombination via tunnelling from the ground state is possible. **26**

Figure 2-5. TL glow-curves for a single KF aliquot (from Murray *et al.* 2009). Three TL glow-curves are plotted, showing the natural signal with no preheat ("no ph"), the signal after a 570 Gy dose and no preheat, and the signal after a 570 Gy dose and a 250°C preheat. The 570 Gy, "no ph" curve is plotted again after multiplication by 0.05. The heating rate used was 5 °C/s. **26**

Figure 2-6. Relationships between the K content of individual 500-1000 μm grains and the a) calculated internal dose rate, b) natural IRSL intensity, and c) the D_e. Data are from Lamothe *et al.* (1994). Internal beta dose rates were calculated using data from Mejdahl (1983), and the contributions from internal U, Th and Rb were not included in the internal dose rate calculations (Lamothe *et al.* 1994). K content error bars are smaller than the size of the symbols. **35**

Figure 2-7. Scatterplots of D_e versus KF grain internal dose rate from K (a), and equivalent dose versus total dose rate for each grain (b). Data are from Lamothe *et al.* (1994). **36**

Figure 4-1. Flow chart for heavy liquid separation (from Mejdahl 1985; Aitken 1998). The numbers shown are a measure of specific gravity in g/cm^3. The left branch at each step indicates which minerals float and the right branch indicates which minerals sink. **47**

Figure 4-2. A K-rich feldspar aliquot from sample KHUT-1 containing a mixture of K-rich feldspar, quartz, plagioclase and possibly other minerals. Sodium polytungstate (ρ<2.58 g/cm^3) was used to remove quartz, plagioclase and heavy minerals from the 180-212 μm grain size fraction. The separate was then etched for 10 min with a diluted HF acid (10%) solution. The microphoto was taken using a digital camera mounted on a Leica MZ16A stereo microscope. **48**

Figure 4-3. Grains obtained from a K-rich feldspar separate from sample KHUT-1 with bright, rapidly decaying luminescence signals (except for Grain #26) (a), and slowly decaying luminescence signals (b). The luminescence decay curve of a grain with a sharply decaying signal (Grain #30, dashed line) is highlighted in 'b'. EDS analysis of this grain suggests that it is plagioclase. c) The luminescence decay curves in 'a' are replotted using a logarithmic scale on the y-axis, and the decay curve of Grain #26 (dashed line) is highlighted. EDS analysis suggests that this is a plagioclase grain, while all others are orthoclase grains. See Table 4-2 and Figure 4-7 for the elemental concentrations of all grains. **49**

Figure 4-4. SEM microphotographs of a subset of feldspar grains with bright, rapidly-decaying luminescence signals (e.g., Figs 4-3a, 4-3c). All grains are likely K-rich feldspars, except for Grain 26, which is likely plagioclase and is much dimmer than the rest. See Table 4-2 for EDS elemental concentrations. **53**

Figure 4-5. SEM microphotographs of a subset of grains with dim, slowly-decaying luminescence signals (e.g., Fig. 4-3b). Most of these grains are likely quartz grains. The elevated proportion of Na and Ca in Grain 30 suggests that it may be a quartz grain with plagioclase inclusions or a plagioclase grain with a weak signal. Grain 37 was crushed while being transferred from the single-grain disc hole to the specimen stub. See Table 4-2 for EDS elemental concentrations. **54**

Figure 4-6. EDS spectrum of a potassium-rich feldspar grain. The peaks associated with the Kα X-ray lines of C, O, Na, Al, Si, K and Ca, and the Kβ X-ray lines of K and Ca are highlighted in green. The red signal represents the background signal (also known as "Bremsstrahlung") derived from interactions between incident electrons and atomic nuclei. **55**

Figure 4-7. Donut plots showing the elemental concentrations of individual grains from sample KHUT-1 (ac) and museum specimens (dg) and (see Tables 4-1 and 4-2 for raw data). Grains obtained from a KF extract are shown in 'a' (bright, rapidly-decaying signals) and 'b' (dim, slowly-decaying signals). Note the lack of potassium in the grains shown in 'b'. c) Grains from a quartz separate from KHUT-1. The elemental concentrations of museum speciments of orthoclase, anorthite, laboradorite, and quartz are shown in 'd', 'e', 'f' and 'g', respectively, for comparison. **57**

Figure 4-8. Donut plots showing the elemental composition of individual K-rich feldspar grains (n=115) (a) and plagioclase, Fe-rich aluminosilicate, and quartz grains (n=25) (b). Each ring in each donut plot represents the elemental composition of a single grain. The rings in 'a' are very thin but 12 subgroups of rings is visible on the plot. All grains are from sample GHO-2 and are classified as homogeneous at the scale of a single grain (i.e., the three WDS spot measurement values for each grain were consistent within 2%). The elemental composition of the brightest quartz and plagioclase grains are highlighted in 'b'. **62**

Figure 4-9. The IRSL decay curves for the K-rich feldspar, plagioclase, quartz and Fe-rich aluminosilicate grains in Figure 4-8 are shown in 'a', 'b', 'c', and 'd', respectively. Plots 'e – h' show the same decay curves but plotted with a y-axis on a logarithmic scale. **64**

Figure 4-10. Luminescence test dose (T_n) signal brightness plotted against major element concentration for all K-rich feldspar (black diamonds), plagioclase (white squares), and quartz (grey triangles) grains. The x-axes in plots 'b', 'c', 'd' and 'f' are plotted on a logarithmic scale for clarity, and points with 0% element concentrations are plotted as 0.0001 % in these plots to avoid their omission. **65**

Figure 4-11. D_e versus major element concentration for all homogeneous K-rich feldspar (black damonds), plagioclase (white squares), and heterogeneous feldspar (white circles) grains (n=51). Grains are considered heterogeneous if their three WDS spot measurement values differ by more than 2%. The x-axes in plots 'b', 'c', and 'd' are plotted on a logarithmic scale for clarity, and points with 0% element concentrations are plotted as 0.0001 % in these plots to avoid their omission. **68**

Figure 4-12. Fading-corrected age versus major element concentration for all homogeneous K-rich feldspar (black diamonds), plagioclase (white squares), and heterogeneous feldspar (white circles) grains (n=51). Grains are considered heterogeneous if their three WDS spot measurement values differ by more than 2%. The x-axes in plots 'b', 'c', 'd' and 'f' are plotted on a logarithmic scale for clarity, and points with 0% element concentrations are plotted as 0.0001 % in these plots to avoid their omission. **69**

Figure 4-13. *g*-value versus major element concentration for all homogeneous K-rich feldspar (black diamonds), plagioclase (white squares), and heterogeneous feldspar (white circles) grains (n=51). Grains are considered heterogeneous if their three WDS spot measurement values differ by more than 2%. The x-axes in plots 'b', 'c', 'd' and 'f' are plotted on a logarithmic scale for clarity, and points with 0% element concentrations are plotted as 0.0001 % in these plots to avoid their omission. **70**

Figure 5-1. a) The IRSL signal of a laboratory-bleached and dosed (70 Gy) KF grain after IR stimulation using a range of laser powers. b) A close-up of the decay curve in 'a' in the stimulation time range of 0 to 3.7 s. c) The amount of IR (laser) stimulation time (90% power) it takes for the luminescence signal of 65 KF grains to be reduced to less than 10% of the initial value. Eighty-six percent of grains are reduced to less than 10% of their initial signal after 6 s of IR laser stimulation. c) The distribution of signal intensities from single quartz grains and KF grains from the same sample. The OSL signal was measured from the quartz grains, and the IRSL signal was measured from the feldspar grains. The quartz grain data was supplied by Jacqui Fenwick (unpublished data). All measurements were made on sample KHUT-1. **74**

Figure 5-2. a) Degradation of the ~150° C TL peak of a single KF grain as the result of holding it at 50° C for durations of 10, 100, 500 and 1000 s. b) A close-up view of the left limbs of the TL curves shown in 'a'. Note the lateral shift of the left limb of the peak (b). c) TL curves after a laboratory dose and IRSL (diode) stimulation for different durations (2 s, 10 s and 40 s). d) TL curves after a laboratory dose and stimulation at 0% power to monitor for TL signal degradation due to heating at 50°C. e) and f) are the same graphs as in c) and d), respectively, but with focus on the glow curve region up to 80°C. The background signal from a blank disc has been subtracted from all TL curves, and all TL curves have been corrected for sensitivity change (see Table 5-1). **77**

Figure 5-3. a) TL curves after a laboratory dose and IR (laser) stimulation for different durations (2 s, 10 s and 40 s). b) TL curves after a laboratory dose and stimulation at

0% power to monitor for TL signal degradation due to heating at 50°C. c) and d) are the same graphs as in a) and b), respectively, but with focus on the glow curve region up to 80°C. The background signal from a blank disc has been subtracted from all TL curves, and all TL curves have been corrected for sensitivity change (see Table 5-1). **78**

Figure 5-4. Typical IRSL decay curve from a KF grain. The signal in the first 0.134 s of stimulation minus the average count rate from the last 1.742 s of stimulation (shaded areas) was used in all calculations. The inset graph shows a typical IRSL decay curve from a quartz grain. **79**

Figure 5-5. Dose recovery test results using laboratory-bleached and heated (IR diode bleach for 1000 s, at 290 °C) grains. The given laboratory dose of 70 Gy was measured using preheats of 120, 160, 200, 240, and 280 °C for 10 s. Weighted mean (CAM) measured dose/given dose ratios and average recuperation values are shown for tests without a hotwash in 'a' and 'b', and with a hotwash listed in 'c' and 'd'. Error bars represent 1σ. The percentage of grains that passed all rejection criteria are in brackets on the x-axis. OD refers to the overdispersion calculated using the CAM. **80**

Figure 5-6. Grain rejection statistics for dose recovery tests shown in Figure 5-5. Dose recovery tests in 'a' do not include a hotwash, and those in 'b' include a hotwash. All preheat durations are 10 s. "RR1" and "RR2" refer to the recycling ratios calculated from the repeat dose points measured at the low-dose region of the dose-response curve and at the high-dose region of the dose response curve, respectively. **81**

Figure 5-7. Dose recovery tests on sun-bleached (2 days) KF grains. A given laboratory dose of 124 Gy was measured using preheats of 120, 160, 200, 240, and 280 °C for 10 s. Weighted mean (CAM) measured/given dose ratios and average recuperation values are shown for tests analyzed without a previous background (BG) subtraction (a and b), and with a previous BG subtraction (c and d). Error bars represent 1σ. The percentage of grains that passed all rejection criteria are listed in brackets on the x-axis. OD refers to the overdispersion calculated using the CAM. **83**

Figure 5-8. Grain rejection statistics for dose recovery tests shown in Figure 3-6 analyzed without (a), and with (b) the "Previous BG subtraction" data analysis method. "RR1" and "RR2" refer to the recycling ratios calculated from the repeat dose points measured at the low-dose region of the dose-response curve and at the high-dose region of the dose response curve, respectively. **84**

Figure 5-9. a) T_x/T_n graph showing the dependence of T_x on regenerative dose and SAR cycle number. If the background count rate from each natural/regenerative dose signal is subtracted from the following test dose signal (called a "previous BG subtraction"), the non-linear curvature in the dose response curve (b) is reduced. **85**

Figure 6-1. a) Shine-down curves for a KF grain and a quartz grain (inset) from sample GHO-2. The integration limits for the initial (first 0.134 s) and background (last 1.742 s) signals are shaded in grey. b) Growth curve for the same KF grain. The KF grain has a K concentration of 12.2%, and the quartz grain is 99.5% SiO2 (both measured using WDS; see text). **99**

Figure 6-2. a) Distribution of measured dose/given dose ratios obtained from the dose recovery test for sample GHO-2. The grey band is centered on 1, and the black line is centered on the weighted mean of the distribution. b) D_e distribution for sample GHO-2. c) The lRSL decay curves for the circled points in 'b'. d) D_e distribution of a modern sample (KHUT-10) collected from a sand bar in the Son River channel.

Grains with negative natural dose values, and values greater than 5 Gy lie outside the scale of the radial plot but are shown in the histogram (n=366). **100**

Figure 6-3. a) Single-grain *g*-value distribution for sample GHO-2 (n=475). All *g*-values are normalised to a delay period of 2 days. A single-aliquot *g*-value distribution (n=24) from GHO-3 is shown for comparison in 'b'. Each aliquot consists of ~25 grains that were mounted on stainless steel discs with silicone oil. Fading plots for individual grains from sample GHO-2 that exhibit a low (c) and a high (d) fading rate, respectively. e) A fading plot for one ~25-grain aliquot from sample GHO-3. **101**

Figure 6-4. a) The fading-corrected age distribution for 24 single-aliquots (white-filled circles) superimposed on the single-grain fading-corrected age distribution for sample GHO-2 (black-filled circles, n=467). b) Quarz single-grain age distribution for sample GHO-2 (n=337). c) Single-grain fading-corrected age distribution for all KF grains with *g*-values statistically equivalent to zero (within 2σ) (n=209). Black lines in plots 'a', 'b' and 'c' delineate the approximate age ranges (excluding outliers) of the feldspar and quartz single-grain distributions. d) Single-grain fading-corrected age distribution of microprobe-measured KF grains (n=51); each point is shaded according to measured K content (in weight %). **102**

Figure 7-1. a) The study area. The locations of Palaeolithic, Mesolithic and Neolithic artefacts are after Sharma and Clark (1983). Sedimentary logs for sediments containing YTT ash at Ghoghara (b) and Khunteli (c) in the Middle Son Valley, Madhya Pradesh. A 50 cm stick is used for scale in the photos of YTT ash unit in (b). A microphoto of a sample from the whitest (10YR 8/1) part of the YTT ash unit at Ghoghara (b) was taken using a digital camera mounted on a Leica MZ16A stereo microscope. **114**

Figure 7-2. a) WorldView-1 50 cm panchromatic imagery of the Rehi-Son confluence showing cliff sections where ash was observed in this study. The sites labelled 1, 2, 3 and 4 in 'a' corrospond to photographs 1, 2, 3 and 4, respectively, in 'b'. The lower ~4 cm of ash at the Ghoghara main section (photograph 1 in 'b') is thought to be primary ash (Gatt et al. 2011). The ash unit in photographs 2, 3 and 4 in 'b' show evidence of re-working in the form of a deformed lower contact with evidence of mixing with underlying deposits (2), and diffusive/gradational contacts with the surrounding sediment (3, 4). **115**

Figure 7-3. a) $IRSL_{50}$ and $pIRIR_{225}$ decay curves. The $pIRIR_{225}$ signal was measured immediately after the $IRSL_{50}$ signal on the same aliquot after it was given a laboratory dose of 28 Gy followed by a preheat of 250 °C for 10 s. Normalized decay curves are shown in the inset graph. b) $IRSL_{50}$ dose response curve. c) $pIRIR_{225}$ dose response curve. Dose response curves in 'b' and 'c' are measured on different aliquots. The solid grey lines in 'b' and 'c' illustrate where L_n/T_n was projected onto the sensitivity-corrected dose-response curve to determine D_e. The dashed grey lines on either side of the solid grey line mark the errors of L_n/T_n and D_e at 1σ. **119**

Figure 7-4. a) D_e versus preheat temperature for the $IRSL_{50}$ and $pIRIR_{225}$ signals. Recycling ratios and recuperation values for the $IRSL_{50}$ (b) and $pIRIR_{225}$ (c) signals. d) Measured dose/given dose ratios for both signals. e) Residual doses measured from KF grains that have been sun-bleached for 2 days. A 250°C/10 s preheat was used. f) Measured dose/given dose ratios obtained when the residuals of each signal (calculated as the average of all aliquots in 'e') are subtracted from the measured dose (errors have been propagated into the final measured dose/given dose estimates). Each symbol represents one aliquot, and error bars represent one standard error on all plots. All measurements were made on sample GHO-3. **120**

Figure 7-5. Representative $IRSL_{50}$ (a) and $pIRIR_{225}$ (b) fading plots for aliquots of sample GHO-3, and $IRSL_{50}$ (c) and $pIRIR_{225}$ (d) *g*-value distributions for sample GHO-3. **124**

Figure 7-6. Single-grain (a) and multi-grain aliquot (b) quartz D_e distributions for the modern sample (KHUT-10). Multigrain aliquot distributions for KF grains from the same sample measured using the $IRSL_{50}$ (c) and the $pIRIR_{225}$ signals (d). The grey shaded area should capture 95% of the points if they were statistically consistent with 0 Gy in 'c' and 5 Gy in 'd' (Galbraith *et al.* 1999). **125**

Figure 7-7. Radial plots of fading-corrected age distributions for samples GHO-2 (a), GHO-3 (b), KHUT-1 (c), and KHUT-4 (d). Solid circles are aliquots measured using the $IRSL_{50}$ signal and open triangles are aliquots measured using the $pIRIR_{225}$ signal. Residual doses of 0.635 ± 0.003 Gy and 5.61 ± 0.03 Gy have been subtracted from the $IRSL_{50}$ and $pIRIR_{225}$ data, respectively, and the errors on the residual doses have been propagated through into the error on the aliquot ages. **127**

Figure 7-8. Radial plots of single-grain quartz age distributions for samples GHO-2 (a), GHO-3 (b), KHUT-1 (c), and KHUT-4 (d). The $IRSL_{50}$ KF aliquot fading-corrected ages (open triangles) are superimposed on the quartz single-grain age distributions. e) Single-grain $IRSL_{50}$ fading-corrected ages (black dots) and $IRSL_{50}$ fading-corrected aliquot ages (open triangles) from sample GHO-2. A residual dose of 0.635 ± 0.003 Gy has been subtracted from the $IRSL_{50}$ data and the errors on the residual doses have been propagated through into the error on the KF ages. Black solid lines are centred on the component ages identified by the Finite Mixture Model (FMM) of Roberts *et al.* (2000) for the quartz and KF single-grain data. The grey shaded band is centered on the age calculated for the KF aliquot data using the MAM (Table 7-4). f) The proportion of total brightness versus the proportion of quartz and KF measured grains from sample KHUT-1. **128**

Figure 7-9. Slumped river bank deposits, including fallen silty-ash blocks adjacent to the Son River channel near the Ghoghara main section. During the monsoon season, these deposits are inundated by rising river water, washed into the river channel and transported downstream. **131**

Figure 7-10. Radial plots of single-grain quartz age distributions for samples GHO-2 (a), GHO-3 (b), KHUT-1 (c), and KHUT-4 (d). The $pIRIR_{225}$ KF aliquot fading-corrected ages (open triangles) are superimposed on the quartz single-grain age distributions. A residual dose of 5.61 ±0.03 Gy was subtracted from the $pIRIR_{225}$ data and the errors on the residual doses have been propagated through into the error on the aliquot ages. The grey shaded band is centered on the age calculated for the KF aliquot data using the MAM (Table 7-4). . **134**

Figure 7-11. Quartz and KF luminescence ages imply one of two possible scenarios: 1) the YTT ash sampled at Ghoghara and Khunteli have been reworked by fluvial processes and re-deposited either as fluvial silts or as mobile, cohesive blocks, several thousand years after the Toba event (a and b), or 2) the YTT ash was deposited soon after the volcanic event ~74 ka ago, but the underlying sediments have since been eroded and implaced by younger, inset fluvial sediments (c). **141**

Figure 8-1. Schematic cross-section of the Middle Son Valley looking east from the Rehi-Son confluence, modified after Williams and Royce (1983) to include the new Khunteli Formation introduced by Williams *et al.* (2006). Formation ages are after Williams *et al.* (2006). The ages of the Patpara and Khunteli formations include a question mark as these are debated (see Chapter 1, Section 1.2 for details). A "depositional surface" is defined here as one in which the most recent stratigraphic formation deposited is still preserved after lateral migration of the channel and/or

incision of the river into the floodplain, while an "erosional surface" is one in which one or more stratigraphic formations have been eroded, exposing one or more older underlying stratigraphic formations. It is possible that some erosion has occurred on all alluvial surfaces immediately before lateral migration of the channel and/or incision of the river into the floodplain. **145**

Figure 8-2. a) The Middle Son Valley (MSV) and the locations of archaeological sites along the banks of the Son River after Sharma and Clark (1983). b) WorldView-1 50 cm panchromatic imagery of the study area. c) White dashed lines delineate the prominent WSW-ENE trending terrace escarpment ~500-700 m south of the Son River and the gentle break in topography parallel to the dirt road north of this. Yellow lines delineate topographic survey transects A-A' and B-B'. Luminescence sample sites are indicated by yellow dots, and the three archaeological sites of the Dhaba locality of Haslam *et al.* (2012) are indicated by black dots. **146**

Figure 8-3. a) View south across the Son River from Dhaba sites 2 and 3 (Haslam et al. 2012). b) View northwest from the location of IRSL sample 5, which was taken from the highest terrace on the south side of the Son River. The dirt road along which IRSL samples 2, 4 and 6 were collected (Fig. 8-2b) is visible just south of the Son River. **147**

Figure 8-4. Topographic profiles A-A' and B-B'. The current river floodplain, as well as IRSL age estimates of near-surface alluvial sediments are indicated. The depositional age of the YTT is unclear (see Chapter 7). The elevation of YTT as in the Ghoghara main section is shown in B-B'. See Figure 8-2c for a plan view of the traverses and IRSL sample locations. **150**

Figure 8-5. Alluvial sediments sampled for luminescence dating. Samples H-1 and H-5 were taken from the highest terrace south of the Son River. Samples M-2, M-4 and M-6 were taken beside the dirt road ~240-340 m away from the river channel. Samples L-3 and L-7 were taken in gullies near the edge of the lowest terrace. Meter stick for scale. Refer to Figure 8-2c for sample locations. **151**

Figure 8-6. Typical IRSL decay curve (a) and dose-response curve (b) for sample H-1. IRSL signal in the first 1 s of stimulation minus the mean background from the last 20 s of stimulation (grey shading in 'a') was used to calculate the De values and estimate the fading rates. c) A fading plot for one aliquot from sample H-1. d) Calculated g-values for aliquots from all samples in Table 8-1, as well as two samples (KHUT-1 and KHUT-4) collected from above and below YTT ash at the Khunteli Formation type-section (n=264). e) The same g-values in 'd' displayed in a radial plot. **154**

Figure 8-7. $IRSL_{50}$ fading-corrected aliquot ages for each sample, displayed on a radial plot. The grey shaded area is centered on the CAM age estimate and should capture 95% of the points if they were statistically consistent with each other (Galbraith et al. 1999). The black line is centered on the MAM age estimate. **157**

Figure 8-8. Schematic cross-section of the Middle Son Valley looking east from the Rehi-Son confluence, modified after Williams and Royce (1983). Proposed ages of near-surface sediments on the south side of the Son River are based on IRSL age estimates from this study. Sediments consistent in age and sedimentology of the Patpara Formation of Williams *et al.* (2006) may exist at some depth below the surface (see text for explanation). See Figure 8-1 for a specific definition of "depositional surface". **160**

Figure 8-9. The Summer Monsoon Factor of Clemens and Prell (2003) based on stacked Arabian Sea core records and the modelled SW Indian monsoon record is from Prell and Kutzbach (1987). The boundaries between marine isotope stages (MIS) are from Waelbroeck et al. (2002). Periods of alluvial aggradation and incision for the

Middle Ganga Plains (Roy et al. 2011), the southern Ganga Plains (Gibling et al. 2005), the Sabarmati River (Srivastava et al. 2001) the Belan Valley (Gibling et al. 2008) and the Middle Son Valley (Williams et al. 2006) are indicated by black bars. Yellow arrows mark incision events. The timing of alluviation and incision is approximate. The Middle Son Valley formation age estimates are from Williams et al. (2006) and the luminescence age estimates are from this study (Tables 7-5 and 8-1). **162**

Figure 8-10. NW Indian lacustrine records from Prasad et al. (1997) (a), Wasson et al. (1984) (b), and Enzel et al. (1999) (c) as interpreted by Prasad and Enzel (2006), and the lacustrine record from Sharma et al. (2004) (d) as interpreted in this study. e) The speleothem isotope record from Oman (Fleitmann et al. 2003). The interpretation of the NW India lacustrine records is presented only in relative wetness terms for the different basins; the absolute water levels of lake or ground water or their transfer to values of precipitation are still problematic (Prasad and Enzel 2006). The Oman cave record was proposed to represent variations in SW monsoon rainfall. The arrow indicates the time when the trend towards aridity began as inferred by Prasad and Enzel (2006). The grey shaded areas represent the luminescence age estimates of the tops of the lowest (~10 m) and middle (~20 m) terraces across from the Rehi-Son confluence in the Middle Son Valley (this study). **164**

List of Tables

Table 1-1. Estimated ages of stratigraphic formations and their artefact and fossil assemblages in the Middle Son Valley (after Williams & Royce 1982; Pal *et al.* 2005; and Williams *et al.* 2006). **6**

Table 1-2. Numerical ages for Middle Son Valley deposits, updated from Jones and Pal (2009). **7**

Table 2-1. Advantages and disadvantages of using quartz or feldspar for luminescence dating (modified after Lian 2007a). **21**

Table 2-2. The SAR protocol for single aliquots (from Wintle and Murray 2006, after Murray and Wintle 2000, 2003). **24**

Table 2-3. Light wavelengths, intensities, and energy parameters of the light sources associated with the RisøTL/OSL system, Model TL/OSL-DA-20. Note that the intensity and energy per unit time per unit area of the IR laser is an order-of-magnitude greater than that of the the green laser, making it the most powerful light source available. **32**

Table 3-1. Luminescence samples used in this thesis. **42**

Table 3-2. Lx/Tx errors calculated from two aliquots of sample GHO-2 containing ~25 grains each. Aliquot 1 was prepared using silicone oil, and Aliquot 2 was prepared using Crystalbond 509. **43**

Table 3-3. SAR measurement protocol for KF grains. **44**

Table 4-1. Anomalous fading SAR measurement protocol for single KF grains. **50**

Table 4-2. Elemental concentrations of single grains of feldspar (F) and quartz (Q), as determined through EDS analysis. **56**

Table 4-3. Elemental concentrations of one quartz and three feldspar museum specimens, as determined using EDS. **56**

Table 4-4. WDS crystal types, standards and detection limits for all elements measured for single KF grains of sample GHO-2. **60**

Table 4-5. Microprobe-measured grains from a K-rich feldspar separate from sample GHO-2. **61**

Table 5-1. The measurement protocol followed to test for grain heating. This sequence (performed on a laboratory-bleached grain) was followed for both stimulation sources: the IR diodes (90% power), and the IR laser (90% power). **75**

Table 5-2. The SAR measurement protocol for single KF grains. **79**

Table 6-1. De and age estimates for sample GHO-2, together with their overdispersion (OD) values. **98**

Table 6-S1. L_x/T_x errors calculated from two aliquots of sample GHO-2 containing ~25 grains each. Aliquot 1 was prepared using silicone oil, and Aliquot 2 was prepared using Crystalbond 509. **108**

Table 6-S2. Environmental dose rates for sample GHO-2 (in Gy/ka). **108**

Table 6-S3. The SAR measurement protocol for single KF grains. **108**

Table 6-S4. KF grain rejection statistics for sample GHO-2. **109**

Table 6-S5. Anomalous fading SAR measurement protocol for single KF grains. **109**

Table 6-S6. WDS crystal types, standards and detection limits for all elements measured for single KF grains of sample GHO-2. **110**

Table 7-1. Geological sections examined by Gatti *et al.* (2011). Modified after Gatti *et al.* (2011). **113**

Table 7-2. Lithofacies codes, descriptions and interpretations (after Miall 2006). **116**

Table 7-3. SAR measurement protocols for KF aliquots measured using the $IRSL_{50}$ and $pIRIR_{225}$ signals. **118**

Table 7-4. Anomalous fading SAR measurement protocol. **122**

Table 7-5. IRSL50 and pIRIR225 De values, average recycling ratios, recuperation rates, fading rates and ages, together with quartz OSL FMM component ages for the same samples. **123**

Table 7-6. Radionuclide activities (in Bq/kg) of samples collected from sediments that bracket the YTT ash at Khunteli and Ghoghara. See text for details. **136**

Table 7-7. External dose rates measured using HRGS for samples collected above and below YTT ash. **138**

Table 7-8. External dose rates measured using low-level beta counting and *in-situ* gamma spectrometry. **139**

Table 8-1. De values, fading rates, and calculated IRSL age estimates for all samples. **153**

Table 8-2. Environmental dose rates for all samples. **156**

Chapter 1 – Introduction and Project Aims

1.1 Introduction

Palaeoanthropological studies that aim to understand the history of human evolution and expansion out of Africa have focussed largely on a wealth of archaeological evidence in the Levant, or peripheral geographic zones such as western Europe, but relatively little work has been done in the Arabian Peninsula or the Indian subcontinent (Petraglia 2007). This PhD project is part of a larger study conducted by an international team of archaeologists, geologists, volcanologists and palaeobiologists that is focussed on the chronology of human occupation and the potential influence of the ~74 ka Toba super-eruption in northern Sumatra on the environment and human populations in India (Williams *et al.* 2009; Haslam & Petraglia 2010; Williams *et al.* 2010; Petraglia *et al.* 2012; Jones 2012; Williams 2012a, b). The Toba volcanic eruption is the largest known eruption in the Quaternary (Chesner *et al.* 1991). It formed a 100 x 30 km caldera (Toba Lake) and erupted ~2800 km^3 of rhyolitic magma. The minimum mass of ashfall has been estimated to be 2 x 10^{15} kg, representing ~30% of the total mass of erupted material (Rose & Chesner 1987). Ash from the Toba super-eruption (also known as Youngest Toba Tuff, or YTT) has been found in the South China Sea, the Arabian Sea, as well as various locations across the Indian subcontinent (Gatti *et al.* 2011: Fig. 1). Some have suggested that the global cooling triggered by this event may have resulted in near extinction of human populations (Rampino & Self 1993; Ambrose 1998; Rampino & Ambrose 2000; Ambrose 2003).

Between 2003 and 2009, multiple field seasons involving geological and archaeological excavations have been conducted in the Jerreru Valley, Andhra Pradesh, and in the Middle Son Valley, Madhya Pradesh (Petraglia *et al.* 2012). A series of archaeological sites spanning from the Acheulian to the historic period were identified in the Jerreru Valley, as well as a buried YTT tephra deposit estimated to exceed 1 million cubic meters in volume. Middle Palaeolithic artefacts were found above and below YTT ash at two sites in the Jerreru Valley, and technological analyses of these assemblages show no evidence of any major shifts in tool manufacturing techniques up until 38 ka (Petraglia *et al.* 2007; Petraglia *et al.* 2009; Haslam *et al.* 2010). Petraglia *et al.* (2007) reported optically stimulated luminescence (OSL) ages of 77 ± 6 ka and 74 ± 7 ka from samples collected from artefact-bearing deposits below and above the YTT ash, respectively. New OSL ages from nine Indian sites reported at a conference by Roberts *et al.* (2010) gave pre-Toba dates of ~74 ka or earlier, as expected, but nearly all of the post-Toba dates were ~55 ka or younger. These new ages call into question the validity of the original ~74 ka age estimate for post-Toba artefact-bearing deposits in the Jerreru Valley. Some argue that strong evidence for human occupation *immediately* after the Toba event is still lacking, as the precision of

existing luminescence age estimates is too low (Balter 2010; Williams *et al.* 2010; Williams 2012a).

Terraced alluvial deposits in the Middle Son Valley, Madhya Pradesh, India contain YTT ash and Palaeolithic, Mesolithic and Neolithic artefacts (Sharma & Clark 1983; Williams *et al.* 2006) (Fig. 1-1a). Despite the many archaeological and geological excavations and surveys that have been conducted in the past, (e.g., Sharma & Clark 1983; Williams & Royce 1983; Williams & Clarke 1984; Haslam *et al.* 2011; Haslam *et al.* 2012), as well during this study, no sites could be found that contain stratified YTT ash in close association with artefacts. However, additional support for the argument that Middle Palaeolithic hominins were present in India soon after (and perhaps prior to) the Toba eruption is provided by a newly discovered archaeological site, Dhaba, on the north bank of the Son River, a few tens of meters west of its confluence with the Rehi River (Haslam *et al.* 2012) (Dhaba sites 2 and 3 are shown in Fig. 1-1b), but these sites are currently undated. This PhD project is focussed on developing and applying luminescence dating techniques to alluvial sediments in the Middle Son Valley in order to help constrain the time of final deposition of YTT ash- and artefact-bearing alluvial deposits.

1.2 The Middle Son Valley

The Middle Son Valley lies within the Vindhyachal Basin (60,000 km^2) in north-central India (Korisettar 2007) (Fig. 1-1a). It is one of four valleys in north-central India (including the Ganga, Yamuna and the Belan valleys) that preserve a cultural sequence going back to the early Acheulean (Sharma 1973; Sharma *et al.* 1980; Sharma & Clark 1983; Misra & Pal 2002). The stratigraphy in the Middle Son Valley has been correlated with that of the neighbouring Belan Valley (Williams *et al.* 2006; Gibling *et al.* 2008). The Son River is the largest southern tributary to the Ganges, and runs east-west through north-eastern Madhya Pradesh. It is not free to move laterally by more than 10 km and the alignment of the valley is controlled by the east-west trending Narmada-Son tectonic lineament that is still prone to seismic activity (Vita-Finzi 2004). The Middle Son Valley is bound to the north by the Kaimer Range, the eastern-most extension of the Vindhya Range, and the Baghelkhand Plateau to the south. The Kaimer Range consists of Vindhya Formation limestones, sandstones and shales that rise up to ~200 m above the alluvial plain of the Middle Son Valley, which is situated in an ancient tectonic graben. The local climate is subtropical, and heavily influenced by the monsoon season, which lasts from July to September.

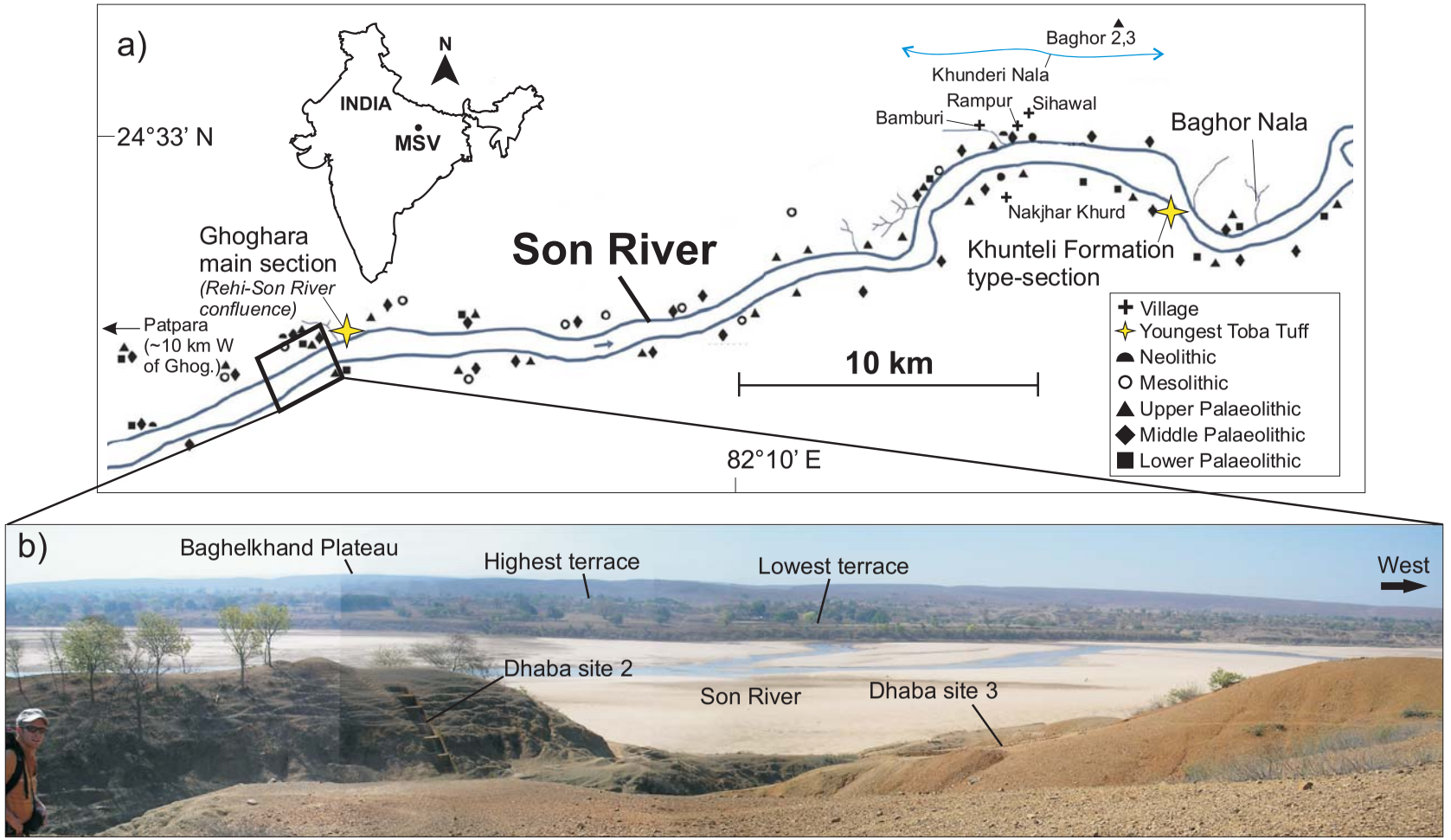

Figure 1-1. a) The Middle Son Valley (MSV) and the locations of archaeological sites and preserved YTT ash along the banks of the Son River after Sharma and Clark (1983). B) View south across the Son River from Dhaba sites 2 and 3 of Haslam *et al.* (2012).

1.2.1 Alluvial deposition in the Middle Son Valley

Alluvial terraces, ranging from ~5 to ~35 m above river level, have been observed to extend over 70 km along the length of the Son River, between Baghor in the east and Chorhat in the west (Williams & Royce 1983) (Fig. 1-1b). These terraces are thought to have formed during a period of tectonic stability, when changes in river sedimentation reflected changes in local plant cover and river load-to-discharge ratios, which in turn, were influenced by regional climate (Williams & Royce 1982; Williams *et al.* 2006). The stratigraphic sequence in the neighbouring Belan Valley has also been interpreted in light of palaeoclimatic proxies and local changes to the river course (Gibling *et al.* 2008).

The climate of the Middle Son Valley (as well as the Belan Valley) is influenced by the Southern Oscillation, the NE (winter) monsoon, and to a large extent, the SW (summer) monsoon (Prasad & Enzel 2006; Williams *et al.* 2006). In the summer months of June to September, the Intertropical Convergence Zone (ITCZ) migrates northwards and the surface SW monsoon winds bring large amounts of precipitation to the Indian subcontinent. During the winter, northeasterly surface winds bring cold, dry continental air. The precipitation associated with the SW monsoon drives river discharge and can substantially influence river flow dynamics, sedimentation and morphology (Srivastava *et al.* 2001; Williams *et al.* 2006; Gibling *et al.* 2008; Roy *et al.* 2011). Palaeoclimate data and climate model simulations suggest that two mechanisms exert the dominant forcing on millennial-scale variations in SW monsoon strength. These are changes in the orbit of the Earth, predominantly in the precession of the equinoxes which control the amount of insolation reaching the Earth as a function of season, and hence the ability of the Tibetan Plateau to warm in the summer. Second, changes in glacial boundary conditions (i.e., ice volume, sea surface temperature (SST), albedo, and atmospheric trace-gas concentrations), which alter the way in which the monsoon reacts to astronomical forcing. Clemens and Prell (1991) and Clemens *et al.* (1991) have argued that while precession-forced insolation changes are the major pacemaker of monsoon strength, glacial boundary conditions have played a relatively minor role in determining the timing and strength of the Arabian Sea monsoon.

The Middle Son Valley terraces are comprised of sediments that have been subdivided into five stratigraphic formations that represent major phases in the alluvial history (Williams & Royce 1982, 1983; Williams & Clarke 1984, 1995; Williams *et al.* 2006) (Fig. 1-2), including a major phase of prolonged aggradation that is thought to have occurred between ~39 ka and ~16 ka ago. These include (from oldest to youngest) the Sihawal, Khunteli, Patpara, Baghor and Khetaunhi Formations, and their sedimentology, estimated ages and associated archaeology are summarized in Table 1-1. Published numerical ages for all stratigraphic formations are listed in Table 1-2.

1.2.2 Sihawal Formation

The Sihawal Formation is the oldest formation and is thought to record mass flow movements (largely in the form of mudflows and alluvial fan gravels) and the accumulation of colluvium on the exposed and eroded bedrock surface under semi-arid conditions and reduced south-west monsoonal input (Williams & Royce 1983; Haslam *et al.* 2011). During this period, the Son River discharge is thought to have been low, with ephemeral or seasonal streams draining channels on the valley sides. The mottled clay overlying the basal gravels is thought to be reworked aeolian loess (Williams & Royce 1983). Lower Palaeolithic artefacts are reported to underlie this loess (Williams & Royce 1983; Haslam *et al.* 2011). The type-section for this formation is ~1 km east of Sihawal and it was initially estimated to be ≥100 ka in age (Pal *et al.* 2005; Williams *et al.* 2006). This age estimate is based on a thermoluminescence (TL) age of 104 ± 4 ka and a polymineral fine-grain infrared stimulated luminescence (IRSL) age of ~100 ka (Pal *et al.* 2005) from trenches near Nakhjar Khurd. More recently, single-grain optically stimulated luminescence (OSL) ages of ~125 ka to ~131 ka have been reported for sediments associated with the Sihawal Formation containing Acheulean artefacts at an archaeological site called Bamburi (Fig. 1-1a, Table 1-2) (Haslam *et al.* 2011).

.

Table 1-1. Estimated ages of stratigraphic formations and their artefact and fossil assemblages in the Middle Son Valley (after Williams & Royce 1982; Pal *et al.* 2005; and Williams *et al.* 2006).

Formation	Artefact/fossil assemblage	Sedimentological characteristics	Estimated age
Sihawal	Lower Palaeolithic (Acheulian) artefacts	Rests unconformably on eroded Proterozoic bedrock and consists of angular mudstone, sandstone and quartzite clasts (up to 50 cm in diameter) set in a matrix of structurelss, mottled grey and brown silty clay. Locally, the boulder clay is overlain by mottled grey and brown silty clay loam with an erosional upper contact with the Patpara Formation. Maximum observed thickness of 1.5 m.	≥100 ka
Khunteli[1]		Consists of a pale yellow brown unconsolidated medium sand with a discontinuous bed of volcanic ash ~1.5 m thick. This ash-rich sand is unconformably overlain by gravel, which, in turn, is conformably overlain by a series of calcareous clays, loams and sands.	~74 ka?
Patpara[2]	Fresh and abraded Middle Palaeolithic artefacts	Unconformably overlies the Sihawal Formation. Dark reddish medium to very coarse sands, granules, pebbles and gravels consisting of locally derived sandstone, mudstone and quartzite, as well as agate, chalcedony, and other microcrystalline silicic rocks derived from the Deccan Trap Basalts in the headwater region of the Son River. Structureless or crudely developed undulose lamination, and partially cemented by iron oxide. Overlain by dark reddish-brown indurated silty clay in places, but this is commonly eroded by the overlying Baghor Formation. Maximum exposed thickness of 10 m.	~58 to ~40 ka?
Baghor *coarse lower member*	Rolled and abraded Middle Palaeolithic artefacts and well preserved fossils, including buffalo, hippo, crocodile, antelope, elephant and tortoise	Unconsolidated cross-bedded sand with granules, pebbles and cobbles composed mainly of quartz and minor concentrations of sandstone, mudstone, quartzite, chalcedony, and chert. Calcium carbonate cementation is concentrated along planar bedding surfaces and foreset laminae. Maximum thickness ~10 m.	~39 to ~20 ka
Baghor *finer upper member*	Fresh Upper Palaeolithic artefacts	Forms the highest aggradational surface in the Son Valley, and rests conformably on the underlying coarse member of the Baghor Formation. Horizontal layers of silts, clays, and less commonly, fine sands, which vary in thickness from 1 to 4 m and continue laterally for 23 km. Blocky or massive structure and irregular pedogenic calcium carbonate nodules, tubules and plates at well- defined levels. These become more heavily concentrated near the top.	~20 to ~16 ka
Khetaunhi	Microlithic and Neolithic artefacts	Forms a prominent aggradational terrace ~10 m above river level. Interbedded silts and clays with occasional fine sand beds. Maximum thickness ~10 m.	<10 ka

[1]The introduction of the Khunteli Formation has recently been deemed problematic on the grounds that few exposures have been identified with confidence, and its stratigraphic position relative to other formations has not been demonstrated clearly (Jones & Pal 2009). See Section 1.2.5 for details.

[2]The proposed age of the Patpara Formation was originally based on one IRSL age of 58 ± 6 ka. The validity of this age has been recently questioned in light of archaeological evidence, the stratigraphic context of the IRSL sample, and the fact that the IRSL age was not corrected for fading (Jones & Pal 2009). See Section 1.2.3 for details.

Table 1-2. Numerical ages for Middle Son Valley deposits, updated from Jones and Pal (2009).

Date (ka) (^{14}C ka cal BP[1])	Method/location	Stratigraphic formation (associated archaeology)	Reference
3.215 ± 0.07 (3.26–3.63)	^{14}C (shell)/ not specified	Khetaunhi (Neolithic)	Williams and Clarke (1984)
4.13 ± 0.11 (4.25–5.00)	^{14}C (charcoal)/ not specifid	Khetaunhi (Neolithic)	Williams and Clarke (1984)
4.74 ± 0.08 (5.31–5.61)	^{14}C (shell)/ not specified	Khetaunhi (Neolithic)	Williams and Clarke (1984)
5.305 ± 0.09 (5.91–6.28)	^{14}C ($CaCO_3$)/ not specified	Baghor fine member	Mandal (1983) Williams and Royce (1982)
6.66 ± 0.18	^{14}C (charcoal) Baghor 3	Baghor fine member (microliths)	Mandal (1983)
8.33 ± 0.22	^{14}C (charcoal)\ Baghor 2	Baghor fine member (microliths)	Mandal (1983)
11.87 ± 0.12 (13.4–14.0)	^{14}C (shell)/ Rampur	Baghor fine member or coarse member (Upper Palaeolithic)	Williams and Clarke (1984) Clark and Williams (1987)
12.81 +0.22/-0.21	^{14}C (pedogenic $CaCO_3$)/ Baghor Nala	Baghor coarse member	Mandal (1983)
13.145 ± 0.14 (15.1–16.1)	^{14}C (pedogenic $CaCO_3$)/ Baghor Nala	Baghor coarse member	Mandal (1983) Williams and Royce (1982)
19 ± 2	IRSL (coarse-grained feldspar)/ Baghor Nala	Baghor fine member	Pal *et al.* (2005) Williams *et al.* (2006)
20.135 ± 0.22 (23.45–24.75)	^{14}C (shell)/ Khunderi Nala	Baghor fine member?	Williams and Clarke (1984, 1995)
24 ± 3 (or 22 ka in Pal et al.(2005))	IRSL (coarse-grained feldspar)/ Baghor Nala	Baghor coarse member	Pal *et al.* (2005) Williams *et al.* (2006)
26.1 ± 5.4	TL (polymineral fine grains)/ Nakhjar Khurd	Baghor coarse member	Pal *et al.* (2005)
26.25 ± 0.42 (29-~31)	^{14}C (shell)/ Rampur	Baghor coarse member? (Upper Palaeolithic?)	Williams and Clarke (1984, 1995) Clark and Williams (1987)
39 ± 9	IRSL (coarse-grained feldspar)/ Baghor Nala	Baghor coarse member	Pal *et al.* (2005) Williams *et al.* (2006)
26.85 +0.82/-0.75	^{14}C (pedogenic $CaCO^3$)/ Gerwa well, (location not specified)	Patpara	Mandal (1983) Sharma and Clarke (1982)
140 ± 11	OSL (quartz)/ Patpara	Patpara (late Acheulean)	Haslam *et al.* (2011)
137 ± 10	OSL (quartz)/ Patpara	Patpara (late Acheulean)	Haslam *et al.* (2011)
58 ± 6	IRSL (coarse-grained feldspar)/ Sihawal	Patpara	Pal *et al.* (2005) Williams *et al.* (2006)
~100	IRSL (polymineral fine grains)/ Nakhjar Khurd	Sihawal	Pal *et al.* (2005)
104 ± 20	TL (polymineral fine grains)/ Nakhjar Khurd	Sihawal	Williams and Clarke (1995) Clark and Williams (1987)
131 ± 10	OSL (quartz)/ Bamburi	Sihawal (late Acheulean)	Haslam *et al.* (2011)
125 ± 13	OSL (quartz)/ Bamburi	Sihawal (late Acheulean)	Haslam *et al.* (2011)
131 ± 9	OSL (quartz)/ Bamburi	Sihawal (late Acheulean)	Haslam *et al.* (2011)

[1]Calibrated radiocarbon ages are from Williams *et al.* (2006), and are expressed at the 95% confidence interval..

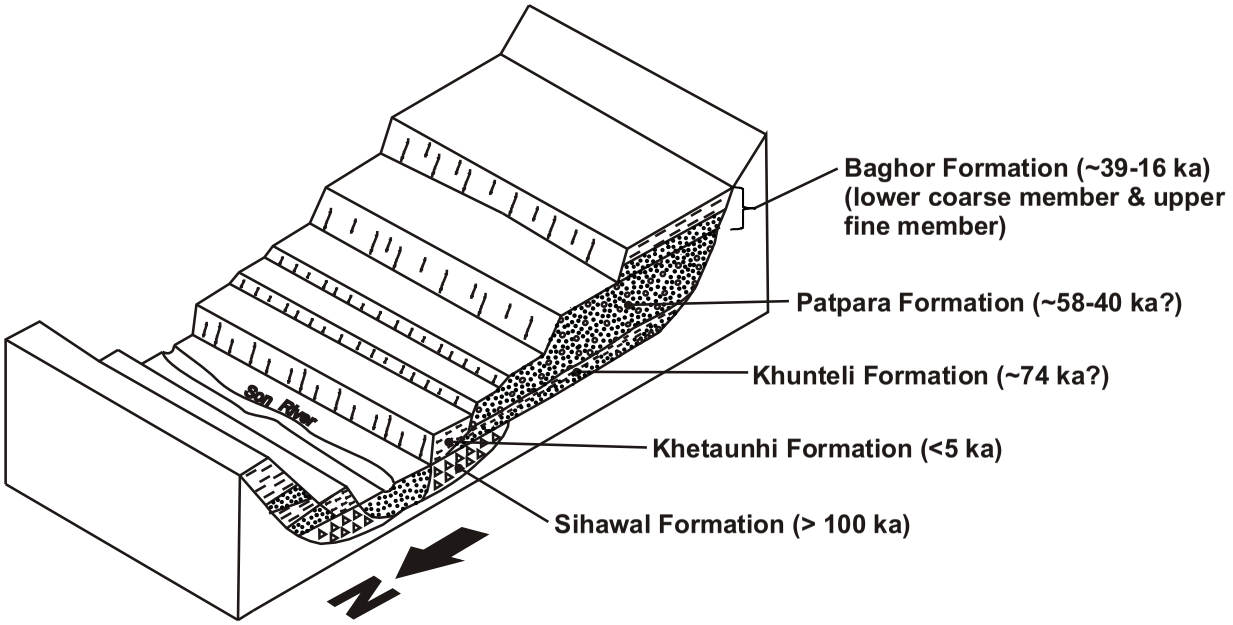

Figure 1-2. Schematic cross-section of the Middle Son Valley looking east from the Rehi-Son confluence, modified after Williams and Royce (1983) to include the new Khunteli Formation introduced by Williams *et al.* (2006). Formation ages are estimated from reports from Williams and Royce (1982), Pal *et al.* (2005), and Williams *et al.* (2006). The ages of the Patpara and Khunteli formations include a question mark as these are debated (see Section 1.2 for details).

1.2.3 Patpara Formation

The Patpara Formation was initially thought to record rapid sediment deposition in a channel at peak or falling-peak flood stage, sometime in the Late Pleistocene (Williams & Royce 1983). The undulose laminations and massive structure have been attributed to rapid rates of channel bed aggradation, and the alternating coarse and fine sediment units were thought to record a shifting channel. Its distinct red colour was attributed to the mobilisation and precipitation of iron and manganese throughout the deposit during a period of moist conditions, followed by a return to drier conditions (Williams & Royce 1983). Stratified occurrences of Middle Palaeolithic artefacts have been reported in this formation at the type locality, located ~10 km west of the Ghoghara main section (Blumenschine *et al.* 1983). The proposed age of the Patpara Formation is disputed and was initially based on only one IRSL age of 58 ± 6 ka from near the village of Sihawal (Pal *et al.* 2005; Williams *et al.* 2006) (Fig. 1-1a, Table 1-2). The validity of this age estimate has been questioned in light of archaeological evidence, the stratigraphic context of the IRSL sample (which is poorly constrained) (Jones & Pal 2009), the fact that the IRSL age was not corrected for fading (Pal *et al.* 2005), and new single-grain OSL ages from sediments in the Patpara Formation type locality at Patpara (Fig. 1-1a, Table 1-2) (Haslam *et al.* 2011).

Jones and Pal (2009) state that a ~58 ka age for the Patpara Formation contradicts available archaeological evidence, as the Patpara Formation preserves late Lower Palaeolithic and Middle Palaeolithic artefacts (Blumenschine *et al.* 1983) that should be older than ~74 ka according to what is currently known about the Indian Palaeolithic record for this period (Misra 1989; Misra 2001; James & Petraglia 2005). Sediments near the base of an exposed sequence at the Patpara type locality have been recently dated to ~137 and ~140 ka using single-grain OSL techniques, suggesting that their deposition occurred at about the same time as sediments associated with the Sihawal Formation at Bamburi and Nakhjar Khurd (Section 1.2.2) (Haslam *et al.* 2011). Haslam *et al.* (2011) note that sediments associated with the Sihawal Formation are the product of activity within the main Son River channel, while the Patpara type locality sediments, more than 30 km away, are derived from local sources separated from the main river channel by an east-west trending bedrock ridge (Haslam *et al.* 2011: Fig. 1). They propose that assessing the temporal and spatial continuity between the two formations will require reanalysis of Sihawal-like sediments near the base of the Patpara Formation in the Patpara type locality, and Patpara-like sediments near the upper part of the Sihawal Formation type-section.

1.2.4 Baghor Formation

The Baghor Formation has been divided into a coarse lower member and a fine upper member (Williams & Royce 1983). The coarse member is associated with rolled Middle Palaeolithic artefacts and well preserved fossils, including buffalo, hippo, crocodile, antelope, elephant and tortoise. It is thought to record channel scour and sand deposition within a low sinuosity bed-load river with a high load-to-discharge ratio (Williams & Royce 1983). Post-depositional calcium carbonate-cemented horizons suggest a trend towards aridity (Williams & Royce 1983). The fine member is thought to record a change from a bed-load to suspended-load flow regime, with intermittent overbank accretion of fine sediment on a floodplain, and is associated with fresh Upper Palaeolithic artefacts (Williams & Royce 1983). The Baghor Formation is thought to represent a major phase of aggradation during a period of aridity leading up to and encompassing the Last Glacial Maximum (Williams *et al.* 2006). This arid period has also been documented in other parts of India (Chapter 8) and the intertropical world (Williams *et al.* 2006, and references therein). The age of the Baghor Formation has been constrained by 11 dates including radiocarbon ages from carbonates, charcoal and shell, IRSL ages from coarse-grained feldspar, and one TL age from polymineral fine grains (Table 1-2). The age estimates are derived from samples collected at archaeological sites Baghor 2 and 3, north of Khunderi Nala, Khunderi Nala, Rampur, Baghor Nala, and Nakhjar Khurd (Fig. 1-1a, Table 1-2).

1.2.5 Khunteli Formation

The Khunteli Formation, located on the south side of the Son River ~25 km east of the Ghoghara main section (Fig. 1-1a), was introduced by Williams *et al.* (2006) to account for YTT ash-bearing sediments in the valley, but recent work has shown that the introduction of this formation and its temporal relationship with other formations is problematic (Jones & Pal 2009). It is thought to record erosion and deposition of fluvial sands, gravels, clays and loams, and the choking of tributary streams with YTT ash ~74 ka ago (Williams *et al.* 2006). Williams *et al.* (2006) hypothesized that the Khunteli Formation and its YTT ash deposits are actually older than the Patpara Formation (40-58 ka, Table 1-1), but alternative hypotheses have been proposed. For example, Williams and Royce (1982) reported the YTT as part of the coarse member of the Baghor Formation, Williams and Clarke (1995) placed the YTT before the Baghor Formation, and Jones and Pal (2005) and Jones (2010) believed the YTT accumulated sometime after deposition of the Patpara Formation. Sedimentological observations made by Gatti *et al.* (2011) suggest that the ash deposit at this location has been reworked. At the time of writing of this thesis, no numerical ages associated with the Khunteli Formation, or sediments encasing the YTT ash, have been published. Numerical

ages from YTT and/or YTT ash-bearing alluvial sediments are needed to clarify its position within the stratigraphic sequence in the Middle Son Valley.

1.2.6 Khetaunhi Formation

After deposition of the fine member of the Baghor Formation ~16 ka ago, the Son River is thought to have gone through episodes of downcutting in response to global warming and a wetter climate, before an aggradational phase in the Holocene (Williams & Royce 1983; Williams *et al.* 2006). This aggradational phase led to the deposition of the Khetaunhi Formation in the form of a ~10 m-high inset terrace, which is best observed on the south bank of the Son River near the Rehi-Son River confluence. Three radiocarbon ages ranging from ~3.2 to ~4.7 ka have been obtained from shell and charcoal from this formation (Williams & Clarke 1984) (Table 1-2), but the precise locations of the radiocarbon sample sites were not specified.

1.2.7. The need for better chronological control

Terraced alluvial sediments in the Middle Son Valley extend for over 25 km from the Rehi-Son confluence to the Khunteli Formation type-section, but the chronology of these sediments is constrained by only a few numerical ages that are spread over a wide area (Fig. 1-1a, Table 1-2). Moreover, the geomorphic and sedimentary contexts of many dated sites are poorly documented (Table 1-2) (Jones & Pal 2009). This makes lateral correlations between "known age" stratigraphic units and their associated artefacts difficult and possibly misleading. Further work is necessary to extend this chronology to more sites using robust numerical dating techniques, in conjunction with more detailed sedimentological and geomorphological observations.

1.3 YTT ash – a reliable chronostratigraphic marker?

YTT ash was examined at two locations in this study: one near the confluence of the Son and Rehi Rivers (24°30'7.608"N, 82°1'2.748"E) (including the Ghoghara main section, and seven additional sections, all within ~100 meters of each other, described by Gatti *et al.* (2011), see Chapter 7), and one ~25 km east of the Rehi River, on the south side of the Son River in the Khunteli Formation type-section (82°16'33.59"E, 24°32'27.718"N) (Fig. 1-3) (Williams *et al.* 2006; Gatti *et al.* 2011). The YTT exposed near the Rehi-Son confluence was first discovered by Williams and Royce in 1980 (Williams & Royce 1982). The ash exposed at both sites has been sampled and studied extensively in previous geological and

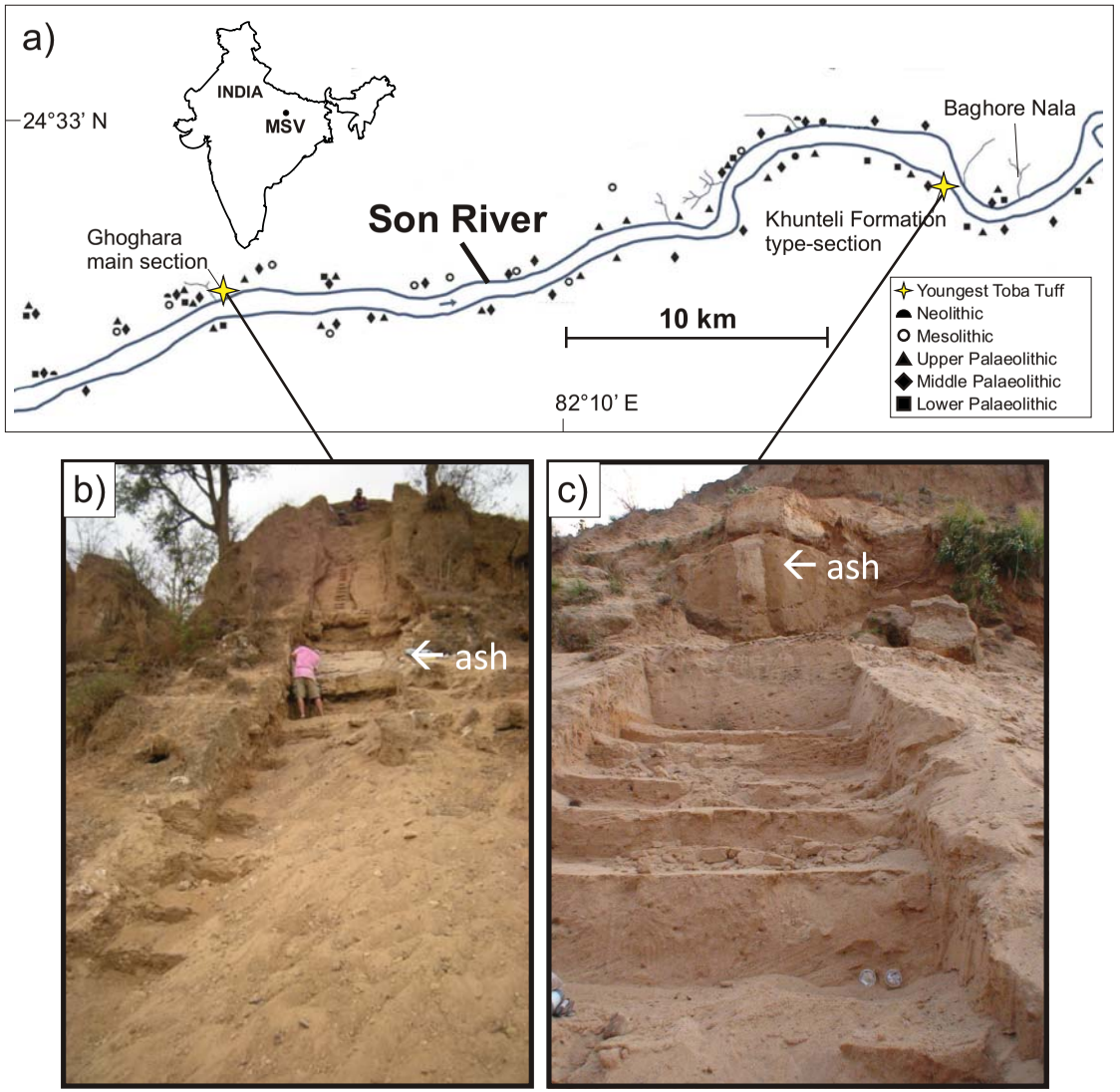

Figure 1-3. a) Study area. b) Ghoghara main section containing YTT ash. The lower 4 cm of this ash unit is thought to be primary ash. c) Khunteli Formation type-section containing YTT ash-rich sandy silt *(photo courtesy of R.G. Roberts)*. This ash unit is thought to be re-worked (Gatti *et al.* 2011).

palaeoenvironmental studies (e.g., Acharyya & Basu 1993; Williams & Clarke 1995; Westgate *et al.* 1998; Williams *et al.* 2006; Petraglia *et al.* 2007; Williams *et al.* 2009; Jones 2010; Gatti *et al.* 2011).

To date, there have been no attempts to date the ash directly, however, extensive geochemical analyses on the deposits suggests that it is YTT. Acharyya and Basu (1993) showed that the chemical composition of whole-ash samples from Khunteli (spelled Khutiali in their Table 2) is comparable to that of ash samples collected from Orissa, the Central Narmada Valley basin, the Kudki basin in Maharashtra, the YTT deposits in the Toba Caldera, Sumatra, as well as glass shard fractions from ash collected from deep sea cores in the Indian Ocean, the Bay of Bengal, and Kota Tampan, Malaysia. Instrumental neutron activation analyses showed that chondrite-normalized rare earth element abundancies in ash from the Middle Son Valley are similar to those of other ash samples from the Indian subcontinent, as well as Indian Ocean deep sea cores and Toba pumice (Acharyya & Basu 1993). Electron microprobe analyses on individual glass shards by Shane *et al.* (1995), Westgate *et al.* (1998), and Petraglia *et al.* (2007), and on biotite by Smith *et al.* (2011), also confirm that the ash correlates with the ~74 ka YTT event in Sumatra. The YTT ash units at Ghoghara and Khunteli have been used as chronostratigraphic markers to help correlate the stratigraphies of the Son and neighbouring Belan Valleys (Williams *et al.* 2006), as well as the Middle Son Basin and the Central Narmada Basin (Acharyya & Basu 1993). Carbon isotope compositions of pedogenic carbonates sampled above, within, and below the ash from excavated sections at both locations have been used to infer changes in C_3 and C_4 biomass before and after the Toba eruption (Williams *et al.* 2009). Based on this evidence, it has been proposed that C_3 forest was replaced by wooded to open C_4 grassland in north-central India after the Toba eruption (Williams *et al.* 2009).

The reliability of the YTT ash as a chronostratigraphic marker has been questioned due to contradictions in the literature regarding its relation to other stratigraphic formations (see Jones & Pal 2009, and discussion in Section 1.2.5), and to sedimentological observations made from YTT ash-bearing sediments (Jones 2010; Gatti *et al.* 2011). Gatti *et al.* (2011) and Matthews *et al.* (2012) consider the lowermost 4 cm of the YTT ash unit at the Ghoghara main section to be primary ash fall based on its sedimentological characteristics. These include weakly-developed planar bedding but no cross-bedding, a uniform thickness and bedding, a white colour (Munsell colour 10YR 8/1) and an absence of detrital (non-volcanic) material. Sedimentological observations by Gatti *et al.* (2011) suggest that the ash deposit at the Khunteli Formation type-section (Fig. 1-3b) has been reworked, as it shows evidence of mixing with siliclastic silt and sand and, therefore, cannot be used as a chronostratigraphic marker. Clearly, improved chronological control on the

final deposition of the ash is needed before it can be used as a chronostratigraphic marker in geological and palaeoenvironmental investigations.

1.4 Constraining the time of final deposition of alluvial deposits and their artefacts – methods used previously

The depositional age of Middle Son Valley alluvial sediments and their associated artefacts have been constrained using radiocarbon, TL, IRSL, and OSL dating techniques (Table 1-2). These methods, and some of their limitations, are described below.

1.4.1 Radiocarbon dating

Radiocarbon dating exploits the fact that ^{14}C in living creatures, which is in equilibrium with that available in the atmosphere or surrounding waters, begins to decay after their death with a half-life of 5730 years (Roberts & Jacobs 2008). Radiocarbon ages from shell or charcoal in the Middle Son Valley reflect the time of death of the organism, but not necessarily the time of final deposition of the shell or charcoal. If the shell or charcoal has been reworked after death of the organism, then radiocarbon ages from this material can overestimate the burial age of the artefacts or alluvial sediments in question. Radiocarbon dates from shell in the alluvial sediments in the Belan Valley are commonly several thousand years older than OSL dates obtained from the same bed (Gibling *et al.* 2008). The accuracy of the radiocarbon ages from pedogenic carbonates ($CaCO_3$) in the Middle Son Valley are undetermined (Mandal 1983). These would be minimum ages if the pedogenic carbonate precipitated sometime after the deposition of the host sediment, or maximum ages if the carbonates have been re-mobilized and re-deposited. Because of its half-life, radiocarbon dating is not useful for materials older than ~55,000 years (Roberts & Jacobs 2008); luminescence dating techniques, by contrast, can yield ages for materials up to several hundreds of thousands of years old (Aitken 1998).

1.4.2 Thermoluminescence dating

Thermoluminescence dating exploits the fact that many natural minerals absorb and store ionizing energy from radiation emitted from radioisotopes within mineral grains and in their immediate surroundings, as well as from cosmic rays. If the mineral is heated to a sufficiently high temperature, some of the stored energy is released in the form of light, called thermoluminescence (TL) (Lian 2007b). To determine a TL age, it is necessary to obtain 1) the laboratory dose of radiation that produces the same intensity of TL as did the environmental radiation dose (called the equivalent dose, D_e) and 2) a measure of the environmental dose rate (Lian 2007b).

1.4.3 OSL dating

OSL dating was developed from TL dating in the mid 1980s (Huntley *et al.* 1985), and has major advantages over TL dating for sun-bleached sediments. The main advantage in OSL dating is that the most appropriate electron traps are emptied – that is, those that have likely been emptied in antiquity by sunlight exposure, rather than by heat. Because only the most light-sensitive electron traps are sampled, there is less likelihood of age overestimation due to insufficient sunlight exposure and much younger sediments can be dated. Also, determination of the D_e in OSL dating is generally simpler than in TL dating, can produce more accurate ages by performing a range of internal checks on sample integrity and suitability for dating, and usually result in better precision (Lian 2007a).

OSL ages from single grains of quartz have been determined for two archaeological sites (Bamburi and Patpara) in the Middle Son Valley for sediments last exposed to sunlight about 130–140 ka ago (Haslam *et al.* 2011) (Fig. 1-1a, Table 1-2). The quartz from these sites was shown to be suitable for single-aliquot regenerative-dose (SAR) dating procedures (see Chapter 2, Section 2.4 for a description of SAR), and the robustness of the OSL ages was evaluated using a range of data analysis techniques and assumed sediment burial conditions (Haslam *et al.* 2011). Thus, these ages are thought to reliably constrain the deposition of sediments and late Acheulean artefacts at these sites, although the D_e values lie at the upper end of the range achievable using quartz.

1.4.4 IRSL dating

IRSL ages from polymineral fine grains and coarse-grained feldspars have also been used to constrain the chronology of artefact-bearing stratigraphic formations in the Middle Son Valley (Table 1-2) (Pal *et al.* 2005; Williams *et al.* 2006). These ages are problematic, however, because a multiple-aliquot additive-dose method was used to estimate the D_e values, and the dating protocol did not include a correction for anomalous fading (Williams *et al.* 2006). Multiple-aliquot techniques require 20–50 aliquots of sample to be prepared, dosed, heated and measured in the laboratory, with normalization between aliquots (Lian 2007a). Single-aliquot techniques are generally preferred because 1) they minimize the amount of sample and measurement time required in the laboratory (Duller 1991), 2) single-aliquot regenerative-dose techniques allow for the self-normalization and sensitivity correction of each aliquot, 3) each aliquot provides an independent measure of D_e to construct a D_e distribution, and 4) the resulting D_e distributions facilitate the identification of aliquots that contain grains that have not been fully bleached by sunlight before burial, or that are contaminated by grains from older or younger deposits. The identification of

incompletely bleached or contaminating grains is best achieved when each aliquot is composed of only a single grain (Jacobs & Roberts 2007).

Ideally, attempts to date feldspars should include tests and corrections for anomalous fading, a phenomenon thought to be the result of the quantum-mechanical tunnelling of electrons from one defect site to another (Spooner 1994a) (see Chapter 2); they should also make use of a single mineral (e.g., potassium feldspar, KF), instead of a mixture of minerals that likely respond differently to dosing, heating and irradiation in the laboratory (Duller 1997). Geochronological investigations in the Middle Son Valley would benefit from research that assesses the suitability of KF grains to single-aliquot techniques for D_e determination and for fading measurement and correction, as luminescence ages from KF grains could provide an independent source of chronological control with which quartz luminescence ages can be compared.

1.5 The aims of this research and structure of the thesis

The main aims of this thesis are threefold: 1) to explore the luminescence dating potential of individual grains and multi-grain aliquots of potassium feldspar from alluvial sediments in the Middle Son Valley using single-aliquot regenerative-dose dating techniques, fading measurements and corrections; 2) to assess the time of final deposition of YTT ash-bearing deposits at the Ghoghara main section and at the Khunteli type-section using luminescence dating techniques; and 3) to test and refine current models of alluvial deposition of the Middle Son Valley (Williams *et al.* 2006; Gatti *et al.* 2011) using new IRSL ages and field observations. The specific research objectives include the following:

1. To explore the IRSL dating potential of individual KF grains using single-aliquot regenerative-dose (SAR) dating techniques, fading measurements and corrections. This includes:
    a. an investigation into the possibility of using the luminescence characteristics of individual grains to differentiate between KF grains and contaminating quartz, plagioclase or other mineral grains in a sample;
    b. investigations into the suitability of single KF grains for SAR measurement procedures; and
    c. an assessment of the source of spread (or overdispersion) in a KF single-grain age distribution for a sample collected from deposits underlying YTT.
2. To use luminescence ages from both quartz and KF grains to assess the depositional age of YTT ash-bearing deposits at the Ghoghara main section and the Khunteli Formation type-section. This involves:

a. evaluating the reliability of IRSL ages obtained from small KF aliquots of samples collected from YTT ash-bearing deposits using single-grain quartz OSL ages from the same samples and the KF single-grain age distribution obtained in research objective 1.
b. evaluating the reliability of previous palaeoenvironmental interpretations made from isotope compositions of pedogenic carbonates sampled above, within, and below the ash (Williams *et al.* 2009).

3. To determine new IRSL ages from KF aliquots of samples collected from a series of alluvial terraces near the confluence of the Son and Rehi Rivers, and combine these with topographic data and field observations to help test and refine a model of alluvial deposition for the Middle Son Valley (Williams *et al.* 2006). The reliability of these new IRSL ages are informed by the results of research objective 2.

The following sections of the thesis are organized into 8 chapters (Chapters 2-9), and these are summarized below:

- Chapter 2 is a literature review on luminescence dating principles and procedures for quartz and feldspar.
- Chapter 3 describes the methods of luminescence sample collection, preparation and measurement used in this thesis.
- Chapter 4 explores relationships between KF grain major element concentrations and luminescence signals, D_e values, fading rates and calculated KF grain ages (research objective 1a).
- Chapter 5 describes a series of dose-recovery experiments on single KF grains to determine their suitability to SAR measurement procedures (research objective 1b). These include a series of dose recovery tests on sun-bleached and laboratory-bleached grains, as well as assessments of the effects of IR laser power and stimulation duration on KF grain IRSL signals. An attempt to assess the potential of grain heating by the IR laser is also described.
- Chapter 6 explores sources of age overdispersion in a K-rich feldspar sample using measurements of D_e, fading corrections applied to single-grain ages, and measurements of K content in individual grains (research objective 1c). These results are contained in a manuscript that has been accepted for publication in *Radiation Measurements*, and is referred to here as Neudorf *et al.* (2012).
- Chapter 7 assesses the age of YTT ash deposits at two sites in the Middle Son Valley using both quartz and KF grains extracted from sediments bracketing the ash deposits (research objective 2a), and discusses the implications for

palaeoenvironmental reconstructions using pedogenic carbonates collected from these sediments.

- Chapter 8 combines new IRSL ages for river terrace sediments near the Rehi Son confluence with field observations and topographic profiles to test a model of alluvial deposition for the Middle Son Valley (Williams *et al.* 2006) (research obective 3).
- Chapter 9 includes a summary and conclusions, as well as some recommendations for future research directions.

Chapter 2 – Luminescence dating

OSL dating is a numerical dating technique that exploits the luminescence properties of minerals (usually quartz or feldspar) to estimate the time since their last exposure to sunlight (e.g., the time of sediment deposition and burial). The calibrated OSL intensity of a mineral is used as a measure of the total radiation dose absorbed by that mineral since burial. This data is combined with independent measurements of the environmental dose rate at the sample site to obtain a burial age of the sediment using the following equation:

$$\text{Age (ka)} = D_e \text{ (Gy)} / \text{environmental dose rate (Gy/ka)} \quad (1)$$

OSL dating was introduced by Huntley *et al.* (1985) as an alternative to TL dating, a technique first developed in the 1960s where D_e estimates are obtained through thermally stimulated luminescence measurements (Lian 2007b). OSL dating has since gained popularity in the geosciences and archaeology, because the depositional age of sediment can be estimated directly (Roberts 1997; Lian & Roberts 2006) and because the age range goes well beyond that of radiocarbon dating, spanning the last glacial-interglacial cycle (Rittenour 2008). Methods are currently being developed to extend the age range of quartz (e.g., Yoshida *et al.* 2000; Chauhan *et al.* 2009; Jain 2009; Duller & Wintle 2012). If anomalous fading in feldspars is absent or can be corrected for, theoretically feldspars could be used to date sediments well over a million years old (Wallinga *et al.* 2007).

2.1 Luminescence dating principles

Minerals contain structural defects and chemical impurities that can act as traps for freely roaming (unbound) electrons in the conduction band (Aitken 1998). Unbound electrons are produced by ionization radiation (alpha, beta and gamma rays) emitted by the mineral grains and surrounding sediments, and unknown sources from outer space (cosmic rays). The term "dose" (such as the equivalent radiation dose measured from a sample, or a laboratory-administered radiation dose) is defined as the energy absorbed per kilogram, and the unit of measurement is the Gray (Gy) where 1 Gy = 1 J/kg. For the dating of Quaternary events, dose rates are usually expressed in Gray per thousand years (Gy/ka).

The number of electrons that accumulate in traps in the crystal lattice of a mineral is proportional to the radiation dose absorbed by that mineral (Aitken 1998). These electrons can be evicted from traps by exposure to light or heat. In the case of light, the integrated luminescence (or total area beneath an OSL or IRSL decay curve) of a mineral is proportional to the number of trapped electrons, and hence to age. The luminescence intensity at any point in an OSL or IRSL decay curve is also proportional to the number of

trapped electrons (Aitken 1998). Therefore, the energy stored by an aliquot or a grain as a result of radiation exposure can theoretically be estimated by measuring the OSL or IRSL signal.

The efficiency with which a trap type is emptied by light (or the detrapping probability) is dependent on the trap depth below the conduction band (deeper traps requiring higher excitation energies, as measured in electron volts (eV)), the trap thermal stability, optical sensitivity, and the temperature and wavelength used during stimulation (some traps being more sensitive to specific wavelengths of light) (Bailey *et al.* 1997; Aitken 1998; Singarayer & Bailey 2003; Thomsen *et al.* 2008; Jain 2009). The detrapping probability (b) is proportional to the photoionization cross-section of the trap (σ) (the probability that a photon will eject an electron from the trap), and the maximum stimulation light intensity (I_0) (i.e., $b = \sigma I_0$) (Bulur 1996).

The sensitivity (or OSL per unit dose) of a mineral in response to optical stimulation is proportional to the number of evicted electrons that recombine at luminescence recombination centres (Murray & Wintle 2000). Under certain conditions, a proportion of evicted electrons will recombine in non-radiative recombination centres, and/or occupy other shallow or deep traps that are less optically sensitive, reducing the OSL sensitivity of the mineral (Murray & Roberts 1998; Murray & Wintle 2000). The luminescence efficiency per unit trapped charged and the rate of trap filling per unit ionization in natural aliquots or grains may be different to that in samples that have been bleached and/or given radiation doses in the laboratory (Murray & Wintle 2000). These sensitivity changes need to be monitored and corrected for when using single-aliquot regenerative-dose dating protocols (see Section 2.2) (Murray & Roberts 1997; Murray & Roberts 1998; Galbraith *et al.* 1999; Murray & Mejdahl 1999; Wallinga *et al.* 2000).

2.2 Quartz or feldspar?

The choice of quartz or feldspar for luminescence dating depends on the abundance of these minerals in the desired grain size fraction, their suitability for dating sediments of a particular age range, and the luminescence characteristics of these minerals at a particular site (Lian 2007a). The mineral of interest is typically extracted from a sample using heavy liquid separation techniques (Aitken 1998), but if the sampled sediment is composed predominantly of silt and clay, then heavy liquid separation of minerals can be difficult (Kim *et al.* 2009). The quartz fraction can be targeted using post-IR blue stimulation (Banerjee *et al.* 2001; Roberts & Wintle 2001; Zhang & Zhou 2007). Quartz can also be chemically isolated in fine grain sediments using hydrofluorosilicic acid (H_2SiF_6) or hydrofluoric acid (HF) (Roberts 2007 and references therein).

The advantages and disadvantages associated with luminescence dating of quartz and feldspar have been summarized by Lian (2007a and references therein), and are listed in Table 2-1. The following sections describe the luminescence characteristics of quartz and feldspar, and commonly used regenerative-dose measurement protocols for these minerals.

Table 2-1. Advantages and disadvantages of using quartz or feldspar for luminescence dating (modified after Lian 2007a).

Quartz		Feldspar	
Advantages	***Disadvantages***	***Advantages***	***Disadvantages***
Highly resistant to weathering	Relatively low luminescence intensity; some samples emit no luminescence	Luminescence saturates at higher radiation doses	Weathers more readily in nature than does quartz
Luminescence signal bleaches more rapidly in sunlight than that from feldspar	Luminescence saturates at low radiation doses compared to that of feldspar	Luminescence intensity may be orders of magnitude higher than that of quartz	Suffers from anomalous fading
Does not appear to suffer from anomalous fading	Thermal transfer can be higher in quartz than in feldspar	The high K content in KF grains make them less sensitive to differences in beta dose received by individual grains in their burial environment (beta microdosimetry)	The luminescence signal bleaches more slowly than that of quartz

2.3 The luminescence process in quartz

The luminescence process in quartz can be summarized by an energy level diagram (Fig. 2-1). Irradiation of the crystal causes electrons to become detached from their parent nuclei and subsequently trapped at local defects in the crystal lattice that are attractive to electrons (T). Subsequent heating or optical stimulation can release these electrons, and those that recombine radiatively at luminescence centres (L) will emit a photon of light. Only traps sufficiently deep below the conduction band (~1.6 eV or more) are useful for OSL dating, because they can hold electrons for several millions of years (Aitken 1998).

Figure 2-2 shows TL curves for quartz measured before and after a 10 s exposure to a green (514 nm) laser beam delivering 5 mW/cm^2 to the sample. The detection window was centred on the violet/near-UV region and the sample was heated at 10 °C/s. The peak at 325°C is easily bleachable, has an emission peak at 380 nm, and is presumed to be the main source trap for OSL in quartz (Wintle 1997; Aitken 1998). The peak at 375°C has been termed the 'slowly bleaching peak' and has an emission peak at 480 nm (Wintle 1997).

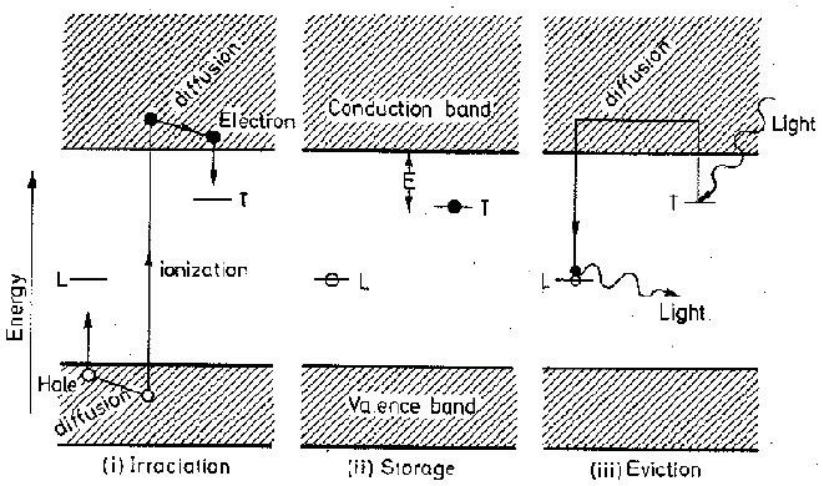

Figure 2-1. The luminescence process in quartz. (i) Ionization due to exposure of the crystal to nuclear radiation, with trapping of electrons and holes at defects L and T, respectively. (ii) Storage during antiquity. (iii) Electron eviction from T and subsequent recombination at L in response to optical stimulation. Alternatively, electrons may recombine at non-luminescence centres, be recaptured by a trap of the same type, or be captured by another type of trap. From Aitken (1998).

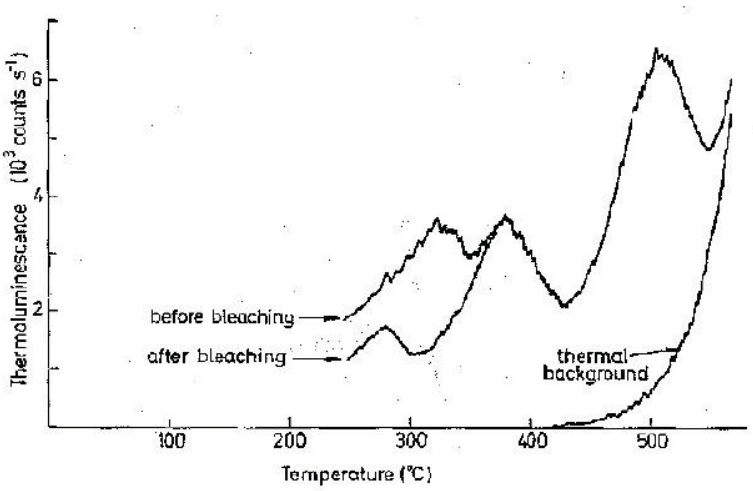

Figure 2-2. The effect of bleaching (with a green laser beam for 10 s) on the TL glow-curve of quartz grains (from Aitken 1998, based on Rhodes (1990)).

Other peaks (not shown in Figure 2-2) can appear at 110°C, 160°C, 180°C and 220°C (Wintle 1997; Murray & Roberts 1998). The 160°C and 280°C peaks have been shown to be relatively insensitive to optical stimulation, and can be a source of thermally transferred charge to the main (325°C) OSL trap during preheating (Murray & Roberts 1998). The 110°C TL peak is absent in natural samples and accumulates charge during

irradiation, or phototransferred charge during illumination, of the sample in the laboratory (Murray & Roberts 1998). This peak can be used to monitor sensitivity change in quartz (Murray & Roberts 1998; Singhvi *et al.* 2009).

Typically, luminescence signals (an example shown in Fig. 2-3) are measured using continuous-wave (CW) stimulation where the prompt luminescence emission is recorded during constant power excitation (Bulur *et al.* 2000). The decrease in quartz CW-OSL intensity with stimulation time is slower than what would be expected in a curve exhibiting exponential decay (McKeever *et al.* 1997). This is attributed to the contribution of multiple components (each approximated by an exponential equation) to the overall signal (Bailey *et al.* 1997; Jain *et al.* 2003) and to retrapping of electrons in non-luminescence centres or other traps (McKeever *et al.* 1997). Quartz CW-OSL decay curves can be fitted using an equation that equals the sum of 3 or more exponential terms representing first-order components of the signal. These components usually consist of a fast, medium and at least one slow component (Bailey *et al.* 1997; Wintle & Murray 2006).

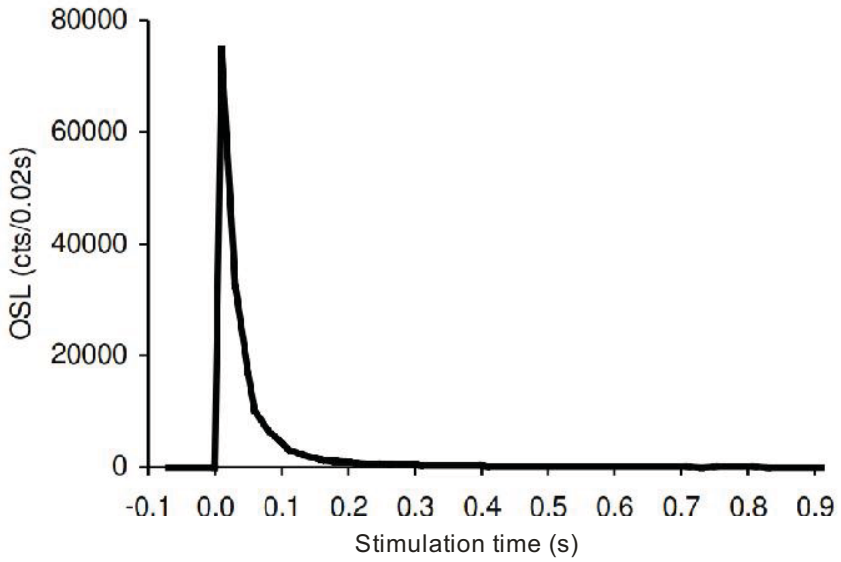

Figure 2-3. An OSL decay curve from a single quartz grain. The OSL signal intensity is reported in photon counts (cts) per 0.02 s of green (532 nm) laser stimulation. From Duller *et al.* (2003).

2.4 OSL measurement protocols

The most commonly used (and likely the most robust) technique for measuring the D_e in quartz aliquots or grains is the single-aliquot regenerative-dose (SAR) protocol (Murray & Roberts 1998; Roberts *et al.* 1998; Galbraith *et al.* 1999; Murray & Wintle 2000). This protocol involves constructing an OSL dose-response curve by repeatedly dosing, heating, and optically stimulating a sample (Table 2-2). The measurement of the natural signal (L_n) is followed by the measurement of a laboratory-given test dose (T_n). A dose-

response curve is then generated from the induced signals (L_x) arising from a series of regenerative doses given in the laboratory, each followed by another test dose measurement (T_x) to correct for sensitivity changes (Galbraith *et al.* 1999). L_x/T_x ratios at each dose point result in a sensitivity-corrected dose-response curve onto which L_n/T_n is projected to determine D_e. Quartz dose-response curves are typically fitted by a saturating exponential or saturating exponential-plus-linear function (Galbraith *et al.* 1999; Murray & Wintle 2000).

Table 2-2. The SAR protocol for single aliquots (from Wintle and Murray 2006, after Murray and Wintle 2000, 2003).

Step	Treatment	Observed
1	Give dose[1], D_i	
2	Preheat (160-300°C for 10 s)	
3	Stimulate for 40 s at 125°C	$\rightarrow L_i$[2]
4	Give test dose, D_T	
5	Heat (160-300°C)	
6	Stimulate for 40 s at 125°C	$\rightarrow T_i$[2]
7	Stimulate for 40 s at 280°C	
8	Return to 1	

[1]For the natural sample, i=0 and D_n is the natural dose.
[2]L_i and T_i are derived from the stimulation curve, typically the first 1-10 s of initial OSL signal, minus a background estimated from the last part of the stimulation curve.

To determine whether or not a sample is appropriate for the SAR, tests have been integrated into the SAR procedure to check for negligible recuperation (the "zero-dose point") and proper correction for sensitivity change (the "recycling ratio") (Murray & Wintle 2000). The "zero-dose point" is the sensitivity-corrected signal obtained from a 0 Gy regenerative dose. The resulting signal is called the recuperated signal (Aitken & Smith 1988). This signal may include a residual signal from the test dose measured in the preceeding SAR cycle that was not completely depleted during OSL stimulation, and/or charge that has been thermally transferred from optically insensitive traps to optically sensitive traps during the previous irradiation, heating and optical stimulation (Huntley & Clague 1996; Murray & Wintle 2000). Murray and Wintle (2000) suggest that the recuperated signal should not exceed 5% of L_n/T_n.

At the end of a SAR run, the signal from an additional regenerative dose (or a "repeat dose point") of the same magnitude as one measured earlier in the SAR run (usually the first regenerative dose after the natural) is used to check for proper sensitivity correction of the regenerative-dose signals. The ratio of the sensitivity-corrected repeat dose signal to the first regenerative-dose signal after the natural is termed the "recycling ratio". If SAR is

successful in correcting for sensitivity change, then this ratio should be unity, but a range of values between 0.90 and 1.10 is commonly considered acceptable (Murray & Wintle 2000). Recuperation and build up of background signal during a SAR cycle may be minimized by applying a high temperature OSL stimulation after each SAR cycle (Murray & Wintle 2003), restricting L_x and T_x measurements to the first few channels of the OSL decay curve (this method also serves to minimize detection of medium and slow components), and (or) applying early-light background subtraction techniques (e.g., Cunningham & Wallinga 2010). Dose recovery tests (the recovery of a laboratory dose after bleaching by artificial light or sun-light) (Roberts *et al.* 1999; Wallinga *et al.* 2000) also provide a check on the suitability of a sample to the SAR protocol.

The SAR procedure assumes that the sensitivity of the test dose is directly proportional to the sensitivity of the preceding regenerative dose, and that the test dose following the measurement of the natural adequately corrects for any sensitivity change of the natural after the first measurement cycle (Murray & Roberts 1997; Murray & Roberts 1998; Murray & Wintle 2000).

2.5 The luminescence process in feldspar

It is thought that the IRSL signal arises from a single trap type (Baril & Huntley 2003) corresponding to a TL peak at ~400°C (Murray *et al.* 2009). Poolton *et al.* (2002a; 2002b) have suggested that the IRSL from feldspar is the product of two processes: i) localised recombination by tunnelling from the excited state of the trap to the recombination centre (hole trap), and ii) electronic transfer through the conduction band-tail states to the recombination centre. Band-tail states occur between the conduction and valence bands of the crystal lattice. They are the result of impurities or defects resulting in non-standard bond angles between atoms that create several isolated deformations in the conduction band potential (Poolton *et al.* 2002a). Band-tail states are areas that allow some (restricted) electron mobility. IRSL recombination can occur when electrons are lifted into an excited state, then transferred into these band-tail states before recombining at a trapping hole (Poolton *et al.* 2002a) (Fig. 2-4).

Feldspar TL curves can vary from sample to sample because of changes in mineralogy from aliquot to aliquot or grain to grain (Duller 1997). Two peaks are commonly observed in natural KF TL curves when measured using a blue-biased transmission filter and a heating rate of 5°C/s. One appears between 250 and 330°C, and another closer to 400°C (Fig. 2-5). Irradiated samples of KF also include a broad peak at 150-180°C (Duller 1997; Murray *et al.* 2009). Earlier work has shown that both the 250-280°C and 330°C peaks are bleachable, and do not seem to be sourced from different trap types (Duller 1997). More recent work has shown that two TL peaks in KF appear to be

depleted by IR stimulation: a peak at 140°C and another at 410°C (Murray *et al.* 2009). Comparisons between TL glow curves and pulse annealing curves suggested that the 140°C TL peak does not contribute to the IRSL signal. Rather, the source of the IRSL seems to be derived predominantly from charge associated with the 410°C TL peak, even though for both

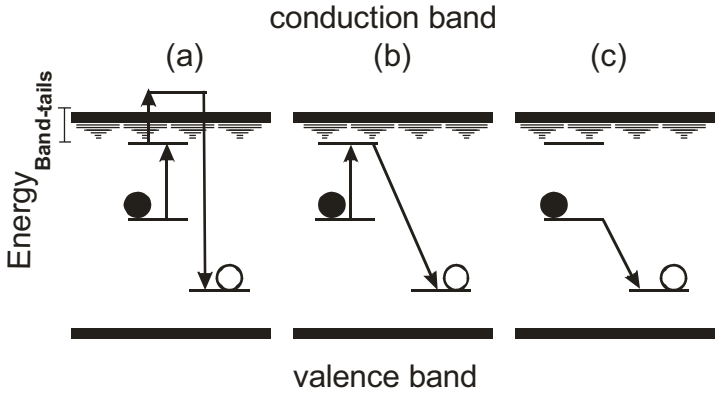

Figure 2-4. The luminescence process in feldspar, involving an electron trap and a hole trap (Poolton *et al.* 2002a). (a) Low energy optical excitation (~1.4 eV) raises the electron to deep-lying band-tail states, and thermal energy from the lattice allows thermal ionization, followed by recombination. (b) If the defects are close, recombination via tunnelling is possible from the excited state with no thermal activation. (c) If the electron and hole traps are very close, recombination via tunnelling from the ground state is possible.

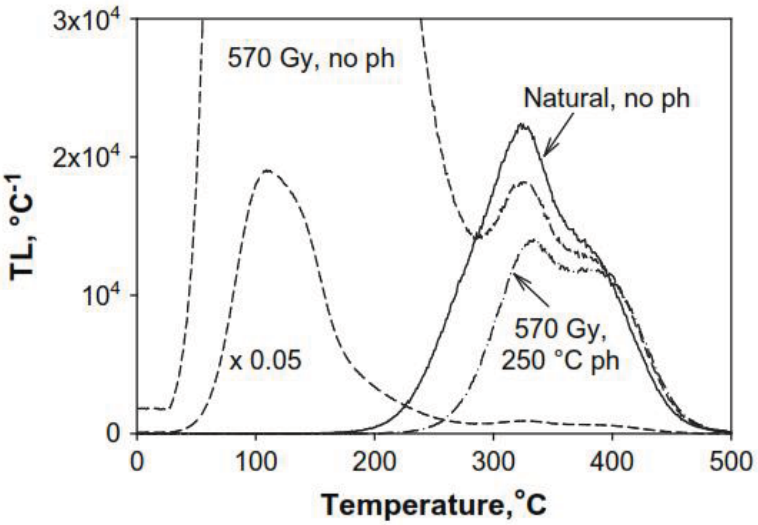

Figure 2-5. TL glow-curves for a single KF aliquot (from Murray *et al.* 2009). Three TL glow-curves are plotted, showing the natural signal with no preheat ("no ph"), the signal after a 570 Gy dose and no preheat, and the signal after a 570 Gy dose and a 250°C preheat. The 570 Gy, "no ph" curve is plotted again after multiplication by 0.05. The heating rate used was 5 °C/s.

peaks, there is a linear correlation between the IRSL observed and the loss in TL signal due to IRSL stimulation. This correlation has been explained by a reduction in recombination centres in both TL peaks during IRSL stimulation (Murray *et al.* 2009). IRSL stimulation does not cause a shift in TL peak position, and this has been interpreted as supporting evidence that the electrons are derived from a single trap type (Murray *et al.* 2009).

IRSL decay curves from feldspar have never been described using a single exponential function. However, linear modulated (LM-) IRSL curves of single feldspar grains (Bøtter-Jensen *et al.* 2003) and dose reduction versus stimulation time curves that follow a single exponential decay for KF aliquots (Thomsen *et al.* 2008), provide supporting evidence that the IRSL signal of feldspar is dominated by a single trap type. The non-exponential decay of the IRSL signal may be attributed to the detrapping and recombination probabilities of electrons, as suggested by Thomsen *et al.* (2008). Some electrons may become re-trapped or recombine at non-luminescent centres during stimulation, as is common for quartz (Aitken 1998), and some electrons may only become evicted after prolonged stimulation times (i.e., during the later part of the IRSL decay curve), as a result of increased donor (electron)-acceptor (hole) distances (Thomsen *et al.* 2008).

2.6 Anomalous fading

2.6.1 Causes and geological control

The traps most useful for IRSL dating require at least 1.4 eV of excitation energy to evict their electrons (Aitken 1998). In practice, however, it has been found that at 20°C the IRSL signal from these deep traps fades over time contrary to kinetic predictions of their thermal stability, and this is attributed to the loss of electrons from traps that should be thermally stable at ambient temperatures over geological time, to other defects and centers in the feldspar crystal lattice (Wintle 1973; Spooner 1994a). This effect has been attributed to quantum-mechanical tunnelling, where charge recombines without travelling through the conduction band (Visocekas 1985; Spooner 1994a; Visocekas 2002; Huntley 2006). Anomalous fading occurs in all feldspar types (Spooner 1994a). Rates have been thought to be higher for volcanic feldspar than sedimentary feldspar (Aitken 1998), although evidence to the contrary has been given by Huntley and Lian (2006). In plagioclase feldspar the fading rate seems to correlate positively with Ca and Fe content (Huntley & Lian 2006). Tsukamoto and Duller (2008) measured fading rates from four basalt samples and found that samples containing olivine, pyroxene and plagioclase phenocrysts had higher fading rates than glassy samples.

2.6.2 Toward a non-fading signal

Recently, work has focussed on identifying a non-fading signal in feldspar (e.g., Jain & Ankjærgaard 2011). The far-red (710 nm) TL emission in feldspar has been shown to be resistant to fading (Visocekas *et al.* 1994; Visocekas 2000; Visocekas & Guérin 2006). Tsukamoto and Duller (2008) showed that, for their basalt samples, fading rates measured using OSL signals detected in the UV, and TL signals detected in the blue, are generally higher than fading rates measured using IRSL signals detected in the blue. After experimentation with various stimulation wavelengths, detection windows and temperatures, Thomsen *et al.* (2008) found that the fading rates after IR stimulation were the highest, followed by green, blue and post-IR blue stimulation. They attributed this to the density of donor and acceptor electron traps, where IR stimulation led to the recombination of electrons between close donor-acceptor pairs (where anomalous fading is more likely), and blue and post-IR blue stimulation led to the recombination of electrons between more widely spaced donor-acceptor pairs. They also observed lower fading rates for higher stimulation temperatures and for the later part of the luminescence decay curve than for the initial part. They suggested that the luminescence from the later part of the curve represents the recombination of electrons in more distal traps via the conduction band or tunnelling from an excited state. Due to increased donor-acceptor trap distances, these electrons were thought to be less susceptible to anomalous fading (Thomsen *et al.* 2008). The lowest fading rates observed were obtained using a post-IR IR stimulation at an elevated temperature (i.e., IRSL signals measured at 225°C after stimulating the sample with IR at 50°C), using the later part of the luminescence decay curve (Thomsen *et al.* 2008).

Subsequent investigations using post-IR IR signals measured at 225°C or 290°C after the sample is stimulated with IR at 50°C showed that these signals are less susceptible to fading than the conventional IRSL signal (measured at 50°C), but their source traps tend to be difficult to bleach (Buylaert *et al.* 2009; Thiel *et al.* 2010; Buylaert *et al.* 2011; Reimann *et al.* 2011; Stevens *et al.* 2011; Thiel *et al.* 2011; Lowick *et al.* 2012; Sohbati *et al.* 2012). Buylaert *et al.* (2009) have tested a post-IR IR SAR protocol on samples from a range of locations and depositional environments. Their post-IR IR SAR protocol measures the IR-stimulated signal at 225°C and they found that this had significantly lower fading rates than the IRSL signal measured at 50°C. After fading correction, both signals yielded consistent ages, but the post-IR IR protocol was preferred because its ages rely less on the assumptions underlying fading-correction models (Buylaert *et al.* 2009). The post-IR IR signal was found to be not quite as bleachable as the conventional IRSL signal, but for older samples, the residual post-IR IR signal after bleaching was expected to be small relative to the accumulated dose (Buylaert *et al.* 2009). Reimann *et al.* (2011) tested the conventional

IRSL and post-IR IR SAR protocols on coarse grained KF extracted from Holocene and late Pleistocene coastal sands on the southern Baltic Sea coast. Although low fading rates for the post-IR IR signal were obtained, they concluded that thermal transfer of the post-IR IR signal may cause a problem in young sediments, but it could be reduced by using a lower post-IR IR stimulation temperature (180°C) (Reimann *et al.* 2011). Post-IR IR measurements on polymineral fine grains from waterlain sediments in Switzerland yielded high residual doses on laboratory-bleached samples, suggesting that insufficient bleaching of this signal in waterlain sediments may be a significant problem (Lowick *et al.* 2012).

A non-fading, multi-elevated-temperature post-IR IRSL (MET-pIRIR) signal, proposed by Li and Li (2011), utilizes an IRSL signal that is measured by progressively increasing the stimulation temperature from 50 to 250°C in steps of 50°C. Li and Li (2011) showed that the fading rate of the IRSL signal decreases with increasing stimulation temperature, but that the bleaching rate of the IRSL signal also decreases with increasing stimulation temperature. The MET-pIRIR signals measured at 200°C and 250°C have been shown to have negligible fading rates and give reliable ages for Chinese loess (polymineral fine grains) deposited within the last glacial-interglacial period (Fu *et al.* 2012).

2.6.3 Fading rate measurements and corrections

Protocols for measurement of fading rates involve comparing luminescence intensities measured shortly after irradiation in the laboratory with those measured after some time delay (Aitken 1998). Several methods have been proposed to correct for anomalous fading. These include the *fadia* method for single grains (Lamothe & Auclair 1999), the *g*-value method for multiple aliquots (Huntley & Lamothe 2001) and single aliquots (Auclair *et al.* 2003), and the dose rate correction (DRC) model for single aliquots (Lamothe *et al.* 2003). These correction models work best for samples that have a D_e falling on the linear part of the dose-response curve (Huntley & Lamothe 2001; Auclair *et al.* 2003), and models that predict fading rates for older, more saturated, samples (e.g., Lamothe *et al.* 2003) have yet to be rigorously tested. To overcome this obstacle, Kars *et al.* (2008) developed a model that reconstructs natural fading-corrected dose-response curves using fading rate and dose-response measurements in the laboratory. Kars and Wallinga (2009) have reported consistencies between their modelled fading-corrected IRSL ages and independent age control.

2.7 Luminescence measurements on single KF grains

Luminescence dating techniques that make use of multi-grain aliquots assume that the luminescence properties are the same and that all grains within an aliquot have been sufficiently bleached by the sun before burial and have not been subsequently mixed with

contaminating grains from overlying (younger) or underlying (older) sedimentary units, or with grains weathered from deteriorating bedrock. Single-grain OSL dating techniques have been developed so that partially bleached grains, or grains that are unsuitable for regenerative dating protocols, can be excluded from analyses (Murray & Roberts 1997; Roberts *et al.* 1997; Roberts *et al.* 1998; Olley *et al.* 1999; Roberts *et al.* 1999; Duller *et al.* 2000; Jacobs *et al.* 2003; Olley *et al.* 2004; Duller 2006; Jacobs *et al.* 2006a; Olley *et al.* 2006; Jacobs 2008). There are relatively few investigations on the dating potential of single feldspar grains (e.g., Lamothe *et al.* 1994; Lamothe & Auclair 2000; Duller *et al.* 2003; Huot & Lamothe 2003; Feathers & Tunnicliffe 2011; Huot & Lamothe 2011; Smedley *et al.* 2012) and an efficient procedure for dating single grains of KF has yet to be developed. Such a procedure should entail measurements of the internal dose rates and anomalous fading rates of individual KF grains (Duller *et al.* 2003).

The first optically stimulated measurements made on individual mineral grains were performed by Lamothe *et al.* (1994) on K-rich feldspars extracted from a late-glacial (~10 ka) marine sand. Large (500–1000 μm diameter) KF grains were individually mounted on stainless-steel discs with silicone oil, and stimulated with 30 infrared (880 nm) emitting diodes. The power at the sample was 35 mW/cm^2. D_e values were measured using the single-aliquot additive-dose method, in conjunction with a luminescence-correction procedure that involved separate IRSL measurements on natural aliquots to account for the erosion of the IRSL signal as a result of the long (10 min) preheats (Duller 1991, 1992). Checks or corrections for anomalous fading were not conducted (Lamothe *et al.* 1994).

Grain-to-grain natural IRSL intensities were shown to be variable (<100,000->2,000,000 photons per second), and D_e values measured from 15 grains ranged from 25 to 322 Gy (Lamothe *et al.* 1994). There was a systematic tendency for bright grains to yield large D_e values, and this was interpreted as evidence that the variability in natural IRSL intensities was due to partial bleaching. Grains that yielded ages closest to the expected age of the sample still systematically underestimated the true age by ~30%. Lamothe *et al.* (1994) suggested that this discrepancy may be due to supralinearity in the IRSL growth curves, potential problems with the luminescence correction method, and/or anomalous fading.

The luminescence properties of single KF grains have been subsequently investigated by these and other authors for the purpose of distinguishing between quartz and feldspar in density separated aliquots (Duller 2003), demonstrating homogeneity in the luminescence properties within individual grains (Huot & Lamothe 2003), and identifying sediment mixtures composed of partially bleached grains or grains that are prone to anomalous fading (Lamothe & Auclair 1997, 1999, 2000). IRSL stimulation of coarse-grained KF in these studies was conducted using an array of 30 infrared (880 nm) emitting

diodes at 30 mA attached to a Daybreak 1100 TL reader (Lamothe & Auclair 2000; Huot & Lamothe 2003), or an unfocussed infrared (830 nm) laser diode delivering ~400 mW/cm^2 to the whole sample disc (Bøtter-Jensen *et al.* 2000; Duller 2003).

By 2003, a 150 mW IR laser (830 nm) was incorporated into the single-grain Risø attachment to facilitate screening of quartz for feldspar inclusions, and the stimulation of single grains of feldspar on single-grain discs (Bøtter-Jensen *et al.* 2003). The IR laser beam intensity exhibits a Gaussian spatial distribution along a plane perpendicular to the laser beam, with 90% of the power contained within a spot of <20 μm on a sample disc (Anonymous 2007). It is assumed that internal reflection within 300 μm diameter holes on single-grain discs insures that each grain is illuminated evenly. If we assume that the power is spread evenly across each grain hole, then the power density of the IR laser beam is approximately 500 W/cm^2 (Duller *et al.* 2003). The IR laser is by far the most powerful light source that has been incorporated into OSL/TL systems, with an energy per unit time per unit area an order-of-magnitude greater than that of the green laser, three orders-of-magnitude greater than that of the IR laser diode and IR diode array, and four orders-of-magnitude greater than that of the blue diode array (Bøtter-Jensen *et al.* 2000; Bøtter-Jensen *et al.* 2003) (Table 2-3). There is concern that the high power of the IR laser may cause grains to heat up during stimulation, but strong evidence for this has yet to be reported (Duller *et al.* 2003).

The first luminescence measurements on single KF grains using the IR laser were made by Duller *et al.* (2003). Feldspar IRSL decay curves generated using the IR laser showed an intense initial signal that decayed very rapidly, with very little signal observed after 0.2 s, and decay curve shapes were very similar from one grain to another (Duller *et al.* 2003). Quartz grains stimulated with the laser showed a non-decaying signal more than 10 times the background count of the detection system (Duller *et al.* 2003). At least 40% of feldspar grains from two samples made a contribution to the total IRSL emitted, and almost half of the feldspar grains on a single-grain disc could be used to generate growth curves (Duller *et al.* 2003). Similar results were obtained by Li *et al.* (2011). This is in contrast to quartz, where typically fewer than 10% of grains contribute over 90% of the total OSL signal (e.g., Jacobs *et al.* 2003).

Table 2-3. Light wavelengths, intensities, and energy parameters of the light sources associated with the RisøTL/OSL system, Model TL/OSL-DA-20. Note that the intensity and energy per unit time per unit area of the IR laser is an order-of-magnitude greater than that of the the green laser, making it the most powerful light source available.

	Blue diode array	IR diode array	IR laser diode	Green laser	IR laser
Wavelength, λ (s^{-1})[1]	4.70E-07	8.75E-07	8.30E-07	5.32E-07	8.30E-07
Maximum intensity ($W*cm^{-2}$)[1]	0.05	0.135	0.400	50	500
Light frequency (m)[2]	6.38E+14	3.43E+14	3.61E+14	5.64E+14	3.61E+14
Energy of a single photon, *E* (W*s)[2]	4.23E-19	2.27E-19	2.40E-19	3.74E-19	2.40E-19
Number of photons per unit time per unit area[2]	1.18E+17	5.94E+17	1.67E+18	1.34E+20	2.09E+21
Energy per unit time per unit area (W*s)[2]	5.00E-02	1.35E-01	4.00E-01	5.00E+01	5.00E+02

[1]The light wavelength and maximum intensity of all stimulation sources are from Bøtter-Jensen *et al.* (2000; 2003).

[2]Light frequency (v) is derived from the expression v = c / λ, where c is the speed of light (3.00 x 10^8 m/s), and λ is the wavelength of the light source (row 1 of this table). The energy of a single photon (E) is calculated as E = h v, where h is Planck's constant (6.63 x 10^{-34} W s^2). The number of photons emitted per unit time per unit area is derived by dividing the maximum intensity of the light source by the energy of a single photon (E), and the energy per unit time per unit area is determined by multiplying E by the number of photons per unit time per unit area emitted by the light source (Choi *et al.* 2006).

KF dose-response curves measured by Duller *et al.* (2003) were best described using a single saturating exponential function:

$$I = I_0 + I_{max} (1 - e^{-D/D_0}) \quad (1)$$

where I is the sensitivity corrected luminescence signal, D is the given laboratory dose, I_0 and I_{max} refer to the signals measured at the beginning and the end of the dose-response curve, respectively, and D_0 is a constant (the characteristic saturation dose) that describes the shape of the curve (Duller *et al.* 2003). Unlike quartz, single-grain KF dose-response curves showed little variation in the onset of saturation (Duller *et al.* 2003).

Li *et al.* (2011) made measurements on single grains of Na- and K-feldspar for the purpose of improving precision in isochron dating techniques using synthetic aliquots. They showed that, although the decay curves of Na- and K-feldspar are similar in shape, KF grains tend to be slightly brighter. Sixty-three percent of KF grains gave signal intensities that were greater than 3σ of the background signal, but only 25% of Na-feldspar grains did the same (Li *et al.* 2011). Pulse annealing tests were conducted on 150–180 μm grains of both K-feldspar and Na-feldspar (100 grains each). Sensitivity-corrected IRSL measurements (L_x/T_x) were made on laboratory-bleached grains after successive cut-heats ranging from 200°C to 420°C. After heating to 300°C, up to 80% of the IRSL signal in KF remained, and only 50% of the signal remained in Na-feldspar. This supported the authors' conclusion that a larger proportion of the IRSL signal from Na-feldspar originates from shallow traps, and the IRSL signal from Na-feldspar is less thermally stable than that from KF (Li *et al.* 2011).

Li *et al.* (2011) conducted dose recovery tests on laboratory-bleached, 180–212 μm, KF grains using a modified SAR procedure with the same preheat (260°C for 10 s) for both the main IRSL measurement (L_x) and the test dose measurement (T_x), following Blair *et al.* (2005). Rejection criteria, similar to those applied by Jacobs *et al.* (2006a), were used to reject grains that exhibited dim signals, abnormal growth curves, uncorrected sensitivity changes, and high recuperation (Li *et al.* 2011). Only 45 of 300 grains passed all rejection criteria, and accurate dose recoveries were only achieved if the recuperated signal of accepted grains was less than 10% of the natural (Li *et al.* 2011). The criterion that led to the rejection of the largest number of grains was recuperation. The inclusion of grains with high recuperation lead to underestimations of D_e in dose recovery tests in all grain size fractions measured (90–125 μm, 125–150 μm, 150–180 μm, 180–212 μm, and 212–250 μm) (Li *et al.* 2011).

Interestingly, when dose-response curves were generated from synthetic aliquots made up of the sum of the IRSL laser measurements of 100 individual KF grains, recuperation values (~10%) were higher than those of single-aliquot measurements of the same sample using IR diodes (~2%) (Li *et al.* 2011). The authors attributed this effect to the different stimulation sources (the IR laser versus the IR diodes, Table 2-3), and the differential extent to which the IRSL signal is removed in each SAR cycle (Li *et al.* 2011).

Although many luminescence studies have examined the D_e distributions of quartz (e.g., Olley *et al.* 1999; Jacobs *et al.* 2003; Olley *et al.* 2004; Jacobs *et al.* 2006a, b; Arnold *et al.* 2007; Jacobs & Roberts 2007; Arnold & Roberts 2009), few studies have looked at the D_e distributions of single KF grains or their overdispersion (OD). OD refers to the relative standard deviation of a D_e distribution after allowing for measurement uncertainties (Galbraith *et al.* 1999). Sources of OD may include: 1) differences in beta dose received by individual grains in their burial environment; 2) insufficient or heterogeneous exposure of some grains to heat or sunlight before burial; 3) post-depositional intrusion of younger grains into older deposits or vice versa; and/or 4) non-identical field and laboratory conditions, as well as sample-to-sample variability (Jacobs *et al.* 2008, and references therein). OD values of 13–19% have been reported for KF grains from well-bleached desert sands from northern China that were not corrected for fading (Li *et al.* 2011). An OD range of 22–38% has been reported for KF grains from aeolian sand samples from Saudi Arabia (Trauerstein *et al.* 2012). OD values measured from seven fluvial sediment samples from southwestern British Columbia, Canada ranged from ~53–133% (Feathers & Tunnicliffe 2011). An eighth sample from this latter study yielded an OD value of only ~1.3%, but this unusually low value was attributed to the rejection of relatively old grains in the sample that had L_n/T_n values that failed to intersect the dose-response curve.

2.8 Internal dose rates of KF grains

While the U, Th, Rb, and K contents of quartz grains are usually too small to contribute significantly to the internal dose rate, these elements can occur in large enough concentrations to contribute to the internal dose rate of KF (Zhao & Li 2005). Because the ^{40}K content within individual KF grains is responsible for a large fraction of the total dose rate experienced by a grain in nature (Lamothe *et al.* 1994; Zhao & Li 2005), grain-to-grain variations in K content may induce scatter in D_e distributions. For example, the total dose rate of a pure, 180–211 μm KF grain from ~24 ka New Zealand dune sand has been calculated to be 2.87 ± 1.62 Gy/ka (Duller *et al.* 2003). This is 0.80 Gy/ka greater than the total dose rate of a similar sized grain containing no ^{40}K from the same sample, suggesting that variations in ^{40}K content alone could lead to D_e values ranging from 50 to 69 Gy in these sediments (Duller *et al.* 2003).

Li *et al.* (2011) found that the internal dose rate contributed ~15% of the total dose to their KF grains, and they obtained lower D_e estimates from their low K, Na-feldspar aliquots than from their KF aliquots (21.5 ± 1.5 Gy compared to 37.7 ± 0.5 Gy). In this case, such a large discrepancy in D_e could not be attributed to differences in internal dose rates between the two minerals, but rather to the lower thermal stability of the IRSL signal in Na-feldspar (Li *et al.* 2011).

Microprobe measurements of individual KF grains from sediments have shown that grain-to-grain variations in K content are small (Lamothe *et al.* 1994; Zhao & Li 2005), and K contents seem to be distributed homogeneously along the surface of each grain (Zhao & Li 2005); the microprobe measurements were made in spot mode, which typically sample a volume of ~0.3–3 μm^3. Large grain-to-grain variability in K content in KF separates is most likely to occur as a result of imperfect density separation procedures that lead to quartz and plagioclase contamination in the sample (Huntley & Baril 1997; Li *et al.* 2011). Lamothe *et al.* (1994) used a microprobe to measure the K contents of 8 out of 15 grains previously used for age determination. Ten spot measurements of 5 μm in diameter were made on each 500–1000 μm grain, and the calculated average K-content of all 8 grains (11.66%) was applied to the remaining 7 grains. It was found that for this grain size fraction, the internal dose rate contribution from K was 50% of the total dose rate (Lamothe *et al.* 1994: Table 2). Among the 8 grains that were measured directly with a microprobe, there was a correlation (R^2 = 0.68) between the K content and the calculated internal dose rate (Fig. 2-6). No clear correlation existed between K content and natural IRSL intensity or D_e, but this may have been due to the low number of grains measured (Fig. 2-6), or to partial bleaching of the sample before burial (Lamothe *et al.* 1994). There also appeared to be no correlation between D_e and the internal dose rate of the grains, or the total dose rate to the grains (Fig. 2-7).

a)

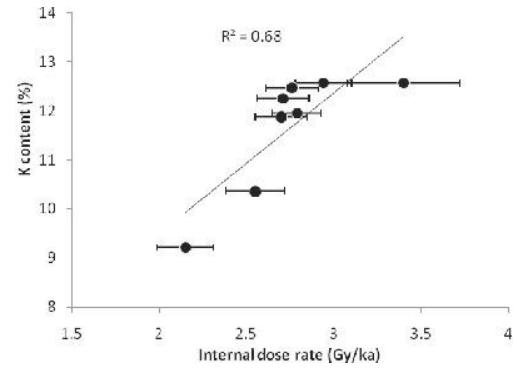

b)

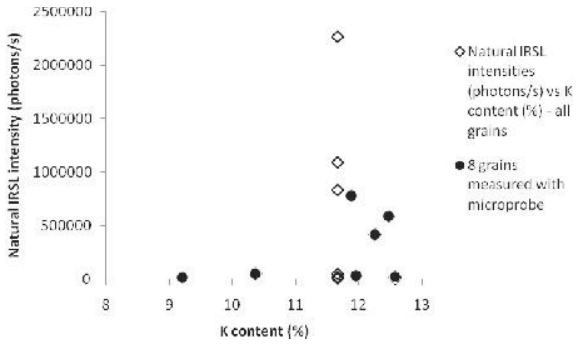
Natural IRSL intensity (photons/s)
K content (%)
Natural IRSL intensities (photons/s) vs K content (%) - all grains
8 grains measured with microprobe

c)

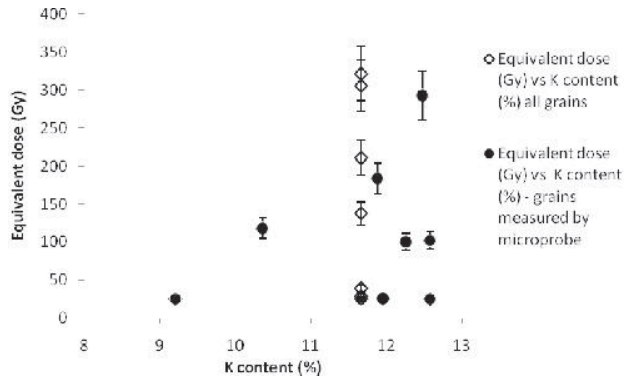
Equivalent dose (Gy)
K content (%)
Equivalent dose (Gy) vs K content (%) all grains
Equivalent dose (Gy) vs K content (%) - grains measured by microprobe

Figure 2-6. Relationships between the K content of individual 500-1000 µm grains and the a) calculated internal dose rate, b) natural IRSL intensity, and c) the D_e. Data are from Lamothe *et al.* (1994). Internal beta dose rates were calculated using data from Mejdahl (1983), and the contributions from internal U, Th and Rb were not included in the internal dose rate calculations (Lamothe *et al.* 1994). K content error bars are smaller than the size of the symbols.

a)

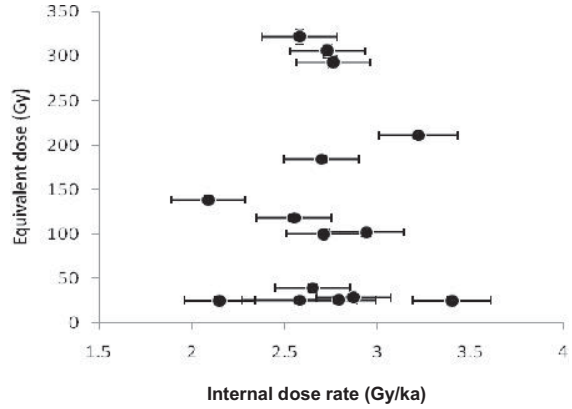

b)

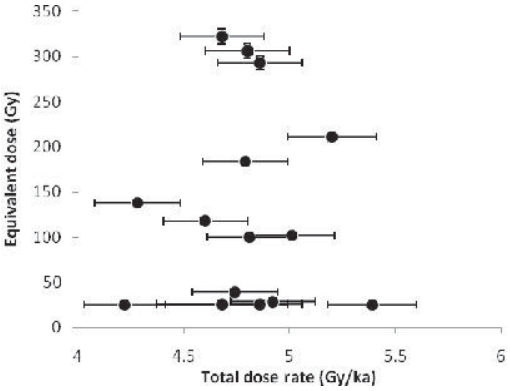

Figure 2-7. Scatterplots of D_e versus KF grain internal dose rate from K (a), and equivalent dose versus total dose rate for each grain (b). Data are from Lamothe *et al.* (1994).

In routine luminescence dating studies using KF, the U and Th contribution to the dose rate is assumed to be negligible due to their low concentrations in KF grains (Mejdahl 1987), and Rb contents are estimated using previously published correlations between K and Rb concentrations (Huntley & Hancock 2001). Beta dose absorption factors from Mejdahl (1979) are commonly used to estimate internal dose rates from U, Th and K for a range of grain sizes. Readhead (2002) provides similar absorption factors for internal beta dose rates from ^{87}Rb.

Zhao and Li (2005) measured the U and Th contents of individual KF grains from sediment and crushed granite samples from China using laser-ablation inductively-coupled plasma mass spectrometry (ICP-MS). Although their results can only be considered qualitative, due to lack of known-concentration standards, some grains had relatively high concentrations of U (1.4 ppm) and Th (1.7 ppm), while others had low concentrations: U (~50 ppb) and Th (~100 ppb). Solution ICP-MS analyses of bulk sediments showed that U, Th and Rb concentrations were high enough to contribute significantly to the internal dose rate (Zhao & Li 2005). Their data also suggested that

the commonly used K:Rb ratio of 200:1 (Aitken 1998) is appropriate. U and Th were found to contribute up to 24% of the total internal dose rate in one sample, and it was concluded that internal dose rate contributions from these elements should be considered in luminescence dating procedures using single grains of KF (Zhao & Li 2005).

2.9 External dose rates

Naturally-occurring ionizing radiation causes the redistribution and trapping of electrons in the crystal lattice of buried mineral grains (Aitken 1998). This radiation is composed of alpha particles, beta particles and gamma rays as well as cosmic rays from outer space. Alpha particles, beta particles, and gamma rays are derived from potassium (^{40}K), thorium (^{232}Th and its daughter products) and uranium (^{238}U and ^{235}U and their daughter products) in the surrounding sediment. ^{40}K in sediment will emit beta and gamma radiation, and will dominate the internal dose rate to KF grains (Aitken 1998). The relative contribution of radiation from ^{87}Rb in sediment is typically small, and consists of beta particles (Aitken 1998).

External dose rates can be determined by estimating the concentrations of potassium, rubidium, thorium and uranium in sediments using neutron activation, atomic absorption, X-ray fluorescence, flame photometry, or inductively coupled plasma mass spectrometry (ICP-MS) and determining their dose-rate components using conversion tables (e.g., Appendix A of Aitken 1998). However, dose rates determined this way fail to take into account the dose rate contributions from daughter products in the uranium and thorium decay chains, which, in nature, are commonly not in secular equilibrium with their parents (Olley *et al.* 1996) and consequently produce inaccurate estimates of dose rate. The condition of secular equilibrium is attained in "closed" systems where the rate of decay (activity) of each daughter is the same as the rate of decay of its parent. In "open" systems, however, where there is a removal or addition of one of the daughter products, a condition of radioactive disequilibrium is attained, where some of the daughter activities are no longer equal to the parent activity (Aitken 1998). Whether or not radioactive equilibrium is present in sampled sediments can be checked by high-resolution gamma spectrometry (HRGS) or alpha spectrometry. These methods measure the activities of several individual nuclides in the uranium and thorium decay chains and allow the determination of dose rates whether or not equilibrium exists.

2.9.1 Alpha particles

Alpha particles are highly ionizing, but their penetrating distance in mineral grains is only ~25 μm from the emitting nucleus (Aitken 1998). When sand-sized grains are considered, the external alpha contribution does not penetrate to the internal core of a

grain. This can result in uncertainties in determining the external alpha dose rate, because different regions of the same grain will have received different alpha contributions (Aitken 1998). To circumvent this problem of partial penetration and inhomogeneous alpha irradiation, the external alpha contribution is typically reduced to negligible levels by removing the outer rind of each grain by HF acid etching samples during preparation (Aitken 1998). This acid-etching procedure was followed in this study.

2.9.2 Beta particles and gamma rays

Beta particles and gamma rays travel a distance of up to 3 mm and 30 cm, respectively, through most sediments and rocks (Aitken, 1998). Most of the environmental dose rate comes from the contribution of beta particles and gamma rays, so it is most important to determine these accurately when estimating the total dose rate. Beta dose rates are commonly measured using a low-level beta counter (e.g., Haslam *et al.* 2012). This approach does not give information on whether the beta emissions originated from the uranium or thorium decay chains, or from ^{40}K, but instead gives the total counts from these sources (Haslam *et al.* 2012). Because ~60% of the beta dose rate from the ^{238}U decay chain originates from decaying radioisotopes in the lower part of the decay chain, beta counting is superior to methods, such as ICP-MS or atomic absorption, for example, which measure the concentrations of parent radionuclides, only (Haslam *et al.* 2012). Gamma dose rates can be measured using HRGS, gamma scintillometry, or a portable gamma ray spectrometer. Portable gamma ray spectrometers are preferred because they take into account spatial heterogeneity in the gamma radiation field within 30 cm of each OSL sample, as gamma rays can penetrate this distance through sediments and rock (Haslam *et al.* 2012). They provide an estimate of the dose rate from gamma-ray emitters in the uranium and thorium decay chains and from ^{40}K, and therefore are less sensitive to U-series disequilibria than methods that measure the concentration of parental nuclides, only (Haslam *et al.* 2012).

2.9.3 Cosmic rays

Cosmic rays come from outer space, and, after penetrating the ground surface, are dominated by muons (Prescott & Hutton 1994; Aitken 1998). The cosmic-ray flux is dependent on latitude and altitude (Prescott & Hutton 1994), thickness and density of sediment and rock overburden, and sample water content (Readhead 1987).

2.9.4 Adjustments for water content, organic matter and calcium carbonate

Pore water, calcium carbonate, and organic matter can severely inhibit the absorption of ionizating radiation by sediment grains in nature (Lian *et al.* 1995; Aitken

1998; Lian & Huntley 1999), as the absorption coefficients of the above are much higher than that of quartz or feldspar. For the external beta, gamma and cosmic ray dose rates to be estimated accurately, corrections need to be made for the presence of water, carbonate content and organic matter in the sediment during the time of burial.

Corrections for water content are made by dividing dry dose rates by attenuation factors to obtain wet dose rates. Attenuation factors can be calculated as 1+HWF, where H = 1.50 for the alpha dose rate, 1.25 for the beta dose rate, and 1.14 for the gamma dose rate, W = is the saturation water content (defined as the weight of water divided by the dry weight of sediment), and F is the fraction of saturation corresponding to the assumed average water content over the entire burial period (Zimmerman 1971; Aitken 1998). Updated attenuation factors, which can take into account carbonate contents determined using loss-on-ignition, can be determined using a dose rate model designed by Nathan and Mauz (2008) which assumes a linear increase of carbonate mass and linear decrease of water mass in pores between sediment particles during burial.

2.10 Summary

This section discussed the basic principles of luminescence dating, some of the luminescence characteristics of quartz and feldspar, some commonly used single-aliquot dating procedures, and the contributions to internal and external (environmental) dose rates. The luminescence signal in feldspar is susceptible to fading through time, but if this can be corrected for, or if a non-fading signal can be utilized, there are advantages to using this mineral in luminescence studies. The luminescence signal in feldspar usually saturates at higher doses than in quartz, enabling the dating of older sediments. The internal ^{40}K content of KF grains makes them less sensitive to differences in the external dose rates to individual grains in their burial environment. Luminescence ages obtained from feldspars also provide an independent source of chronological control with which quartz luminescence ages can be compared.

The vast majority of luminescence studies using feldspar have made use of multi-grain aliquots, and relatively few studies have focussed on the dating potential of feldspar at the single-grain level. Dating feldspars at the single-grain level would allow the rejection of grains that are unsuitable for SAR measurement procedures and the identification of potentially poorly bleached grains in partially bleached sediments, or contaminating younger or older grains in sediment mixtures. Therefore, this thesis begins with the luminescence dating potential of single KF single-aliquot grains in Chapters 4-6, and uses this data to inform interpretations of KF aliquot fading-corrected age distributions in Chapters 7 and 8. The following chapter outlines the luminescence dating methodology applied in this thesis, including a summary of sample collection and

preparation procedures, methods of D_e calculation, and procedures used to estimate internal and external dose rates.

Chapter 3 – Luminescence dating methodology and samples

3.1 Samples and sample collection

All luminescence samples were collected by hammering steel tubes, ~5 cm in diameter, into the section face, extracting them, and sealing both ends with multiple layers of black plastic. After the tubes were extracted, the sample holes were widened and an *in situ* gamma spectrometer detector was inserted for gamma radioactivity measurements. Bagged samples of sediment (~60–200 g) were collected from the walls of the gamma spectrometer detector holes for water content measurements and low-level beta counting in the laboratory.

Four luminescence samples in this thesis were collected from the Khunteli type-section exposure, located on the south side of the Son River (82°16'33.59"E, 24°32'27.718"N), and the Ghoghara main exposure (24°30'7.608"N, 82°1'2.748"E), located on the north side of the river, ~25 km west of Khunteli, near the Rehi-Son confluence (Fig. 1-1a, Chapter 1). One modern sample (KHUT-10) was collected from a sand bar in the Son River channel ~50 m away from the base of the Khunteli type-section. Seven samples for luminescence dating were also collected from alluvial sediments on the south side of the Son River, across from the Rehi-Son confluence (Fig. 8-2c, Chapter 8). These include two samples (H-1 and H-5) collected from the top of the highest terrace, three samples (M-2, M-4 and M-6) collected from sediments along a dirt road below the highest terrace, and two samples (L-3 and L-7) collected from gully exposures in the lowest terrace next to the river channel.

3.2 Sample preparation and measurement

The 180–212 μm diameter grain-size fraction of all samples was treated with HCl acid (10%) and H_20_2 acid (10%) to ensure the removal of any traces of carbonates and organic material. A KF-rich extract was obtained using sodium polytungstate heavy liquid separation (ρ<2.58 g/cm^3) and etched with a diluted HF acid (10%) solution for 10 minutes to remove the outer alpha-irradiated layer of the grains. After HF acid etching, the samples were sieved again to remove any grains that had been reduced to less than 180 μm in size.

All measurements were made using a Risø TL/OSL DA-20 reader equipped with a calibrated ^{90}Sr/^{90}Y beta source. KF single grains were loaded into 300 μm diameter holes on gold-plated aluminum discs and stimulated using the IR (830 nm) laser, fitted with an RG780 filter to absorb a resonant wavelength at 415 nm. An IR laser power of 30% was used to reduce the potential effects of grain heating by the laser (Duller *et al.* 2003). Because the dose rate from the ^{90}Sr/^{90}Y beta source is not uniform over the entire area of a disc, the dose rate to each individual disc hole position was calibrated using gamma-irradiated quartz supplied by Risø.

Table 3-1. Luminescence samples used in this thesis.

Sample	Location	Geomorphic/stratigraphic context	Chapter discussed
GHO-2	Ghoghara main section	below YTT	4, 7, 8
GHO-3	Ghoghara main section	above YTT	7, 8
KHUT-1	Khunteli type-section	below YTT	5, 7, 8
KHUT-4	Khunteli type-section	above YTT	7, 8
KHUT-10	~50 m from base of Khunteli type-section	modern sand bar	6, 7
H-1	terraced sediments across from Rehi-Son River confluence	highest terrace	8
M-2	terraced sediments across from Rehi-Son River confluence	dirt road (between the highest and lowest terraces)	8
L-3	terraced sediments across from Rehi-Son River confluence	lowest terrace	8
M-4	terraced sediments across from Rehi-Son River confluence	dirt road (between the highest and lowest terraces)	8
H-5	terraced sediments across from Rehi-Son River confluence	highest terrace	8
M-6	terraced sediments across from Rehi-Son River confluence	dirt road (between the highest and lowest terraces)	8
L-7	terraced sediments across from Rehi-Son River confluence	lowest terrace	8

Multi-grain aliquots, each composed of ~25 grains, were mounted on stainless-steel discs and stimulated using IR (875 nm) light-emitting diodes (LEDs). The IRSL signals in the blue-violet region were detected using a bialkali EMI 9235QB photomultiplier tube, fitted with Schott BG-39 and Corning 7-59 filters. For single-aliquot anomalous fading measurements, KF grains from sample GHO-2 were adhered to discs using a transparent thermoplastic polymer adhesive, Crystalbond 509 (see Section 3.3), and KF grains for all other samples were adhered to discs using silicone oil.

3.3 Aliquot preparation methods using Crystalbond 509

In luminescence studies, silicone oil is typically used to adhere grains to discs, but we found that, after several hours to days, the oil dries and the grains can move or slide off the disc. If enough grains are lost, L_x and T_x signals may be hampered by poor counting statistics, leading to an increase in error in fading measurements. To prevent this, a transparent thermoplastic polymer adhesive, Crystalbond 509, was used for multi-grain

aliquots of sample GHO-2, following the approach of Huntley and Lamothe (2001). After measurement of the D_e, a small amount of Crystalbond was dissolved in acetone and dropped onto the grains on each disc using a pipette, and allowed to air-dry for at least two hours before measurement. This adhesive did not adversely affect L_x/T_x errors of multi-grain aliquots (Table 3-2), but did reduce the thermal reproducibility of the fading measurements. As a consequence, I used silicone oil for fading measurements of all other samples.

Table 3-2. L_x/T_x errors calculated from two aliquots of sample GHO-2 containing ~25 grains each. Aliquot 1 was prepared using silicone oil, and Aliquot 2 was prepared using Crystalbond 509.

Aliquot number[1]	Adhesive	Mask size (mm)	L_x[1] (photon counts)	T_x[1] (photon counts)	L_x/T_x	L_x/T_x standard error	L_x/T_x relative standard error (%)
1	Silicone oil	1	172933	74898	2.31	0.01	0.46
2	Crystalbond	1	83195	37636	2.21	0.01	0.67

[1]Both aliquots were measured after being given a laboratory dose of 28 Gy and a preheat of 250°C for 10 s. The test dose was 11 Gy.

3.4 D_e determination

The D_e from KF grains from all samples in this study was determined using a SAR measurement procedure similar to that described by Wallinga *et al.* (2007) and Buylaert *et al.* (2009) (Table 3-2), unless otherwise stated. This procedure included the measurement of the natural signal (L_n) followed by the measurement of a laboratory-given test dose (T_n). A dose-response curve was then generated from the signals induced by a series of regenerative doses given in the laboratory (L_x), each followed by a test dose measurement (T_x) to correct for sensitivity changes (Galbraith *et al.* 1999; Murray & Wintle 2000). L_x/T_x ratios at each dose point resulted in a sensitivity-corrected dose-response curve onto which L_n/T_n was projected to determine D_e. A 1.5% instrumental error was added in quadrature to the uncertainty due to counting statistics for each L_x, T_x, L_n, and T_n measurement for multi-grain aliquots, and a 2.0% instrumental error was used for single grains (e.g., Jacobs *et al.* 2006a; Duller 2007). The IRSL signal induced by 1 s of IR stimulation minus the mean background count rate over the last 20 s of stimulation was used in all D_e calculations from KF multi-grain aliquots. The IRSL signal in the first 0.134 s minus the mean background count rate over the last 1.742 s was used for all KF single-grain D_e calculations. Both the conventional IRSL signal (i.e. the signal measured at 50°C) and a post-IR IR signal (the IRSL signal measured at 225°C after a 100 s IRSL stimulation at 50°C) was used on KF aliquots in this thesis, and both signals were measured using a stimulation duration of 100 s for aliquots. The conventional IRSL signal (measured at 50°C) was measured using a stimulation time of 6.7 s for single KF grains.

For both single grains and multi-grain aliquots, the D_e and its uncertainty was calculated by the Monte Carlo stimulation (Duller 2007) using the software package Analyst version 3.24. All KF grain dose response curves were fitted with a single saturating exponential function of the form:

$$I = I_0 + I_{max} (1 - e^{-D/D_0}) \quad (1)$$

where I is the sensitivity corrected luminescence signal, I_0 and I_{max} refer to the signals measured at the beginning and the end of the dose-response curve, respectively, D is the given laboratory dose, and D_0 is a constant (the characteristic saturation dose) that describes the shape of the curve (Duller *et al.* 2003).

Table 3-3. SAR measurement protocol for KF grains.[1]

1.	Natural / Regenerative Dose	
2.	Preheat (250°C, 10 s)	
3.	IRSL	→ L_n, L_x
4.	Test dose	
5.	Preheat (250°C, 10 s)	
6.	IRSL	→ T_n, T_x
7.	IRSL bleach (290°C, 40 s)	
8.	Return to step 1.	

[1]This protocol is slightly modified for the post-IR IR signal measured from aliquots in Chapter 7. See Table 7-2, Chapter 7.

3.5 Internal dose rates to KF and quartz grains

In this thesis, the internal dose rates to KF grains were not measured directly, but were instead estimated using assumed U, Th, ^{40}K and ^{87}Rb concentrations based on values widely used in the literature. Internal U and Th contents were assumed to be 0.3 ± 0.1 ppm and 0.7 ± 0.1 ppm, respectively, following Medjahl (1987). The internal ^{87}Rb concentration was assumed to be 400 ± 100 ppm (Huntley & Hancock, 2001), and the internal ^{40}K content for KF grains was assumed to be 12.5 ± 0.5% (Huntley & Baril, 1997), unless otherwise stated (see Chapter 6). The internal alpha and beta dose rate contributions from the U and Th decay chains, and the internal beta dose rate contribution from ^{40}K, were calculated using the conversion factors of Adamiec and Aitken (1998). An alpha efficiency factor (a-value) of 0.09 ± 0.03 was assumed, based on previously reported values for polymineral fine grains in the literature (Rees-Jones 1995; Lang & Wagner 1997; Banerjee *et al.* 2001; Lang *et al.* 2003), and dose rates were corrected for beta absorption using absorption factors from Brennan (2003). An assumed internal dose rate of 0.03 ± 0.01 Gy/ka was used for quartz.

3.6 External dose rate determination

The environmental dose rates from beta, gamma and cosmic radiation were estimated for each sample. To circumvent the problem of partial penetration and inhomogeneous alpha irradiation, the external alpha contribution was reduced to negligible levels by removing the outer portion of each grain by HF acid etching all samples during preparation (Section 3.2) (Aitken 1998). The external beta and gamma dose rates were estimated by low-level beta counting and *in situ* gamma spectrometry, respectively, and a contribution added for the dose rate from cosmic rays (Prescott & Hutton 1994). Because beta particles travel a relatively short distance, an adequate representation of the bulk beta dose rate can be estimated in the laboratory using sediment samples of a few hundred grams. In this thesis, the bulk beta dose rate was measured from the bagged samples using a low-level Risø beta counter (GM-25-5) (Bøtter-Jensen & Mejdahl 1985; Bøtter-Jensen & Mejdahl 1988), making allowance for beta dose attenuation due to grain size and HF acid etching (Brennan 2003). The radiation from beta particles constitutes ~20–80% of the total environmental dose rate in samples collected from alluvial deposits in the Middle Son Valley.

Gamma dose rates were measured in the field using a portable (*in situ*) gamma-ray spectrometer to take into account any spatial heterogeneity in the gamma radiation field within 30 cm of each OSL sample (as gamma rays can penetrate this distance through most sediments and rocks). The radiation dose from gamma rays constitutes ~18–50% of the total dose rate in samples from the Middle Son Valley.

By measuring external dose rates using beta counting and *in situ* gamma spectrometry, we have assumed that the dose rate measured at the time of sample collection has prevailed throughout the burial history of the sample. However, significant time-dependent radioactive disequilibria in the U or Th decay chains in the sediment, due to the migration of radioniclides, may indicate that this is not the case (Olley *et al.* 1996). To check for disequilibria in the sediments at the Ghoghara main section and the Khunteli type section, the activities of ^{238}U, ^{226}Ra, ^{210}Pb, ^{228}Th, and ^{228}Ra were measured from dried and powdered sub-samples using high-resolution gamma-ray spectrometry at the CSIRO Land and Water laboratory, Canberra. These samples were collected in the field from sediment around the luminescence sample tubes, and the results are discussed in Chapter 7.

The approach described in Prescott and Hutton (1994) was used to determine the contribution of cosmic rays to the total environmental dose rate. This approach takes into consideration the location of the sample in terms of its latitude, longitude and altitude (in metres above sea level), as well as the overburden thickness and density during the burial history of the sample; the latter was determined by estimating the sample's depth below the

modern surface and assuming an average bulk sediment density of 1.8 g/cm^3. The cosmic-ray dose rate constitutes ~5–6% of the total environmental dose rate in samples from the Middle Son Valley.

3.7 Adjustments for water content, organic matter and calcium carbonate

The sediments sampled in this study are generally well-sorted alluvial silts, sands and gravels, and very little organic matter or calcium carbonate was observed in the field, so the calculated environmental dose rates were not adjusted to account for these. External dose rates were calculated for an estimated long-term, time-averaged water content of ~5–10% for all samples (Chapters 6, 7 and 8). These estimates and their uncertainties take into consideration the field water contents measured in the laboratory (these range from 0.2 to 10% of the dry sample in samples in this study), the free-draining nature of the sampled sediments, their collection during the dry season, and the monsoonal climate of the region. A 1% increase in estimated water content leads to a ~1% increase in calculated age for samples from the Middle Son Valley.

3.8 Summary

This chapter summerized the luminescence dating methodology used in this thesis. This included methods of luminescence sample collection, preparation and measurement, as well as methods of environmental dose rate determination. In the next three chapters (Chapter 4-6), the luminescence dating potential of single KF grains is explored and this data are later used to inform interpretations of KF single-aliquot fading-corrected age distributions in Chapters 7 and 8. Chapter 4 begins the single-grain investigations with a study of the possible use of the luminescence characteristics of individual grains to differentiate between KF grains and contaminating quartz, plagioclase or other mineral grains.

Chapter 4 – Elemental Analyses

4.1 Introduction

Standard heavy liquid separation techniques for separating minerals (Fig. 4-1) do not work perfectly and typically result in KF-rich extracts that are contaminated with quartz and plagioclase grains (Huntley & Baril 1997) (Fig. 4-2). In this chapter, luminescence measurements and elemental analyses are conducted on two samples (GHO-2 and KHUT-1) collected from sediments underlying YTT ash, to examine the relationship between grain elemental composition and luminescence characteristics, D_e, and fading rate. Elemental analyses were conducted on KF grains from sample KHUT-1 using energy-dispersive X-ray spectroscopy (EDS) in the Faculty of Engineering, University of Wollongong, and the relationship between IRSL decay curves and grain mineralogy are reported. Elemental analyses were also conducted on a subset of grains from sample GHO-2 that were used for D_e determination and fading measurements (see also Chapter 6), using wavelength-dispersive spectroscopy (WDS) at Macquarie University. The WDS measurements on sample GHO-2 allowed the assessment of the influence that elemental composition of individual grains has on IRSL signal brightness, decay curve shape, D_e, fading rate, and fading-corrected age. The implications these results have for single-grain dating of feldspars are discussed in Section 4.8.

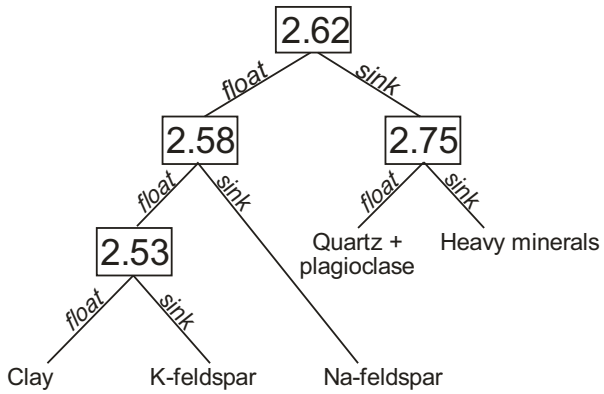

Figure 4-1. Flow chart for heavy liquid separation (from Mejdahl 1985; Aitken 1998). The numbers shown are a measure of specific gravity in g/cm^3. The left branch at each step indicates which minerals float and the right branch indicates which minerals sink.

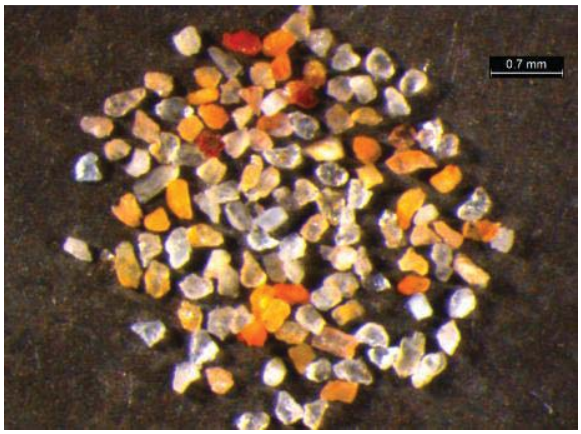

Figure 4-2. A K-rich feldspar aliquot from sample KHUT-1 containing a mixture of K-rich feldspar, quartz, plagioclase and possibly other minerals. Sodium polytungstate (ρ<2.58 g/cm^3) was used to remove quartz, plagioclase and heavy minerals from the 180–212 µm grain size fraction. The separate was then etched for 10 min with a diluted HF acid (10%) solution. The microphoto was taken using a digital camera mounted on a Leica MZ16A stereo microscope.

4.2 Heavy liquid separation and luminescence measurements

KF-rich extracts containing 180–212 µm sized-grains were obtained from samples GHO-3 and KHUT-1 using sodium polytungstate heavy liquid separation (ρ<2.58 g/cm^3, Fig. 4-1) and etched with a diluted HF acid (10%) solution for 10 min to remove the outer, alpha-irradiated layer of the grains. A quartz extract containing 180–212 µm sized-grains was also obtained from KHUT-1 using density separation procedures (ρ<2.62 g/cm^3, Fig. 4-1) and etched with HF acid (40%) solution for 40 min. The decay curves of nineteen grains from the K-rich feldspar extract and 10 grains from the quartz separate from sample KHUT-1 were measured before elemental analysis using EDS. All luminescence measurements were made using a Risø TL/OSL DA-20 reader using the beta source, detection filters and PMT described in Chapter 3.

Before EDS analysis, grains from the KF extract from sample KHUT-1 were bleached using a 1000 s IR (diode) stimulation at 290°C, given a beta dose of 70 Gy, and preheated to 250°C for 10 s before IR laser stimulation at 30% power. After applying a 250°C (10 s) preheat, each grain from the KF extract was heated to 50°C for 10 s, and the IR laser was switched on after 1.67 s and switched off again after 8.33 s to generate a decay curve. The decay curves of quartz and KF grains from the KF extract from sample KHUT-1 are shown in Figure 4-3. The grains from the quartz extract were not measured.

D_e, fading measurements (also made using the IR laser at 30% power), and fading-corrected age determination of KF grains from sample GHO-2 followed the protocols outlined in Chapter 6 (Neudorf *et al.* 2012), and these are described below. The relationships between grain D_e, fading measurements, and fading-corrected ages and grain elemental composition are discussed in Section 4.7.4.

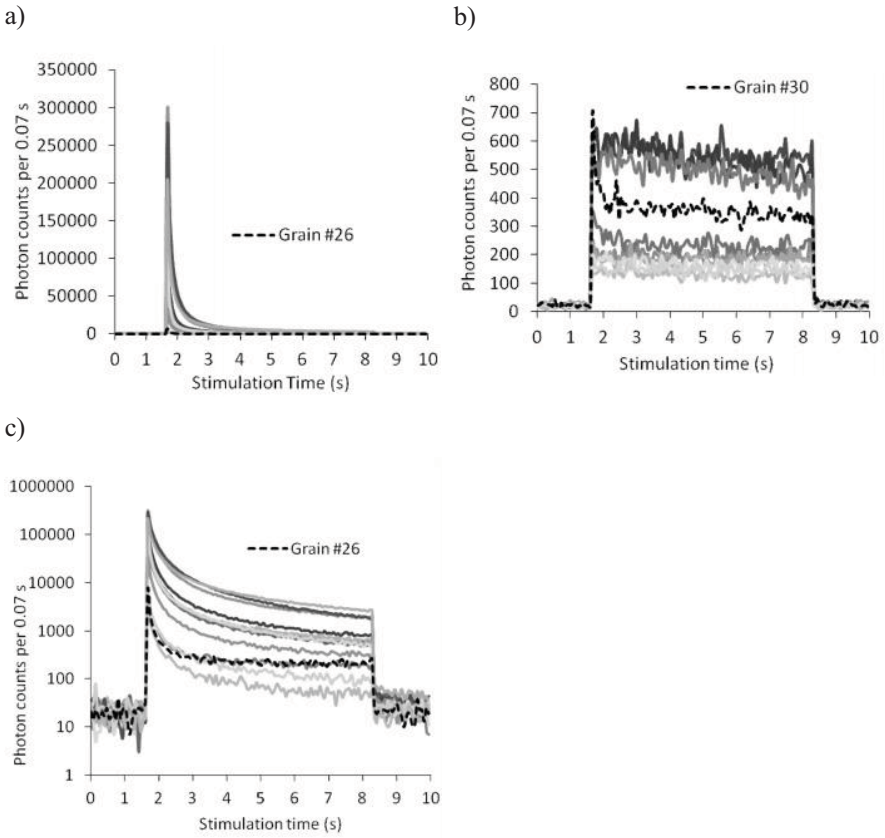

Figure 4-3. Grains obtained from a K-rich feldspar separate from sample KHUT-1 with bright, rapidly decaying luminescence signals (except for Grain #26) (a), and slowly decaying luminescence signals (b). The luminescence decay curve of a grain with a sharply decaying signal (Grain #30, dashed line) is highlighted in 'b'. EDS analysis of this grain suggests that it is plagioclase. c) The luminescence decay curves in 'a' are replotted using a logarithmic scale on the y-axis, and the decay curve of Grain #26 (dashed line) is highlighted. EDS analysis suggests that this is a plagioclase grain, while all others are orthoclase grains. See Table 4-2 and Figure 4-7 for the elemental concentrations of all grains.

4.3 D_e determination and rejection criteria

The D_e from grains from sample GHO-2 was measured using an IRSL SAR procedure described in Chapter 3 (Table 3-3). The temperature and duration of the preheat (250°C, 10 s) preceding the L_n and L_x measurements were identical to those preceding the T_n and T_x measurements, following Huot and Lamothe (2003), and all IRSL measurements were made while holding the sample at 50°C (Table 3-3). At the end of each SAR cycle, all grains on each disc were bleached using IR LEDs for 40 s at 290°C to reduce recuperation.

KF grains were rejected if: 1) they exhibited an IRSL decay curve typical of holes occupied by quartz grains; 2) their signals failed to grow systematically with increasing regenerative dose (i.e., they had no dose-response curve); 3) the sensitivity-corrected zero-

dose signal was greater than 5% of L_n/T_n; 4) the first 0.134 s of the test dose signal following the natural IRSL measurement was less than 3 times the background; 5) the recycling ratio differed from unity by more than 2σ (Jacobs & Roberts 2007); and 6) grains were rejected if their natural and/or regenerative signals greater than 268,000 counts per 0.134 s to prevent partial saturation of the photomultiplier tube.

4.4 Anomalous fading measurements

Fading tests for single grains followed the procedure of Auclair *et al.* (2003). After D_e measurement of single grains, each grain (still located in the same hole) was stimulated repeatedly with the IR laser after being given a laboratory dose of 34 Gy (L_x) and following a series of delay times after irradiation and preheating (Table 4-1). Each L_x measurement was immediately followed by a test dose (14 Gy) measurement (T_x) to correct the L_x signal for sensitivity change. A prompt measurement (i.e., an L_x/T_x measurement made after no delay period) was made immediately after each delayed L_x/T_x measurement to ensure that any sensitivity changes of L_x/T_x measurements throughout the fading test are accounted for (Huot, 2007). Maximum delay times for each grain were ~44 h.

Table 4-1. Anomalous fading SAR measurement protocol for single KF grains.

1.	Dose (34 Gy)
2.	Preheat (250 °C, 10 s)
3.	IRSL[1] (IR laser, 50 °C, 10 s) → L_x (prompt)
4.	Test dose (14 Gy)
5.	Preheat (250 °C, 10 s)
6.	IRSL[1] (IR laser, 50 °C, 10 s) → T_x (prompt)
7.	IRSL bleach (diodes, 290 °C, 40 s)
8.	Dose (34 Gy)
9.	Preheat (250 °C, 10 s)
10.	Delay[2]
11.	IRSL[1] (IR laser, 50 °C, 10 s) → L_x (delay)
12.	Test dose (14 Gy)
13.	Preheat (250 °C, 10 s)
14.	IRSL[1] (IR laser, 50 °C, 10 s) → T_x (delay)
15.	IRSL bleach (diodes, 290 °C, 40 s)
16.	Return to step 1 for the remaining delay times.

[1]IR laser stimulation commenced 1.675 s after the disc temperature reached 50°C and lasted for 6.7 s.
[2]Delay times ranged from ~4 min (prompt measurements) to 44 h after irradiation.

4.5 Fading rate and fading-corrected age calculations

In this study, the *g*-value of each grain was calculated using Equation 4 of Huntley and Lamothe (2001):

$$I/I_c = 1 - (g/100) * \log_{10}(t/t_c) \quad (1)$$

where I/I_c is the L_x/T_x measurement (I) normalized to the first prompt L_x/T_x measurement (I_c), $t \approx t_1 + (t_2 - t_1) / 2$, where t_1 is the time elapsed since the end of irradiation and the measurement of L_x, t_2 is the time elapsed since the beginning of irradiation and the measurement of L_x, and t_c is t for the first prompt measurement. Thus, the *g*-value is the slope of the weighted regression line of I/I_c plotted against $\log_{10}(t/t_c)$, multiplied by 100. The error of the *g*-value for each grain was calculated as the standard error of the slope of this weighted regression line, multiplied by 100. The weighted linear regression (weighted according to the square of the inverse of the measurement error for each I/I_c) was performed using the linear model function called '**lm**' in the R package (http://www.r-project.org). Following convention, the *g*-value and its uncertainty were evaluated for $t_c = 2$ days (Huntley and Lamothe, 2001).

To calculate the fading-corrected age of each grain from sample GHO-2, the single-grain D_e values, *g*-values (normalized to 2 days), and the total dose rate for the bulk sample (2.42 ± 0.08 Gy/ka), as well as their uncertainties, were used as parameters in the Huntley and Lamothe (2001) fading-correction model. The calculations were performed using the Excel spreadsheet and macro provided by Sébastien Huot. The fading-corrected age for each grain (T) was calculated using Equation A5 of Huntley and Lamothe (2001):

$$T_f/T = D_{ef}/D_e = I_f/I = 1 - \kappa\,[\ln(T/t_c) - 1] \quad (2)$$

where $T_f = D_e/D_a$ (i.e., the calculated age before correction for fading), D_e is the measured equivalent dose, D_a is the total dose rate for the bulk sample, and D_{ef} and I_f are the values of D_e and I that would be obtained if there were no fading.

The associated uncertainty on this age (at 1σ) was calculated as:

$$T * \{[(T_{max} - T_{min}) / (2*T)]\text{^}2 + (\Delta T_f/T_f)\text{^}2\}\text{^ } 0.5 \quad (3)$$

where T_{max} and T_{min} are the fading-corrected ages obtained using the measured *g*-value (normalized to 2 days) plus 1σ and minus 1σ, respectively, and ΔT_f is the uncertainty on T_f. ΔT_f was calculated as:

$$T_f * [(\Delta D_e/D_e)^2 + (\Delta D_a/D_a)^2]^{0.5} \quad (4)$$

where ΔD_e and ΔD_a are the 1σ uncertainties on D_e and D_a, respectively.

4.6 EDS analysis

4.6.1 Measurements

The EDS system at University of Wollongong is equipped with an electron beam gun and a lithium-drifted silicon (Si(Li)) solid state X-ray detector, and is integrated into a JEOL JEM LV 6490 scanning electron microscope (SEM). The gun emits an electron beam to a sample target (in this case, a single sand grain). Electron bombardment by the beam causes electron transitions between inner atomic orbitals in the sample that result in the emission of X-rays from different energy-level shells (K, L and M) in different elements (Reed 1995). The energy of individual X-rays is converted to electrical voltages of proportional size, and these electrical pulses correspond, in turn to the characteristic X-rays of each element detected in the sample.

All grains from the K-rich feldspar extract from sample KHUT-1 were analyzed. The elemental concentrations of museum specimens of orthoclase, anorthite, laboradorite and quartz were also measured for comparison. These specimens were obtained from the Howard Worner mineral and rock collection in the School of Earth and Environmental Sciences at the University of Wollongong.

All sand grains and rock specimens were mounted on specimen stubs with a double-sided adhesive carbon-filled conductive disc. The specimens were then carbon coated in a sputter coater to prevent the accumulation of static electric charge on their surface during irradiation (Welton 1984). The specimen stubs were placed in a holder in a vacuum-pumped specimen chamber, where a pressure of less than 10^{-4} mbar was maintained to prevent electrons in the beam from being scattered by gas atoms.

EDS measurements were made in "spot" mode using a beam diameter of 67 μm and a probe current of 1 nA. Spot measurements were made on relatively flat surfaces of the specimens that were tilted toward the detector, as seen in topographic, secondary electron (SE) images (or SEM micrographs). SEM microphotographs for a subset of the measured sand grains are shown in Figures 4-4 and 4-5. The counting time for each spot measurement was 50 s using a minimum count rate of 5000 counts per second. Each spot measurement yields an EDS spectrum, which is portrayed as a plot of X-ray counts versus energy (in kilo-electron volts or KeV) (Fig. 4-6). The characteristic X-rays of each element in the specimen

appear as peaks, and the elemental composition of a specimen can be determined by comparing the peak-height ratios of each element to those of a known standard.

a) Grain 1

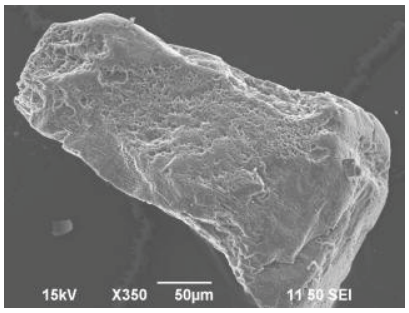

b) Grain 5

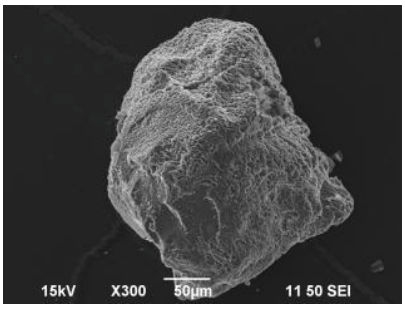

c) Grain 7

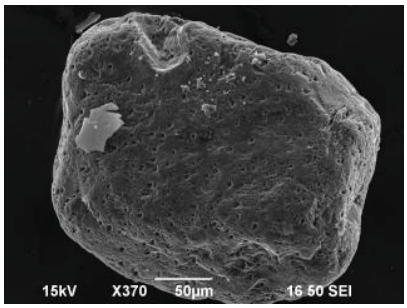

d) Grain 8

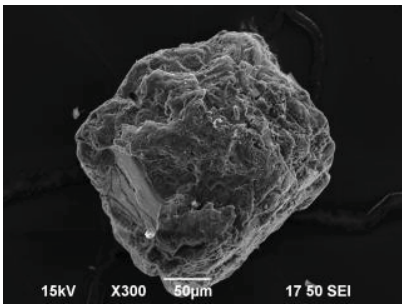

e) Grain 26

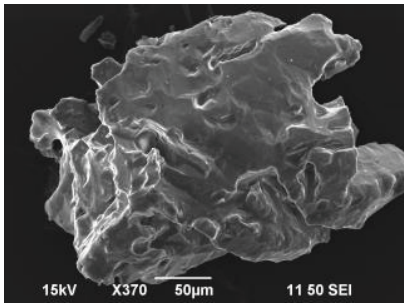

f) Grain 82

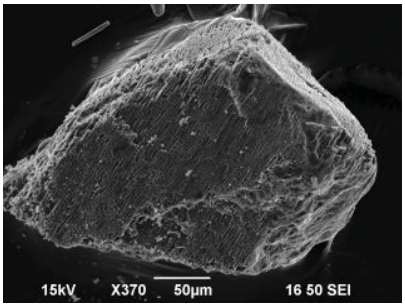

Figure 4-4. SEM microphotographs of a subset of feldspar grains with bright, rapidly-decaying luminescence signals (e.g., Figs 4-3a, 4-3c). All grains are likely K-rich feldspars, except for Grain 26, which is likely plagioclase and is much dimmer than the rest. See Table 4-2 for EDS elemental concentrations.

a) Grain 4

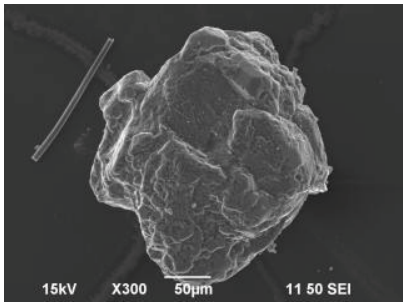

b) Grain 27

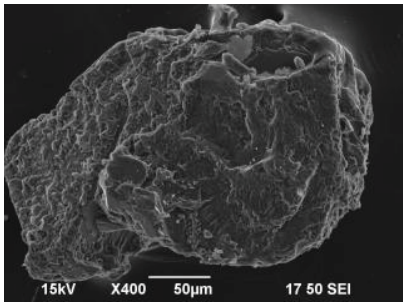

c) Grain 30

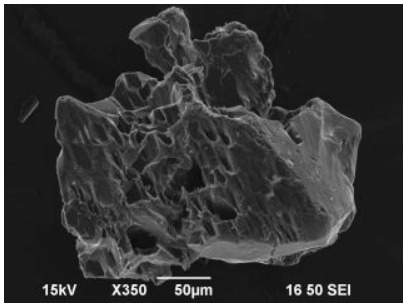

d) Grain 34

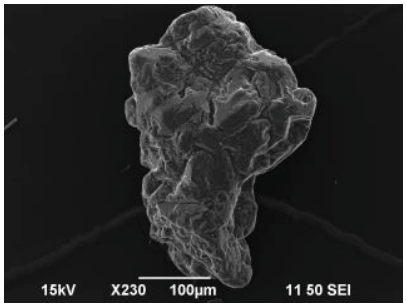

e) Grain 37

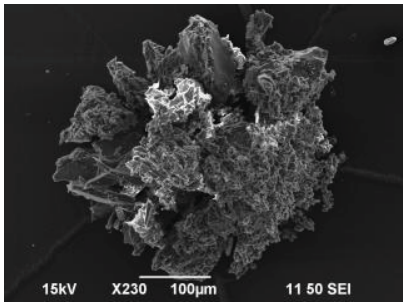

f) Grain 36

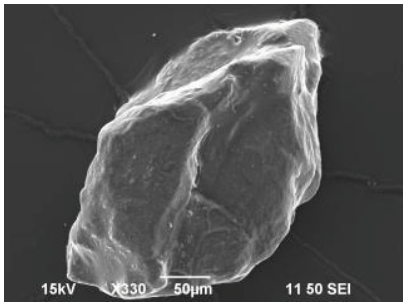

Figure 4-5. SEM microphotographs of a subset of grains with dim, slowly-decaying luminescence signals (e.g., Fig. 4-3b). Most of these grains are likely quartz grains. The elevated proportion of Na and Ca in Grain 30 suggests that it may be a quartz grain with plagioclase inclusions or a plagioclase grain with a weak signal. Grain 37 was crushed while being transferred from the single-grain disc hole to the specimen stub. See Table 4-2 for EDS elemental concentrations.

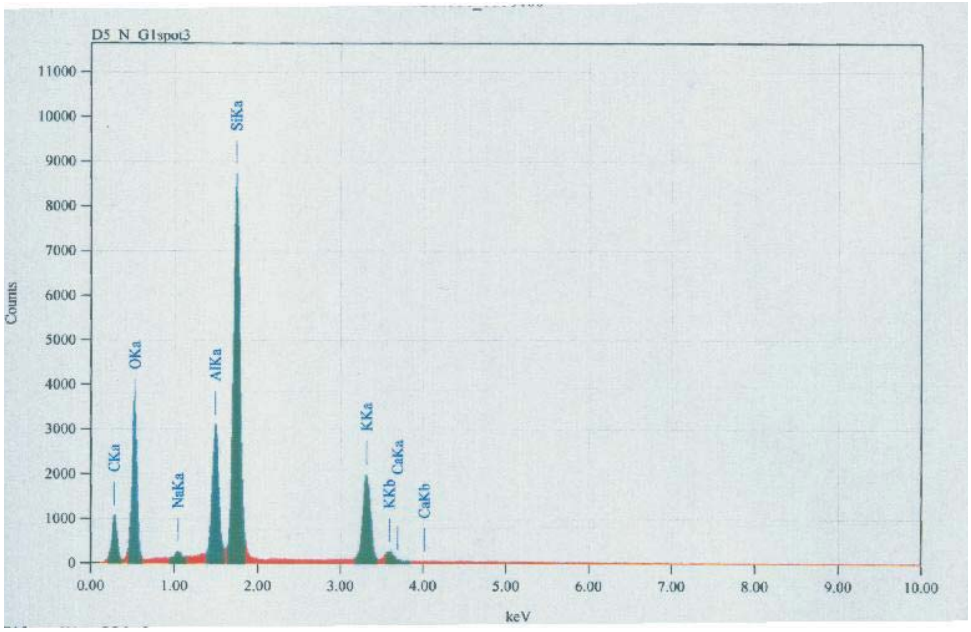

Figure 4-6. EDS spectrum of a potassium-rich feldspar grain. The peaks associated with the Kα X-ray lines of C, O, Na, Al, Si, K and Ca, and the Kβ X-ray lines of K and Ca are highlighted in green. The red signal represents the background signal (also known as "Bremsstrahlung") derived from interactions between incident electrons and atomic nuclei.

An estimate of the relative proportions of Si, Al, K, Na, Ca, and O in each grain was derived using the 'ZAF standardless quantitative method' using standard JEOL software (Yakowitz 1975). The ZAF method uses physical models to correct for atomic number effects (*Z*) (due to differences between the atomic number of the specimen and the standard), absorption of some X-rays by the specimen (*A*), and fluorescence (*F*) (Yakowitz 1975). This method of analysis is considered 'standardless' because data were not compared to known standards measured on the same machine, but rather to default values supplied by JEOL.

4.6.2 EDS results

The elemental concentrations of grains from both the K-rich feldspar and quartz separates are presented in Table 4-2. The compositions of the museum specimens are presented in Table 4-3. All data are graphically displayed in Figure 4-7. The mass concentrations of each element are reported in weight %, with a standard error typically between 0.1 and 0.4 %. These values can only be considered qualitative, because the surfaces of the grains and museum specimens were not polished before measurement (Figs 4-4 and 4-5) and because the thickness of the carbon coating cannot be quantified (Yakowitz & Goldstein 1975; Welton 1984). The carbon coating contributes to the C concentrations shown in Tables 4-2, 4-3, and Figure 4-7.

Table 4-2. Elemental concentrations of single grains of feldspar (F) and quartz (Q), as determined through EDS analysis.[1]

Grain #	Q/F[2]	Decay Curve[3]	Si (wt %)	Al (wt %)	K (wt %)	Na (wt %)	Ca (wt %)	O (wt %)	C[4] (wt %)	Sum[5]
1	F	B	20.58	7.12	7.03	0.52	0	42.55	22.20	100.00
5	F	B	18.46	5.82	5.25	0.60	0.1	42.13	27.73	100.00
7	F	B	20.85	7.36	7.61	0.30	0	43.56	20.12	99.80
8	F	B	15.37	5.58	5.12	0.33	0	45.84	27.66	99.90
26	F	B	16.63	5.21	0.03	2.27	1.38	36.16	38.32	99.99
33	F	B	18.45	6.66	6.17	0.46	0	46.43	21.74	99.91
39	F	B	12.18	4.28	3.71	0.47	0	45.82	33.54	100.00
44	F	B	19.96	7.14	7.41	0.35	0	41.13	23.87	99.86
55	F	B	13.35	4.86	4.42	0.38	0	45.64	31.23	99.88
82	F	B	7.90	2.95	2.45	0.41	0	36.28	49.94	99.93
99	F	B	20.40	7.26	7.72	0.20	0	42.56	21.75	99.89
Average			**16.73**	**5.84**	**5.17**	**0.57**	**0.13**	**42.55**	**28.92**	
4	F	D	23.64	0	0.01	0.08	0.02	39.31	35.47	98.53
27	F	D	26.79	0.35	0	0	0	51.84	21.01	99.99
30	F	D	17.36	8.30	0.10	4.84	1.84	47.34	20.06	99.84
34	F	D	23.52	0.39	0	0.07	0	52.3	23.72	100.00
37	F	D	40.41	0	0	0.01	0.01	4.06	55.47	99.96
36	F	D	19.42	1.41	0.08	0	0.11	45.13	33.86	100.01
64	F	D	17.82	6.35	0	0.28	0	45.71	23.40	93.56
81	F	D	28.29	0.50	0	0.03	0.10	50.44	20.73	100.00
Average			**24.66**	**2.16**	**0.02**	**0.66**	**0.26**	**42.02**	**29.22**	
1	Q	n/a	29.04	0.30	0.01	0.07	0	55.00	15.59	100.01
2	Q	n/a	29.64	0.41	0	0	0.01	54.55	15.39	100.00
3	Q	n/a	25.29	0.30	0	0	0.03	55.73	18.66	100.01
4	Q	n/a	27.67	0.48	0	0.02	0.03	52.61	19.18	99.99
5	Q	n/a	33.66	0.37	0	0.06	0.05	52.19	13.68	100.01
6	Q	n/a	29.71	0.34	0	0.02	0	51.15	18.75	99.97
7	Q	n/a	33.56	0.36	0	0.04	0.01	53.34	12.65	99.96
8	Q	n/a	33.52	0.42	0.01	0	0.01	53.23	12.81	100.00
9	Q	n/a	34.46	0.35	0.01	0.06	0.04	50.23	14.85	100.00
10	Q	n/a	34.27	0.53	0.09	0.03	0	49.49	15.6	100.01
Average			**31.52**	**0.39**	**0.01**	**0.03**	**0.02**	**52.25**	**15.77**	

[1]Standard errors of each spot measurement are not reported, but range between 0.1 and 0.4 %.
[2]F = grains are obtained from a density-separated ($\rho < 2.58$ g/cm^3) and HF etched K-rich feldspar separate that likely includes some quartz and plagioclase grains. Q = grains are obtained from a density-separated ($\rho > 2.62$ g/cm^3) and HF etched quartz separate. Both separates are from sample KHUT-1.
[3]B = a bright, rapidly-decaying signal, D = a dim, slowly-decaying signal. n/a = decay curves were not measured on the density-separated quartz grains.
[4]The carbon content of each grain is derived predominantly from the carbon coating applied to the specimen before measurement.
[5]Deviations from 100.00% are due to statistical uncertainties in elemental concentration calculations, and the presence of other elements (e.g., Mg) that appear in such low concentrations that their X-ray peaks cannot be differentiated from the background counts or X-ray peaks of other elements in the EDS spectrum.

Table 4-3. Elemental concentrations of one quartz and three feldspar museum specimens, as determined using EDS.[1]

Museum Sample	Si (wt %)	Al (wt %)	K (wt %)	Na (wt %)	Ca (wt %)	O (wt %)	C[1] (wt %)	Unknown (wt %)	Sum[1]
Laboradorite	16.16	7.96	0.23	1.52	1.97	47.96	18.96	4.80	95.20
Anorthite	12.23	5.19	1.36	2.84	8.24	43.41	22.76	3.96	96.04
Orthoclase	20.36	7.19	7.02	0.63	0	41.43	23.25	0.15	99.85
Quartz	19.31	0.78	0.01	0.08	0.02	41.63	38.16	0.01	99.99

[1]See footnotes 1, 4 and 5 of Table 4-2.

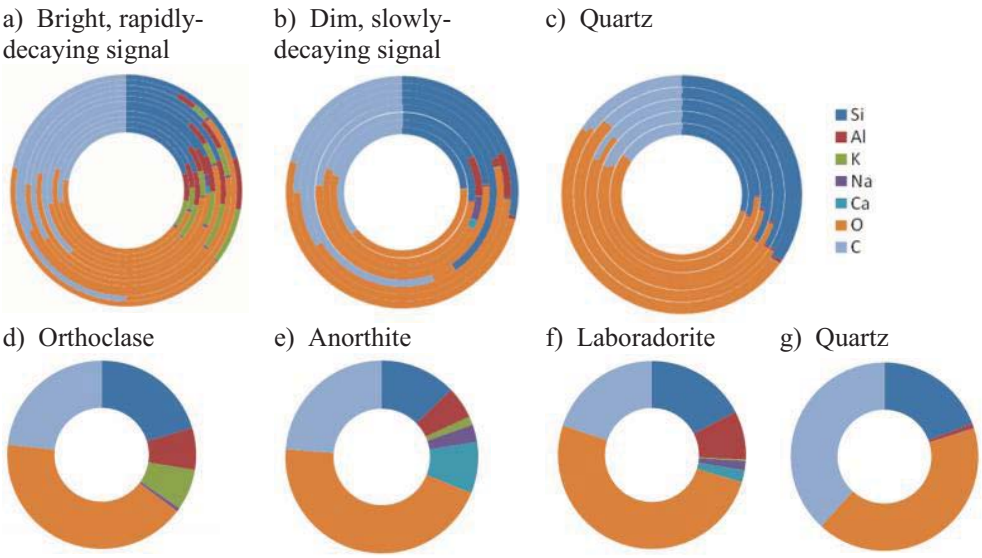

Figure 4-7. Donut plots showing the elemental concentrations of individual grains from sample KHUT-1 (a–c) and museum specimens (d–g) and (see Tables 4-1 and 4-2 for raw data). Grains obtained from a KF extract are shown in 'a' (bright, rapidly-decaying signals) and 'b' (dim, slowly-decaying signals). Note the lack of potassium in the grains shown in 'b'. c) Grains from a quartz separate from KHUT-1. The elemental concentrations of museum speciments of orthoclase, anorthite, laboradorite, and quartz are shown in 'd', 'e', 'f' and 'g', respectively, for comparison.

4.6.3 Luminescence intensity versus feldspar type

Most grains characterised by bright, rapidly decaying signals have detectable amounts of Si, Al, K, Na and O and little or no Ca. The measured K concentration of these grains (excluding a low-K grain, Grain #26) averages 5.17 wt% with a standard deviation of 1.80 %, and this value is comparable to the measured K concentration of the orthoclase museum specimen (7.02%). Thus these grains are likely KF grains. One grain (Grain #26) has a negligible K concentration, but higher concentrations of Na and Ca, and therefore is likely plagioclase. Grain #26 is characterised by a luminescence signal that is significantly weaker than that of other KF grains (Figs 4-3a and c).

Grains with slowly decaying IRSL signals (Fig. 4-3b) usually have abundant Si and O, but little or no detectable K, Na or Ca (Table 4-2, Fig. 4-7). Most of these grains are likely quartz grains. The elevated proportion of Na and Ca in one of these grains (#30, Table 4-2) suggests that this may be a quartz grain with plagioclase inclusions or a plagioclase grain with a weak IRSL signal. Closer inspection of the decay curve of this grain (Fig. 4-3b) shows a rapidly decaying peak in the first 0.5 s of stimulation, and this may be the remnant of a dim or partially depleted feldspar luminescence signal.

The intensity and thermal stability of IRSL emissions from feldspars centred around the 400 nm band has been shown to be somewhat dependent on feldspar type. Pulse anneal experiments on multi-grain aliquots by Tso *et al.* (1996) suggest that the source traps of the IRSL signal from Na-rich feldspars is less thermally stable than that of K-rich feldspars,

resulting in a shorter lifetime (0.9 x 10^4 years for Na-rich feldspars than the lifetime of 1.0 x 10^9 years for K-rich feldspars at an ambient temperature of 10°C). Pulse anneal experiments on individual grains by Li *et al.* (2010) also suggest that the source traps of Na-feldspar IRSL signals are less thermally stable than those of K-rich feldspars, and this may result in dimmer signals and lower D_e estimates in Na-feldspar grains. Differences in signal intensity (in signals centred around 400 nm) between different feldspar types may also be attributed to differences in their luminescence emission spectra. Early studies of TL and IRSL spectra have shown that K-feldspars tend to have strong emissions in centred around 400 nm while Na-rich and Ca-rich feldspars have strong emissions centred around 570 nm (Huntley *et al.* 1988; Huntley *et al.* 1991). Prescott and Fox (1993) have shown that thermoluminescence emissions centred around 400 nm are strongest for feldspars with more than 80% mole orthoclase, but weaker for all other alkali and some plagioclase feldspars. Spooner (1992) measured the TL and IRSL (880 Δ 80 nm) luminescence intensities of feldspars with a range of Albite:Orthoclase:Anorthite molecular percentage ratios with a focus on emissions centered around 400 nm. He found lower IRSL and TL sensitivities for Ca-rich feldspars than for Na- or K-rich feldspars, but with considerable variation in intensity superimposed on this trend. Deviations from the main trend were thought to be due to crystal structure state, thermal history, and trace element concentrations. It is suggested here that the relatively low signal-to-noise ratios observed in Grains 26 and 30 (Fig. 4-3) may reflect increased thermal erosion of the signal source traps, relative to the other K-rich feldspar grains during the preheat.

The grains from the quartz separate and the quartz museum specimen are similar in that both are dominated by Si and O, with small detectable amounts of Al. The Al is likely present as an impurity within quartz crystals that crystallized in close proximity to Al sources (Dennen *et al.* 1970). No grains in the quartz separate contained detectable amounts of K, Na or Ca above 0.1 wt%, suggesting that the density separation procedures used here were successful in minimizing the number of contaminating feldspar and other mineral grains.

4.7 WDS analysis

4.7.1 WDS measurements

WDS measurements were made on 151 grains from sample GHO-2 that were used for D_e estimation and fading measurements, to detect any relationships between their elemental composition and luminescence characteristics, D_e values, fading rates and fading-corrected ages. WDS measurements were made using a Cameca SX-100 electron microprobe in the Department of Earth and Planetary Sciences, at Macquarie University,

Australia. Unlike energy-dispersive spectrometers, which record an entire spectrum of X-ray wavelengths simultaneously, WD spectrometers consist of an analytical crystal and a gas proportional counter detector, which detect X-rays of only one wavelength at a time. WDS systems commonly make use of multiple WD spectrometers and high electron beam currents (up to 100 nA) that enable a higher count rate of X-rays. As a result, WDS systems achieve a much higher X-ray spectral resolution than EDS systems, and elemental concentrations of flat, polished specimens can be determined with detection limits as low as 10 ppm (Reed 1995).

All grains from three single-grain discs were lifted out of the holes using double-sided sticky tape. The other side of the tape was then adhered to a flattened, polished base of a round plastic capsule ~30 mm in diameter and 20 mm deep. The capsule was then filled with epoxy resin and cured. After curing, the resin block was ground with glass paper of progressively finer grades (240, 800, 1200, 2000) to the centre of the layer of single grains. To ensure that grain surfaces were as flat and smooth as possible, the surface of the block was polished using 6, 3, and 1 μm diamond paste. Approximately half of the grains from each single-grain disc were lost during the grinding process. A vacuum-evaporated carbon coating (~20 nm thick) was applied to the top of the resin block using a sputter coater.

The polished block was inserted into a holder in a vacuum-pumped specimen chamber and the locations of spot measurements were identified and recorded using standard software and a high-power optical microscope and charge-coupled device (CCD) camera imaging system. Three spot measurements were made on each grain using an electron beam size of 5 μm and a beam current of 20 nA. The beam current samples a volume no greater than 3 μm^3. Most grain surfaces still contained rough spots after polishing, so spot measurement locations were restricted to flat grain surfaces with an homogeneous appearance. Five WDS spectrometer reference crystals were used to isolate the characteristic X-rays (Kα X-ray lines) of K, Mg, Si, Ca, Fe, Na, and Al. The detection crystal types, standards used, as well as the average detection limits achieved for each element are listed in Table 4-4. The elemental concentration of each spot measurement was quantified using the ZAF (Z—backscatter effect, A—absorption of radiation within the grain, F—fluorescence) quantitative method (Reed, 1995). The elemental concentration of each grain (reported as an absolute value in weight %) was calculated as the average of the three spot measurements.

Table 4-4. WDS crystal types, standards and detection limits for all elements measured for single KF grains of sample GHO-2.

Element	**K**	**Mg**	**Si**	**Ca**	**Fe**	**Na**	**Al**
Crystal	Pentaerythritol (PET)	Thallium acid phthalate (TAP)	Thallium acid phthalate (TAP)	Pentaerythritol (PET)	Lithium fluoride (LIF)	Thallium acid phthalate (TAP)	Thallium acid phthalate (TAP)
Standards	orthoclase (12.79% K)	olivine (30.62% Mg)	kyanite (17.3% Si)	$CaSiO_3$ (34.5026% Ca)	Fe (100% Fe)	albite (8.71% Na)	kyanite (17.3% Si)
Average detection limits (ppm)	350	164	289	252	532	234	233

4.7.2 WDS results

Single-grain elemental compositions are shown as donut plots in Figure 4-8a. Each ring in each donut plot represents the elemental composition of a single grain (the rings are very thin but 12 subgroups of rings are visible on the plot). Most grains (76%) are classified as K-rich feldspars (i.e., they have measured K contents of 8% or more). Eleven percent of grains contain more than 90% SiO_2, and thus are classified as quartz. Three grains have significant amounts of aluminum and iron and are classified as Fe-rich aluminosilicates. Four percent of grains contain significant amounts of Ca, Na, and Al and are classified as plagioclase (Fig. 4-8a, Table 4-5). Seven percent of grains exhibit heterogeneity in their elemental composition (i.e., values of the three spot measurements differed by more than 2%), so these grains were excluded from further analyses (Table 4-5). These heterogeneous grains may contain mineral inclusions.

Table 4-5. Microprobe-measured grains from a K-rich feldspar separate from sample GHO-2.

	Number of grains	**% of total grains**
Total number of grains measured	151	
K-rich grains (> 8% K)	115	76
Quartz (>90% SiO_2)	16	11
Fe-rich aluminosilicate	3	2
Ca/Na-rich feldspar	6	4
Heterogeneous elemental composition	11	7

a) K-rich feldspar grains

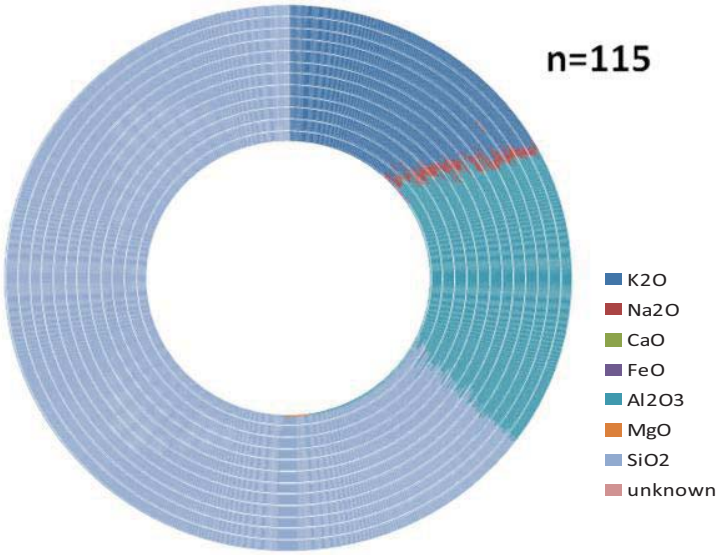

b) Quartz, plagioclase, and Fe-rich aluminosilicate grains

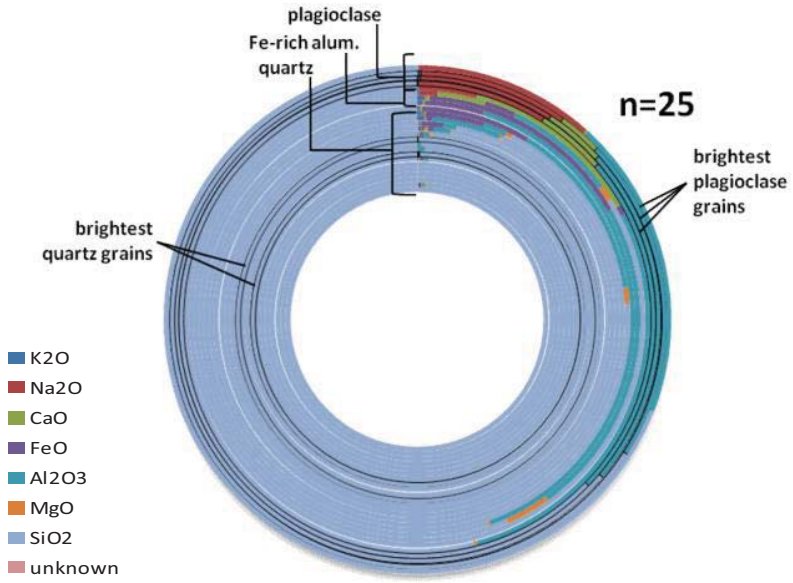

Figure 4-8. Donut plots showing the elemental composition of individual K-rich feldspar grains (n=115) (a) and plagioclase, Fe-rich aluminosilicate, and quartz grains (n=25) (b). Each ring in each donut plot represents the elemental composition of a single grain. The rings in 'a' are very thin but 12 subgroups of rings are visible on the plot. All grains are from sample GHO-2 and are classified as homogeneous at the scale of a single grain (i.e., the three WDS spot measurement values for each grain were consistent within 2%). The elemental composition of the brightest quartz and plagioclase grains are highlighted in 'b'.

4.7.3 Major element content and IRSL

The IRSL decay curves for all K-rich, plagioclase, quartz, and Fe-rich aluminosilicate grains are shown in Figure 4-9 'a–d'. These signals come from the first test dose (T_n) measured after the natural signal used for D_e determination. These curves are plotted again in Figure 4-9 'e–h' with a logarithmic y-axis, so that the decay curve shapes of both bright and dim grains are visible. All grains were heated to 50°C for 10 s, and the laser was switched on after 1.67 s and switched off again after 8.33 s. Each channel represents 0.067 s of photon detection and each grain was stimulated with the laser for 6.66 s.

Grains in the K-rich feldspar, plagioclase and quartz groups can have both bright, rapidly decaying luminescence curves, and dim, slowly-decaying IRSL curves (Figs 4-9). The Fe-rich aluminosilicate IRSL curves show little or no decay during the full 6.7 s of stimulation (Fig. 4-9). The brightest grains (up to ~88,000 counts in the first channel of laser stimulation) fall into the K-rich feldspar group, although 7% of grains in this group also emit less than 100 counts per channel. Three out of the six plagioclase grains measured have signal intensities less than 100 counts per channel, with the three brightest grains emitting 1609, 9734 and 19,265 counts in the first channel of laser stimulation. Most quartz grains (13 out of 16) emit less than 100 counts per channel, with the two brightest emitting 1304 and 3617 counts in the first channel of IRSL stimulation.

The elemental compositions of the brightest quartz and plagioclase grains are highlighted in Figure 4-8b, and their signals cannot be explained by their major element compositions, as these do not appear to be unique or unusual. The K-feldspar grain-to-grain variations in signal intensity also cannot be explained by elemental composition, as the elemental composition is fairly consistent from grain to grain (Fig. 4-8a). The three Fe-rich aluminosilicate grains are very dim, with the brightest emitting ~200 counts in the first channel of laser stimulation. Scatterplots in Fig. 4-10 show no clear correlation between IRSL brightness and major element composition for any of the minerals measured.

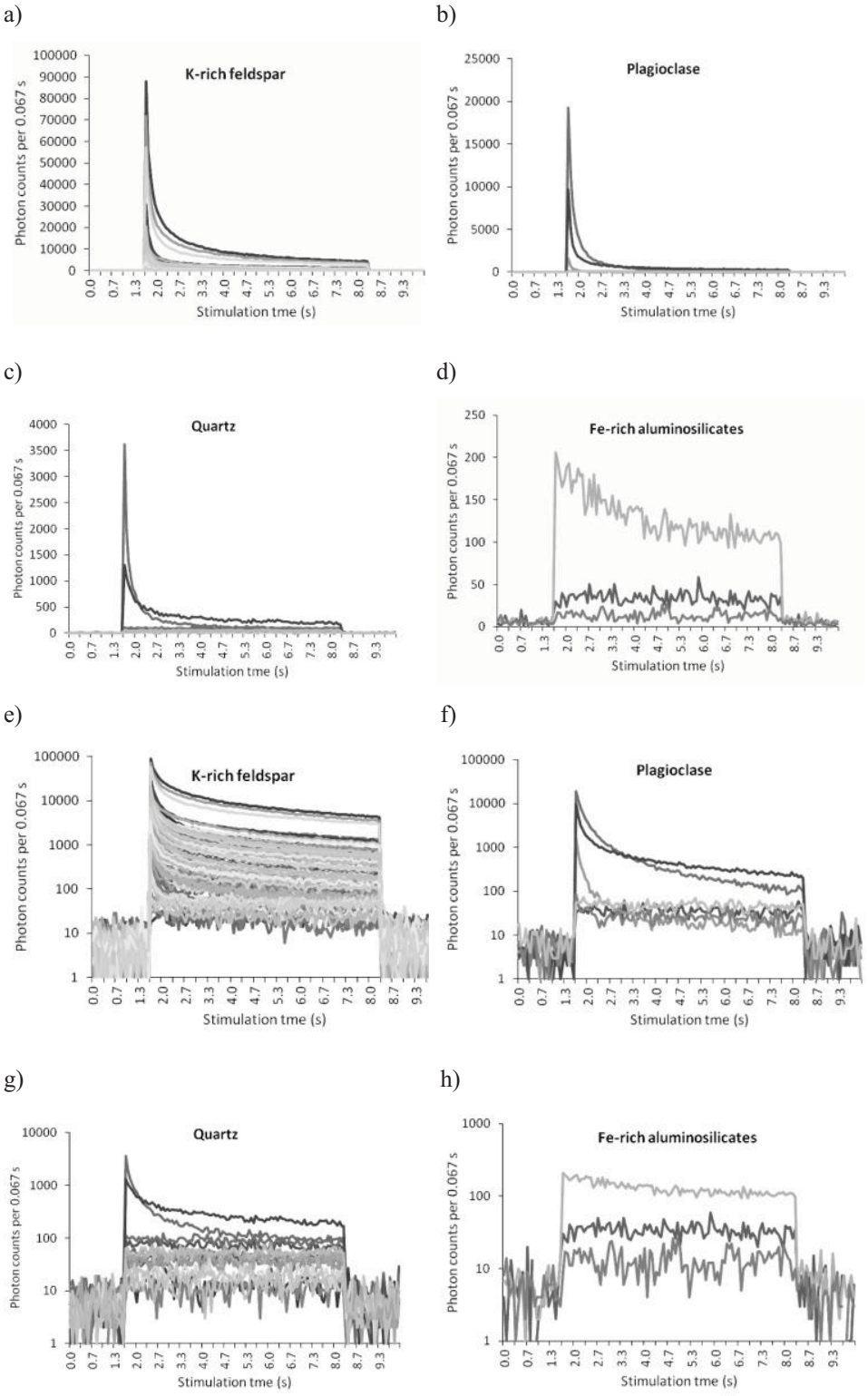

Figure 4-9. The IRSL decay curves for the K-rich feldspar, plagioclase, quartz and Fe-rich aluminosilicate grains in Figure 4-8 are shown in 'a', 'b', 'c', and 'd', respectively. Plots 'e–h' show the same decay curves but plotted with a y-axis on a logarithmic scale.

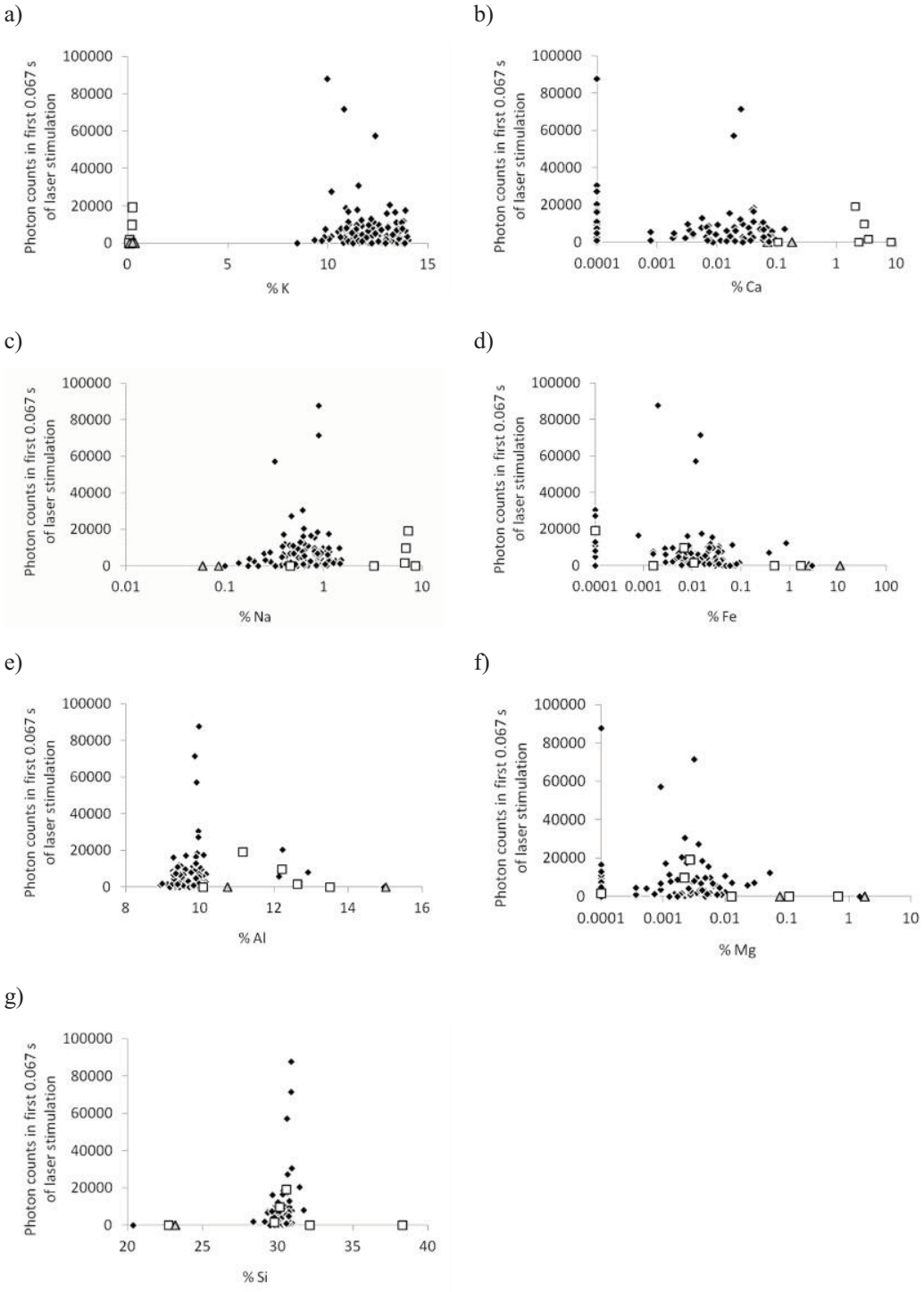

Figure 4-10. Luminescence test dose (T_n) signal brightness plotted against major element concentration for all K-rich feldspar (black diamonds), plagioclase (white squares), and quartz (grey triangles) grains. The x-axes in plots 'b', 'c', 'd' and 'f' are plotted on a logarithmic scale for clarity, and points with 0% element concentrations are plotted as 0.0001 % in these plots to avoid their omission.

The signal characteristics of most K-feldspar and quartz grains measured in this study are consistent with those reported in the literature. Duller *et al.* (2003) have shown that quartz grains exhibit a weak, slowly decaying signal when stimulated with the IR laser (their Fig. 1d), and similar signals have been observed from IR (830 nm) stimulated quartz aliquot (Bailey 1998, 2010). Spooner (1994b) has shown that IR (~860 nm) stimulation of quartz using a 20 mW/cm^2 Ar-ion laser can yield a weak signal at stimulation temperatures as low as 70°C (his Fig. 5-8), and suggested that weak IRSL (not detectable by his apparatus) would be likely to occur at temperatures below this. In this study, the IRSL signals detected from the single-grain disc holes containing quartz or Fe-rich aluminosilicate grains may be due not only to weak IRSL emissions from the quartz grains or feldspar inclusions inside them, but also to stray IRSL emissions from adjacent bright KF grains (i.e., crosstalk) (Duller 2008).

The rapidly decaying curves exhibited by the bright K-rich feldspar grains (Fig. 4-9a) are consistent with observations made by Duller *et al.* (2003) and Li *et al.* (2010). The shape of the decay curves of the brightest plagioclase grains are indistinguishable from those of the K-rich feldspars (Fig. 4-9e, f), but more plagioclase grains should be measured to conclusively determine whether or not they tend to be dimmer than K-rich feldspar grains in this sample. Few plagioclase grains appear in the K-rich feldspar separate (Table 4-5), suggesting that the density separation procedures used to separate plagioclase and K-rich feldspars were effective.

4.7.4 Feldspar elemental composition, D_e and fading rate

Past research has suggested that feldspar elemental composition may influence feldspar D_e values and fading rates. Because the ^{40}K content within individual KF grains is responsible for a significant fraction of the total dose rate to a grain in nature (Lamothe *et al.* 1994; Zhao & Li 2005), grain K contents are expected to influence D_e values.

The source traps for the IRSL signal from feldspars from each main compositional regime of the ternary system, and from a range of provenances have been shown to fade (Spooner 1992, 1994a; Huntley & Lamothe 2001; Huntley & Lian 2006) and some work suggests that feldspars from volcanic sediments are more susceptible to fading than feldspars from non-volcanic sources (Wintle 1973). Huntley and Lian (2006) found a positive correlation between Fe and Ca content and fading rate in plagioclase feldspars, but no relationship was found between fading rates and the major and minor elemental concentrations or the structural state of alkali feldspars. Aside from these studies, little work has been published on the relationships between feldspar elemental compositions and D_e, fading rates, and fading-corrected ages. Figures 4-11, 4-12 and 4-13 show major element content plotted against the D_e, *g*-value, and fading-corrected age for WDS-measured grains

from sample GHO-2 that passed all rejection criteria in Chapter 4 (see Section 4.3 for rejection criteria). No clear correlation is evident in any of the plots.

In sample GHO-2, the beta radiation from ^{40}K inside feldspar grains contributes up to 43% of the total dose rate, but there is no detectable correlation between individual grain K-content and D_e or fading-corrected age (Figs 4-11a, 4-12a). As will be discussed in Chapter 6, a dependency of grain age on K content may be masked by the fact that other sources of ionizing radiation account for two-thirds of the total dose rate, and any influence of elemental composition on K-feldspar single-grain ages may be masked by inhomogeneous bleaching of this fluvial sample. Pulse anneal experiments on individual grains by Li *et al.* (2010) suggested that Na-feldspar IRSL signals are less thermally stable than those of K-rich feldspars, and this may result in dimmer signals and lower D_e estimates in Na-feldspar grains. This result could not be verified in the present study, but few plagioclase grains were found in the K-rich feldspar extract. The two WDS-measured plagioclase grains that passed the single-grain rejection criteria (Section 4.3) do not appear to have unusually low D_e values (Fig. 4-10a).

No correlation between K-rich feldspar elemental composition and fading rate was found (Fig. 4-12a) and this is consistent with the findings of Huntley and Lian (2006). Unlike these authors, however I did not detect a correlation between Ca and Fe content and fading rate in plagioclase grains (Fig. 4-12b, d), but more plagioclase grains need to be measured to confirm this result.

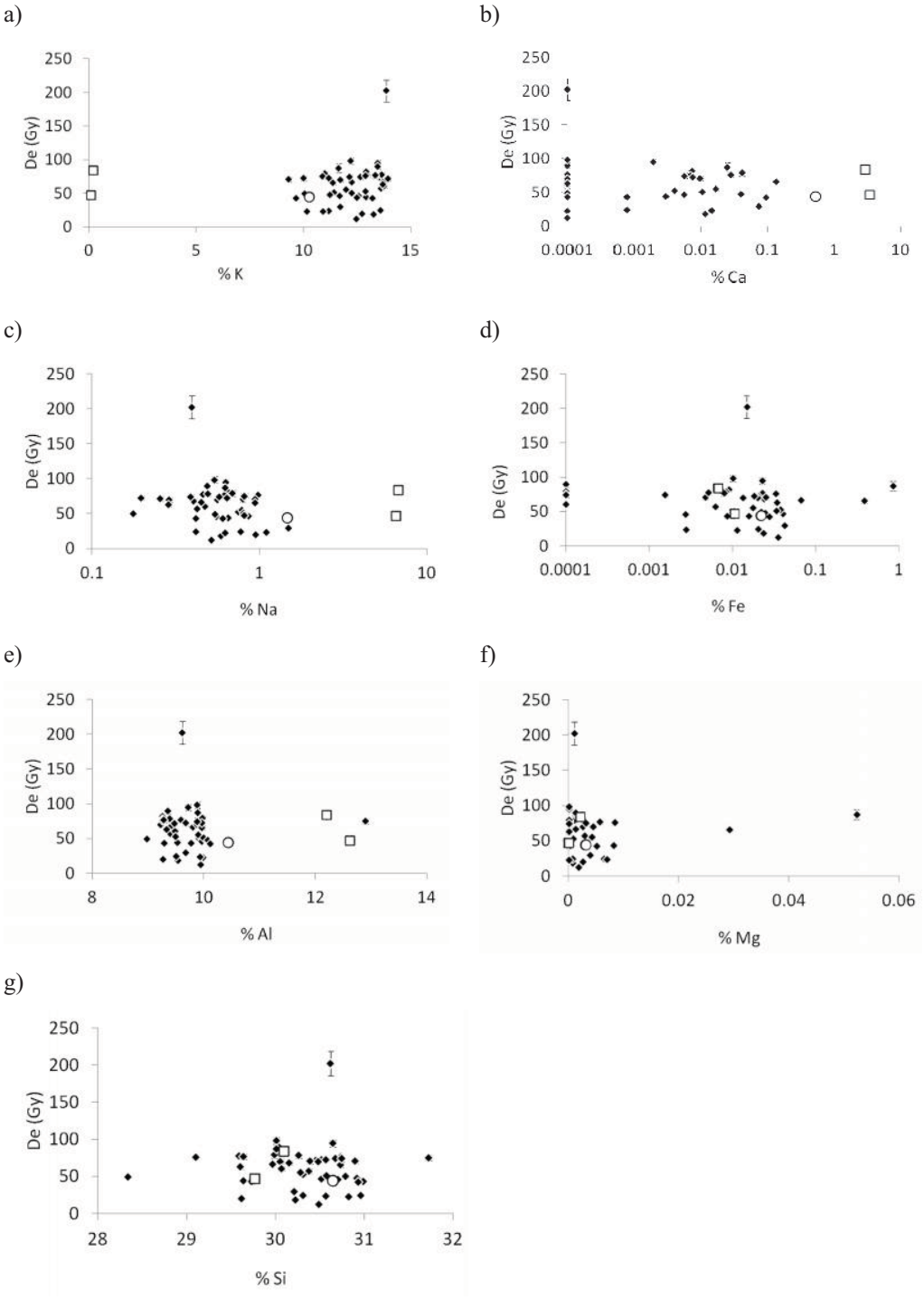

Figure 4-11. D_e versus major element concentration for all homogeneous K-rich feldspar (black damonds), plagioclase (white squares), and heterogeneous feldspar (white circles) grains (n=51). Grains are considered heterogeneous if their three WDS spot measurement values differ by more than 2%. The x-axes in plots 'b', 'c', and 'd' are plotted on a logarithmic scale for clarity, and points with 0% element concentrations are plotted as 0.0001 % in these plots to avoid their omission.

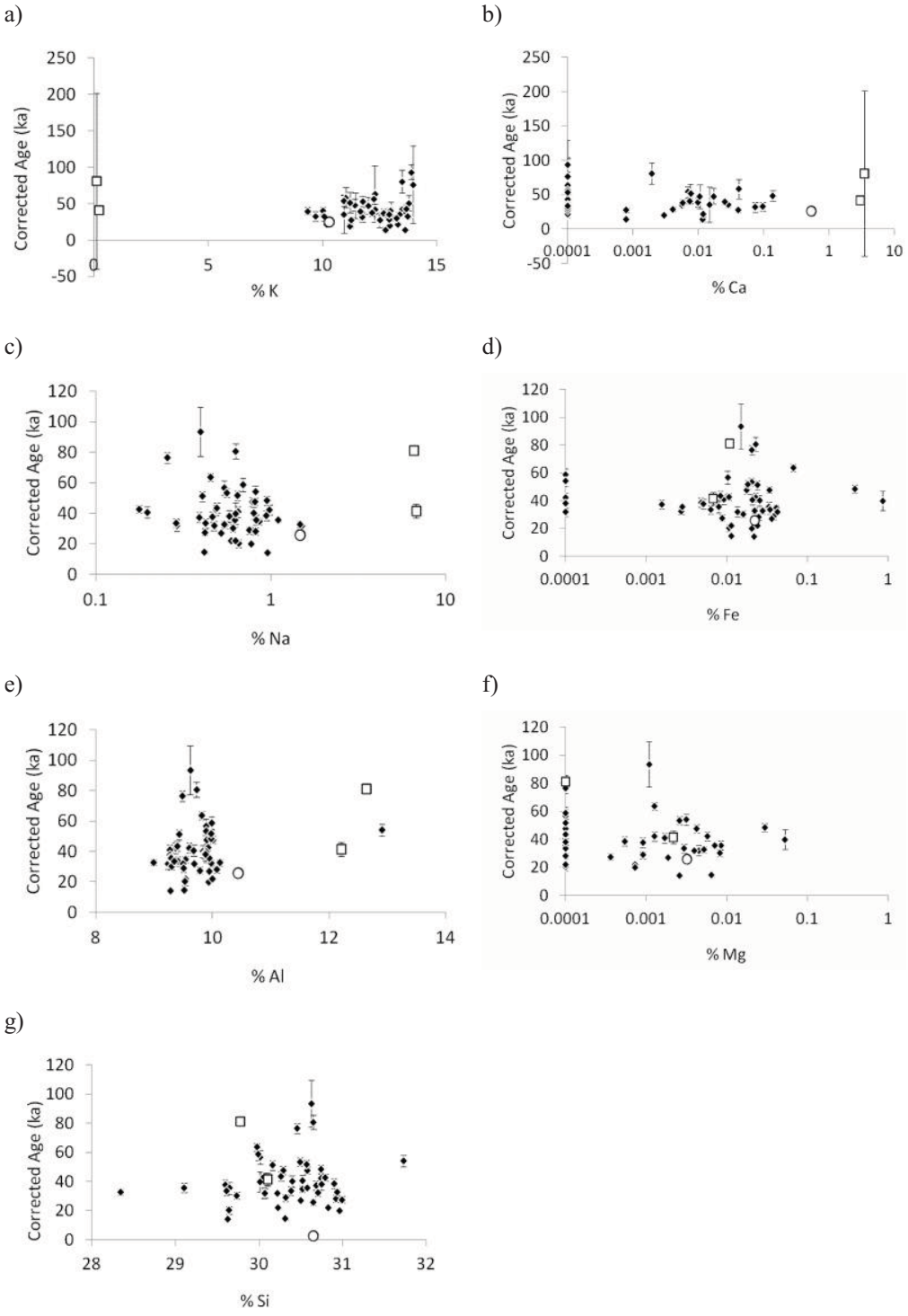

Figure 4-12. Fading-corrected age versus major element concentration for all homogeneous K-rich feldspar (black diamonds), plagioclase (white squares), and heterogeneous feldspar (white circles) grains (n=51). Grains are considered heterogeneous if their three WDS spot measurement values differ by more than 2%. The x-axes in plots 'b', 'c', 'd' and 'f' are plotted on a logarithmic scale for clarity, and points with 0% element concentrations are plotted as 0.0001 % in these plots to avoid their omission.

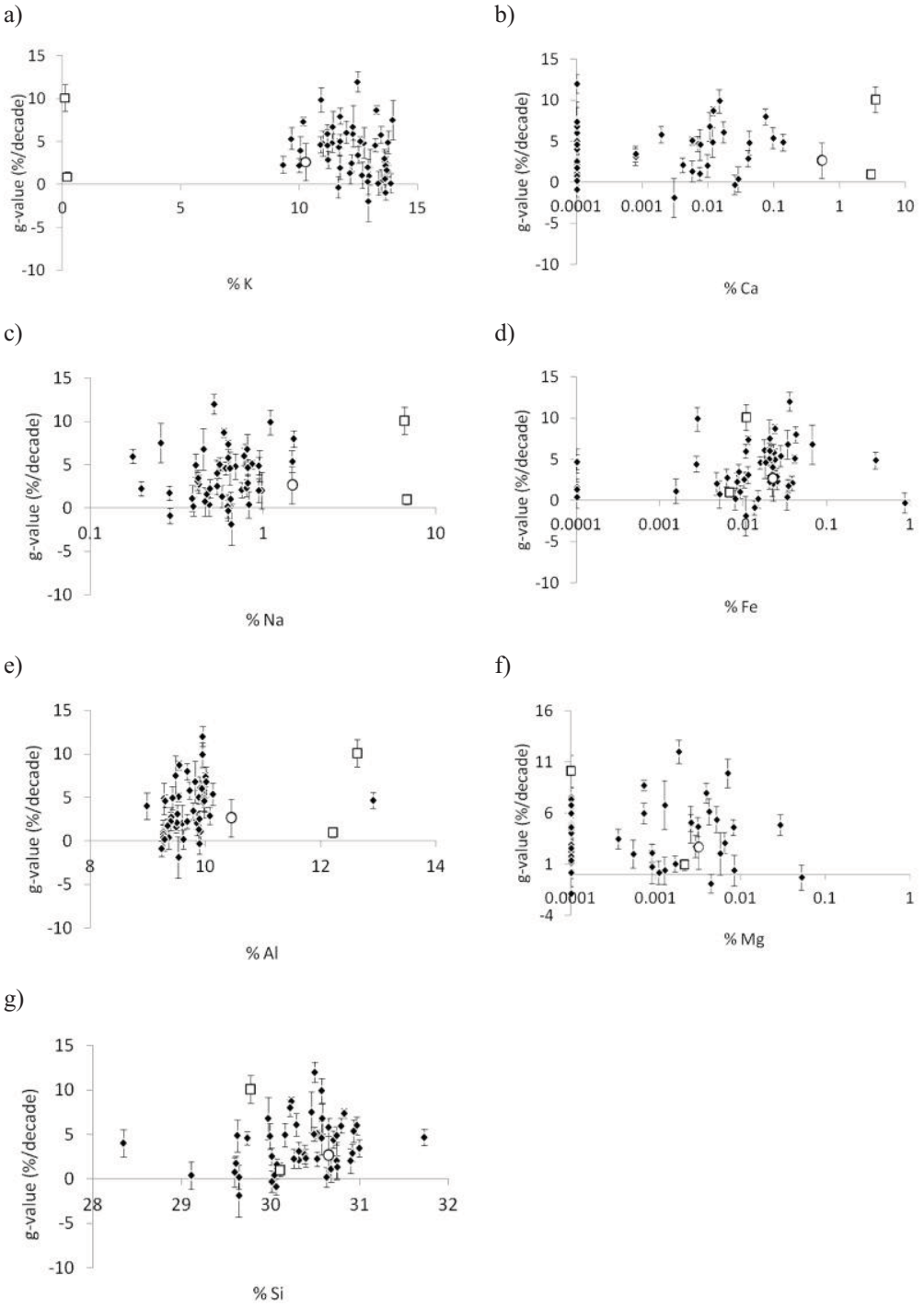

Figure 4-13. *g*-value versus major element concentration for all homogeneous K-rich feldspar (black diamonds), plagioclase (white squares), and heterogeneous feldspar (white circles) grains (n=51). Grains are considered heterogeneous if their three WDS spot measurement values differ by more than 2%. The x-axes in plots 'b', 'c', 'd' and 'f' are plotted on a logarithmic scale for clarity, and points with 0% element concentrations are plotted as 0.0001 % in these plots to avoid their omission.

4.8 Limitations of WDS and EDS measurements

In the previous sections, EDS analyses showed that plagioclase grains tend to be dimmer than KF grains, but subsequent WDS analyses showed no correlations between feldspar grain elemental composition and IRSL intensity, decay curve shape, D_e, fading rate or fading-corrected age. This may be due, in part, to the limitations of the approach in estimating grain elemental composition in this chapter. TL, OSL and IRSL emission spectra of minerals will be biased towards those wavelengths where a sample (a grain) emits efficiently. Unlike quartz, feldspar grains tend to be opaque, and a substantial part of their luminescence signal may be absorbed inside the grain (Wintle & Duller 1991; Duller 1997). Thus, the IRSL signal measured by the photomultiplier tube may be only that emitted by the near-surface portion of the grain. Because the elemental composition of each grain may not be homogeneous (e.g., Baril 2004), we cannot assume that the elemental composition of the luminescence-emitting surface of the grain is necessarily the same as 1) that measured from surface of the grain that has since been polished flat for WDS analyses; or 2) the volume of sample measured in spot mode (beam diameter 67 μm) during EDS analyses. If significant differences exist, then any measured correlations between grain luminescence properties and measured element concentrations will be erroneous.

4.9 Summary and implications for single-grain dating

This chapter explored the relationships between the luminescence properties and elemental composition of individual grains from K-rich feldspar and quartz separates, as part of the investigations into the single-grain dating potential of KF grains in the Middle Son Valley. Elemental analyses of grains from samples GHO-2 and KHUT-1 showed that density separation procedures appear to be effective in minimizing the number of contaminating feldspar minerals in quartz separates and the number of contaminating quartz, plagioclase and other minerals in K-rich feldspar separates. Only 24% of all WDS-measured grains from the K-rich feldspar separate from sample GHO-2 consist either of some mineral other than K-rich feldspar or show heterogeneity in their elemental composition (Table 4-5).

Clear differences exist between feldspar and quartz grains with respect to their luminescence intensity and decay curve shapes when stimulated with the IR laser. This implies that luminescence decay curves can be used to reject quartz grains from further analyses in single-grain feldspar dating studies. No clear differences were found between the IRSL decay curve shapes for bright plagioclase grains and K-feldspar grains, so plagioclase grains cannot be rejected in a similar manner.

Elemental composition of feldspar grains appears to have no significant influence on D_e, fading rate, or fading-corrected age for the samples measured in this study, despite the

fact that past research has shown that the thermal stability and fading rate of feldspar IRSL signals can depend on feldspar type (Huntley & Lian 2006; Li *et al.* 2010). This may be due, in part, to differences between the elemental composition of the luminescence-emitting surface of each grain and the polished grain-surface measured with WDS. Also, some correlations may have been detected if more plagioclase grains had been measured. Nonetheless, these results suggest that if density separation procedures are effective at minimizing the number of contaminating plagioclase and other mineral grains in K-rich feldspar separates, then grain-to-grain variations in elemental composition should contribute little scatter to KF single-grain D_e and fading-corrected age distributions.

The source of scatter in a single-grain D_e and fading-corrected age distribution is investigated more fully in Chapter 6, but before this, Chapter 5 reports on preliminary luminescence measurements on KF grains from sample KHUT-1 using the IR laser. These include an assessment of the effects of IR laser power and stimulation duration on KF grain IRSL signals, as well as an attempt to determine whether or not grains are heated by the IR laser during IR stimulation. A series of dose-recovery experiments on single KF grains are then conducted to determine their suitability to SAR measurement procedures.

Chapter 5.0 – Preliminary single-grain IRSL measurements

5.1 Introduction

The power density of the IR laser beam is approximately 500 W/cm^2 (Duller *et al.* 2003). The IR laser is by far the most powerful light source that has been incorporated into OSL/TL systems, with an energy per unit time per unit area that is three orders-of-magnitude greater than that of the IR diode array (Bøtter-Jensen *et al.* 2000; Bøtter-Jensen *et al.* 2003) (Table 2-3). In this chapter, the potential effect of IR laser power and stimulation duration on KF grain IRSL signals is investigated, and a series of experiments that attempt to find evidence for grain heating by IR laser stimulation are described. This is followed by a series of dose-recovery experiments on single KF grains to determine their suitability to SAR measurement procedures. All measurements in this chapter were made on KF grains from sample KHUT-1.

5.2 Assessing laser power, stimulation duration, and the proportion of grains that contribute to the total IRSL signal

The IRSL signal of a previously used and subsequently laboratory-bleached KF grain was observed after IR stimulation using a range of laser powers. The grain was given a dose of 70 Gy and preheated to 260 °C for 10 s before each IR laser stimulation. Each stimulation was followed by the measurement of a test dose (~11 Gy), and a hot optical wash using IR diodes (270 °C, 100 s). The power of the IR laser appears to have little effect on the IRSL signal intensity of the KF grain (Fig. 5-1a, b). Figure 5-1c shows the length of IR (laser) stimulation time it takes for the luminescence signal of 65 KF grains to be reduced to less than 10% of the initial intensity. These grains had been previously bleached and given a 70 Gy beta dose in the laboratory. Eighty-six percent of grains are reduced to less than 10% of their initial signal intensity after 6 s of IR laser stimulation at 90% power. Six percent of grains required more than 30 s of IR laser stimulation to reduce their signals to less than 10 % of their initial intensity. At least 60% of KF grains contribute to over 80% of the total IRSL signal (Fig. 5-1d), and this is consistent with the data reported by Li *et al.* (2011: Fig. 5).

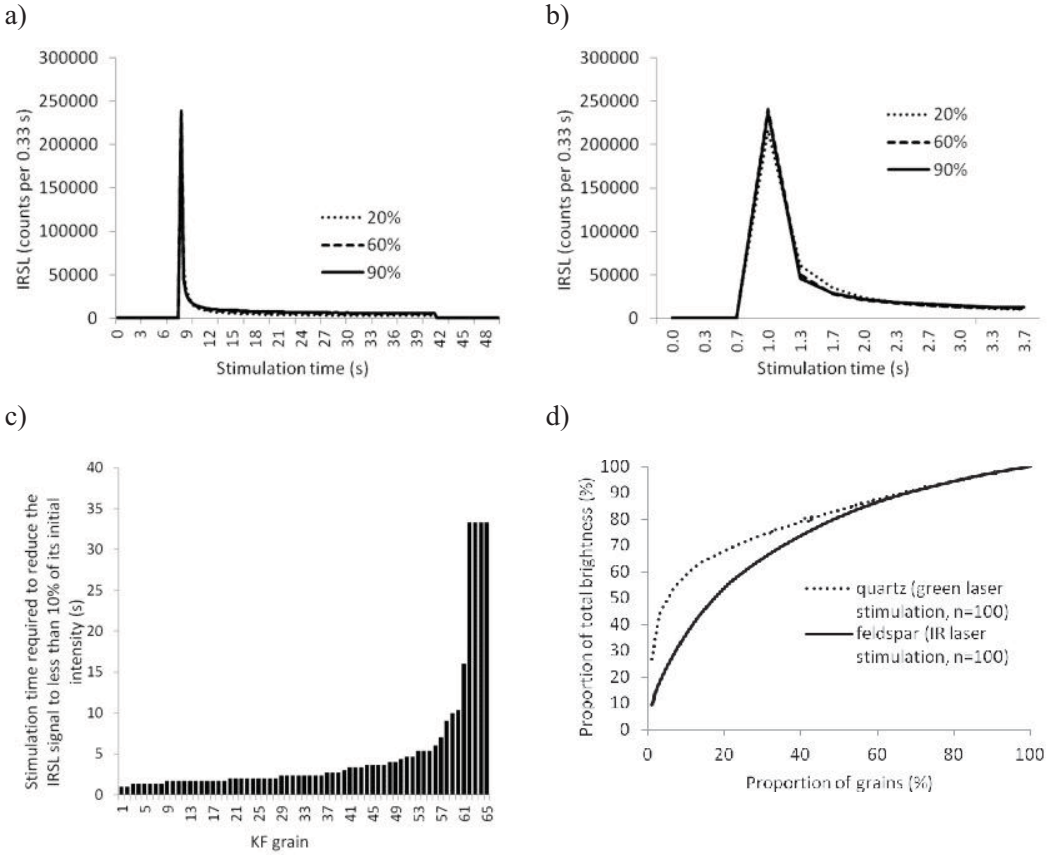

Figure 5-1. a) The IRSL signal of a laboratory-bleached and dosed (70 Gy) KF grain after IR stimulation using a range of laser powers. b) A close-up of the decay curve in 'a' in the stimulation time range of 0 to 3.7 s. c) The amount of IR (laser) stimulation time (90% power) it takes for the luminescence signal of 65 KF grains to be reduced to less than 10% of the initial value. Eighty-six percent of grains are reduced to less than 10% of their initial signal after 6 s of IR laser stimulation. c) The distribution of signal intensities from single quartz grains and KF grains from the same sample. The OSL signal was measured from the quartz grains, and the IRSL signal was measured from the feldspar grains. The quartz grain data was supplied by Jacqui Fenwick (unpublished data). All measurements were made on sample KHUT-1.

5.3 Testing for grain heating by the IR laser

There are concerns that the IR laser may heat up grains during IRSL stimulation (Duller *et al.* 2003). Tests for grain heating by both the IR diodes (at 90% power) and the IR laser (at 90% power) were conducted using a single KF grain. Following the approach of Jacobs (2004), TL curves of a KF grain were observed after IR stimulation. To test for grain heating, a KF grain (that was laboratory bleached and heated in a previous SAR cycle) was given a laboratory dose (140 Gy), and a TL curve (TL curve #1 in Table 5-1) was measured up to 390°C at 5°C/s after IRSL stimulation durations of 2, 10, and 40 s. Immediately after the measurement of these TL curves, the grain was given another 140 Gy laboratory dose, and another TL curve was measured (TL curve #2, Table 5-1). The area underneath the TL curves measured after IRSL

stimulation (TL curve #1) was divided by the area underneath the TL curves measured immediately after (TL curve #2) in order to provide a correction for sensitivity change (steps 4 and 5, Table 5-1). For all IRSL stimulation durations, this process was repeated in an identical manner, except with the IR stimulation source switched off (steps 13, Table 5-1). This generated a series of TL curves (TL curve #3) that allowed monitoring of the degradation of the TL signal as a result of holding the grain at 50°C during IR stimulation.

Table 5-1. The measurement protocol followed to test for grain heating. This sequence (performed on a laboratory-bleached grain) was followed for both stimulation sources: the IR diodes (90% power), and the IR laser (90% power).

	Action	Purpose
1.	Laboratory dose (140 Gy)	
2.	IRSL stimulation at 50°C for 2 s	
3.	Measure TL curve[1] #1	TL after IRSL stimulation for 2 s
4.	Laboratory dose (140 Gy)	
5.	Measure TL curve[1] #2	Sensitivity correction for TL curve #1
6.	Laboratory dose (140 Gy)	
7.	IRSL stimulation at 50°C for 2 s	
8.	Measure TL curve[1] #3	Monitoring TL curve degradation due to heating to 50°C during IRSL stimulation
9.	Laboratory dose (140 Gy)	
10.	Measure TL curve[1] #4	Sensitivity correction for TL curve #3
11.	Repeat steps 1-10 for IRSL stimulation durations of 10 s and 40 s	
12.	Repeat steps 1-11 on a blank disc[2]	
13.	Repeat steps 1-13 with the IR stimulation source switched off [3]	

[1]TL curves were measured on a K-feldspar grain mounted on a stainless steel disc for the IR diode heating experiment. TL curves were measured on the same grain on an aluminium single grain disc for the IR laser heating experiment. All TL curves were measured up to 380°C using a heating rate of 5°C/s.

[2]For the IR diodes experiment, a blank stainless steel disc with silicone oil was used. For the IR laser experiment, a blank aluminium single grain disc was used.

[3]The IR stimulation source is switched off during steps 2 and 7, but the disc is still heated to 50°C for the same duration as when the IR stimulation source was switched on.

The sequence in Table 5-1 was followed twice to test for grain heating by both the IR laser and the IR diodes. For the IR diodes, the grain was mounted on a stainless-steel disc with silicone oil, and, for the IR laser, the grain was inserted into a hole near the centre of an aluminium single-grain disc. Steps 1-11 of the procedure were repeated on a blank disc (a

stainless-steel disc with silicone oil for the IR diode test, and a single-grain aluminium disc for the IR laser test) to generate TL curves that were subtracted from those measured from the K-feldspar grain to clear the background signal.

The TL curves measured after the laboratory dose in Figure 5-2a show a large peak at ~150°C, and a much smaller peak at ~330°C. These are consistent with TL signals measured from laboratory-irradiated K-rich feldspar aliquots that have received no preheat (Duller 1997; Murray *et al.* 2009). Both the high temperature and low temperature TL peaks are bleachable by IR stimulation (Duller 1997; Murray *et al.* 2009). Recent work by Murray *et al.* (2009) has shown that IR diode stimulation will cause a vertical drop in TL peaks, but lateral shifts of the peaks were not observed for successive stimulation periods of 10, 100 and 1000 s. This is interpreted here as evidence that the diodes did not heat the sample beyond the stimulation temperature (the stimulation temperature was not reported by Murray *et al.* (2009), but presumably, it was room temperature). The left limb of a TL peak, and the peak itself, shifts to the right after the TL signal has been eroded due to heating as shown in Figure 5-2a and b. Heating experiments in this section show that while there may be some thermal erosion of the 150°C TL peak due to the 50°C stimulation temperature (Fig. 5-2b and d), the diodes do not erode the peak any further (Fig. 5-2c). If the grain is heated by the diodes, it is likely not heated much beyond ~50°C; the temperature at which the left limb of the 150°C TL peak starts to rise (Fig. 5-2c). However, this inference assumes that there has been negligible phototransfer of charge from high temperature traps to low temperature traps during IR stimulation.

Figure 5-3 shows the results of the same heating experiment conducted with the IR laser at 90% power. The IR laser is capable of depleting the 150°C TL peak at a faster rate (Fig. 5-3a). However, the left limb of the 150°C TL peak does not migrate to the right with the laser switched on much more than it does when the laser is turned off (Fig. 5-3c, d). This suggests that, even for stimulation durations of up to 40 s, the IR laser does not heat the grain much beyond the stimulation temperature of ~50°C. For all subsequent luminescence measurements on single KF grains in this thesis, a 30% IR laser power is used.

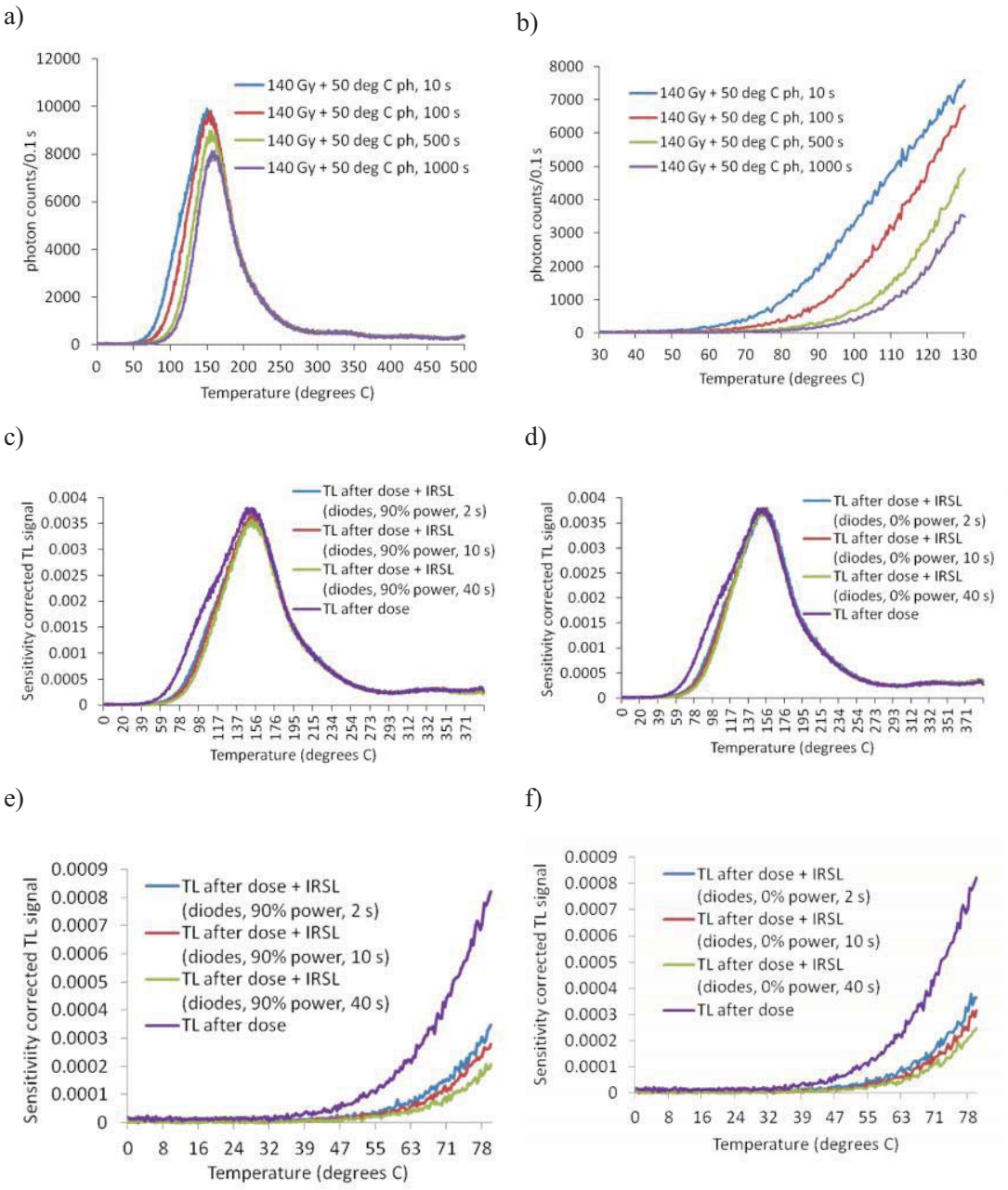
a)
b)
c)
d)
e)
f)
photon counts/0.1 s
Temperature (degrees C)
140 Gy + 50 deg C ph, 10 s
140 Gy + 50 deg C ph, 100 s
140 Gy + 50 deg C ph, 500 s
140 Gy + 50 deg C ph, 1000 s
Sensitivity corrected TL signal
TL after dose + IRSL (diodes, 90% power, 2 s)
TL after dose + IRSL (diodes, 90% power, 10 s)
TL after dose + IRSL (diodes, 90% power, 40 s)
TL after dose
TL after dose + IRSL (diodes, 0% power, 2 s)
TL after dose + IRSL (diodes, 0% power, 10 s)
TL after dose + IRSL (diodes, 0% power, 40 s)

Figure 5-2. a) Degradation of the ~150° C TL peak of a single KF grain as the result of holding it at 50° C for durations of 10, 100, 500 and 1000 s. b) A close-up view of the left limbs of the TL curves shown in 'a'. Note the lateral shift of the left limb of the peak (b). c) TL curves after a laboratory dose and IRSL (diode) stimulation for different durations (2 s, 10 s and 40 s). d) TL curves after a laboratory dose and stimulation at 0% power to monitor for TL signal degradation due to heating at 50°C. e) and f) are the same graphs as in c) and d), respectively, but with focus on the glow curve region up to 80°C. The background signal from a blank disc has been subtracted from all TL curves, and all TL curves have been corrected for sensitivity change (see Table 5-1).

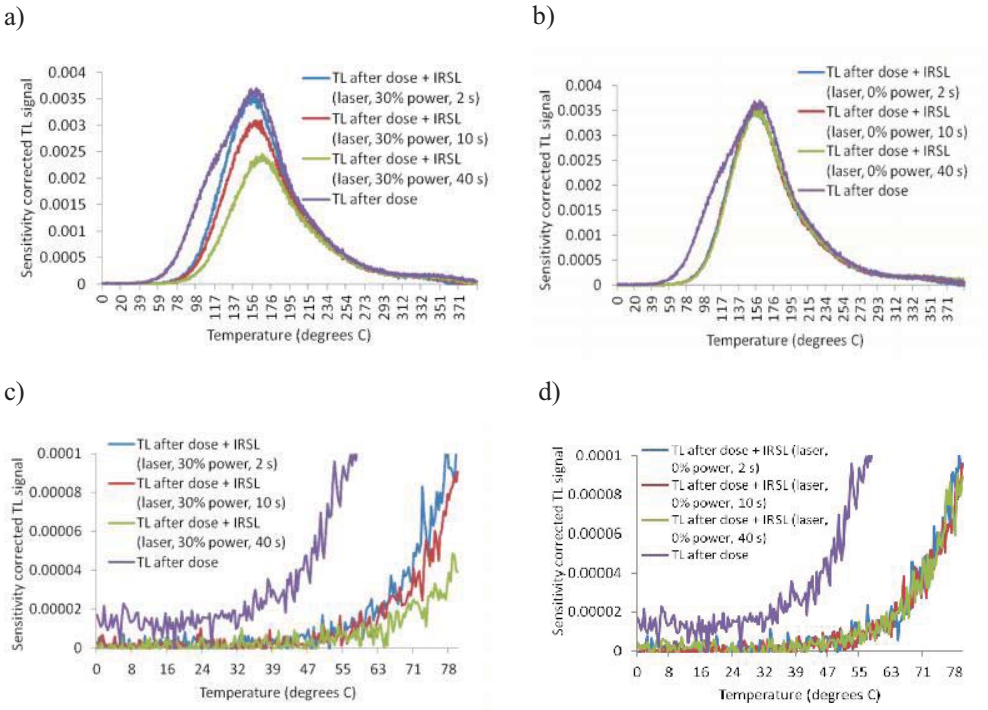
a)
b)
c)
d)
Sensitivity corrected TL signal
Temperature (degrees C)
TL after dose + IRSL (laser, 30% power, 2 s)
TL after dose + IRSL (laser, 30% power, 10 s)
TL after dose + IRSL (laser, 30% power, 40 s)
TL after dose
TL after dose + IRSL (laser, 0% power, 2 s)
TL after dose + IRSL (laser, 0% power, 10 s)
TL after dose + IRSL (laser, 0% power, 40 s)

Figure 5-3. a) TL curves after a laboratory dose and IR (laser) stimulation for different durations (2 s, 10 s and 40 s). b) TL curves after a laboratory dose and stimulation at 0% power to monitor for TL signal degradation due to heating at 50°C. c) and d) are the same graphs as in a) and b), respectively, but with focus on the glow curve region up to 80°C. The background signal from a blank disc has been subtracted from all TL curves, and all TL curves have been corrected for sensitivity change (see Table 5-1).

5.4 Dose recovery tests

In this section, a series of dose recovery tests were performed on single KF grains from sample KHUT-1 using a series of SAR measurement protocols and data analysis methods. The goal of these experiments was to identify a SAR protocol that successfully recovers a known (given) laboratory beta dose, and minimizes the total number of grains that must be rejected due to dim signals, poor sensitivity correction and high recuperation. Dose recovery tests were conducted on grains that were bleached and heated in the laboratory (IR diode bleach for 1000 s at 290°C, Section 5.4.1), and on grains that were bleached in the sun for 2 days (Section 5.4.2). Dose recovery tests using laboratory-bleached and heated grains were conducted using a 125°C stimulation temperature, and those using sun-bleached grains were conducted using a 50°C stimulation temperature to see if stimulation temperature had a dramatic effect on results. In both cases, dose recovery tests were conducted following the SAR protocol in Table 5-2 using a range of preheat temperatures. A zero dose point was applied to monitor for recuperation, and two repeat dose points were included to monitor that any sensitivity changes had been adequately corrected for. One duplicate dose point was placed in the low-dose region of the dose response curve (RR1), and one in the high-dose

region of the dose response curve (RR2) (e.g., Jacobs *et al.* 2006c) (Table 5-2). The signal in the first 0.134 s of stimulation minus the average count rate from the last 1.742 s of stimulation was used in all calculations (Fig. 5-4). One single-grain disc containing ~90-100 grains was measured for each preheat condition.

Table 5-2. The SAR measurement protocol for single KF grains.[1]

1	Laboratory dose (70 Gy)	
2	Preheat[2]	
3	IRSL (7 s)	→ L_n/L_x
5	Test dose (~11 Gy)	
6	Preheat	
7	IRSL (7 s)	→ T_n/T_x
8	IR (diode) bleach (290 °C, 40 s)	
9	Return to step 1.	

[1]Regenerative doses of 28, 56, 84, 111, 139, 209, 0, 28, and 139 Gy were measured.
[2]Preheats of 120, 160, 200, 240, and 280 °C were applied for 10 s. Preheats applied before the regenerative and test dose measurements are identical.

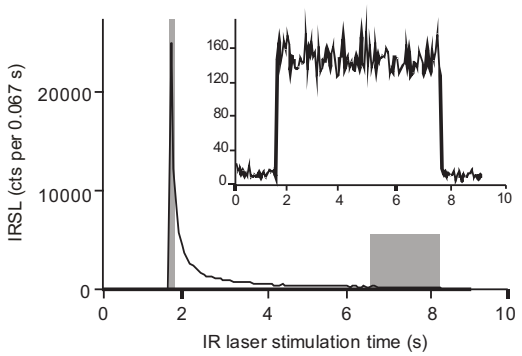

Figure 5-4. Typical IRSL decay curve from a KF grain. The signal in the first 0.134 s of stimulation minus the average count rate from the last 1.742 s of stimulation (shaded areas) was used in all calculations. The inset graph shows a typical IRSL decay curve from a quartz grain.

Approximately 30–50% of the grains on each disc had plateau-like decay curves (Fig. 5-4). The elemental analyses conducted in Chapter 4 suggest that these are probably quartz grains. These grains have been excluded from analyses. The remaining feldspar grains were rejected only if: 1) the sensitivity-corrected recuperated signal was greater than 5% of the sensitivity-corrected natural signal (Murray & Wintle 2000); 2) the test dose (T_n) signal (as measured in the first 0.134 s of stimulation) was less than 3 times the average count rate in the last 1.742 s; and 3) one or both of the recycling ratio values fall outside of 2 standard deviations of unity (Jacobs *et al.* 2006a). The weighted mean measured dose/given

dose ratios are calculated using the Central Age Model (CAM) of Galbraith *et al.* (1999), and the OD values for these ratios are also reported in Figures 5-5 and 5-7.

5.4.1 Laboratory-bleached and heated grains

The dose recovery tests for the laboratory-bleached and grains were conducted both with and without a 40 s IR hotwash (290°C) at the end of each SAR cycle (step 8 in Table 5-2) to investigate if recuperation would be reduced. The stimulation temperature was 125°C. The weighted mean measured dose/given dose ratios for these experiments are shown in Figure 5-5. The grain rejection statistics for the same dataset are shown graphically in Figure 5-6. Measured dose/given dose ratios are all within 5% of unity for all measurement conditions, except for the 120 °C preheat with no hotwash condition, where the D_e is underestimated by ~8% (Fig. 5-5a). Without the hotwash, recuperation values for accepted grains are between 3 and 4%, and do not increase significantly with preheat temperature. When the hotwash is applied, there is a 38–163% increase in the number of accepted grains, as fewer grains are rejected due to high recuperation, and the recuperation of accepted grains decreases to between 1 and 2.5% (Figs 5-5, 5-6).

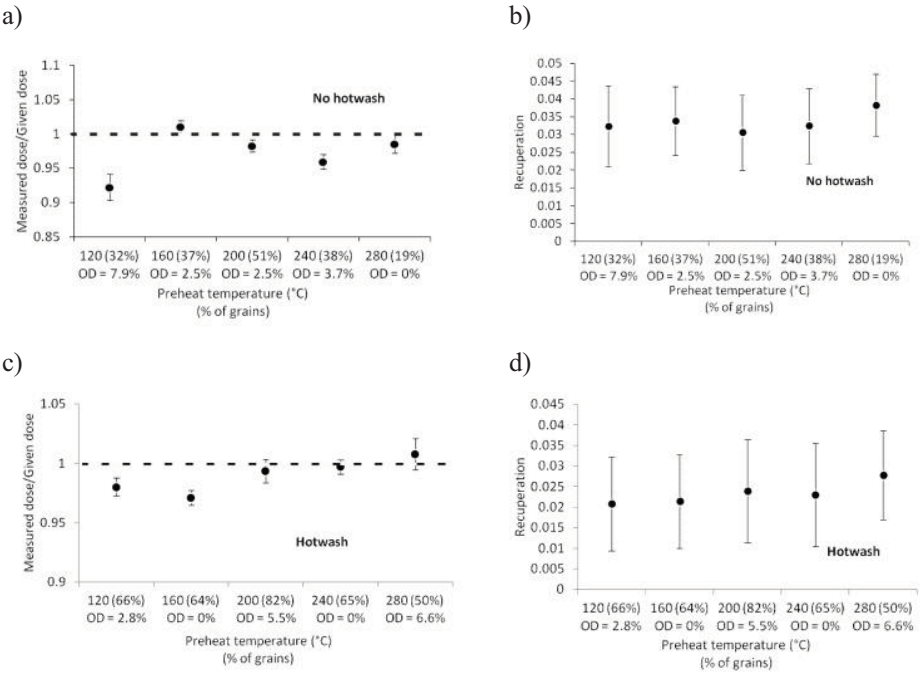

Figure 5-5. Dose recovery test results using laboratory-bleached and heated (IR diode bleach for 1000 s, at 290 °C) grains. The given laboratory dose of 70 Gy was measured using preheats of 120, 160, 200, 240, and 280 °C for 10 s. Weighted mean (CAM) measured dose/given dose ratios and average recuperation values are shown for tests without a hotwash in 'a' and 'b', and with a hotwash listed in 'c' and 'd'. Error bars represent 1σ. The percentage of grains that passed all rejection criteria are in brackets on the x-axis. OD refers to the overdispersion calculated using the CAM.

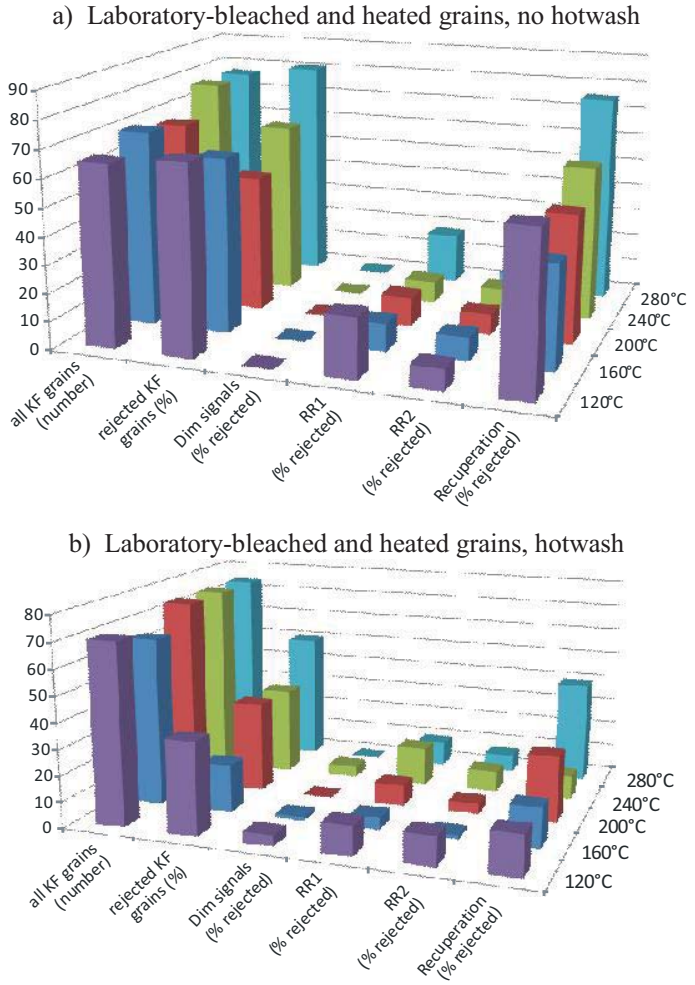

Figure 5-6. Grain rejection statistics for dose recovery tests shown in Figure 5-5. Dose recovery tests in 'a' do not include a hotwash, and those in 'b' include a hotwash. All preheat durations are 10 s. "RR1" and "RR2" refer to the recycling ratios calculated from the repeat dose points measured at the low-dose region of the dose-response curve and at the high-dose region of the dose response curve, respectively.

5.4.2 Sun-bleached grains

Because, in nature, sand grains in the Son River would have been bleached by sunlight, dose recovery tests similar to those above were repeated on KF grains that were bleached in unfiltered sunlight for two days. It must be noted that this bleaching method likely does not serve as a perfect analogue for the natural bleaching conditions in the Son River. Waterlain sediments are commonly incompletely bleached (Olley *et al.* 1999) and may be partially shielded from the UV component of sunlight before burial (Huntley & Clague 1996). In these tests, the stimulation temperature was reduced to 50 °C, which is consistent with IRSL measurement protocols commonly reported in the literature (e.g., Auclair *et al.* 2003; Buylaert *et al.* 2009; Davids *et al.* 2010), and the hotwash was included

in order to minimize the number of grains rejected due to recuperation values >5%. A laboratory dose of 124 Gy was administered, as measurements on natural grains suggested that this lay within the range of D_e values.

For all preheat conditions applied, measured dose/given dose ratios are generally within 6% of unity, and the recuperation values lie between 1.0 and 2.5% (Fig. 5-7). Thirty-nine percent to 63% of KF grains passed all rejection criteria, and the percentage of accepted grains generally decreased with increasing preheat temperature (Figs 5-7, 5-8). More grains were rejected due to poor sensitivity correction in the high-dose region of the dose response curve than in the low-dose region (Fig. 5-8). This was not observed in dose recovery tests using laboratory-bleached and heated grains (Section 5.3.1). OD values are slightly higher than those reported for the laboratory-bleached and heated grains (Section 5.3.1), but still remain below 12% (Fig. 5-7).

5.4.3 L_n and L_x residual signals

When a dose response curves were constructed for single KF grains, T_x/T_n graphs showed evidence that a residual signal from the L_n and L_x measurements was contributing to the T_n and T_x signals. Figure 5-9 shows that the relative magnitude of T_x/T_n is dependent on SAR cycle, which is, in turn dependent on the preceding regenerative dose (Fig. 5-9a). These residual L_n and L_x signals probably occur because it is difficult to deplete the IRSL source traps in the laboratory (Section 5.2), and this effect will theoretically lead to underestimations in L_x/T_x ratios and an accentuated bend in the growth curve (Fig. 5-9b). Thus, the data from these dose recovery tests were re-analyzed using the "Previous BG subtraction" option in Analyst, following Murray and Wintle (2000). In this method of analysis, the same background counts used to derive the corresponding net natural and regenerative signals are used to derive the net test dose signals. The resulting measured dose/given dose ratios, average recuperation values, and grain rejection statistics are included in Figures 5-7 (plots 'c' and 'd') and 5-8 (plot 'b'). There is little change in the measured dose/give dose ratios and recuperation values after the "Previous BG subtraction" method is applied, but the total number of accepted grains decreases by ~10-40%.

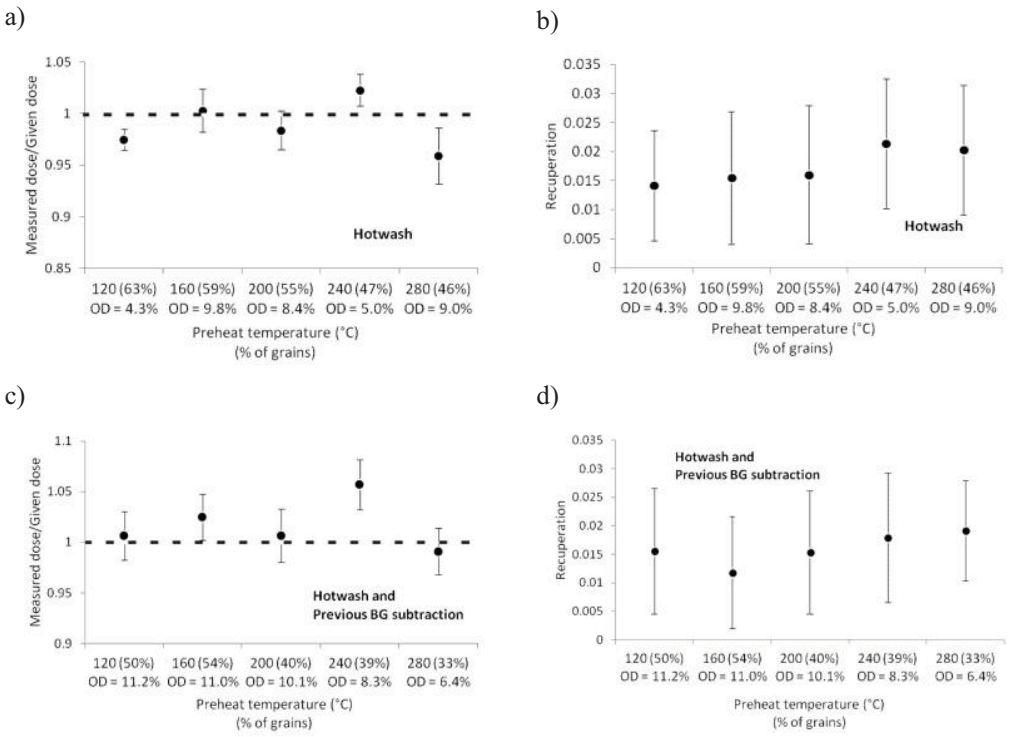

Figure 5-7. Dose recovery tests on sun-bleached (2 days) KF grains. A given laboratory dose of 124 Gy was measured using preheats of 120, 160, 200, 240, and 280 °C for 10 s. Weighted mean (CAM) measured/given dose ratios and average recuperation values are shown for tests analyzed without a previous background (BG) subtraction (a and b), and with a previous BG subtraction (c and d). Error bars represent 1σ. The percentage of grains that passed all rejection criteria are listed in brackets on the x-axis. OD refers to the overdispersion calculated using the CAM.

a) Sun-bleached grains, hotwash

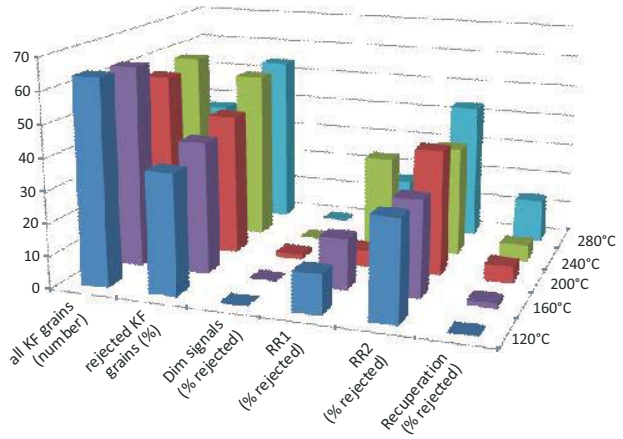

b) Sun-bleached grains, hotwash and previous BG subtraction

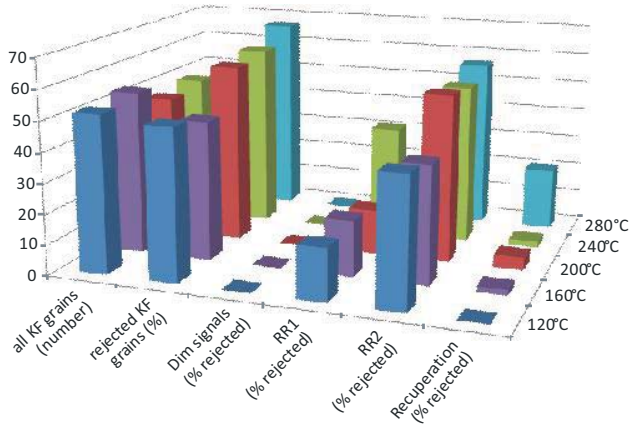

Figure 5-8. Grain rejection statistics for dose recovery tests shown in Figure 3-6 analyzed without (a), and with (b) the "Previous BG subtraction" data analysis method. "RR1" and "RR2" refer to the recycling ratios calculated from the repeat dose points measured at the low-dose region of the dose-response curve and at the high-dose region of the dose response curve, respectively.

a)

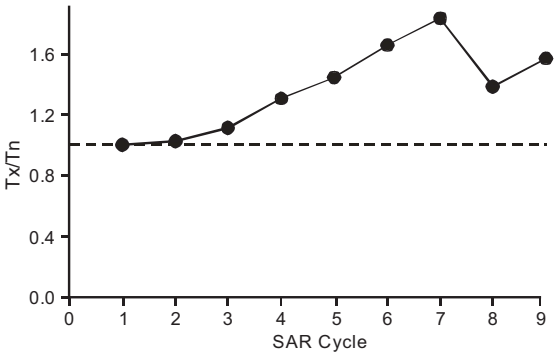

SAR cycle	Regenerative dose (Gy)
1	Natural dose
2	28
3	56
4	84
5	111
6	139
7	209
8	0
9	28

b)

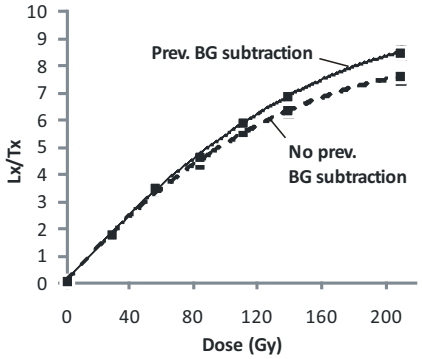

Figure 5-9. a) T_x/T_n graph showing the dependence of T_x on regenerative dose and SAR cycle number. If the background count rate from each natural/regenerative dose signal is subtracted from the following test dose signal (called a "previous BG subtraction"), the non-linear curvature in the dose response curve (b) is reduced.

.

5.5 Summary

This section reported on a series of IRSL measurements made on single KF grains from sample KHUT-1. These included a series of dose recovery tests on sun-bleached and laboratory-bleached and heated grains to determine the suitability of KF grains from the Middle Son Valley to SAR, as well as assessments of the effects of IR laser power and stimulation duration on KF grain IRSL signals. An attempt to assess the potential of grain heating by the IR laser was also described. TL curves measured from a single KF grain after IR laser stimulation suggest that, even for stimulation durations of up to 40 s, the IR laser (at 90% power) does not heat grains much beyond the stimulation temperature of 50°C. The dose recovery tests in this chapter showed that laboratory doses can be recovered to within 10% of the given dose from single KF grains using preheats ranging from 120 °C to 280 °C, and stimulation temperatures of 50 °C or 125 °C. The number of grains that passed all rejection criteria were maximized by using a hotwash and lower preheats with no previous BG subtraction (i.e., 120 °C or 160 °C), but a significant number of grains (i.e., >30%) are still accepted when using higher (>200°C) preheats and a previous BG subtraction (Fig. 5-7c). Measured OD values were consistently low (less than 12%).

There is evidence that L_x signals are not always completely bleached, even after more than 30 s of IR laser stimulation at 90% power, and this may be due to re-trapping and re-release of electrons during stimulation. T_x/T_n graphs show that some of the L_x residual signal contributes to the following T_x signals. This process may lead to L_x/T_x underestimates, especially at high doses, and cause an increase in the curvature of the dose response curve. This increase in curvature can be reduced by applying the "Previous BG subtraction" technique during analysis.

Chapter 6 – Sources of overdispersion in a K-rich feldspar sample from north-central India: insights from D_e, K content and IRSL age distributions for individual grains

This chapter explores sources of OD in a K-rich feldspar sample using measurements of D_e, fading-corrected single-grain age distributions, and measurements of K content from individual grains. This is a manuscript that has been accepted for publication in *Radiation Measurements*.

The focus of this paper is on measurements and analyses conducted on KF grains from sample GHO-2. Quartz grain data from the same sample were used to compare the shape of the single-grain D_e distributions. Measurements from multi-grain KF aliquots from sample GHO-3 and single KF grains from sample KHUT-10 were used in the discussion on fading rates and signal resetting in the Son River. I was responsible for sample preparation of KF grains, all luminescence measurements and analyses of KF grain data, wavelength-dispersive spectrometry (WDS) measurements of KF grains, and the writing of the manuscript. My supervisors (R.G. Roberts and Z. Jacobs) have contributed the measured and analyzed quartz single-grain data, and valuable input on my data analysis, presentation, and interpretations. Sébastien Huot (Université de Montréal, Canada) has provided advice and Excel macros for fading correction, and Kevin Grant and Norman Pearson (Macquarie University, Sydney) have provided advice and assistance with WDS measurements at Macquarie University, Sydney.

In this chapter the D_e values and fading-corrected ages are calculated for individual KF grains from a sample collected from below the YTT ash at the Ghoghara main section as part of the larger research aim of assessing the time of final deposition of YTT ash in the Middle Son Valley (sample GHO-2). Although no evidence for grain heating by the IR laser was found in Chapter 5 (Section 5.2), measurements on single grains were made using an IR laser power of 30% to reduce the chance of grain heating, as it was found that KF grain signal intensities are not adversely affected by this stimulation power (Section 5.2). Also, grains exhibiting plateau-like IRSL decay curves were rejected from further analyses, as elemental analyses (Chapter 4) suggested that they are probably quartz grains. A 250°C preheat was used in measurements of both the D_e and fading rate following Auclair *et al.* (2003) and Feathers and Tunnicliffe (2011). Dose recovery tests in this chapter showed that laboratory-given doses should be recoverable and at least 30% of grains should pass rejection criteria using this preheat temperature.

Sources of overdispersion in a K-rich feldspar sample from north-central India: insights from D_e, K content and IRSL age distributions for individual grains

C.M. Neudorf*, R.G. Roberts, Z. Jacobs

Centre for Archaeological Science, School of Earth and Environmental Sciences, University of Wollongong, NSW, 2522, Australia

**Corresponding author: Tel.: +61 02 4221 4686, E-mail: cmn821@uowmail.edu.au*

ABSTRACT

Luminescence dating of individual sand-sized grains of quartz is a well-established technique in Quaternary geochronology, but the most ubiquitous mineral on the surface of the Earth—feldspar—has received much less attention at the single-grain level. In this study, we estimated single-grain equivalent dose values and infrared stimulated luminescence (IRSL) ages for K-rich feldspar (KF) grains from a fluvial sample underlying Youngest Toba Tuff (YTT) deposits in north-central India, and compared these ages (corrected for anomalous fading) with those obtained from individual grains of quartz from the same sample. Both minerals have broadly similar single-grain age distributions, but both are greatly overdispersed and most grains have ages substantially younger than the expected age of the YTT deposit (~74 ka). Almost half (45%) of KF grains used for age calculation have fading rates statistically consistent with zero, but the age distribution of these grains is as dispersed as that of the entire population. We obtained a similar distribution of ages calculated for 51 grains using their individually measured internal K contents, which exhibited only minor grain-to-grain variation. Given the lack of dependency of single-grain ages on the measured fading rates and internal K contents, and the overall adequacy of bleaching of grains collected from a sand bar in the modern river channel, we consider the spread in ages is most likely due to mixing, at the time of deposition and after the YTT event, of potentially well bleached fluvially-transported sediments with older grains derived from slumping of riverbank deposits. Some spread may also be due to natural variations in the IRSL properties of individual KF grains.

Keywords: potassium feldspar; IRSL dating; single grains; age overdispersion; anomalous fading; Youngest Toba Tuff

6.1 Introduction

Luminescence dating procedures that make use of multi-grain aliquots of quartz or feldspar, and in which more than one grain contributes significantly to the luminescence signal, implicitly assume that all contributing grains have suitable luminescence properties for dating and have been sufficiently bleached by sunlight before burial, and have not been mixed after burial. Single-grain optically stimulated luminescence (OSL) dating techniques have been available for quartz for more than a decade, enabling the identification of partially bleached grains or intrusive grains from overlying or underlying sedimentary units, as well as the rejection of grains with unsuitable characteristics for reliable dose determination using single-aliquot regenerative-dose (SAR) procedures (Galbraith et al., 1999; Jacobs and Roberts, 2007). Similar single-grain dating techniques are rarely used for potassium (K)-rich feldspars but would also entail measurements of the internal dose rates (due principally to ^{40}K) and anomalous (athermal) fading rates of individual grains (Duller et al., 2003). Risø readers equipped with a 150 mW infrared (IR) (830 nm) laser allow for the direct stimulation of individual feldspar grains (Duller et al., 2003). In this paper, we describe the use of the IR laser to obtain single-grain equivalent dose (D_e) values and fading-corrected ages for K-rich feldspar (KF) grains from a fluvial sample collected from a sand unit underlying Youngest Toba Tuff (YTT) deposits in the Middle Son Valley, Madhya Pradesh, India. This study is part of a larger luminescence dating program to assess the time of deposition of the alluvial deposits and YTT ash in the Middle Son Valley. Experiments were conducted on two additional samples (one from the same geological section, and one from a modern sand bar in the Son River channel) to assess potential sources of overdispersion (OD) in the KF grain age distribution. The impact of single-grain fading rates and K contents on the KF single-grain age distribution is also examined.

6.2 Samples

IR stimulated luminescence (IRSL) measurements were made on three samples (GHO-2, GHO-3, and KHUT-10). Sample GHO-2 was collected from a well-drained, medium-coarse fluvial sand unit that underlies YTT deposits in a cliff section on the north bank of the Son River (24° 30’ 7.608” N, 82° 1’ 2.748” E) (Jones, 2010). The YTT deposit at this location is thought to have been deposited ~74 ka ago (Jones, 2010, Gatti, et al. 2011, Smith, et al. 2011) but the ash here has not been dated directly. Sample GHO-3 was collected from a fine-medium sand unit immediately above the YTT deposit, and ~2 m above sample GHO-2. No carbonate concretions or organic matter was observed in the two sand units in the field. KHUT-10 was collected from a modern-day sand bar in the Son River channel, ~25 km upstream of the GHO section. See Supplementary Materials for

further details on sample preparation, equipment and environmental dose rate calculations (Tables 6-S1, 6-S2).

6.3 Testing a SAR protocol

6.3.1 Natural IRSL signals

Most KF grains (60–80%) from sample GHO-2 are characterized by bright initial signals (commonly greater than 40,000 counts in the first 0.134 s) that decay rapidly upon laser stimulation, but fail to reach a constant background (Fig. 6-1a). Approximately 20–40% of grains from sample GHO-2 exhibit dim and very slowly decaying, IRSL signals (Fig. 6-1a, inset). Elemental (microprobe) analyses (Section 6.6.4) show that the bright grains are most commonly orthoclase and some are plagioclase, and the dim IRSL signals are usually derived from holes occupied by quartz grains, both minerals identified on the basis of their elemental compositions. The IRSL signals detected from the holes containing quartz grains may be due to weak IRSL emissions from the quartz grains or feldspar inclusions inside them, or stray IRSL emissions from adjacent bright KF grains. Approximately 10% of measured feldspar grains have natural and/or regenerative signals greater than 268,000 counts per 0.134 s. These grains were excluded from further analyses as such intense signals induced partial saturation of the photomultiplier tube.

6.3.2 The SAR procedure and data rejection criteria

The D_e was measured using an IRSL SAR procedure similar to that described by Wallinga et al. (2007). The temperature and duration of the preheat (250°C, 10 s) preceding the L_n and L_x measurements were identical to those preceding the T_n and T_x measurements, following Huot and Lamothe (2003) and all IRSL measurements were made while holding the sample at 50°C (Table 6-S3). At the end of each SAR cycle, all grains on each disc were bleached using IR LEDs for 40 s at 290°C to reduce recuperation. A typical KF grain dose response curve is shown in Fig. 6-1b.

KF grains were rejected if: 1) they exhibited an IRSL decay curve typical of holes occupied by quartz grains, 2) their signals failed to grow systematically with increasing regenerative dose (i.e., they had no dose-response curve), 3) the sensitivity-corrected zero-dose signal was greater than 5% of L_n/T_n, 4) the first 0.134 s of the test dose signal following the natural IRSL measurement was less than 3 times the background, 5) the recycling ratio differed from unity by more than 2σ (Jacobs and Roberts, 2007), and 6) their natural and/or regenerative signals exceeded 268,000 counts per 0.134 s (to prevent partial saturation of the photomultiplier tube). Signals were analyzed using the 'Previous background (BG) subtraction' option in Analyst, but we note that this method results in D_e values that are

negligibly smaller (by ~0.2%) than those obtained using the standard 'late light' subtraction procedure.

6.3.3 Dose recovery test

A single-grain dose recovery test was performed on KF grains from sample GHO-2 that were bleached in the sun for 2 days before measuring a laboratory beta dose of 68 Gy using the SAR procedure outlined in Table 6-S3. Out of 590 measured grains, 232 (39%) passed all rejection criteria (Table 6-S4). The distribution of measured dose/given dose ratios is shown in a radial plot in Fig. 6-2a. The weighted mean ratio is 0.97 ± 0.01, and the OD is 6.9 ± 0.5%. Both statistics were calculated using the Central Age Model (CAM) of Galbraith et al. (1999). These dose recovery results suggest that the SAR protocol is appropriate for the majority of KF grains in this sample.

6.4 D_e determination and sources of overdispersion

The single-grain D_e distribution of sample GHO-2 is shown in Fig. 6-2b and the decay curves for two extreme values are plotted in Fig. 6-2c; the latter exhibit no obvious differences in shape. Of 1149 measured grains, 475 (41%) passed all rejection criteria (Table 6-S4). The weighted mean (CAM) D_e of all accepted grains is 52.7 ± 1.6 Gy, with an OD of 46.5 ± 1.5% (Table 6-1). The OD and relative spread in values of this sample are much larger than those obtained in the dose recovery test, which we attribute to a number of factors, including:

1) natural variations in luminescence properties of KF grains additional to those observed in the laboratory (as bleaching and irradiation conditions in nature are not identical to those used in the dose recovery test),
2) heterogeneous external beta microdosimetry after burial,
3) inhomogeneous bleaching of grains before burial, including the incorporation of older grains into the sample by underwater mixing of slumped riverbank deposits with younger fluvial sediments coming from upstream,
4) variations in ^{40}K contents among grains, leading to differences in internal dose rates, and
5) grain-to-grain variations in fading rates.

Heterogeneous beta microdosimetry likely accounts for some of the OD, but the effect is thought to be minimal because organic matter and calcium carbonate concretions or nodules were not observed in the sedimentary unit. Any beta microdosimetry effects are less important for KF grains than for quartz, because a significant part the environmental dose rate to KF grains (up to ~43% in sample GHO-2) originates from the internal ^{40}K.

Because sample GHO-2 consists of grains that were deposited in a fluvial channel, it is possible that not all grains were completely bleached before burial, when last transported by the river. To examine the issue of inhomogeneous bleaching, single-grain D_e measurements were made on KF grains from a modern sample (KHUT-10) collected from a sand bar in the middle of the Son River channel. The D_e distribution of this sample is shown in Fig. 6-2d. The weighted mean D_e is 1.7 ± 0.2 Gy with an OD of 3.9 ± 0.2 Gy (n = 366), calculated using the unlogged CAM (Arnold et al., 2009). Only 8% of grains have natural doses greater than 5 Gy. If the bleaching conditions of river-transported grains in sample GHO-2 had been similar to those of KHUT-10, then these data suggest that residual doses would probably have been small (i.e., mostly <5 Gy).

It is possible, however, that a significant proportion of the grains in sample GHO-2 were derived from locally, slumped river-bank deposits, in which case the OD of D_e values for GHO-2 may reflect underwater mixing of potentially well-bleached older riverbank sediments with younger fluvial sediments transported from upstream. It may also reflect grain-to-grain variations in fading rate and ^{40}K content. To investigate the latter two possibilities, fading-corrected ages were calculated for all grains accepted for D_e estimation, using the model of Huntley and Lamothe (2001) and K contents were measured for a subpopulation of these grains (Section 6.6.4). For comparison, fading-corrected ages were also calculated from aliquots of the same sample.

6.5 Anomalous fading tests

6.5.1 Fading measurement procedures

Fading tests for both single grains and aliquots in this study followed the procedure of Auclair et al. (2003). After D_e measurement of single grains, each grain (still located in the same hole) was stimulated repeatedly with the IR laser after being given a laboratory dose of 34 Gy (L_x) and following a series of delay times after irradiation and preheating (Table 6-S5). Each L_x measurement was immediately followed by a test dose (14 Gy) measurement (T_x) to correct the L_x signal for sensitivity change. A prompt measurement (i.e., an L_x/T_x measurement made after no delay period) was made immediately after each delayed L_x/T_x measurement to ensure that any sensitivity changes of L_x/T_x measurements throughout the fading test are accounted for (Huot, 2007). Maximum delay times for each grain were ~44 h. Fading tests for multi-grain aliquots followed an identical procedure, but with shorter delay times (maximum delay time of ~14 h). All fading rates were estimated using the measured *g*-value normalized to a delay period of 2 days (Huntley and Lamothe, 2001). Twenty-four aliquots were measured from sample GHO-2, so that single-grain and multi-grain aliquot calculated ages could be compared. However, the fading rates of 24

aliquots from sample GHO-3 were subsequently used in comparisons of single-grain and multi-grain aliquot *g*-value distributions, because the GHO-3 fading measurements appeared to be more thermally reproducible than the GHO-2 fading measurements (see Section 6.5.2).

6.5.2 Fading test results

Multi-grain aliquot fading rates for samples GHO-2 and GHO-3 are statistically indistinguishable, but there is a larger spread in *g*-values from GHO-2 (3.1 ± 2.0 %/decade, n = 24) than from GHO-3 (3.1 ± 0.6 %/decade, n = 24) (the uncertainties are expressed as the standard deviation). Following Huot (2007) we consider this larger spread to be an undesirable measurement artefact caused by poorer thermal reproducibility in the fading measurements for GHO-2. This poor reproducibility is attributed to the Crystalbond adhesive used to mount grains to discs (see Supplementary Material for details).

The distribution of single-grain *g*-values for sample GHO-2 is shown in Fig. 6-3a; it has a weighted mean of 2.9 %/decade and a standard deviation of 7.1 %/decade (n = 475). The multi-grain aliquot *g*-value distribution of sample GHO-3 is shown in Fig. 6-3b, for comparison. Representative single-grain and multi-grain fading plots are shown in Figs 6-3c, d and e. The single-grain *g*-value distribution has a much larger spread than the multi-grain aliquot distribution. We attribute this to the relatively poor precision of fading measurements on single grains, and to grain-to-grain variations in fading rates that are averaged out in multi-grain aliquot measurements.

6.6 KF grain age distributions

6.6.1 Single-grain and multi-grain KF ages

The fading-corrected single-aliquot and single-grain age distributions for sample GHO-2 are shown in Fig. 6-4a, and the calculated weighted mean (CAM) ages are shown in Table 6-1. The single-grain weighted mean age for all grains is 29.3 ± 1.3 ka and this is consistent with the weighted mean age of 29.3 ± 1.7 ka for 24 aliquots of the same sample. The multi-grain aliquot age OD (20.0 ± 3.5%) is smaller than that of the single-grain age (37.3 ± 1.5%), and this is likely due to averaging effects of multiple-grain luminescence signals.

It is important to emphasize that if, as we consider probable, sample GHO-2 consists of an admixture of fluvially transported grains and grains derived from older, locally slumped riverbank deposits, then the weighted mean 'ages' determined using CAM have no meaningful chronological value. We use CAM here only as an indication of central tendency and not as a measure of sample burial age; the latter would require the use of the minimum age model to estimate the burial dose of the mostly recently bleached grains in the sample, or

the finite mixture model to estimate the burial doses of multiple, discrete populations of single grains (Jacobs and Roberts, 2007).

6.6.2 Single-grain quartz ages

The single-grain quartz weighted mean age of sample GHO-2 is 45.6 ± 2.9 ka with an OD of 44.9 ± 2.2%; the age distribution is shown in Fig. 6-4b. The same caveats apply as above to the interpretation of the weighted mean 'age' determined using CAM. The quartz single-grain OSL measurements follow the procedures of Haslam et al. (2011), and the ages were determined by dividing the single-grain D_e values by the environmental dose rate for the bulk sample. The pattern and OD of the quartz single-grain age distribution is not identical to that of the KF grains (e.g., fewer grains have ages between 10 and 30 ka), but the range of ages of both distributions is similar (Figs 6-4a, b). Most quartz and feldspar grains have burial ages noticeably younger than the expected age (~74 ka) of the YTT deposit.

6.6.3 Isolating zero-fading grains

A potential benefit of dating K-feldspars at the single-grain level is that grains with signals that fade significantly can be excluded from analyses. Almost half (45%) of the accepted grains in sample GHO-2 have *g*-values that are statistically consistent with zero at 2σ. We refer to these as 'zero'-fading grains. The weighted mean 'age' of all these grains (26.4 ± 1.2 ka, Table 6-1) is slightly younger than that of the entire grain population, and this is likely because some of these grains do, in fact, fade, but at rates too low to be detected at laboratory timescales and given the measurement precisions achieved in this study. The OD (38.4 ± 2.1%) and pattern of the 'zero'-fading grain age distribution is similar to that of all fading-corrected grains, and the oldest and youngest grain ages of the entire grain population are present in the 'zero'-fading grain age plot (Fig. 6-4c). No simple correlation between single-grain fading rate and fading-corrected age could be identified.

6.6.4 The influence of K content on single-grain age distributions

Because the beta radiation from ^{40}K in individual KF grains from sample GHO-2 contributes up to ~43% of the total dose rate, grain-to-grain variations in K content may induce scatter in single-grain D_e and age distributions. Wavelength-dispersive spectrometry (WDS) measurements were made on 51 individual feldspar grains from sample GHO-2 to detect any relationships between K content and fading-corrected age; these grains had been previously used for D_e measurements. WDS measurements were made using a Cameca SX-100 electron microprobe in the Department of Earth and Planetary Sciences, at Macquarie University, Australia (see Supplementary Material for details).

Fig. 6-4d shows the single-grain age distribution of the WDS-measured grains (n = 51); each point is shaded according to its K content. Two grains have almost negligible K contents (<0.25%) and were identified as plagioclase feldspars on the basis of their Al (~12.5%), Si (~30%), Na (~7%), and Ca (~3%) contents. The remaining grains have K contents of between 9 and 14% (Fig. 6-4d) and, thus, can be classified as orthoclase. This range of K contents is slightly larger than that reported for hand-picked feldspar grains from China (13–14%; Zhao and Li, 2005), but smaller than that reported for KF grains from North America (6.5–16.9%; Huntley and Baril, 1997).

We could find no correlation between K content and fading rate or single-grain age (Fig. 6-4d). A wide range of grain ages appear within each K content class, each of which spans only 1–2%; for example K contents of 13–14%, grain ages range from 13 ka to 82 ka. A dependency of grain age on K content may be masked by the fact that other sources of ionizing radiation account for two-thirds of the total dose rate. Also, any influence of ^{40}K content on KF single-grain ages may be confounded by inhomogeneous bleaching of this sample.

6.7 Discussion and Conclusions

We have reported KF single-grain D_e and fading-corrected ages for a fluvial sand sample collected from north-central India, and considered some potential sources of OD: namely, grain-to-grain variations in luminescence properties, residual doses at deposition, anomalous fading rates and internal K contents. The dose recovery test suggests that at least 6.9% of the OD in D_e may be attributed to natural variations in luminescence properties of the grains. The impact of incomplete bleaching of grains on the OD cannot be measured directly, but measurements from a modern fluvial sample suggest that any residual dose would have been small (<5 Gy or ~10% of the weighted mean D_e) for grains transported by the river immediately before burial. Some grains in the sample (including those with ages of ~70 ka and older, Fig. 6-4a) may be derived from older river bank deposits that slumped into the channel and were mixed with river-transported grains underwater.

Another possible contributor to the spread of single-grain ages is grain-to-grain variation in fading rate. The decrease in OD before and after correcting for fading (46.6 ± 1.5% and 37.3 ± 1.5%, respectively) is at least partly due to the lower precisions of the fading-corrected ages. We also note that the OD of the fading-corrected ages is statistically indistinguishable from the OD of the 'zero'-fading grain ages (38.4 ± 2.1%), so there is no evidence for a significant increase in OD attributable to grain-to-grain variations in fading rates, at least for this sample. Single-grain *g*-value precisions in this study are poor relative to those of multi-grain aliquots (see Section 6.5.2). They are probably hampered mostly by variations in individual grain brightness and by responses to heating and dosing in the

laboratory during fading tests, in addition to suboptimal thermal reproducibility of fading tests (Huot, 2007).

We did not detect a dependency of single-grain fading-corrected age on internal K content, most likely because grain-to-grain variations in K content were small, and any effects were masked by other causes of D_e variation. This suggests that, if single-grain observations are restricted to density-separated K-rich feldspars, then grain-to-grain variations in internal dose rates may have a minimal effect on the shape and OD of the KF single-grain age distribution.

The luminescence ages of some KF grains (4%) and quartz grains (38%) from sample GHO-2 are consistent with the expected age of the overlying YTT deposit. However, most KF and quartz grain ages from this sample are significantly younger than 74 ka (Figs 6-4a, b), which suggest that the sand unit underlying the YTT deposit at this sample location may post-date the YTT event. Sedimentological observations made at this site, as well as additional feldspar and quartz ages from this and other riverbank sections in the Middle Son Valley, are being used to further explore this issue.

Acknowledgements

This project was funded by an ARC Discovery Project grant to Roberts and by University of Wollongong scholarships to Neudorf. Sébastien Huot is thanked for advice and Excel macros for fading correction, and Kevin Grant and Norman Pearson are thanked for their advice and assistance with WDS measurements.

References

Arnold, L.J., Roberts, R.G., Galbraith, R.F., DeLong, S.B., 2009. A revised burial dose estimation procedure for optical dating of young and modern-age sediments. Quat. Geochron. 4, 306–325.

Auclair, M., Lamothe, M., Huot, S., 2003. Measurement of anomalous fading for feldspar IRSL using SAR. Radiat. Meas. 37, 487–492.

Duller, G.A.T., Bøtter-Jensen, L., Murray, A.S., 2003. Combining infrared- and green-laser stimulation sources in single-grain luminescence measurements of feldspar and quartz. Radiat. Meas. 37, 543–550.

Galbraith, R.F., Roberts, R.G., Laslett, G.M., Yoshida, H., Olley, J.M., 1999. Optical dating of single and multiple grains of quartz from Jinmium rock shelter, northern Australia: Part I, experimental design and statistical models. Archaeometry 41, 339–364.

Gatti, E., Durant, A.J., Gibbard, P.L., Oppenheimer, C. 2011: Youngest Toba Tuff in the Son Valley, India: a weak and discontinuous stratigraphic marker. Quat. Sci. Rev. 30, 3925–3934.

Haslam, M., Roberts, R.G., Shipton, C., Pal, J.N., Fenwick, J.L., Ditchfield, P., Boivin, N., Dubey, A.K., Gupta, M.C., Petraglia, M., 2011. Late Acheulean hominins at the Marine Isotope Stage 6/5e transition in north-central India. Quat. Res. 75, 670–682.

Huntley, D.J., Baril, M.R., 1997. The K content of the K-feldspars being measured in optical dating or in thermoluminescence dating. Ancient TL 15, 11–13.

Huntley, D.J., Lamothe, M., 2001. Ubiquity of anomalous fading in K-feldspars and the measurement and correction for it in optical dating. Can. J. Earth Sci. 38, 1093–1106.

Huot, S., 2007. Investigations of alternate and innovative ways of performing luminescence dating in an attempt to extend the age range. Unpublished PhD thesis, Department of Earth Sciences, University of Aarhus, Denmark.

Huot, S., Lamothe, M., 2003. Variability of infrared stimulated luminescence properties from fractured feldspar grains. Radiat. Meas. 37, 499–503.

Jacobs, Z., Roberts, R.G., 2007. Advances in optically stimulated luminescence dating of individual grains of quartz from archeological deposits. Evol. Anthropol. 16, 210–223.

Jones, S.C., 2010. Palaeoenvironmental response to the ~74 ka Toba ash-fall in the Jurreru and Middle Son valleys in southern and north-central India. Quat. Res. 73, 336–350.

Smith, V.C., Pearce, N.J.G., Matthews, N.E., Westgate, J.A., Petraglia, M.D., Haslam, M., Lane, C.S., Korisettar, R., Pal, J.N., 2011. Geochemical fingerprinting of the widespread Toba tephra using biotite compositions. Quat. Internat. 246, 97–104.

Wallinga, J., Bos, A.J.J., Dorenbos, P., Murray, A.S., Schokker, J., 2007. A test case for anomalous fading correction in IRSL dating. Quat. Geochron. 2, 216–221.

Zhao, H., Li, S.-H., 2005. Internal dose rate to K-feldspar grains from radioactive elements other than potassium. Radiat. Meas. 40, 84–93.

Table 6-1. D_e and age estimates for sample GHO-2, together with their overdispersion (OD) values.

	CAM weighted mean [1]	OD (%)
D_e for all KF grains (Gy) (n = 475)	52.7 ± 1.6	46.5 ± 1.5
Uncorrected age for all KF grains (ka) (n = 475)	21.8 ± 1.0	46.5 ± 1.5
Fading-corrected age for KF grains with finite ages (ka) (n = 467)	29.3 ± 1.3	37.3 ± 1.5
Age for KF grains with 'zero' fading (ka) (n = 210)	26.4 ± 1.2	38.4 ± 2.1
Fading-corrected aliquot age (ka) (n = 24)	29.3 ± 1.7	20.0 ± 3.5
Quartz single-grain age (ka) (n = 337)	45.6 ± 2.9	44.9 ± 2.2

[1] CAM weighted mean ages have no meaningful chronological value. They are used here only to indicate the central tendency of each age distribution and should not be interpreted as estimates of sample burial age; see text for explanation.

Figures

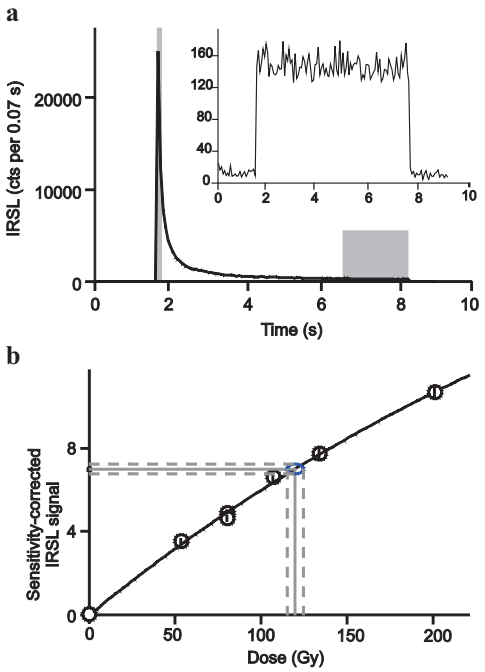

Figure 6-1. a) Shine-down curves for a KF grain and a quartz grain (inset) from sample GHO-2. The integration limits for the initial (first 0.134 s) and background (last 1.742 s) signals are shaded in grey. b) Growth curve for the same KF grain. The KF grain has a K concentration of 12.2%, and the quartz grain is 99.5% SiO2 (both measured using WDS; see text).

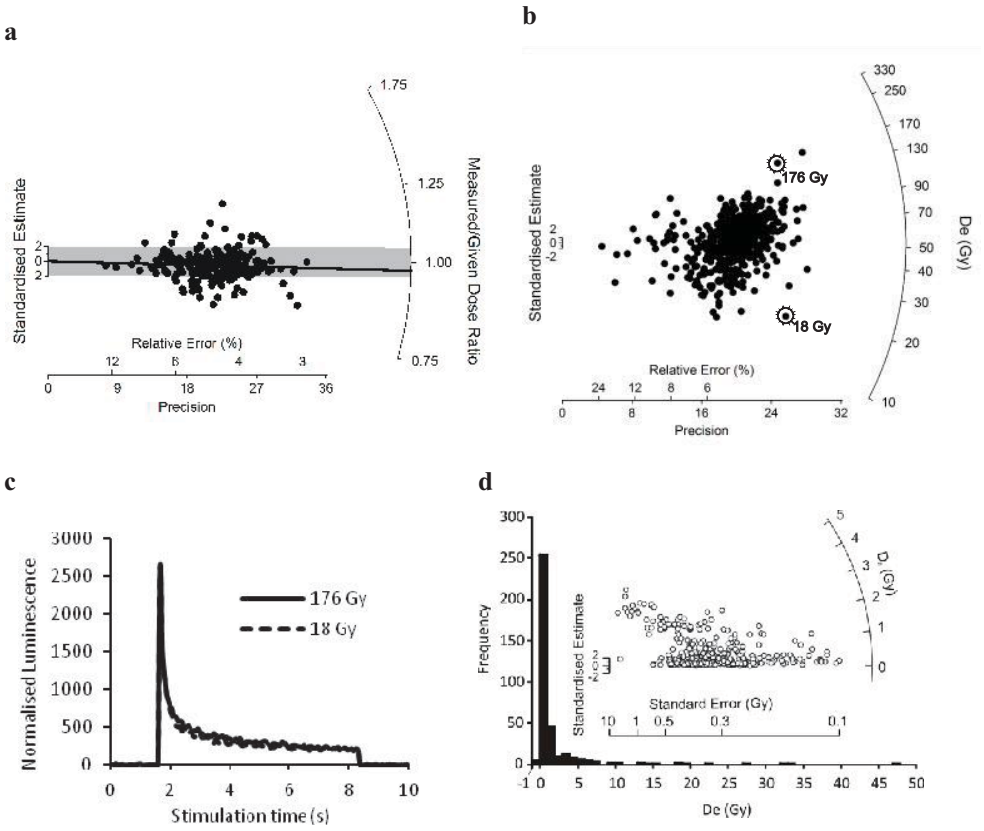

Figure 6-2. a) Distribution of measured dose/given dose ratios obtained from the dose recovery test for sample GHO-2. The grey band is centered on 1, and the black line is centered on the weighted mean of the distribution. b) D_e distribution for sample GHO-2. c) The lRSL decay curves for the circled points in 'b'. d) D_e distribution of a modern sample (KHUT-10) collected from a sand bar in the Son River channel. Grains with negative natural dose values, and values greater than 5 Gy lie outside the scale of the radial plot but are shown in the histogram (n=366).

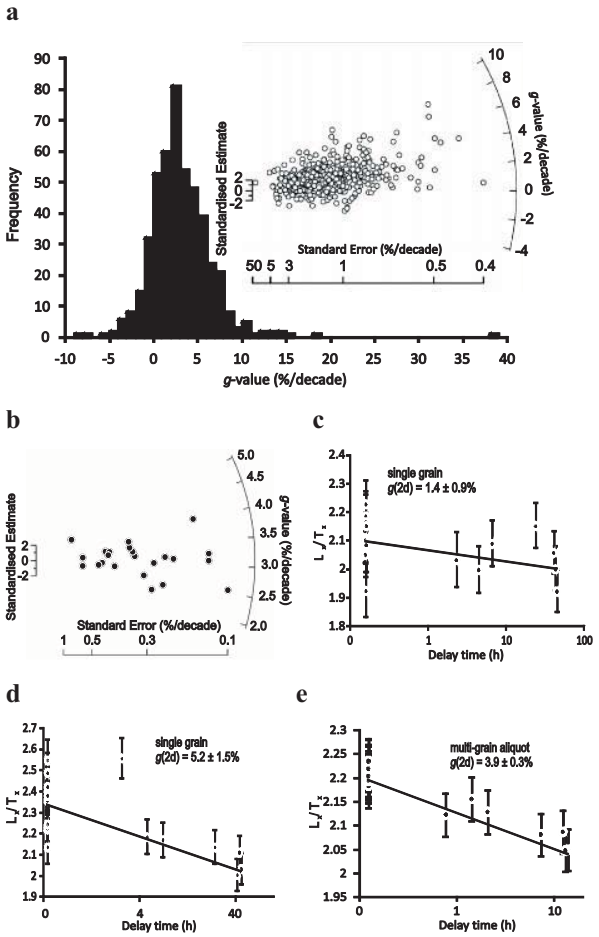

Figure 6-3. a) Single-grain *g*-value distribution for sample GHO-2 (n=475). All *g*-values are normalised to a delay period of 2 days. A single-aliquot *g*-value distribution (n=24) from GHO-3 is shown for comparison in 'b'. Each aliquot consists of ~25 grains that were mounted on stainless steel discs with silicone oil. Fading plots for individual grains from sample GHO-2 that exhibit a low (c) and a high (d) fading rate, respectively. e) A fading plot for one ~25-grain aliquot from sample GHO-3.

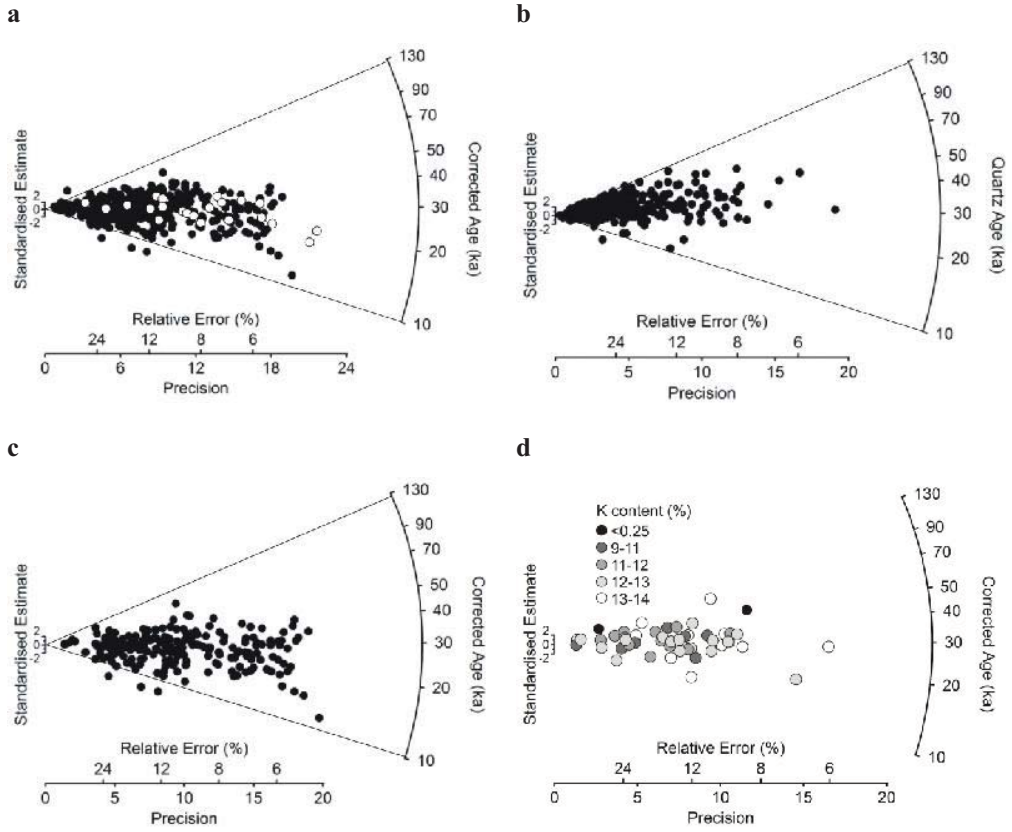

Figure 6-4. a) The fading-corrected age distribution for 24 single-aliquots (white-filled circles) superimposed on the single-grain fading-corrected age distribution for sample GHO-2 (black-filled circles, n=467). b) Quarz single-grain age distribution for sample GHO-2 (n=337). c) Single-grain fading-corrected age distribution for all KF grains with *g*-values statistically equivalent to zero (within 2σ) (n=209). Black lines in plots 'a', 'b' and 'c' delineate the approximate age ranges (excluding outliers) of the feldspar and quartz single-grain distributions. d) Single-grain fading-corrected age distribution of microprobe-measured KF grains (n=51); each point is shaded according to measured K content (in weight %).

SUPPLEMENTARY MATERIAL

Sample preparation procedures and equipment

The 180–212 μm diameter grain-size fraction of all samples was treated with HCl acid (10%) and H_20_2 acid (10%) to ensure the removal of any traces of carbonates and organic material. A K-feldspar-rich extract was obtained using sodium polytungstate heavy liquid separation (ρ<2.58 g/cm^3) and etched with a diluted HF acid (10%) solution for 10 minutes to remove the outer alpha-irradiated layer of the grains. After HF acid etching, the samples were sieved again to remove any grains that were reduced to less than 180 μm in size.

All measurements were made using a Risø TL/OSL DA-20 reader equipped with a calibrated ^{90}Sr/^{90}Y beta source. Single grains (samples GHO-2 and KHUT-10) were loaded into 300 μm diameter holes on gold-plated aluminum discs and stimulated using the IR (830 nm) laser, fitted with an RG780 filter to absorb a resonant wavelength at 415 nm. An IR laser power of 30% was used to reduce the potential effects of grain heating by the laser (Duller et al., 2003). Because the dose rate from the ^{90}Sr/^{90}Y beta source is not uniform over the entire area of a disc, the dose rate to each individual disc hole position was calibrated using gamma-irradiated quartz supplied by Risø.

Multi-grain aliquots (samples GHO-2 and GHO-3), each composed of ~25 grains, were mounted on stainless steel discs and stimulated using IR (875 nm) light-emitting diodes (LEDs). The IRSL signals in the blue-violet region were detected using a bialkali EMI 9235QB photomultiplier tube, fitted with Schott BG-39 and Corning 7-59 filters. For multi-grain aliquot anomalous fading measurements, KF grains from sample GHO-2 were adhered to discs using a transparent thermoplastic polymer adhesive, Crystalbond 509 (see below), and KF grains from sample GHO-3 were adhered to discs using silicone oil.

g-value calculations

In this study, the *g*-value of each grain was calculated using Equation 4 of Huntley and Lamothe (2001):

$$I/I_c = 1 - (g/100) * \log_{10}(t/t_c) \qquad (1)$$

where I/I_c is the L_x/T_x measurement (I) normalized to the first prompt L_x/T_x measurement (I_c), $t \approx t_1 + (t_2–t_1) / 2$, where t_1 is the time elapsed since the end of irradiation and the

measurement of L_x, t_2 is the time elapsed since the beginning of irradiation and the measurement of L_x, and t_c is t for the first prompt measurement. Thus, the g-value is the slope of the weighted regression line of I/I_c plotted against $\log_{10}(t/t_c)$, multiplied by 100. The error of the g-value for each grain was calculated as the standard error of the slope of this weighted regression line, multiplied by 100. The weighted linear regression (weighted according to the square of the inverse of the measurement error for each I/I_c) was performed using the linear model function called '**lm**' in the R package (http://www.r-project.org). Following convention, the g-value and its uncertainty were evaluated for t_c = 2 days (Huntley and Lamothe, 2001).

To calculate the fading-corrected age of each grain from sample GHO-2, the single-grain D_e values, g-values (normalized to 2 days), and the total dose rate for the bulk sample (2.42 ± 0.08 Gy/ka), as well as their uncertainties, were used as parameters in the Huntley and Lamothe (2001) fading-correction model. The calculations were performed using the Excel spreadsheet and macro provided by Sébastien Huot. The fading-corrected age for each grain (T) was calculated using Equation A5 of Huntley and Lamothe (2001):

$$T_f/T = D_{ef}/D_e = I_f/I = 1 - \kappa\,[\ln(T/t_c) - 1] \qquad (2)$$

where $T_f = D_e/D_a$ (i.e., the calculated age before correction for fading), D_e is the measured equivalent dose, D_a is the total dose rate for the bulk sample, and D_{ef} and I_f are the values of D_e and I that would be obtained if there were no fading.

The associated uncertainty on this age (at 1σ) was calculated as:

$$T * \{[(T_{max}-T_{min}) / (2*T)]\text{^}2 + (\Delta T_f/T_f)\text{^}2\}\text{^ } 0.5 \qquad (3)$$

where T_{max} and T_{min} are the fading-corrected ages obtained using the measured g-value (normalized to 2 days) plus 1σ and minus 1σ, respectively, and ΔT_f is the uncertainty on T_f. ΔT_f was calculated as:

$$T_f * [(\Delta D_e/D_e)\text{^}2 + (\Delta D_a/D_a)\text{^}2]\text{^ } 0.5 \qquad (4)$$

where ΔD_e and ΔD_a are the 1σ uncertainties on D_e and D_a, respectively.

Aliquot preparation methods using Crystalbond 509

In luminescence studies, silicone oil is typically used to adhere grains to discs, but we found that after several hours to days, the oil dries and the grains will move or slide off the disc. If enough grains are lost, L_x and T_x signals may be hampered by poor counting statistics, leading to an increase in error in the measured *g*-values. To prevent this, a transparent thermoplastic polymer adhesive, Crystalbond 509, was used for multi-grain aliquots of sample GHO-2, following the approach of Huntley and Lamothe (2001). After measurement of the D_e, a small amount of Crystalbond was dissolved in acetone and dropped onto the grains on each disc using a pipette, and allowed to air-dry for at least two hours before measurement. This adhesive did not adversely affect L_x/T_x errors of multi-grain aliquots (Table 6-S1), but did reduce the thermal reproducibility of the fading measurements (see Section 6.0). As a consequence, we did not use this adhesive on aliquots used for fading measurements of sample GHO-3.

Environmental dose rate calculations

The environmental dose rate was determined for sample GHO-2 for age calculations. The internal dose rates of KF grains were not measured directly, but instead estimated using assumed U, Th, ^{40}K and ^{87}Rb concentrations based on values widely used in the literature. Internal U and Th contents were assumed to be 0.3 ± 0.1 ppm and 0.7 ± 0.1 ppm, respectively, following Medjahl (1987). The internal ^{87}Rb concentration was assumed to be 400 ± 100 ppm (Huntley and Hancock, 2001), and the internal ^{40}K content for KF grains was assumed to be 12.5 ± 0.5% (Huntley and Baril, 1997), except where stated elsewhere in this paper (see Section 7.4). The internal alpha and beta dose rate contributions from the U and Th decay chains, and the internal beta dose rate contribution from ^{40}K, were calculated using the conversion factors of Adamiec and Aitken (1998). An alpha efficiency factor (a-value) of 0.09 ± 0.03 was assumed based on previously reported values for polymineral fine grains in the literature (Rees-Jones, 1995; Lang and Wagner, 1997; Banerjee et al., 2001; Lang et al., 2003), and dose rates were corrected for beta attenuation using beta absorption factors for etched grains from Brennan (2003).

The external beta and gamma dose rates were estimated by low-level beta counting and *in situ* gamma spectrometry, respectively, and a contribution added for the dose rate from cosmic rays. The external dose rate was calculated for an estimated long-term, time-averaged water content of 5 ± 2%. This takes into consideration the field water content measured in the laboratory (0.3%), the free-draining nature of the sample sediments and their

collection during the dry season, and the monsoonal climate of the region. The total dose rate for sample GHO-2 was calculated to be 2.42 ± 0.08 Gy/ka (Table 6-S2).

Wavelength-dispersive spectrometry (WDS) methods

All grains from three single-grain discs were lifted out of the holes using double-sided sticky tape. The other side of the tape was then adhered to a flattened, polished base of a round plastic capsule ~30 mm in diameter and 20 mm deep. The capsule was then filled with epoxy resin and cured. After curing, the resin block was ground with glass paper of progressively finer grades (240, 800, 1200, 2000) to the centre of the layer of single grains. To ensure that grain surfaces were as flat and smooth as possible, the surface of the block was polished using 6, 3, and 1 μm diamond paste. Approximately half of the grains from each single-grain disc were lost during the grinding process. A vacuum-evaporated carbon coating (~20 nm thick) was applied to the top of the resin block using a sputter coater.

The polished block was inserted into a holder in a vacuum-pumped specimen chamber and the locations of spot measurements were identified and recorded using standard software and a high-power optical microscope and charge-coupled device (CCD) camera imaging system. Three spot measurements were made on each grain using an electron beam size of 5 μm and a beam current of 20 nA. Most grain surfaces still contained rough spots after polishing, so spot measurement locations were restricted to flat grain surfaces with an homogeneous appearance. Five WDS spectrometer reference crystals were used to isolate the characteristic X-rays (Kα X-ray lines) of K, Mg, Si, Ca, Fe, Na, and Al. The detection crystal types, standards used, as well as the average detection limits achieved for each element are listed in Table 6-S6. The elemental concentration of each spot measurement was quantified using the ZAF (Z—backscatter effect, A—absorption of radiation within the grain, F—fluorescence) quantitative method (Reed, 1995) using orthoclase (12.79% K) as a standard for K. The K content of each grain in weight % was calculated as the average of the three spot measurements. Seven percent of grains exhibited heterogeneity in their elemental composition (i.e., values of the three spot measurements differed by more than 2%) and thus were excluded from analyses.

REFERENCES

Adamiec, G., Aitken, M.J., 1998. Dose-rate conversion factors: update. Ancient TL 16, 37–50.

Banerjee, D., Murray, A. S., Bøtter-Jensen, L., Lang, A., 2001. Equivalent dose estimation using a single aliquot of polymineral fine grains. Radiat. Meas. 33, 73–94.

Brennan, B.J., 2003. Beta doses to spherical grains. Radiat. Meas. 37, 299–303.

Duller, G.A.T., Bøtter-Jensen, L., Murray, A.S., 2003. Combining infrared- and green-laser stimulation sources in single-grain luminescence measurements of feldspar and quartz. Radiat. Meas. 37, 543–550.

Huntley, D.J., Baril, M.R., 1997. The K content of the K-feldspars being measured in optical dating or in thermoluminescence dating. Ancient TL 15, 11–13.

Huntley, D.J., Hancock, R.G.V., 2001. The Rb contents of the K-feldspar grains being measured in optical dating. Ancient TL 19, 43–46.

Huntley, D.J., Lamothe, M., 2001. Ubiquity of anomalous fading in K-feldspars and the measurement and correction for it in optical dating. Can. J. Earth Sci. 38, 1093–1106.

Lang, A., Hatté, C., Rousseau, D. D., Antoine, P., Fontugne, M., Zöller, L., Hambach, U., 2003. High-resolution chronologies for loess: comparing AMS ^{14}C and optical dating results. Quat. Sci. Rev. 22, 953–959.

Lang, A., Wagner, G. A., 1997. Infrared stimulated luminescence dating of Holocene colluvial sediments using the 410 nm emission. Quat. Sci. Rev. 16, 393–396.

Mejdahl, V., 1987. Internal radioactivity in quartz and feldspar grains. Ancient TL 5, 10–17.

Reed, S.J.B., 1995. Electron probe microanalysis. In: Potts, P.J., Bowles, J.F.W., Reed, S.J.B., Cave, M.R. (Eds), Microprobe Techniques in the Earth Sciences, pp. 49–89. The Mineralogical Society Series, Vol. 6, Chapman & Hall, London.

Rees-Jones, J., 1995. Optical dating of young sediments using fine-grain quartz. Ancient TL 13, 9–14.

Table 6-S1. L_x/T_x errors calculated from two aliquots of sample GHO-2 containing ~25 grains each. Aliquot 1 was prepared using silicone oil, and Aliquot 2 was prepared using Crystalbond 509.

Aliquot number [1]	Adhesive	Mask size (mm)	L_x (photon counts)	T_x (photon counts)	L_x/T_x	L_x/T_x standard error	L_x/T_x relative standard error (%)
1	Silicone oil	1	172933	74898	2.31	0.01	0.46
2	Crystalbond	1	83195	37636	2.21	0.01	0.67

[1] All aliquots were measured after being given a laboratory dose of 28 Gy and a preheat of 250°C for 10 s. The test dose was 11 Gy.

Table 6-S2. Environmental dose rates for sample GHO-2 (in Gy/ka).

	Alpha	Beta	Gamma	Cosmic	Total
External		0.72 ± 0.05	0.61 ± 0.03	0.09 ± 0.01	1.42 ± 0.06
Internal	0.12 ± 0.04	0.79 ± 0.03			1.00 ± 0.05
Total					2.42 ± 0.08

Table 6-S3. The SAR measurement protocol for single KF grains. [1]

1.	Natural or regenerative dose	
2.	Preheat (250°C, 10 s)	
3.	IRSL [2] (50°C, 10 s)	→ L_n, L_x
4.	Test dose (14 Gy)	
5.	Preheat (250°C, 10 s)	
6.	IRSL [2] (50°C, 10 s)	→ T_n, T_x
7.	IR (diode) bleach (290°C, 40 s)	
8.	Return to step 1.	

[1] L_n = natural signal, L_x = regenerative dose signal. Regenerative doses of 54, 81, 108, 135, and 203 Gy were used prior to a zero dose to monitor for recuperation. A repeat dose of 81 Gy was measured after the zero dose to determine the recycling ratio.

[2] IR laser stimulation commenced 1.675 s after the disc temperature reached 50°C and lasted for 6.7 s.

Table 6-S4. KF grain rejection statistics for sample GHO-2.

	Dose recovery test (6 discs)	D_e determination (12 discs)
Measured grains	590 (10 empty holes)	1149 (51 empty holes)
Plateau-like decay curves (quartz)	235	197
Feldspar grains	355	952
Grains with signals that do not systematically grow with increasing regenerative dose (i.e., no dose response curve)	23	106
Grains rejected due to brightness (>268,000 counts per 0.134 s)	36	100
Grains rejected due to test dose signal < 3 x BG	0	0
Feldspar grains rejected due to recycling ratio ≠ 1 at 2σ.	38	149
Feldspar grains rejected due to high recuperation (i.e., zero-dose signal > 5% of L_n/T_n)	38	207
Accepted feldspar grains	232	475
Feldspar grains with finite fading-corrected ages		467

Table 6-S5. Anomalous fading SAR measurement protocol for single KF grains.

1.	Dose (34 Gy)
2.	Preheat (250°C, 10 s)
3.	IRSL[1] (IR laser, 50 °C, 10 s) → L_x (prompt)
4.	Test dose (14 Gy)
5.	Preheat (250°C, 10 s)
6.	IRSL[1] (IR laser, 50°C, 10 s) → T_x (prompt)
7.	IRSL bleach (diodes, 290°C, 40 s)
8.	Dose (34 Gy)
9.	Preheat (250°C, 10 s)
10.	Delay[2]
11.	IRSL[1] (IR laser, 50°C, 10 s) → L_x (delay)
12.	Test dose (14 Gy)
13.	Preheat (250°C, 10 s)
14.	IRSL[1] (IR laser, 50°C, 10 s) → T_x (delay)
15.	IRSL bleach (diodes, 290°C, 40 s)
16.	Return to step 1 for the remaining delay times

[1] IR laser stimulation commenced 1.675 s after the disc temperature reached 50°C and lasted for 6.7 s.
[2] Delay times ranged from ~4 min (prompt measurements) to 44 h after irradiation.

Table 6-S6. WDS crystal types, standards and detection limits for all elements measured for single KF grains of sample GHO-2.

Element	K	Mg	Si	Ca	Fe	Na	Al
Crystal	Pentaerythritol (PET)	Thallium acid phthalate (TAP)	Thallium acid phthalate (TAP)	Pentaerythritol (PET)	Lithium fluoride (LIF)	Thallium acid phthalate (TAP)	Thallium acid phthalate (TAP)
Standards	orthoclase (12.79% K)	olivine (30.62% Mg)	kyanite (17.3% Si)	$CaSiO_3$ (34.5026% Ca)	Fe (100% Fe)	albite (8.71% Na)	kyanite (17.3% Si)
Average detection limits (ppm)	350	164	289	252	532	234	233

Chapter 7 – Assessing the time of final deposition of Youngest Toba Tuff deposits in the Middle Son Valley, India—a luminescence approach using multiple methods

7.1 Introduction

YTT ash preserved in alluvial sediments near the Rehi-Son River confluence and at the Khunteli Formation type-section (Figs 1-3, 7-1) has been used as a chronostratigraphic marker in geological and palaeoenvironmental investigations (e.g., Acharyya & Basu 1993; Williams *et al.* 2006; Williams *et al.* 2009), but the time of final deposition of the ash, and its temporal relationship with other stratigraphic formations in the Middle Son Valley, is disputed (see discussion in Chapter 1). This issue may be resolved by using luminescence dating techniques that assess the burial age of quartz and feldspar grains in alluvial sediments bracketing the YTT deposits.

This chapter assesses the luminescence dating potential of small (~25 grain) aliquots of KF grains extracted from samples GHO-2, GHO-3, KHUT-1, and KHUT-4 (Table 3-1) using two different IRSL signals: the IRSL signal measured at 50°C, and the post-IR IR signal measured at 225°C after an IRSL stimulation at 50°C, which has been shown to be less prone to anomalous fading (Thomsen *et al.* 2008; Buylaert *et al.* 2009). In this chapter, the IRSL signal measured at 50°C is referred to as the $IRSL_{50}$ signal, and the post-IR IR signal measured at 225°C is referred to as the $pIRIR_{225}$ signal. Experiments were conducted to assess the suitability of these samples to SAR measurement protocols and preliminary $IRSL_{50}$ and $pIRIR_{225}$ aliquot age distributions were determined. The single-grain IRSL age distribution of KF grains from sample GHO-2 (discussed in Chapter 6), and single-grain OSL age distributions of quartz grains from all four samples are used to assess the reliability of IRSL ages obtained from the KF aliquots. The implications of all ages obtained from both quartz and feldspar for the time of final deposition of the YTT ash is discussed in Section 7.8.

7.2 YTT ash deposits and samples

7.2.1 Ghoghara main section

The Ghoghara main section is one of eight geological sections near the Son-Rehi confluence that were examined during the 2009 field season and described and interpreted by Gatti *et al.* (2011) (Table 7-1). GPS coordinates of these sites have been published by Gatti *et al.* (2011) and all but one site (RH2) is thought to contain a primary ash layer overlain by secondary ash deposits that show re-working and/or intermixing with siliclastic silt and sand (Gatti *et al.* 2011) (Table 7-1). The base of all sections exposes fining-upward cross-bedded sand and gravel that have been interpreted to represent point-bar or counter-bar formation by

a laterally migrating channel followed by deposition of near-channel overbank sands (Gatti *et al.* 2011). The overbank sands are overlain by clay that is interpreted to represent a distal, low-energy shallow-water depositional environment on a floodplain (Gatti *et al.* 2011). The YTT ash that overlies the clay is thought to have been preserved within a low-energy niche that was later rapidly buried by sediment, such as an oxbow lake or pond on the floodplain (Gatti *et al.* 2011).

Six sites observed in this study, including the Ghoghara main section, are shown in Figure 7-2. Sedimentological evidence of post-depositional re-working of the ash is present in the form of deformed or gradational horizontal contacts and intermixing with the host silt and sand (Fig. 7-2). The ash itself appears massive in all instances except for the ash-rich silt exposed in the Ghoghara main section, which contains ripples (see discussion below). The lateral extent of the ash units observed in this study could not be determined without further excavation.

The Ghoghara main section is a step trench that exposes ~11 m (vertical thickness) of generally fining upward fluvial gravels, sands and silts, with very clean, white (10YR 8/2) YTT ash appearing between 6 and 7 m below the ground surface (Fig. 7-1b). This ash unit is cohesive and breaks apart in blocks, and ash-rich cohesive silt blocks can still be seen partially buried in colluvium at the foot of the exposure. The lower-most 4 cm of the ash is exceptionally white (10YR 8/1), contains sharp upper and lower contacts, and is thought to potentially be a primary ash fall layer (Gatti *et al.* 2011; Matthews *et al.* 2012). The top of this cliff section is estimated to be within ~5-10 m of the maximum height of the Middle Son Valley alluvium in this reach of the Son River. The step trench was dug in a location where the top-most sands and silts of the valley alluvium have been eroded away. There is no evidence of lower Holocene terrace formation at its base.

Each sedimentary unit within the Ghoghara main section has been assigned a lithofacies code using the code scheme of Miall (2006), and the description and interpretation of all facies is shown in Table 7-2. The fining upward sands and gravels at the base of the sequence (*Sp*) are interpreted to represent dune formation and migration within the river channel under progressively lower energy flow conditions due to lateral migration of the river channel. These sands grade into silty fine-medium sand (*Sm*) and clayey silt (*Fsm*) that likely record overbank deposition followed by low energy deposition of fines in an abandoned channel, pond, or oxbow lake on a floodplain. The ash (*YTT*) and ash-rich silt (*Fma*) are indicative of ash deposition and preservation within the same low-energy waterbody. The overlying alternating layers of fine and medium silty sand (*Sma*) and silt with pedogenic features (*P*) represent deposition of overbank sands and floodplain silts followed by soil development on the floodplain. The facies analysis of the sediments in the Ghoghara main section is consistent with the interpretations of Gatti *et al.* (2011).

Table 7-1. Geological sections examined by Gatti *et al.* (2011). Modified after Gatti *et al.* (2011).

Type	Site	Locality	Coordinates	Previously described	Thickness of the primary ash	Thickness of the secondary ash	Selection criteria
Primary + Secondary ash	RH1	Rehi	24°30'9" N 82°0'56" E	no	5 cm	1.6 cm	Western site
	GG1 (Ghoghara main section)	Ghoghara cliffs (main site)	24°30'9" N 82°1'2" E	Williams and Royce, 1982	5 cm	1.5 cm	Main ash site
	GG1,b	Ghoghara cliffs (gully)	24°30'9" N 82°1'2.99" E	no	2–5 cm	1.05 cm	Sedimentological structures
	GG2	Ghoghara cliffs	24°30'9" N 82°1'8" E	no	0.1 cm (disturbed lenses only)	0.90 cm	
	GG3	Ghoghara cliffs	24°30'9" N 82°1'9" E	no	0.45 cm (disturbed)	1.4 cm	
	GG4	Ghoghara cliffs	24°30'9" N 82°1'11" E	no	0.1–0.4 cm	2.28 cm	Eastern site
	GG5	Ghoghara cliffs	24°30'9" N 82°1'20.6" E	no	disturbed lenses only	~1 cm	
Secondary ash only	RH2	Rehi confluence	24°30'9" N 82°0'55" E	no	n/a	1.3 m	Western secondary only site
	KH Khunteli Formation type-section	Khunteli	24°30'9" N 82°16'33" E	Acharyya and Basu, 1993	n/a	2.2 m	Situated on the right side of the river

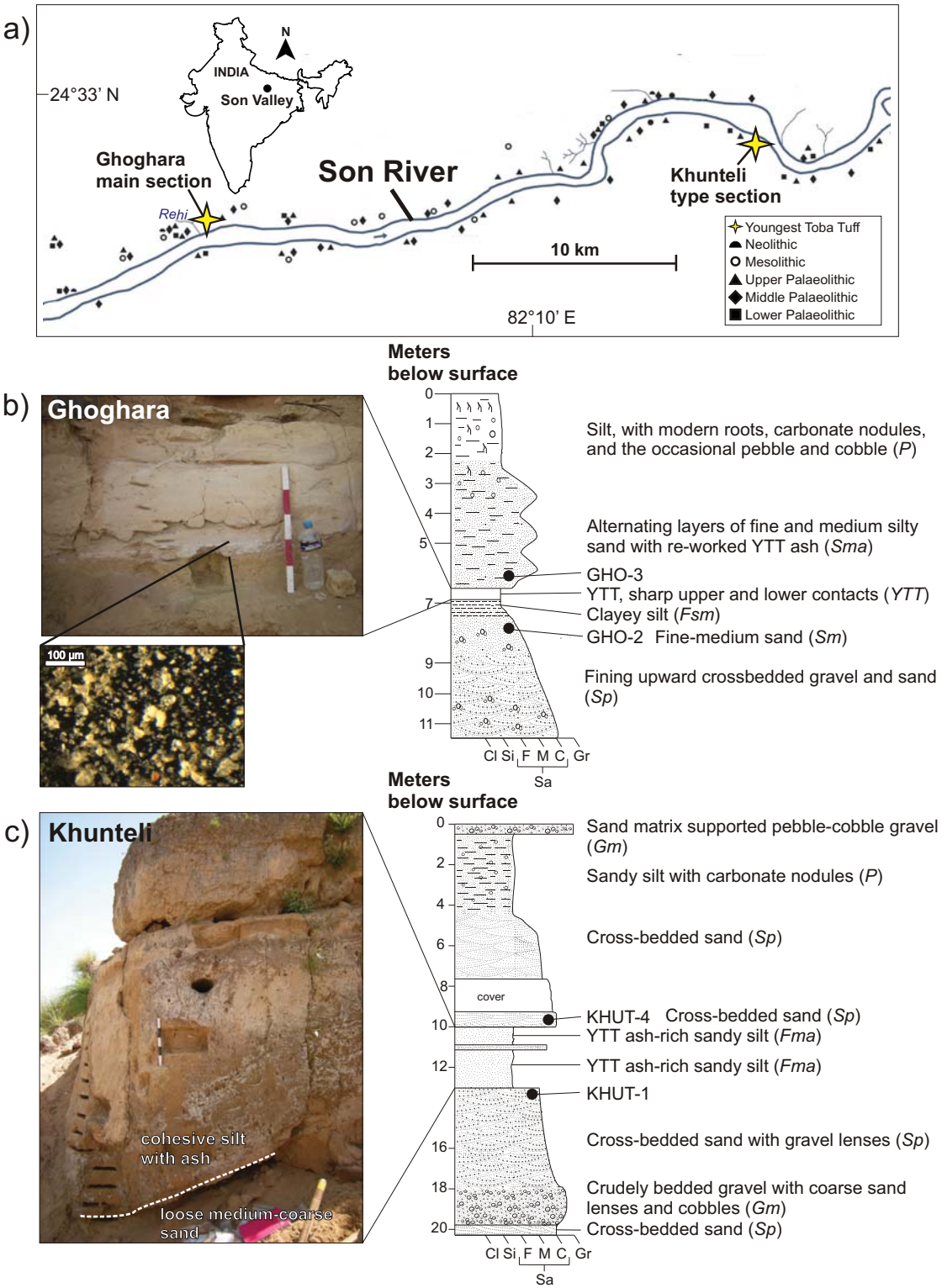

Figure 7-1. a) The study area. The locations of Palaeolithic, Mesolithic and Neolithic artefacts are after Sharma and Clark (1983). Sedimentary logs for sediments containing YTT ash at Ghoghara (b) and Khunteli (c) in the Middle Son Valley, Madhya Pradesh. A 50 cm stick is used for scale in the photos of YTT ash unit in (b). A microphoto of a sample from the whitest (10YR 8/1) part of the YTT ash unit at Ghoghara (b) was taken using a digital camera mounted on a Leica MZ16A stereo microscope.

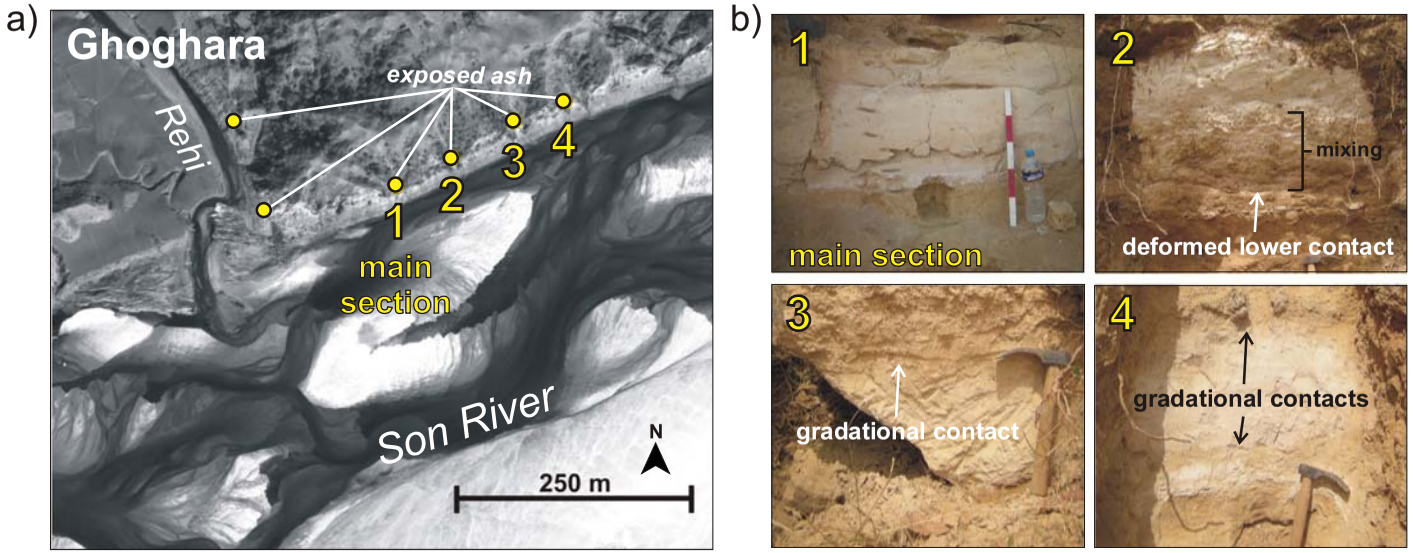

Figure 7-2. a) WorldView-1 50 cm panchromatic imagery of the Rehi-Son confluence showing cliff sections where ash was observed in this study. The sites labelled 1, 2, 3 and 4 in 'a' corrospond to photographs 1, 2, 3 and 4, respectively, in 'b'. The lower ~4 cm of ash at the Ghoghara main section (photograph 1 in 'b') is thought to be primary ash (Gatt *et al.* 2011). The ash unit in photographs 2, 3 and 4 in 'b' show evidence of re-working in the form of a deformed lower contact with evidence of mixing with underlying deposits (2), and diffusive/gradational contacts with the surrounding sediment (3, 4).

Table 7-2. Lithofacies codes, descriptions and interpretations (after Miall 2006).

Lithofacies	Code	Colour	Description	Interpretation	Stratigraphic position	Geological section
Palaeosol	*P*	10 YR 5/4	Silt with modern roots, carbonate nodules and the occasional pebble and cobble	Soil development in overbank fines	Above ash	Khunteli & Ghoghara
Gravel	*Gm*	–	Massive or crudely bedded sand matrix-supported pebble-cobble gravel	Gravel bar or bedform or lag deposit	Above and below ash (Khunteli)/ Below ash (Ghoghara)	Khunteli
Silty sand with re-worked ash	*Sma*	10 YR 7/4	Alternating layers of fine and medium silty sand with re-worked ash and the occasional carbonate rhizolith	Overbank or floodplain fines	Above ash	Ghoghara
Ash-rich silt (secondary ash)	*Fma*	10 YR 8/2	Ash-rich silt that is either massive or exhibits fine cross-lamination and ripples	Abandoned channel/ pond/oxbow lake sediments on a floodplain	Ash	Khunteli
Ash (primary ash?)	*YTT*	10 YR 8/1	Massive with sharp undulating upper contact and sharp planar lower contact	Abandoned channel/ pond/oxbow lake sediments on a floodplain	Ash	Ghoghara
Clayey silt	*Fsm*	10 YR 7/6	Massive yellow clayey silt with gradational lower contact	Abandoned channel/ pond/oxbow lake sediments on a floodplain	Below ash	Ghoghara
Fine-medium sand	*Sm*	10 YR 7/4	Fine-medium silty sand with cross-laminae	Overbank or floodplain fines	Below ash	Ghoghara
Cross-bedded coarse sand and gravel	*Sp*	10 YR 4/4	Micaceous coarse sand with cross-beds and gravel lenses	Sand bars or dunes in a channel	Below ash	Khunteli & Ghoghara

Luminescence samples GHO-2 and GHO-3 were collected from alluvial sediments below and above the YTT unit, respectively (Fig. 7-1b).

7.2.2 Khunteli Formation type-section

A step trench was excavated at the Khunteli Formation type-section that exposes ~20 m (vertical thickness) of fluvial sands, gravels, silts (Fig. 7-1c). This cliff section extends to the maximum height of the Middle Son Valley alluvium in this reach of the Son River, and there is no evidence of lower Holocene terrace formation at its base. This section was also examined by Gatti *et al.* (2011) (Table 7-1). The base of the trench exposes crudely bedded gravel (*Gm*) and cross-bedded sands and gravel (*Sp*) that likely record bar and bedform deposition within a channel. These sediments are overlain by ash-rich sandy silt (*Fma*) that were likely deposited under low-energy or waning flood conditions in a distal environment on the floodplain (Fig. 7-1c). The YTT ash-rich silt is laterally discontinuous and may have been deposited within a hollow or abandoned channel. No other ash exposures have been found within 100 m either side of this section, or within the cliff exposures on the north side of the Son River directly opposite Khunteli. The ash-rich silt is overlain by cross-bedded sands (*Sp*) that likely record overbank deposition in an environment slightly more proximal to the channel. This sand grades into sandy silt with pedogenic features (*P*) indicative of the deposition of floodplain fines in a distal environement, followed by soil formation. A sand-matrix supported pebble-cobble gravel unit (*Gm*), not previously described by Gatti *et al.* (2011), caps the sedimentary sequence and this may be the remnants of a former high-energy river channel deposit that records accelerated flow just prior to incision of the Middle Son Valley alluvium (Fig. 7-1c). Samples for luminescence dating (KHUT-1 and KHUT-4) were collected from below and above the ash-rich silt unit (Fig. 7-1c). Refer to Chapter 3 for details on sample collection and preparation procedures and equipment.

7.3 $IRSL_{50}$ and $pIRIR_{225}$ signal characteristics of small KF aliquots

7.3.1 The $IRSL_{50}$ and $pIRIR_{225}$ signals

The D_e values from KF grains from all samples in this chapter were estimated using both the $IRSL_{50}$ and the $pIRIR_{225}$ signals, using single aliquots and SAR measurement protocols similar to Buylaert *et al.* (2009) (Table 7-3). The temperature and duration of preheats preceding the L_n and L_x measurements were identical to those preceding the T_n and T_x measurements, following Blair *et al.* (2005). At the end of each SAR cycle, the sample was bleached for 40 seconds at 290°C to reduce the extent of recuperation (e.g., Wallinga *et al.* 2007; Buylaert *et al.* 2009) (Table 7-3).

Table 7-3. SAR measurement protocols for KF aliquots measured using the $IRSL_{50}$ and $pIRIR_{225}$ signals.

	$IRSL_{50}$		$pIRIR_{225}$
1.	Natural / Regenerative Dose[1]	1.	Natural / Regenerative Dose[1]
2.	Preheat (250°C, 10 s)	2.	Preheat (250°C, 10 s)
3.	IRSL (50°C, 100 s) → L_n, L_x	3.	IRSL (50°C, 100 s)
4.	Test dose (11 Gy)	4.	IRSL (225°C, 100 s) → L_n, L_x
5.	Preheat (250°C, 10 s)	5.	Test dose (11 Gy)
6.	IRSL (50°C, 100 s)….→ T_n, T_x	6.	Preheat (250°C, 10 s)
7.	IRSL bleach (290°C, 40 s)	7.	IRSL (50°C, 100 s)
8.	Return to step 1.	8.	IRSL (225°C, 100 s) → T_n, T_x
		9.	IRSL bleach (290°C, 40 s)
		10.	Return to step 1.

[1]Ln = natural signal, Lx = regenerative dose signal. For D_e estimations regenerative doses of 46, 68, 91, 114, 0 and 68 Gy were used for the $IRSL_{50}$ signal and regenerative doses of 46, 68, 91, 137, 0 and 68 Gy were used for the $pIRIR_{225}$ signal.

$pIRIR_{225}$ signals are significantly brighter than their preceding $IRSL_{50}$ signals in these samples, but the rate of decay of both signals is similar (Fig. 7-3a), which is consistent with previous results reported in the literature (Thomsen *et al.* 2008; Sohbati *et al.* 2012). The signal induced by 1 s of IR stimulation minus the mean background count rate over the last 20 s of stimulation was used in all D_e and fading rate calculations.

7.3.2 Preheat plateau tests

To determine whether or not the SAR protocol is appropriate for D_e determination, tests have been integrated into the SAR procedure to check for negligible recuperation (the "zero-dose point") and proper correction for sensitivity change (the "recycling ratio") (Galbraith *et al.* 1999; Murray & Wintle 2000; Wallinga *et al.* 2000) (Table 7-3). Preheat plateau tests also provide insight into the influence that preheat conditions have on sensitivity correction, recuperation rates and D_e values (Roberts *et al.* 1998; Roberts *et al.* 1999; Wallinga *et al.* 2000). Here, preheat plateau tests were conducted using both the $IRSL_{50}$ and $pIRIR_{225}$ signals on natural aliquots from sample GHO-3 using a series of 10 s preheats ranging from 180°C to 300°C (Fig. 7-4). The $IRSL_{50}$ signal shows a D_e plateau between 180°C and 220°C, then a step up to another plateau between 240°C and 280°C (Fig. 7-4a). This slight increase may be the result of thermal transfer of charge from optically insensitive traps to optically sensitive traps (Huntley & Clague 1996). The $pIRIR_{225}$ signal shows no significant change in D_e with preheat temperature (Fig. 7-4a).

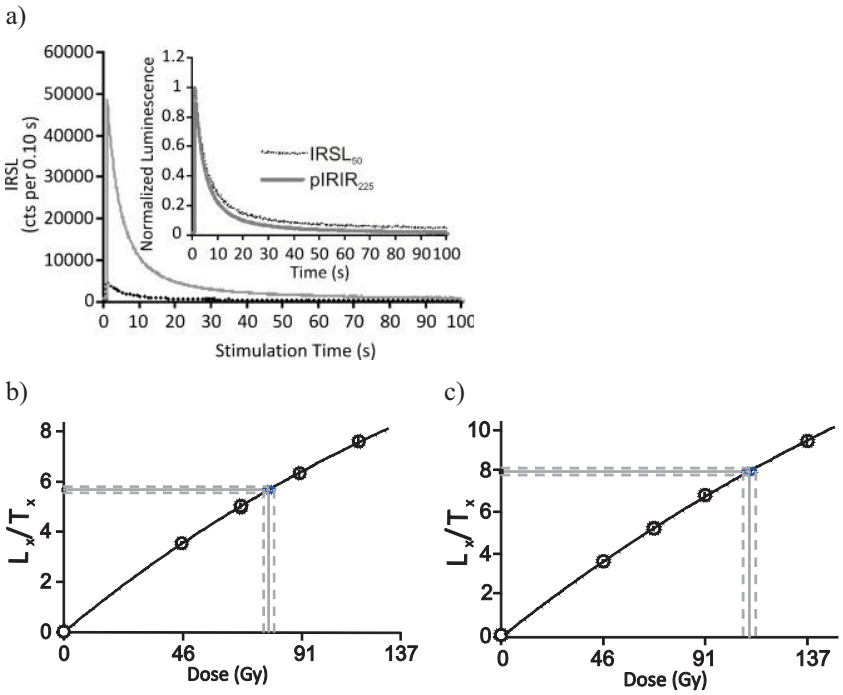

Figure 7-3. a) $IRSL_{50}$ and $pIRIR_{225}$ decay curves. The $pIRIR_{225}$ signal was measured immediately after the $IRSL_{50}$ signal on the same aliquot after it was given a laboratory dose of 28 Gy followed by a preheat of 250 °C for 10 s. Normalized decay curves are shown in the inset graph. b) $IRSL_{50}$ dose response curve. c) $pIRIR_{225}$ dose response curve. Dose response curves in 'b' and 'c' are measured on different aliquots. The solid grey lines in 'b' and 'c' illustrate where L_n/T_n was projected onto the sensitivity-corrected dose-response curve to determine D_e. The dashed grey lines on either side of the solid grey line mark the errors of L_n/T_n and D_e at 1σ.

When using a post-IR IRSL signal, it is considered prudent to use preheat temperatures that are higher than the stimulation temperature (which is, in this case, 225°C) to prevent an unwanted isothermal TL contribution to the signal (Murray *et al.* 2009). It is interesting, therefore to note that the $pIRIR_{225}$ D_e values measured using preheat temperatures of 180, 200 and 220°C do not appear to be significantly higher than those measured at 240, 260 and 280°C and this suggests that any isothermal TL contribution to the signals measured using the lower preheats constitutes a negligible proportion of the natural signals in these samples. For all preheat temperatures, the $pIRIR_{225}$ D_e is ~1 to ~3 times that of the $IRSL_{50}$ D_e value. This may reflect the increased thermal stability and lower fading rate of the $pIRIR_{225}$ signal (Thomsen *et al.* 2011) and/or a decrease in bleachability of the $pIRIR_{225}$ in nature (e.g., Buylaert *et al.* 2011). The bleachability of both signals is investigated further in Section 7.3.5.

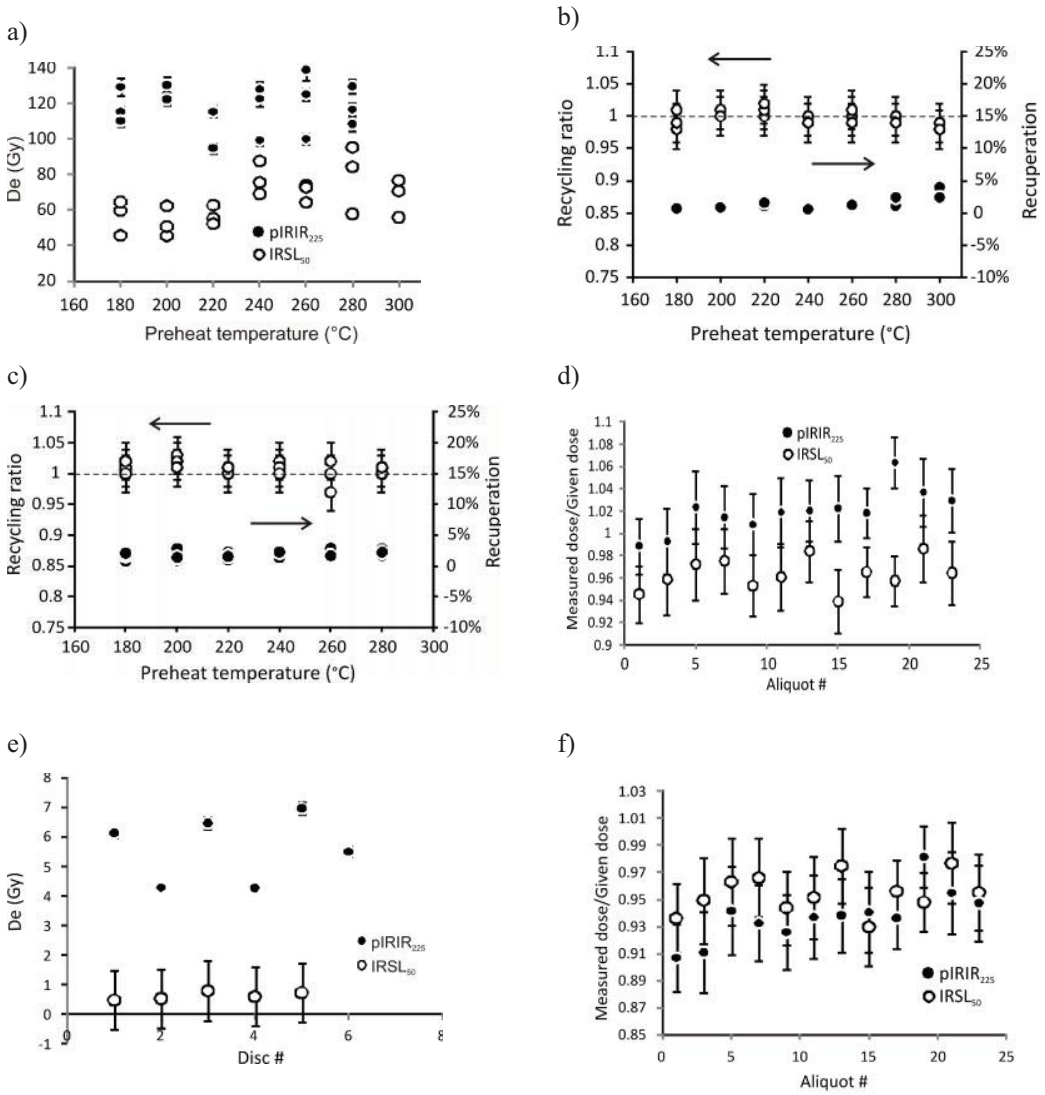

Figure 7-4. a) D_e versus preheat temperature for the $IRSL_{50}$ and $pIRIR_{225}$ signals. Recycling ratios and recuperation values for the $IRSL_{50}$ (b) and $pIRIR_{225}$ (c) signals. d) Measured dose/given dose ratios for both signals. e) Residual doses measured from KF grains that have been sun-bleached for 2 days. A 250°C/10 s preheat was used. f) Measured dose/given dose ratios obtained when the residuals of each signal (calculated as the average of all aliquots in 'e') are subtracted from the measured dose (errors have been propagated into the final measured dose/given dose estimates). Each symbol represents one aliquot, and error bars represent one standard error on all plots. All measurements were made on sample GHO-3.

The recuperation of both the $IRSL_{50}$ and $pIRIR_{225}$ signals remains below 5% for all preheats (Figs 7-4b and c) and this probably reflects the effectiveness of the 40 s, 290°C hotwash. Recuperation values of 5% are generally thought to have a negligible effect on D_e estimates for older (e.g., >50 Gy) samples (Wallinga *et al.* 2000; Buylaert *et al.* 2008; Davids *et al.* 2010). Recycling ratios average 1.00 ± 0.03 and 1.01 ± 0.03 for the $IRSL_{50}$ and $pIRIR_{225}$ signals, respectively (Figs 7-4b and c). These suggest that, for all preheat temperatures, sensitivity changes between regenerative dose cycles are adequately corrected for. For all subsequent D_e measurements in this study, a preheat of 250°C for 10 s preheat was used.

7.3.3 Dose recovery tests

Dose recovery tests (the recovery of a laboratory dose after bleaching by artificial light or natural sunlight; Roberts *et al.* 1999) can be used to check if KF grains from these samples are suitable for the SAR protocol (Wallinga *et al.* 2000). Dose recovery tests using the $IRSL_{50}$ and $pIRIR_{225}$ signals were conducted on natural aliquots from sample GHO-3 that had been bleached in the sun for 2 days. A laboratory dose of 68 Gy was administered to the aliquots and measured using a SAR protocol. This dose is within the range of natural doses measured during the preheat plateau tests on GHO-3 using the $IRSL_{50}$ signal at preheats greater than 240°C (Fig. 7-4a). Weighted mean ratios of measured dose to given dose of 0.96 ± 0.01 (n=12) and 1.02 ± 0.01 (n=12) were obtained for the $IRSL_{50}$ and $pIRIR_{225}$ signals, respectively (Fig. 7-4d). The calculated OD values for both dose recovery tests are zero. The $IRSL_{50}$ weighted mean measured-dose to given-dose ratio slightly underestimates unity, while that of the $pIRIR_{225}$ signal is consistent with unity. Average residual doses of 0.635 ± 0.003 Gy ($IRSL_{50}$ signal) and 5.61 ± 0.03 Gy ($pIRIR_{225}$ signal) were measured from aliquots that had been sun-bleached for 2 days (Fig. 7-4e). When these residual doses are subtracted from the measured doses in the dose recovery tests, weighted mean measured-dose to given-dose ratios of 0.95 ± 0.01 (n=12) and 0.94 ± 0.03 (n=12) are obtained for the $IRSL_{50}$ and $pIRIR_{225}$ signals, respectively (Fig. 7-4f). Both ratios are within 10% of unity, therefore these samples are considered to be suitable for the SAR procedure.

7.3.4 Fading rates

It is well known that the $IRSL_{50}$ signal in KF grains fades over time, and this is attributed to the loss of electrons from traps that should be thermally stable at ambient temperatures over geological time to other defects and centers in the feldspar crystal lattice (Wintle 1973; Spooner 1994). Recent research has shown that the $pIRIR_{225}$ signal exhibits lower fading rates than the $IRSL_{50}$ signal (Thomsen *et al.* 2008; Buylaert *et al.* 2009; Reimann *et al.* 2011). Fading tests were conducted on all aliquots used for D_e

measurements, using a SAR measurement protocol based on Auclair *et al.* (2003) (Table 7-4). The fading rate was quantified using the *g*-value normalized to 2 days (Huntley & Lamothe 2001), and the calculated age of each aliquot was corrected using its own fading rate. Average $IRSL_{50}$ and $pIRIR_{225}$ *g*-values for each sample are listed in Table 7-5, and representative fading plots and *g*-value distributions for both signals are shown in Fig. 7-5 for GHO-3. Average $IRSL_{50}$ *g*-values range from 3.1 to 3.5 %/decade, and those of the $pIRIR_{225}$ signal range from 1.0 to 1.7 %/decade. These average fading rates for these two signals are comparable to those reported in the literature (Huntley & Lamothe 2001; Wallinga *et al.* 2007; Thomsen *et al.* 2008; Buylaert *et al.* 2009; Sohbati *et al.* 2012).

Table 7-4. Anomalous fading SAR measurement protocol.[1]

1.	Dose (28 Gy)
2.	Preheat (250°C, 10 s)
3.	IRSL (50°C, 100 s) $\rightarrow L_x$ (prompt)
4.	Test dose (10 Gy)
5.	Preheat (250°C, 10 s)
6.	IRSL (50°C, 100 s) $\rightarrow T_x$ (prompt)
7.	IRSL bleach (290°C, 40 s)
8.	Dose (28 Gy)
9.	Preheat (250°C, 10 s)
10.	**Delay**
11.	IRSL (50°C, 100 s) $\rightarrow L_x$
12.	Test dose (10 Gy)
13.	Preheat (250°C, 10 s)
14.	IRSL (50°C, 100 s) $\rightarrow T_x$
15.	IRSL bleach (290°C, 40 s)
16.	Return to step 10 for the remaining delay times.

[1]The $pIRIR_{225}$ fading protocol includes IRSL stimulation of the sample for 100 s at 225°C after steps 3, 6, 11 and 14.

Table 7-5. $IRSL_{50}$ and $pIRIR_{225}$ D_e values, average recycling ratios, recuperation rates, fading rates and ages, together with quartz OSL FMM component ages for the same samples.

Sample	Relation to YTT	Total dose rate (Gy/ka)	n[1]	Average recycling ratio	Average recup. (%)	*g*-value[2] (%/ decade)	Uncorrected D_e[3](Gy) (MAM)	Fading-corrected D_e[3] (Gy) (MAM)	Fading-corrected age (ka) (MAM)[4]	Quartz ages[6] n	OD[5] (%)	% grains	FMM component age (ka)
$IRSL_{50}$ signal													
GHO-3	above ash	3.07 ± 0.09	24	1.00 ± 0.03	1 ± 3	3.1 ± 0.1	66.6 ± 2.6 (OD=11 ± 2%)	96.0 ± 5.6 (OD=11 ± 2%)	**a) 31.2 ± 2.0** *b) 35.0 ± 2.3*	286	35 ± 2	8 ± 2 54 ± 7 38 ± 7	22 ± 2 44 ± 3 68 ± 5
GHO-2	below ash	2.42 ± 0.08	24	1.01 ± 0.03	1 ± 3	3.1 ± 0.1	43.7 ± 2.8 (OD=15 ± 2%)	51.5 ± 3.6 (OD=20 ± 4%)	**a) 21.3 ± 1.6** *b) 23.5 ± 1.8*	337	45 ± 2	3 ± 1 57 ± 5 40 ± 5	12 ± 2 36 ± 3 70 ± 5
KHUT-4	above ash	1.82 ± 0.06	24	1.00 ± 0.03	2 ± 3	3.5 ± 0.1	35.4 ± 1.3 (OD=22 ± 3%)	51.9 ± 4.3 (OD=22 ± 3%)	**a) 28.5 ± 2.5** *b) 30.7 ± 2.7*	129	38 ± 3	15 ± 6 75 ± 6 10 ± 5	22 ± 3 43 ± 3 88 ± 15
KHUT-1	below ash	3.04 ± 0.09	24	1.01 ± 0.03	1 ± 3	3.2 ± 0.1	62.1 ± 3.3 (OD=16 ± 2%)	94.1 ± 5.3 (OD=15 ± 2%)	**a) 30.9 ± 2.0** *b) 34.7 ± 2.7*	218	37 ± 2	8 ± 4 52 ± 9 40 ± 10	20 ± 3 39 ± 3 62 ± 5
KHUT-10	modern sand bar		24					-0.3 ± 0.8 (OD=92 ± 13%)		46	2.5 ± 0.6		**Weighted mean D_e** -0.02 ± 0.12
$pIRIR_{225}$ signal													
GHO-3	above ash	3.07 ± 0.09	24	1.00 ± 0.03	2 ± 3	1.0 ± 0.1	111.4 ± 5.6 (OD=17 ± 3%)	143.3 ± 4.5 (OD=17 ± 3%)	**a) 46.6 ± 2.0** *b) 52.3 ± 2.2*	286	35 ± 2	8 ± 2 54 ± 7 38 ± 7	22 ± 2 44 ± 3 68 ± 5
GHO-2	below ash	2.42 ± 0.08	24	1.00 ± 0.03	2 ± 3	1.7 ± 0.1	110.4 ± 2.3 (OD=11 ± 2%)	112.9 ± 4.8 (OD=11 ± 2%)	**a) 46.6 ± 2.5** *b) 51.4 ± 2.7*	337	45 ± 2	3 ± 1 57 ± 5 40 ± 5	12 ± 2 36 ± 3 70 ± 5
KHUT-4	above ash	1.82 ± 0.06	24	1.01 ± 0.03	2 ± 3	1.7 ± 0.1	60.0 ± 1.9 (OD=24 ± 3%)	75.5 ± 3.8 (OD=24 ± 4%)	**a) 41.5 ± 2.5** *b) 44.7 ± 2.7*	129	38 ± 3	15 ± 6 75 ± 6 10 ± 5	22 ± 3 43 ± 3 88 ± 15
KHUT-1	below ash	3.04 ± 0.09	24	1.00 ± 0.03	2 ± 3	1.2 ± 0.1	127.0 ± 4.9 (OD=9 ± 2%)	158.9 ± 3.7 (OD=9 ± 2%)	**a) 52.2 ± 1.9** *b) 58.5 ± 2.2*	218	37 ± 2	8 ± 4 52 ± 9 40 ± 10	20 ± 3 39 ± 3 62 ± 5
KHUT-10	modern sand bar		24					-0.2 ± 0.2 (OD=64 ± 9%)		46	2.5 ± 0.6		**Weighted mean D_e** -0.02 ± 0.12

[1]Number of aliquots. [2]*g*-value is normalised to 2 days following Huntley and Lamothe (2001). [3]A possible systematic error of 2% for beta source calibration has been added in quadrature to the D_e standard error, and a residual dose of 0.635 ± 0.003 Gy and 5.61 ± 0.03 Gy was subtracted from the $IRSL_{50}$ and $pIRIR_{225}$ D_e values, respectively. [4]Values were calculated using the MAM. Ages are calculated assuming: a) a 5 ± 2% water content, and b) a 22 ± 7% (saturated) water content. The preferred ages (a) are highlighted in bold. [5]OD refers to overdispersion. [6]Single-grain ages obtained using methods outlined in Haslam *et al.* (2011) using external dose rates calculated from beta counting and in situ gamma spectrometry and an assumed water content of 5 ± 2%. 'n' refers to the number of quartz grains. Age components have been derived using the FMM for all samples except KHUT-10.

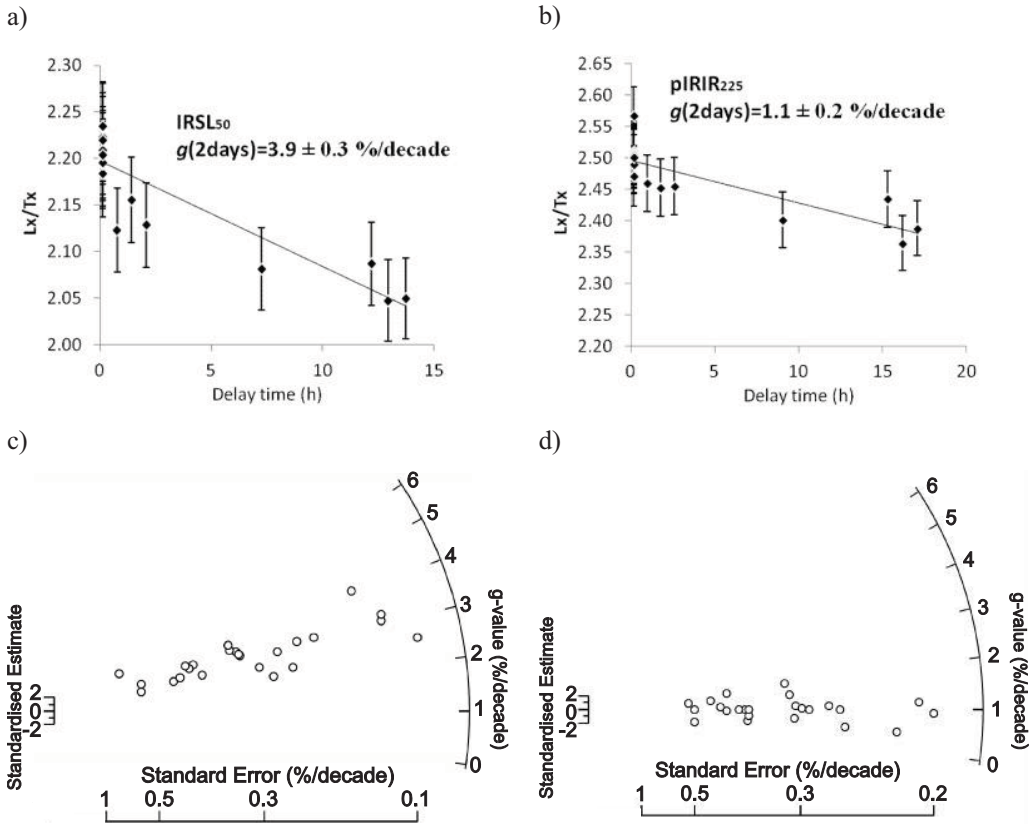

Figure 7-5. Representative $IRSL_{50}$ (a) and $pIRIR_{225}$ (b) fading plots for aliquots of sample GHO-3, and $IRSL_{50}$ (c) and $pIRIR_{225}$ (d) *g*-value distributions for sample GHO-3.

7.3.5 Signal resetting

In fluvial deposits, it is important to assess whether or not the source traps in all grains have been sufficiently emptied by sunlight exposure before burial (homogeneous bleaching). One way of assessing this is to measure the residual dose of a modern sample. The Son River consists of a shallow, wandering sand bed channel that is confined by ~10 m-high terraces. D_e measurements on single grains of quartz and small (~25 grain) aliquots of quartz and KF were made on a sample (KHUT-10) collected ~20 cm below the surface of a modern sand bar in the channel, ~50 m away from the cleaned section at Khunteli. Sediment within this sand bar has been transported by the river and is considered to be at a sufficient distance from the river banks so as not to include older, partially bleached grains from slumped river bank material. The quartz D_e values were determined using the SAR measurement protocol described by Haslam *et al.* (2012) (Fig. 7-5). After excluding an outlying D_e value of 38 Gy, the quartz single-aliquot weighted mean D_e was calculated to be 0.2 ± 0.1 Gy, and the single-grain weighted mean D_e was calculated to be -0.02 ± 0.14 Gy,

suggesting that the source traps for the OSL signal in most quartz grains have been sufficiently emptied by sunlight before burial.

Residual doses were also measured for KF aliquots from KHUT-10 using the $IRSL_{50}$ and $pIRIR_{225}$ signals. The weighted mean D_e values (calculated using the Central Age Model (CAM) of Galbraith *et al.* (1999)) are 1.3 ± 0.2 Gy (n=24) and 17.0 ± 2.0 Gy (n=24) for the $IRSL_{50}$ and $pIRIR_{225}$ signals, respectively, and the D_e distributions are shown in Figures 7-6c and d. A weighted mean D_e of 1.7 ± 0.2 Gy was also measured from 366 single KF grains from sample KHUT-10 using the $IRSL_{50}$ signal (Chapter 6). The average $IRSL_{50}$ and $pIRIR_{225}$ residual doses measured from KF grains that were sun-bleached for 2 days are 0.635 ± 0.003 Gy and 5.61 ± 0.03 Gy, respectively, and aliquot-to-aliquot variability is generally small (i.e., within 1 Gy for the $IRSL_{50}$ signal and within 3 Gy for the $pIRIR_{225}$ signal), suggesting that most grains were well-bleached by this known duration of solar exposure (Fig. 7-4e). The aliquot-to-aliquot variability in the $IRSL_{50}$ and $pIRIR_{225}$ residual

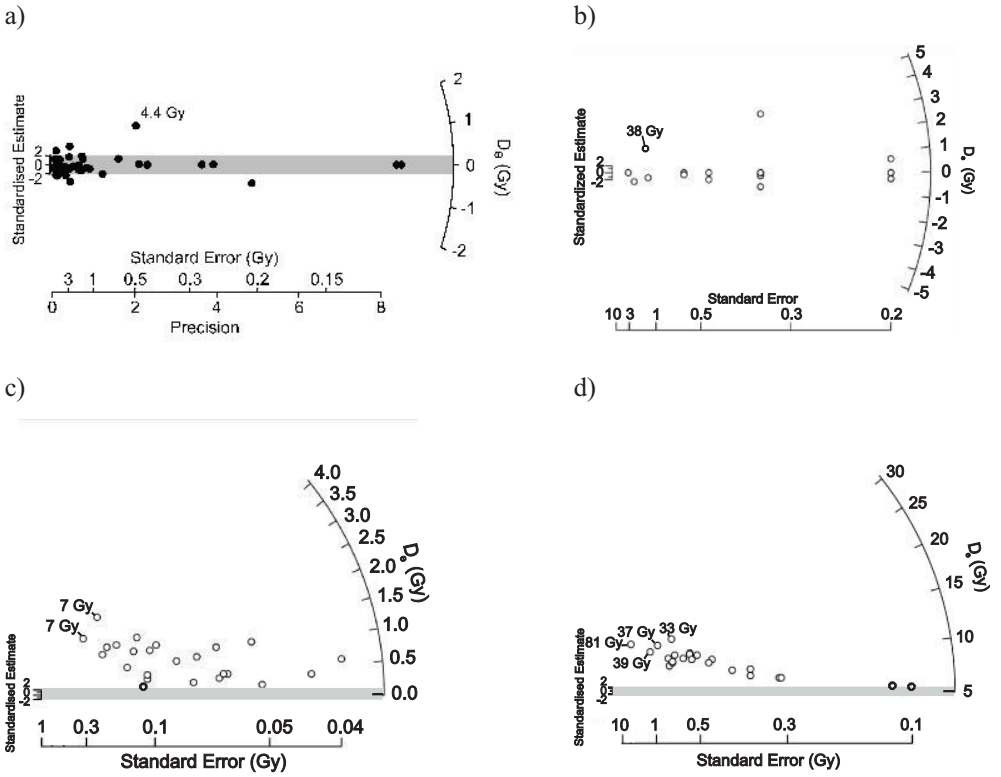

Figure 7-6. Single-grain (a) and multi-grain aliquot (b) quartz D_e distributions for the modern sample (KHUT-10). Multi-grain aliquot D_e distributions for KF grains from the same sample measured using the $IRSL_{50}$ (c) and the $pIRIR_{225}$ (d) signals. The grey shaded area should capture 95% of the points if they were statistically consistent with 0 Gy in 'c' and 5 Gy in 'd' (Galbraith *et al.* 1999).

doses in the modern sample is much larger (~7 Gy difference between the largest and smallest residual doses for the $IRSL_{50}$ signal, and ~75 Gy difference for the $pIRIR_{225}$ signal, Figs 7-5c and d), suggesting that not all grains have been fully bleached before burial. The Minimum Age Model (MAM) of Galbraith *et al.* (1999) was originally designed to estimate the D_e of well-bleached grains in D_e distributions of samples that were not completely bleached before burial. The MAM was used to estimate the $IRSL_{50}$ and $pIRIR_{225}$ D_e values of the most recently bleached KF grains in the modern sample. An OD value of 5% was added in quadrature to the D_e measurement errors before fitting the data with the model; this is considered an appropriate estimate of the maximum OD expected from a KF aliquot age distribution obtained from well-bleached grains, as the dose recovery tests yielded OD values of zero (Section 7.3.3). The MAM $IRSL_{50}$ and $pIRIR_{225}$ D_e values are 0.3 ± 0.8 Gy ($IRSL_{50}$) and 5.4 ± 0.2 Gy ($pIRIR_{225}$), which are similar to the results of the sun-bleached sample. This suggests that the MAM D_e values represent well-bleached grains in the modern sample and that the larger D_e values represent incompletely bleached grains. The difference between the maximum $IRSL_{50}$ and $pIRIR_{225}$ residual doses from the modern sample (i.e., the residual doses obtained from the least-well bleached grains) is ~74 Gy and is much larger than the difference between the $IRSL_{50}$ and $pIRIR_{225}$ residual doses from the grains that were bleached in the sun for 2 days (~5 Gy). These results suggest that the source traps of the $pIRIR_{225}$ signal in KF grains in the Son River are much less likely to be emptied by sunlight exposure than those of the $IRSL_{50}$ signal.

7.4 $IRSL_{50}$ and $pIRIR_{225}$ KF aliquot age distributions

$IRSL_{50}$ and $pIRIR_{225}$ D_e values have been determined for samples GHO-2, GHO-3, KHUT-1 and KHUT-4 (24 aliquots each) and these have been corrected for anomalous fading using the correction model of Huntley and Lamothe (2001) (Table 7-4). Fading-corrected aliquot $IRSL_{50}$ and $pIRIR_{225}$ age distributions for all samples are shown in Figure 7-7. In the next few sections, the KF aliquot $IRSL_{50}$ and $pIRIR_{225}$ data are described and the accuracy of ages calculated from them are assessed using single-grain data from the same samples (Fig. 7-8).

7.4.1 Recycling ratios, OD, and aliquot ages

All $IRSL_{50}$ and $pIRIR_{225}$ recycling ratios are statistically consistent with unity, suggesting that sensitivity changes between consecutive regenerative SAR cycles have been corrected for, and recuperation values are 2% or less (Table 7-5). $IRSL_{50}$ OD values range from ~11% to ~22%, and $pIRIR_{225}$ OD values range from ~9% to ~24%. The OD values of most samples changed little after fading correction, except for sample GHO-2. After fading correction, the OD of this sample increased by ~5%, which may be due to the relatively low

precisions in the fading measurements for this sample as a result of the Crystalbond adhesive used to adhere grains to discs (Chapter 3). Aliquot fading-corrected ages determined using the $pIRIR_{225}$ signal are generally higher than those determined using the $IRSL_{50}$ signal, which may be due to inadequate bleaching of source traps for the $pIRIR_{225}$ signal, as suggested by measurements of a modern sample (Section 7.3.5).

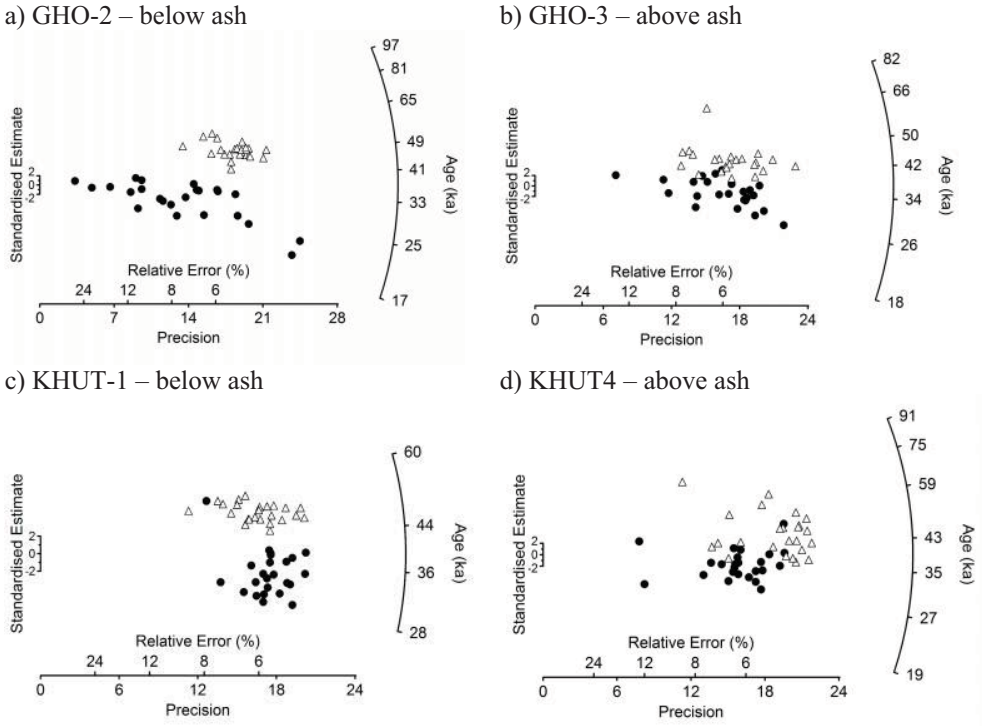

Figure 7-7. Radial plots of fading-corrected age distributions for samples GHO-2 (a), GHO-3 (b), KHUT-1 (c), and KHUT-4 (d). Solid circles are aliquots measured using the $IRSL_{50}$ signal and open triangles are aliquots measured using the $pIRIR_{225}$ signal. Residual doses of 0.635 ± 0.003 Gy and 5.61 ± 0.03 Gy have been subtracted from the $IRSL_{50}$ and $pIRIR_{225}$ data, respectively, and the errors on the residual doses have been propagated through into the error on the aliquot ages.

Neither signal produced a significant number of aliquot fading-corrected ages of ~74 ka (the time of the Toba event) or older (Fig. 7-7). This may be due, in part, to grain-averaging effects. Because of grain-averaging effects, the spread in multi-grain aliquot age distributions may not be truly representative of the grain-to-grain spread in ages in the sample. Also, individual grains that are unsuitable for SAR, and contaminating older or younger grains from other sedimentary units, or grains that have not been completely bleached before burial, cannot be clearly identified in aliquot age distributions. The signal

a) GHO-2, quartz grains OD = 45 ± 2%

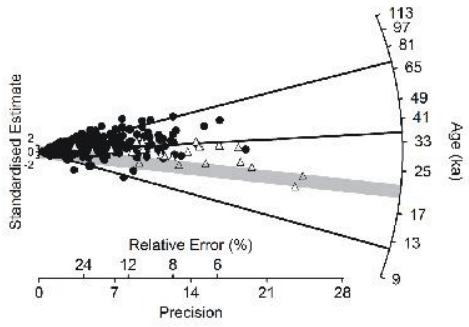

b) GHO-3, quartz grains OD = 35 ± 2%

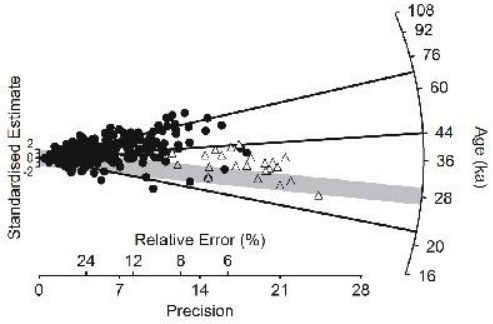

c) KHUT-1, quartz grains OD = 37 ± 2%

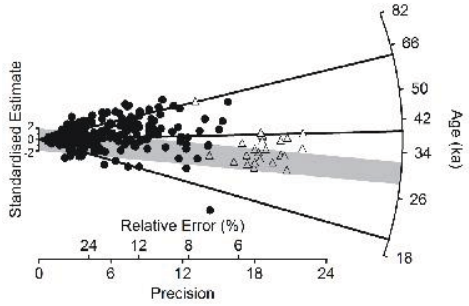

d) KHUT-4, quartz grains OD = 38 ± 3%

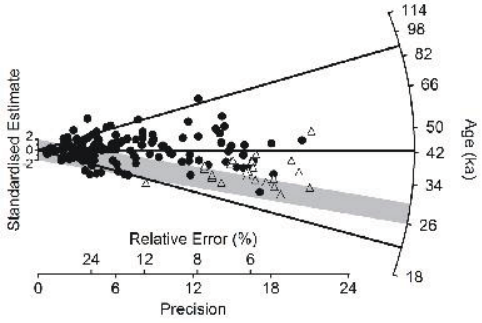

e) GHO-2, KF grains, OD = 37.3 ± 1.5%

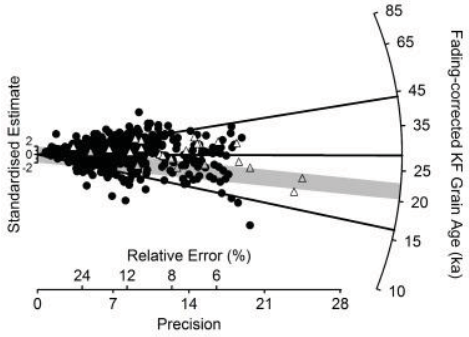

f)

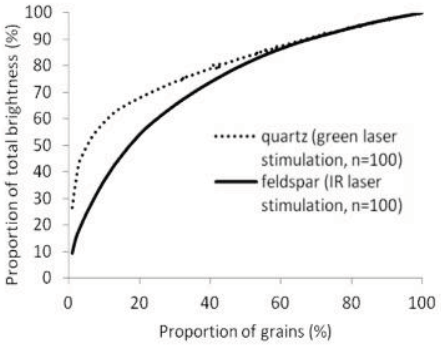
Proportion of total brightness (%)
Proportion of grains (%)
quartz (green laser stimulation, n=100)
feldspar (IR laser stimulation, n=100)

Figure 7-8. Radial plots of single-grain quartz age distributions for samples GHO-2 (a), GHO-3 (b), KHUT-1 (c), and KHUT-4 (d). The $IRSL_{50}$ KF aliquot fading-corrected ages (open triangles) are superimposed on the quartz single-grain age distributions. e) Single-grain $IRSL_{50}$ fading-corrected ages (black dots) and $IRSL_{50}$ fading-corrected aliquot ages (open triangles) from sample GHO-2. A residual dose of 0.635 ± 0.003 Gy has been subtracted from the $IRSL_{50}$ data and the errors on the residual doses have been propagated through into the error on the KF ages. Black solid lines are centred on the component ages identified by the Finite Mixture Model (FMM) of Roberts *et al.* (2000) for the quartz and KF single-grain data. The grey shaded band is centered on the age calculated for the KF aliquot data using the MAM (Table 7-4). f) The proportion of total brightness versus the proportion of quartz and KF measured grains from sample KHUT-1.

measured from aliquots represents a cumulative signal from multiple grains. Single-grain measurements of sample KHUT-1 show that averaging effects are even more pronounced in feldspar than for quartz (Fig. 7-8f). In sample KHUT-1, 20% of quartz grains will contribute 65–70% of the total OSL signal from an aliquot, and 30–40% of grains will contribute a similar proportion of the total IRSL signal (Fig. 7-8f). In the next few sections, the accuracy of ages calculated from $IRSL_{50}$ and $pIRIR_{225}$ KF aliquots is assessed using single-grain OSL and IRSL data from the same samples. But first, single-grain age distributions for both quartz and KF are described and interpreted in Sections 7.5.1 and 7.5.2.

7.5 Single-grain age distributions of quartz and KF and evidence for sediment mixing

7.5.1 Quartz

Single-grain quartz ages for all samples are included in Table 7-5 and their associated age distributions are shown in Figures 7-8a–d. The quartz single-grain OSL ages were obtained using the procedures of Haslam *et al.* (2011). In this chapter, the quartz data is shown as age distributions instead of D_e distributions, which are typically reported for quartz, so that they can be directly compared to KF aliquot fading-corrected age distributions. The quartz age distributions for samples GHO-2, GHO-2, KHUT-1 and KHUT-4 range from less than 20 ka to over 100 ka, and the OD values ranging from 35 to 45% (Table 7-5, Fig. 7-8). Quartz single-grain datasets for samples known or thought to have been fully bleached at burial and not affected by post-depositional disturbance (or by differences in beta dose rate among grains buried at the same time) commonly have OD values of up to 20% (Arnold & Roberts 2009). The relatively high OD values for the samples in this study may be the result of: 1) differences in beta dose received by individual grains in their burial environment due to proximity to pore water, calcium carbonate nodules or organic matter (e.g., Lian *et al.* 1995; Murray & Roberts 1997; Lian & Huntley 1999); 2) insufficient or heterogeneous exposure of some grains to sunlight before burial (e.g., Olley *et al.* 1999); and/or 3) post-depositional intrusion of younger grains into older deposits or vice versa (e.g., Jacobs 2008; Arnold & Roberts 2009).

OSL measurements of a modern sample (KHUT-10) suggest that quartz grains transported by the Son River are generally sufficiently bleached before burial (Section 7.3.5). This suggests that the high OD values associated with samples GHO-2, GHO-3, KHUT-1 and KHUT-4 cannot be attributed solely to heterogeneous bleaching of grains. The sampled sand units above and below the YTT ash (Fig. 7-1) are non-cohesive, medium-coarse sands that drain freely, contain few carbonate nodules and little organic matter. Thus pore water, carbonates and organic matter can be ruled out as major contributors to the spread in quartz

ages. The spread in the single-grain age distributions may best be explained by sediment mixing.

Using the Finite Mixture Model (FMM) described by Roberts *et al.* (2000) and Galbraith (2005), one can estimate the fewest number of discrete components needed to fit any distribution of mixed-age grains in sediment mixtures. It has been tested using synthetic mixtures of laboratory-dosed grains combined in known proportions (Roberts *et al.* 2000; Jacobs *et al.* 2006b), and can be used to estimate the number of components in a distribution, as well as their age, for any specified OD. In this chapter, the FMM was applied to all single-grain quartz age distributions following the approach of Jacobs *et al.* (2008) where the optimal number of components for each sample, the age of each component and the proportion of grains in each component were determined using the maximum log likelihood and the Bayes Information Criterion (Galbraith 2005). Each quartz age distribution was best fitted by three components using OD values of 10–20% (Fig. 7-8a–d). The ages of these components, and the proportion of grains represented by each component, are listed in Table 7-5.

The ages of the components represented by the largest proportion of grains in samples GHO-3, GHO-2, KHUT-4 and KHUT-1 are ~44 ka, ~36 ka, ~43 ka, and ~39 ka, respectively (Table 7-5). The component represented by the largest proportion of grains is the second oldest component in all samples. The oldest components in samples GHO-2 and KHUT-4 are close to or older than 74 ka (the time of the Toba event) and are ~70 ka and ~88 ka, respectively. The oldest components in samples GHO-3 and KHUT-1 are slightly younger (~68 ka and ~62 ka, respectively) (Table 7-5). The vast majority of quartz grains from all samples appear to be younger than 74 ka (Fig. 7-8, Table 7-5). The FMM component ages suggest that 75–97% of the dated grains were last exposed to sunlight sometime between ~30 and ~70 ka (Table 7-5). Younger FMM quartz component ages, associated with 15% or less of grains, may reflect the presence of intrusive grains derived from plant roots penetrating the cliff face.

The large OD values and multi-component structure in the single-grain datasets may reflect mixing between pre-existing older river bank deposits, which have been periodically eroded during floods along the Son River, and younger flood-transported grains. In the Middle Son Valley, the monsoon season causes the Son River to rise, leading to active erosion of the river banks. Slumped river bank deposits are frequently washed into the channel by rising waters (S. C. Jones 2011, pers. comm.) (Fig. 7-9). The sampled fluvial, overbank and floodplain sediments in the Ghoghara and Khunteli sedimentary sequences may have been deposited close enough to the river banks to receive a significant contribution of sediment from older deposits. If this slumped material is not transported a significant

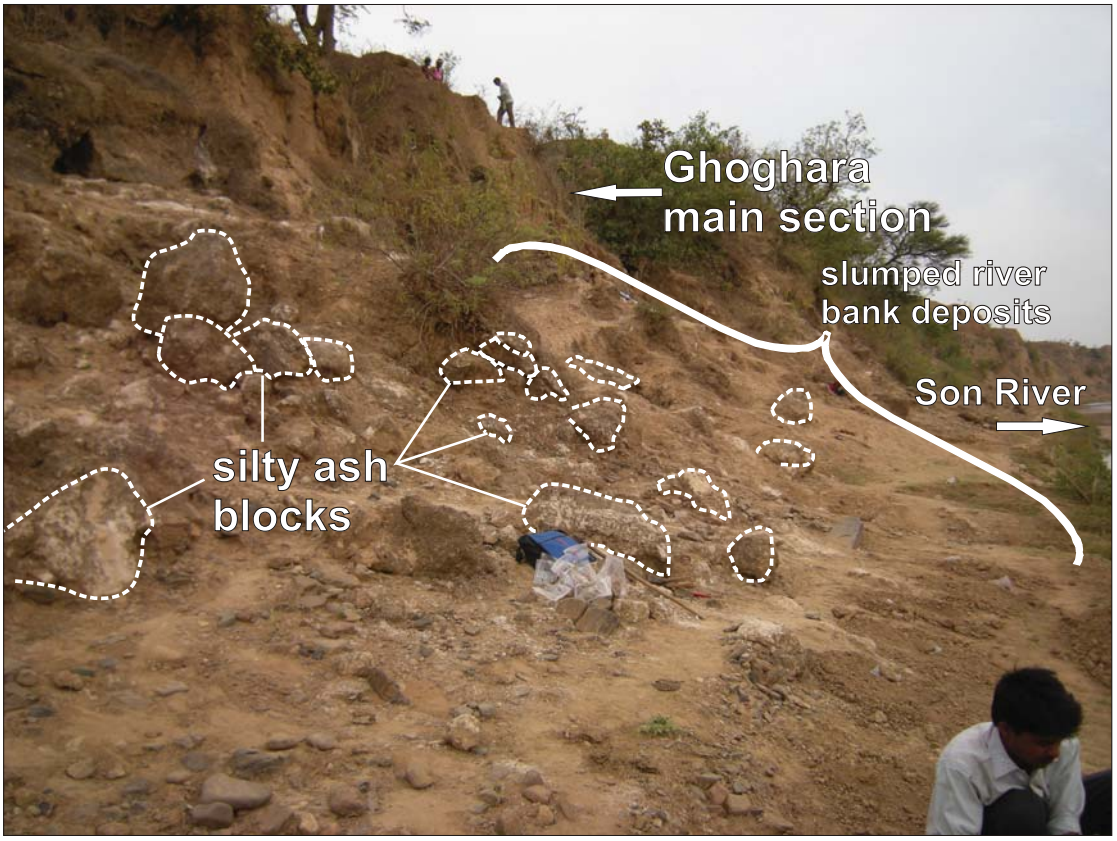

Figure 7-9. Slumped river bank deposits, including fallen silty-ash blocks adjacent to the Son River channel near the Ghoghara main section. During the monsoon season, these deposits are inundated by rising river water, washed into the river channel and transported downstream.

distance, it may remain incompletely bleached before re-deposition in the river channel, adding scatter to single-grain age distributions.

If the youngest FMM components (containing ~15% of grains or less) reflects the presence of intrusive grains derived from plant roots, and the final deposition of the samples is best estimated from the main FMM components, then the quartz FMM ages suggest that final deposition of the sand units bracketing the YTT ash at the Ghoghara main section and the Khunteli type-section occurred sometime between ~36 ka and ~44 ka.

7.5.2 KF grains

In Chapter 6, the D_e values of 952 single feldspar grains from a KF-rich extract from sample GHO-2 were measured using an IR (830 nm) laser. Four hundred and eighty-five of these grains were either so bright that they caused partial saturation of the photomultiplier tube, or had undesirable luminescence characteristics for the SAR measurement protocol (i.e., they had high recuperation, poor sensitivity correction of the regenerative dose measurements, or signals that did not systematically grow with increasing regenerative dose). Fading-corrected ages were obtained from the 467 KF grains with suitable luminescence characteristics for the SAR protocol, using the $IRSL_{50}$ signal, and this age distribution is shown in Figure 7-8e. The OD is 37.3 ± 1.5 %. Given the lack of dependency of KF single-grain ages on the measured fading rates and internal K contents, and the overall adequacy of bleaching of grains collected from a sand bar in the modern river channel (see Chapter 6 for details), the spread in KF single-grain ages in sample GHO-2 is also thought to be mainly due to mixing of potentially well-bleached fluvially-transported sediments with older grains derived from slumping of riverbank deposits sometime after the YTT event.

The KF single-grain age distribution of GHO-2 is also best fitted with three components using the FMM. Seventeen percent of the grains constitute a ~16 ka component, 52% constitute a ~28 ka component, and 31% of the grains constitute a ~43 ka component (Fig. 7-8). The oldest FMM age component (~43 ka) is noticeably younger than that of the quartz age distribution of the same sample (~70 ka) (compare Figs 7-8 ‘a’ and ‘e’), while the youngest component (~16 ka) is similar in age to that of the quartz distribution (~12 ka), but contains a higher proportion of grains (~17% versus ~3%). Thiry-one percent of the KF grains are represented by a ~43 ka component, but most of the grains (52%) are represented by a ~28 ka component.

The reason for the differences between the KF and quartz age distributions is unclear. Feathers and Tunnicliffe (2011) measured individual KF grains from a series of samples from southwestern British Columbia, Canada, and noted that a fraction of the oldest grains from each sample had been rejected because the natural signal did not intersect the dose-response curve. Out of all feldspar grains measured for sample GHO-2, only two were

rejected as a result of the natural signal failing to intersect the dose-response curve, so this does not explain the apparent paucity of "old age" grains in the KF distribution. Another possibility is that the ~70 ka quartz grain population was derived from a sediment layer that contained few KF grains. Because KF grains are more susceptible to weathering than quartz, some sediment units in the Middle Son Valley may contain a paucity of KF grains relative to quartz grains. Approximately 10% of grains in the KF single-grain age distribution are consistent (at 2σ) with the time of the YTT event (~74 ka), within 2σ, but these were too few to be identified by the FMM as part of a discrete age population. As was discovered with quartz, the majority of KF grains in sample GHO-2 appear to have been exposed to sunlight sometime after the YTT event.

7.6 Implications of single-grain data for KF aliquots

7.6.1 Using the MAM to calculate a maximum $IRSL_{50}$ age

The multi-component structure of the quartz and KF single-grain age distributions is attributed to sediment mixing between river-transported sediment and slumped river bank deposits. This multi-component structure is concealed in the single-aliquot data due to grain-averaging effects (Fig. 7-8), so the FMM cannot be used to define discrete age populations in the aliquot data. MAM can be used to estimate the age of aliquots that likely contain the highest proportion of the most recently bleached grains in each age distribution. However, Feathers and Tunnicliffe (2011) have shown that MAM age estimates, even from small aliquots containing only 2-3 grains each, can still yield grossly overestimated ages. In this section, KF aliquot ages were fitted using the MAM, after an OD value of 5% was added in quadrature to each D_e measurement error. This OD value was used as an estimate of the maximum OD expected for KF aliquot age distributions for well-bleached deposits in the Middle Son Valley, as laboratory-dosed KF aliquots used in dose recovery tests exhibited no overdispersion (Section 7.3.3). The $IRSL_{50}$ KF aliquot MAM age of GHO-2 is 21.3 ± 1.6 ka with an OD of 21.3 ± 1.6% (Fig. 7-8e, Table 7-5). This age is ~5.5 ka older than the age of the corresponding youngest (16 ± 1 ka) KF FMM age component that constitutes 17% of grains in this sample. Thus, these data suggest that overdispersed $IRSL_{50}$ KF aliquot MAM ages may only serve as maximum age estimates, producing ages within ~5–6 ka of the true burial age of the youngest, statistically supported age component in a single-grain $IRSL_{50}$ KF age distribution.

7.6.2 Comparisons between quartz and KF single-grain age distributions and KF multi-grain aliquot age distributions

In this section, MAM ages were calculated from all $IRSL_{50}$ and $pIRIR_{225}$ KF aliquot age distributions, as was done for GHO-2 in the previous section. Here these data are

compared to single-grain quartz OSL age distributions from the same samples (Figs 7-8a–d, 7-10a–d, Table 7-5) to determine whether the IRSL aliquot ages should be considered maximum or minimum ages. The calculated $IRSL_{50}$ MAM ages for all samples fall between the youngest and second youngest quartz FMM age components (Figs 7-8a–d, Table 7-5). This suggests that $IRSL_{50}$ MAM aliquot ages are overestimates of the time since a significant proportion of grains in these samples were most recently exposed to sunlight, being too old by ~6 ka (KHUT-4) to ~11 ka (KHUT-1). On the other hand, if the youngest FMM age

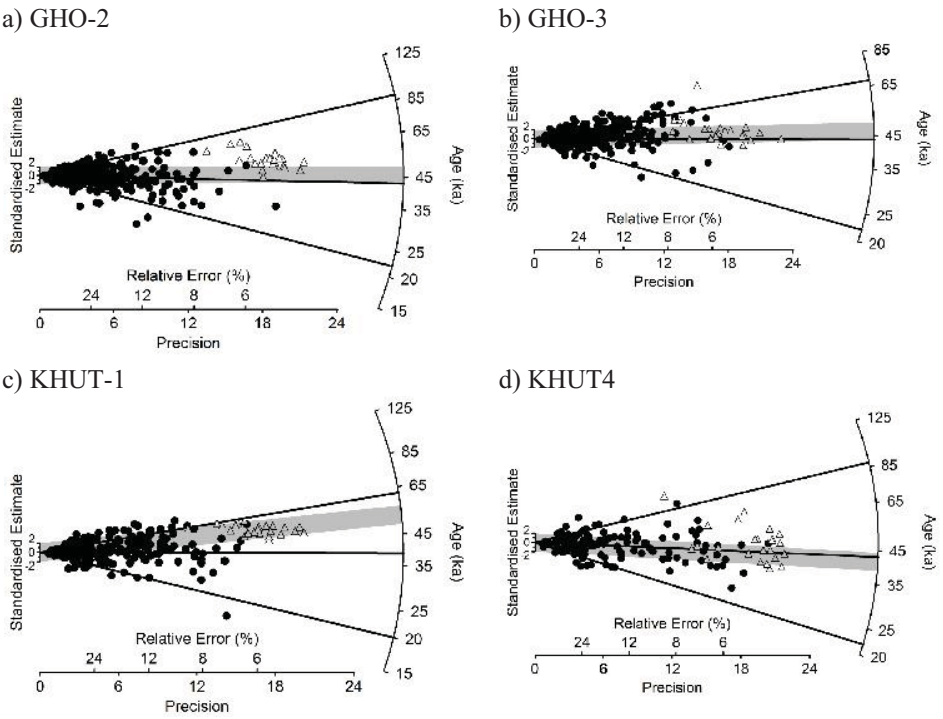

Figure 7-10. Radial plots of single-grain quartz age distributions for samples GHO-2 (a), GHO-3 (b), KHUT-1 (c), and KHUT-4 (d). The $pIRIR_{225}$ KF aliquot fading-corrected ages (open triangles) are superimposed on the quartz single-grain age distributions. A residual dose of 5.61 ±0.03 Gy was subtracted from the $pIRIR_{225}$ data and the errors on the residual doses have been propagated through into the error on the aliquot ages. The grey shaded band is centered on the age calculated for the KF aliquot data using the MAM (Table 7-4).

components (which represent a small proportion of grains in each sample) represent intrusive grains associated with plant roots penetrating the cliff face, and the true burial age of each sample is actually closer to the second youngest (or main) quartz FMM age component (as suggested in Section 7.5.1), then the $IRSL_{50}$ MAM ages (calculated from aliquots that would likely also contain intrusive grains) will underestimate the true burial ages by ~8 ka (KHUT-4) to ~15 ka (GHO-2) (Table 7-5).

MAM $pIRIR_{225}$ KF aliquot ages approximate the age of the main FMM quartz components in "above ash" samples (GHO-3 and KHUT-4), but overestimate the age of the

main FMM quartz components in "below ash" samples by ~10–13 ka (GHO-2 and KHUT-1) (Fig. 7-10a–d, Table 7-5). $pIRIR_{225}$ MAM KF ages overestimate the age of the youngest FMM quartz components by ~20 ka (KHUT-4) to ~35 ka (GHO-2), suggesting that, as with the $IRSL_{50}$ MAM ages, $pIRIR_{225}$ MAM ages can only serve as maximum age estimates of the time since a significant proportion of grains in these samples were most recently exposed to sunlight. In contrast to the $pIRIR_{225}$ MAM ages, $IRSL_{50}$ MAM ages only overestimate the age of the youngest quartz FMM component by ~6–11 ka. Thus, $IRSL_{50}$ MAM age estimates are considered here to be more reliable than $pIRIR_{225}$ MAM age estimates in samples that do not (or are assumed not to) contain a significant proportion of young, intrusive grains as a result of bioturbation.

7.7 Environmental dose rates

7.7.1 Assessing the potential of radioactive disequilibrium in U and Th decay chains

The environmental dose rates for all luminescence samples were determined for age calculations using the methods described in Chapter 3. These involved estimating external beta and gamma dose rates by low-level beta counting in the laboratory and *in situ* gamma spectrometry in the field. A contribution has also been added for the dose rate from cosmic rays using the methods of Prescott and Hutton (1994). By measuring the external dose rates using beta counting and *in situ* gamma spectrometry, it is assumed that the dose rate measured at the time of sample collection has prevailed throughout the burial history of the sample. However, if radionuclides have migrated since sediment deposition, this may not be true. To check for evidence of the ingress or loss of radionuclides in the sediment that may have resulted in time-dependent radioactive disequilibria in the U and Th decay chains, the activities of ^{238}U, ^{226}Ra, ^{210}Pb, ^{228}Th, and ^{228}Ra were measured from dried and powdered sub-samples using high-resolution gamma-ray spectrometry (HRGS) at the CSIRO Land and Water laboratory, Canberra (Table 7-6). These samples were collected from sediment from each luminescence sample hole in the field. Details of the HRGS instrumentation and calibration standards are provided by Olley *et al.* (1996).

Table 7-6. Radionuclide activities (in Bq/kg) of samples collected from sediments that bracket the YTT ash at Khunteli and Ghoghara. See text for details.

		^{238}U series				
Sample	**Relation to YTT ash**	**^{238}U**	**^{226}Ra**	**^{210}Pb**	**^{226}Ra:^{238}U**	**^{210}Pb:^{226}Ra**
GHO-3	above ash	8.57 ± 0.73	10.82 ± 0.16	11.15 ± 0.97	1.26 ± 0.11	1.03 ± 0.09
GHO-2	below ash	10.68 ± 0.81	11.29 ± 0.17	11.18 ± 0.81	1.06 ± 0.08	0.99 ± 0.07
KHUT-4	above ash	6.06 ± 0.64	7.96 ± 0.03	7.7 ± 0.78	1.31 ± 0.14	0.97 ± 0.10
KHUT-1	below ash	12.71 ± 0.84	13.48 ± 0.19	13.71 ± 1.05	1.06 ± 0.07	1.02 ± 0.08

		Th-232 series			^{40}K
Sample	**Relation to YTT**	**^{228}Ra**	**^{228}Th**	**^{228}Th:^{228}Ra**	
GHO-3	above ash	22.77 ± 0.38	22.93 ± 0.40	1.01 ± 0.02	340.6 ± 7.2
GHO-2	below ash	31.90 ± 0.49	31.87 ± 0.53	1.00 ± 0.02	204.7 ± 4.5
KHUT-4	above ash	14.05 ± 0.29	14.13 ± 0.28	1.01 ± 0.03	130.7 ± 3.1
KHUT-1	below ash	33.54 ± 0.50	34.30 ± 0.57	1.02 ± 0.02	353.7 ± 7.5

All activity ratios (^{226}Ra:^{238}U, ^{210}Pb:^{226}Ra, ^{228}Th:^{228}Ra) are statistically consistent with unity, except for the ^{226}Ra:^{238}U activity ratios for "above ash" samples GHO-3 and KHUT-4. In these latter two samples, the ^{226}Ra activity is ~30% higher than that of ^{238}U, which can be explained by either an ingress of ^{226}Ra or a loss of ^{238}U. Because of the relatively short half-life of ^{226}Ra (1602 years), any unsupported excess of ^{226}Ra would have decayed away within 10,000 years of sediment deposition, and would, thus, not be expected to still be present today. The ^{226}Ra:^{238}U ratios are best explained by a loss of ^{238}U, likely due to the binding of uranium with carbonate complexes after sediment deposition. This has probably been an ongoing process that has occurred since sediment deposition, so no time-dependent correction to the dose rate is necessary. The total dose rate for all samples is dominated by Th and K, so even a ~30% change in ^{238}U concentration would amount to only a small change in the total dose rates (e.g., 1.4% in sample GHO-2).

7.7.2 Causes of sample-to-sample variations in ^{40}K content

There are significant variations in ^{40}K content from sample to sample (Table 7-6) and this may be due in part to variations in re-worked YTT ash content. The YTT ash at these two sites contains ~5% K_2O (Petraglia *et al.* 2007) and therefore is a source of radioactive ^{40}K. At the Ghoghara main section, the ^{40}K activity is 205 Bq/kg below the ash (GHO-2) and 341 Bq/kg above the ash (GHO-3). Sample GHO-3 was obtained from fine-medium silty sand that contained re-worked YTT ash (Fig. 7-1) (observed in this study as well as by Chivas 2010, Lewis *et al.* 2011 and Jones *et al.* 2010 from the same exposure), whereas sample GHO-2 was obtained from sand and gravel with no visible YTT ash below the so-called "primary" ash. Sample KHUT-1 was obtained from medium-coarse cross-bedded sands below the ash-rich sandy silt exposed at Khunteli. The high K content in this sample may be derived from re-worked ash particles within the sample that were not visible

in the field and/or ash particles that have leached down the sedimentary profile through time from the overlying ash-rich silts to the relatively porous sandy sediments at the site of sample KHUT-1.

7.7.3 A comparison between external dose rates measured using HRGS and low-level beta counting plus *in situ* gamma spectrometry

The external dose rates measured using HRGS and beta counting plus *in situ* gamma spectrometry are compared in Tables 7-7 and 7-8 below. The beta dose rates obtained using HRGS and beta counting are either identical within statistical error, or very close to it as one would expect from samples with U and Th decay chains that are close to secular equilibrium. The same is true for the gamma dose rates for all samples except for sample GHO-3, which was collected above the ash layer at the Ghoghara main section (Fig. 7-1). The HRGS gamma dose rate for this sample is 0.60 ± 0.01 Gy/ka while the gamma dose rate measured in the field is ~50% higher (0.91 ± 0.05 Gy/ka). The field measurement is likely higher than the HRGS measurement because the *in situ* gamma spectrometer has detected elevated levels of ^{40}K from reworked ash present in the underlying deposits. The HRGS sample for GHO-3, by contrast, would have only consisted of sand close the luminescence sample tubes.

.

Table 7-7. External dose rates measured using HRGS for samples collected above and below YTT ash.

Sample	Relation to YTT ash	Water content (%)		Radionuclide activities[1] (Bq/kg)							External dose rate[2] (Gy/ka)			
		Field	Used	^{238}U	^{226}Ra	^{210}Pb	^{232}Th	^{228}Th	^{228}Ra	^{40}K	Gamma	Beta	Cosmic	Total
GHO-2	below ash	0.3	5 ± 2	10.7 ± 0.8	11.3 ± 0.2	11.2 ± 0.8	31.9 ± 0.4	31.9 ± 0.5	31.9 ± 0.5	204.7 ± 4.5	0.60 ± 0.01	0.72 ± 0.01	0.09 ± 0.01	1.41 ± 0.05
GHO-3	above ash	0.9	5 ± 2	8.6 ± 0.7	10.8 ± 0.2	11.2 ± 1.0	22.8 ± 0.3	22.9 ± 0.4	22.8 ± 0.4	340.6 ± 7.2	0.60 ± 0.01	0.97 ± 0.02	0.11 ± 0.01	1.68 ± 0.05
KHUT-1	below ash	1.4	5 ± 2	12.7 ± 0.8	13.5 ± 0.2	13.7 ± 1.1	33.9 ± 0.4	34.3 ± 0.6	33.5 ± 0.5	353.7 ± 7.5	0.76 ± 0.01	1.08 ± 0.02	0.07 ± 0.01	1.89 ± 0.06
KHUT-4	above ash	2.8	5 ± 2	6.1 ± 0.6	8.0 ± 0.1	7.7 ± 0.8	14.1 ± 0.2	14.1 ± 0.3	14.1 ± 0.3	130.7 ± 3.1	0.32 ± 0.01	0.43 ± 0.01	0.08 ± 0.01	0.83 ± 0.02

[1]Measurements made on dried and powdered subsamples. The associated uncertainties represent one standard error derived from counting statistics.

[2]Beta and gamma dose rates from the ^{238}U decay series were calculated from the fractional contributions of ^{238}U, ^{226}Ra and ^{210}Pb. Beta and gamma dose rates from the ^{232}Th decay series were derived from the ^{232}Th activities, which, in turn, were calculated from the weighted mean of the ^{228}Th and ^{228}Ra activities. Dose rates are calculated using conversion factors from Adamiec and Aitken (1998) and are corrected for water content and beta attenuation using attenuation factors from Zimmerman (1971) and Brennan (2003), respectively. Beta dose errors take into account a 3% uncertainty for beta attenuation factors.

Table 7-8. External dose rates measured using low-level beta counting and *in-situ* gamma spectrometry.

Sample	Relation to YTT ash	Water content (%)		External dose rate[1] (Gy/ka)			
		Field	Used	Gamma	Beta	Cosmic	Total
GHO-2	below ash	0.3	5 ± 2	0.61 ± 0.03	0.72 ± 0.05	0.09 ± 0.01	1.42 ± 0.06
GHO-3	above ash	0.9	5 ± 2	0.91 ± 0.05	1.05 ± 0.05	0.11 ± 0.01	2.07 ± 0.07
KHUT-1	below ash	1.4	5 ± 2	0.79 ± 0.04	1.18 ± 0.06	0.07 ± 0.01	2.04 ± 0.07
KHUT-4	above ash	2.8	5 ± 2	0.30 ± 0.02	0.44 ± 0.02	0.08 ± 0.01	0.82 ± 0.03

[1]Dose rates are corrected for water content and beta attenuation using attenuation factors from Zimmerman (1971) and Brennan (2003), respectively. The total dose rate is the mean ± total (1σ) uncertainty, calculated as the quadratic sum of the random and systematic uncertainties.

7.7.4 Age calculations using water contents approaching saturation

External dose rates were calculated for an estimated long-term, time-averaged water content of 5 ± 2% for all samples in this chapter. These estimates are ~2–5% moister than the measured (field) water contents but are smaller than saturated water contents (~22%) that have been measured in the laboratory from similar sediments in the Middle Son Valley (Haslam *et al.* 2011). These estimates are drier than the saturated water contents in order to take into account their collection during the dry season, the free-draining (not waterlogged) nature of the deposits, and the monsoonal climate of the region which has a wet season that lasts only one quarter of the year. Even if we assume that the sediments have been saturated during their entire burial history, calculated IRSL ages increase by only ~2–4 ka (Table 7-5, age calculation 'b').

7.8 Implications for the time of final deposition of the YTT ash and palaeoenvironmental reconstructions of Toba's impact

All the KF aliquot and single-grain quartz ages suggest that final deposition of the sediments bracketing the YTT ash at Khunteli and Ghoghara occurred sometime (up to a few tens of thousands of years) after the Toba volcanic super-eruption (Table 7-5). These results imply one of three things: 1) the YTT ash sampled at Ghoghara and Khunteli has been reworked by fluvial processes and re-deposited as fluvial silts (Fig. 7-11a), 2) the ash and ash-rich silt was deposited as mobile, cohesive blocks, several thousand years after the Toba event (Fig. 7-11b). In this case, the lower 4 cm of the YTT ash unit at the Ghoghara main section is likely not primary ash, contrary to the suggestions of Gatti *et al.* (2011) and Matthews *et al.* (2012). Or, 3) the YTT ash was deposited soon after the volcanic event ~74 ka ago, but the underlying sediments have since been eroded and replaced by younger, inset fluvial sediments (Fig. 7-11c).

YTT ash and ashy silt observed in the field constitutes cohesive sediment units that are underlain by clayey silt and loose sand (Ghoghara) or loose medium to coarse grained sands (Khunteli) (Fig. 7-1). It is possible that coarser sediment underlying the YTT ash units

has been preferentially eroded and replaced by younger, inset fluvial sediments, however sedimentological evidence for this is lacking. If the sediments underlying the YTT ash have been replaced by inset sediments, one might expect to see such features as a) pieces of ash collapsed down into the undercut areas; b) hollows excavated below the bed and filled with lenses of sediment; c) discontinuous strata below the ash as a result of cut and fill processes. None of these features were observed in the field suggesting that the ash does indeed overlie *in situ*, relatively *older* sediment.

It is possible that the ash and ashy silt units that were sampled are actually remobilized cohesive blocks of sediment that have been eroded from the cliff face and re-deposited and re-buried in younger fluvial sediments in the Son River channel (Fig. 7-11b). Modern-day processes give credence to this latter possibility, as ash-rich cohesive silt blocks can still be seen partially buried in colluvium and fluvial sediments along the banks of the Son River today (Fig. 7-9). However, again, there is a paucity of evidence to support the "remobilized ash block" hypothesis from the sedimentary exposures. All observed ash units contain horizontal upper and lower contacts where contacts are visible (Fig. 7-2b). There are no sedimentological features within the ash units, such as inclined bedding, or sharp irregular contacts with the surrounding sediment that might suggest that the ash has been remobilized as a cohesive block before deposition. Thus, all field observations suggest that the ash has been reworked by fluvial processes and re-deposited as fluvial silts.

Single-grain quartz ages suggest that most grains in the alluvial sediments bracketing the ash were last exposed to sunlight sometime between ~30 and ~70 ka. Quartz single-grain OSL age distributions suggest that samples that bracket YTT ash are composed of a mixture of recently sun-exposed flood-transported grains and older grains from slumping riverbank deposits, and possibly some intrusive grains derived from plant roots penetrating the cliff face. If we take the main quartz FMM component ages, which range from ~36 to ~44 ka, to be the most accurate estimate of the depositional age of the samples in this study, then the ash-bearing sediments can be tentatively correlated with either the lower coarse member of the Baghor Formation (samples GHO-2 and KHUT-1), or the uppermost sediments of the Patpara Formation (samples GHO-3 and KHUT-4) as defined by the stratigraphic model of Williams *et al.* (2006).

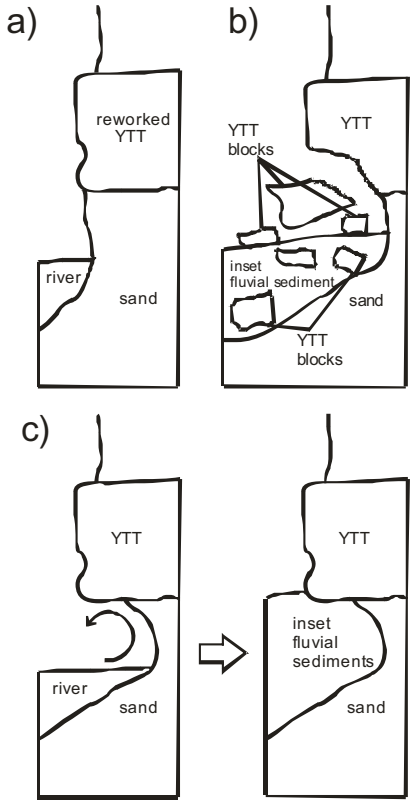

Figure 7-11. Quartz and KF luminescence ages imply one of two possible scenarios: 1) the YTT ash sampled at Ghoghara and Khunteli has been reworked by fluvial processes and re-deposited either as fluvial silts or as mobile, cohesive blocks, several thousand years after the Toba event (a and b), or 2) the YTT ash was deposited soon after the volcanic event ~74 ka ago, but the underlying sediments have since been eroded and replaced by younger, inset fluvial sediments (c).

These results have implications for palaeoenvironmental reconstructions that have been made from pedogenic carbonates sampled from sediments above, below and within YTT ash at excavated sections at the Rehi-Son confluence and in the Khunteli Formation type-section (Williams *et al.* 2009). The carbon isotope compositions of carbonate nodules and rootcasts were used to determine whether the vegetation growing in the soils was dominantly following the Hatch-Slack or C_4 pathway of photosynthesis, such as grasses that grow in strong sunlight, or the Calvin or C_3 pathway of photosynthesis, such as trees, shrubs and grasses growing in shaded forests (Williams *et al.* 2009). Based on this evidence, it was proposed that C_3 forest was replaced by wooded to open C_4 grassland in north-central India after the Toba eruption (Williams *et al.* 2009).

Luminescence investigations in this chapter suggest that the "before and after Toba" palaeoenvironmental reconstruction of Williams *et al.* (2009) is likely erroneous. Luminescence ages in this study suggest that ash-bearing sediments at the Rehi-Son confluence and at the Khunteli Formation type-section were last deposited tens of thousands

of years after the YTT event. Any soils, pedogenic carbonate nodules, and rootcasts associated with these deposits would have formed even later after sediment deposition, and thus should not be considered reliable proxies for palaeoenvironmental reconstruction before and after the Toba eruption. Ideally, palaeoenvironmental reconstructions from pedogenic carbonates should include independent chronological control on the time of final deposition of the sediments from which the carbonates have been sampled, and/or the the time of formation of the carbonates themselves.

7.9 Summary

This chapter presented new single-grain OSL quartz ages from samples collected above and below two YTT ash units in the Middle Son Valley, and investigated the potential of KF grains for luminescence dating using the $IRSL_{50}$ and $pIRIR_{225}$ signals. KF grains in these samples appear to be suited to $IRSL_{50}$ and $pIRIR_{225}$ SAR measurement protocols, and the measured anomalous fading rates of the $IRSL_{50}$ and $pIRIR_{225}$ signals are generally consistent with those reported in the literature. In these samples, fading-corrected $pIRIR_{225}$ ages are ~1.5 to ~2 times those of the $IRSL_{50}$ signal, even after subtraction of residual doses measured from aliquots that have been sun-bleached for 2 days. $IRSL_{50}$ and $pIRIR_{225}$ D_e values measured from a modern sample from a sand bar in the Son River channel suggest that the source traps of the $pIRIR_{225}$ signal in our samples may be more difficult to empty in the Son River than those of the $IRSL_{50}$ signal.

Quartz single-grain OSL age distributions suggest that samples that bracket YTT ash in the Middle Son Valley are composed of a mixture of flood-transported grains and grains from slumping riverbank deposits, and possibly some intrusive grains derived from plant roots penetrating the cliff face. The time of the most recent bleaching event in each sample is best observed in the quartz and KF single-grain data; the aliquot data lacks the multi-component structure apparent in the single-grain data due to grain-averaging effects, and therefore can only provide maximum age estimates of the most recent bleaching event for each mineral, even if the age is calculated using the MAM. MAM $pIRIR_{225}$ KF ages overestimate the age of the youngest FMM quartz components by ~20–35 ka and $IRSL_{50}$ MAM ages overestimate the age of the youngest quartz FMM components by ~6–11 ka. Thus $IRSL_{50}$ MAM ages are considered more reliable age estimates of the most recent bleaching event than are the MAM $pIRIR_{225}$ ages, and these are used in the following chapter.

If we take the main quartz FMM component ages, which range from ~36 to 44 ka, to be the most accurate estimate of the depositional age of the samples below and above YTT ash at Ghoghara and Khunteli, then according to the model of alluvial deposition proposed by Williams *et al.* (2006), the alluvial sediments bracketing the YTT ash were deposited

after the ~74 ka eruption event, and can be tentatively correlated with either the lower coarse member of the Baghor Formation (samples GHO-2 and KHUT-1) or the uppermost sediments of the Patpara Formation (samples GHO-3 and KHUT-4). If the lowermost 4 cm of the YTT ash unit at the Ghoghara main section is indeed primary ash fall as suggested by Gatti *et al*. (2011), then this would imply that the underlying ~36 ka old sands (GHO-2, Table 7-4) are inset sediments deposited after fluvial erosion of non-cohesive sediments underneath the relatively cohesive YTT ash unit. However sedimentological evidence for the erosion and deposition of inset sediments is lacking in the Ghoghara sedimentary sequence, suggesting that the lower 4 cm of the ash at the Ghoghara main section is not "primary ash" but rather ash that has been eroded from some other location and re-deposited.

Previous palaeoenvironmental reconstructions inferred from the carbon isotope composition of pedogenic carbonates sampled above, below and within YTT ash units at Ghoghara and Khunteli (Williams *et al.* 2009) are likely to be erroneous. Luminescence ages in this chapter suggest that the burial age of sediments bracketing the YTT at these locations, and any pedogenic carbonates preserved in them, were most likely deposited tens of thousands of years after the Toba event. Future palaeoenvironmental investigations using pedogenic carbonates should confirm the burial age of the sediment from which they are sourced, and/or the formation age of the carbonates directly using independent chronological control.

The next chapter combines field observations, topographic data and $IRSL_{50}$ ages from small (~25 grain) KF aliquots to test a current model of alluvial deposition in the Middle Son Valley near the Rehi-Son confluence. Comparisons made between single-grain and KF aliquot age distributions in the present chapter suggest that overdispersed KF aliquot age distributions in the next chapter should be considered as maximum IRSL age estimates for the most recent bleaching event in each sample.

Chapter 8 – Testing a model of alluvial deposition in the Middle Son Valley, India using IRSL ages of terraced alluvial sediments

8.1 Introduction

Current models of alluvial deposition for the Middle Son Valley subdivide its alluvium into five stratigraphic formations that represent specific time periods in its geological and archaeological history (Williams & Royce 1982, 1983; Williams *et al.* 2006) (Table 1-1, Chapter 1). In the absence of reliable chronological control, the chronology of human occupation in the Middle Son Valley has been based on weak correlations between artefacts and sediments presumed to be part of one or more of these formations on the basis of their geomorphic context and sedimentological characteristics (Table 1-1) (Williams & Royce 1982; Sharma & Clark 1983; Haslam *et al.* 2012). The chronology of the stratigraphic formations is constrained by few numerical ages spread over a wide area (Fig. 1-1a, Table 1-2) and the sample site locations and sedimentary contexts for some of these ages are poorly documented (Table 1-2) (Jones & Pal 2009).

According to a recently proposed geomorphic model based on a series of numerical ages from both the Son and Belan Valleys (Williams *et al.* 2006), the highest alluvial terraces on either side of the Son River (~30–35 m above river level) record the end of a period of aggradation ~16 ka ago coinciding with the termination of deposition of the fine member of the Baghor Formation. (In this thesis, river level refers to the low-stage level of the river as measured during the winter season.) These terraces, as well as the ~10 m-high terraces comprising the Khetaunhi Formation, are considered depositional features in the landscape (Fig. 8-1) (Williams *et al.* 2006). Terraces that form prominent surfaces at ~25 and ~15 m above river level are considered to be erosional features that expose Patpara Formation sediments (Fig. 8-1) (Williams *et al.* 2006). In this chapter, the accuracy of this model is tested near the Rehi-Son confluence using satellite imagery of the area, field observations, cross-valley topographic profiles and IRSL age estimates from small (~25 grain) aliquots of KF from terraced alluvial sediments. These data provide insights into the fluvial history of the Son River and its response to changes in palaeoclimate, and will inform future archaeological surveys by constraining the geomorphic context of surficial and excavated artefacts in the area.

8.2 Study area

The reach of the Son River examined near the Rehi-Son confluence is shown in Figures 8-2 ‘b’ and ‘c’, and 8-3. North of the river, the topography is variable where gullies and streams have incised non-cohesive alluvial silts and sands. In the northwest, NE-SW

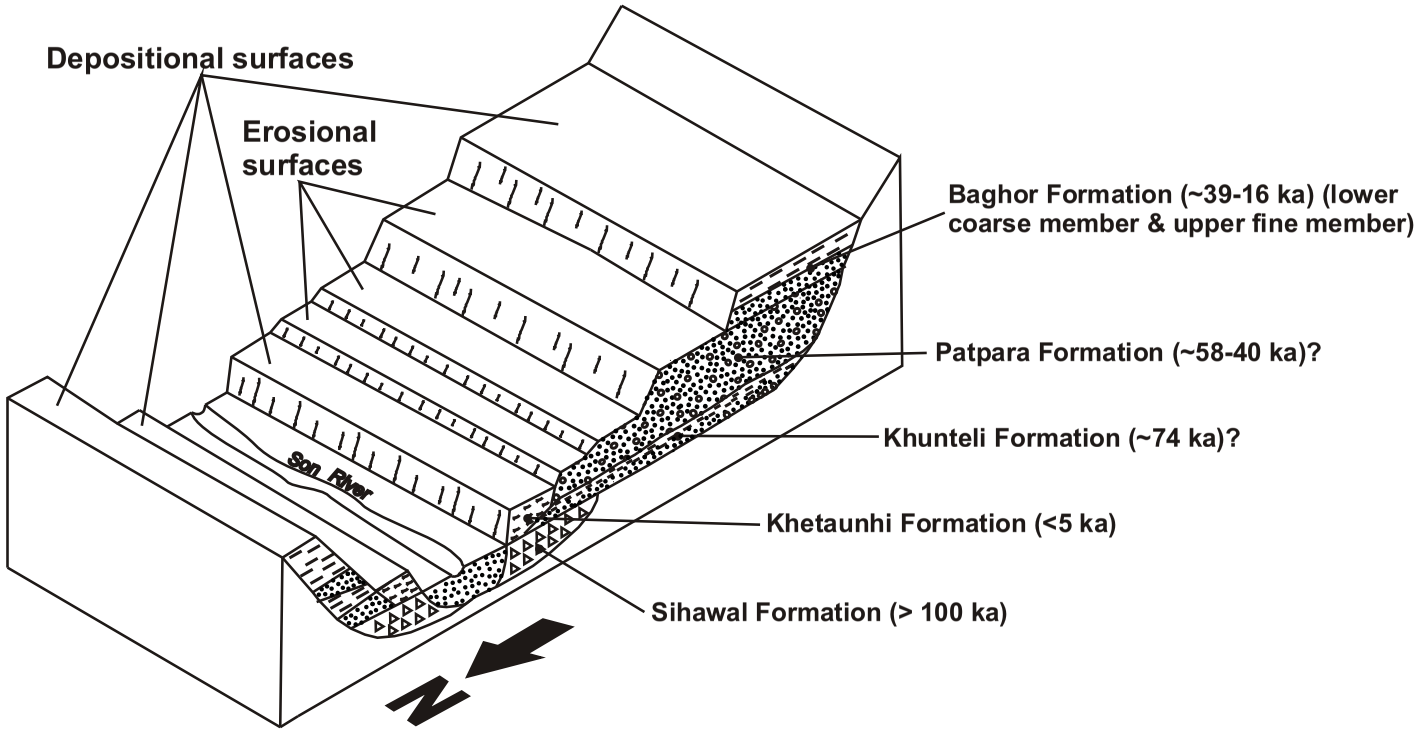

Figure 8-1. Schematic cross-section of the Middle Son Valley looking east from the Rehi-Son confluence, modified after Williams and Royce (1983) to include the new Khunteli Formation introduced by Williams *et al.* (2006). Formation ages are after Williams *et al.* (2006). The ages of the Patpara and Khunteli formations include a question mark as these are debated (see Chapter 1, Section 1.2 for details). A "depositional surface" is defined here as one in which the most recent stratigraphic formation deposited is still preserved after lateral migration of the channel and/or incision of the river into the floodplain, while an "erosional surface" is one in which one or more stratigraphic formations have been eroded, exposing one or more older underlying stratigraphic formations. It is possible that some erosion has occurred on all alluvial surfaces immediately before lateral migration of the channel and/or incision of the river into the floodplain.

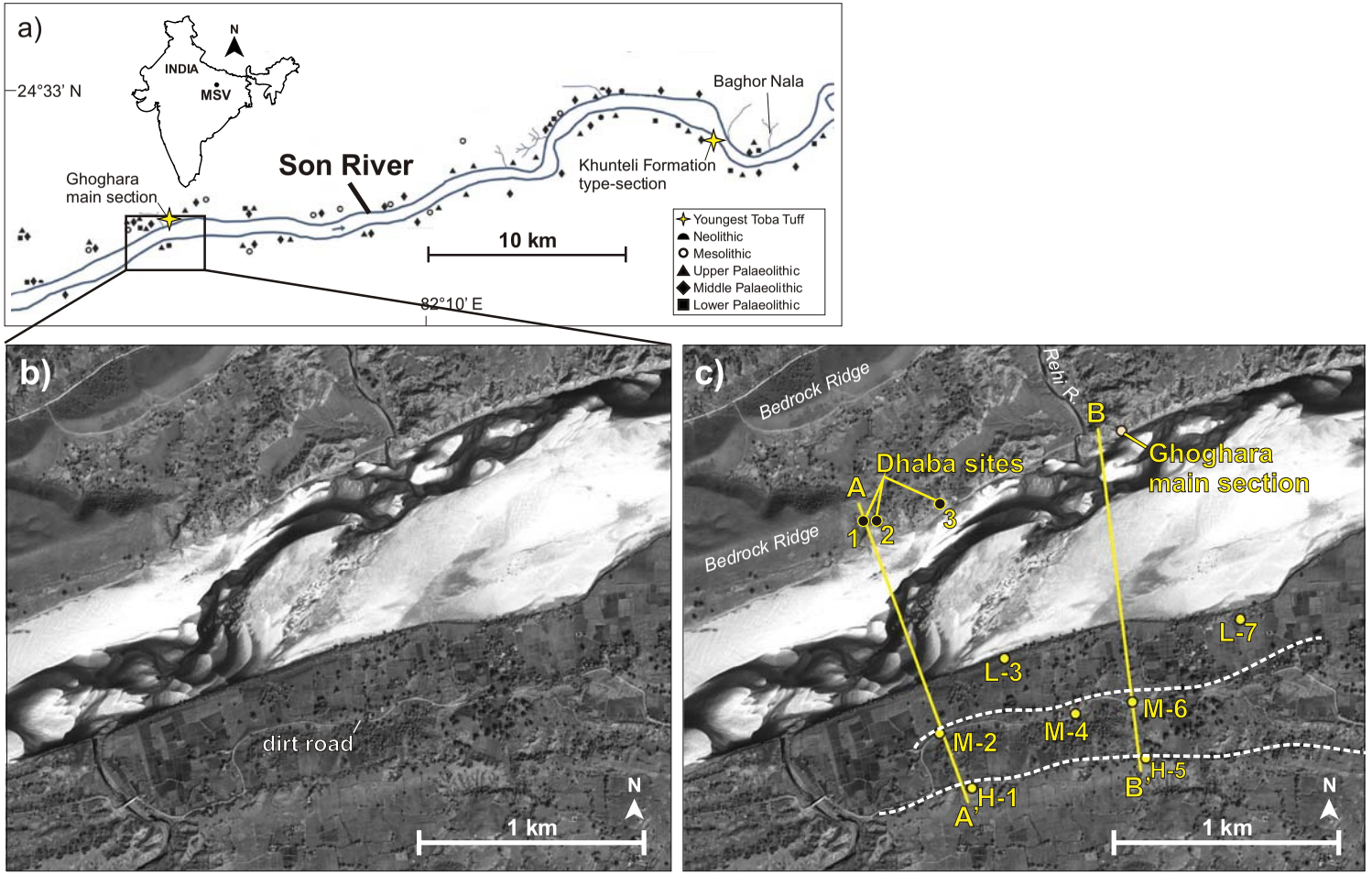

Figure 8-2. a) The Middle Son Valley (MSV) and the locations of archaeological sites along the banks of the Son River after Sharma and Clark (1983). b) WorldView-1 50 cm panchromatic imagery of the study area. c) White dashed lines delineate the prominent WSW-ENE trending terrace escarpment ~500-700 m south of the Son River and the gentle break in topography parallel to the dirt road north of this. Yellow lines delineate topographic survey transects A-A' and B-B'. Luminescence sample sites are indicated by yellow dots, and the three archaeological sites of the Dhaba locality of Haslam *et al.* (2012) are indicated by black dots.

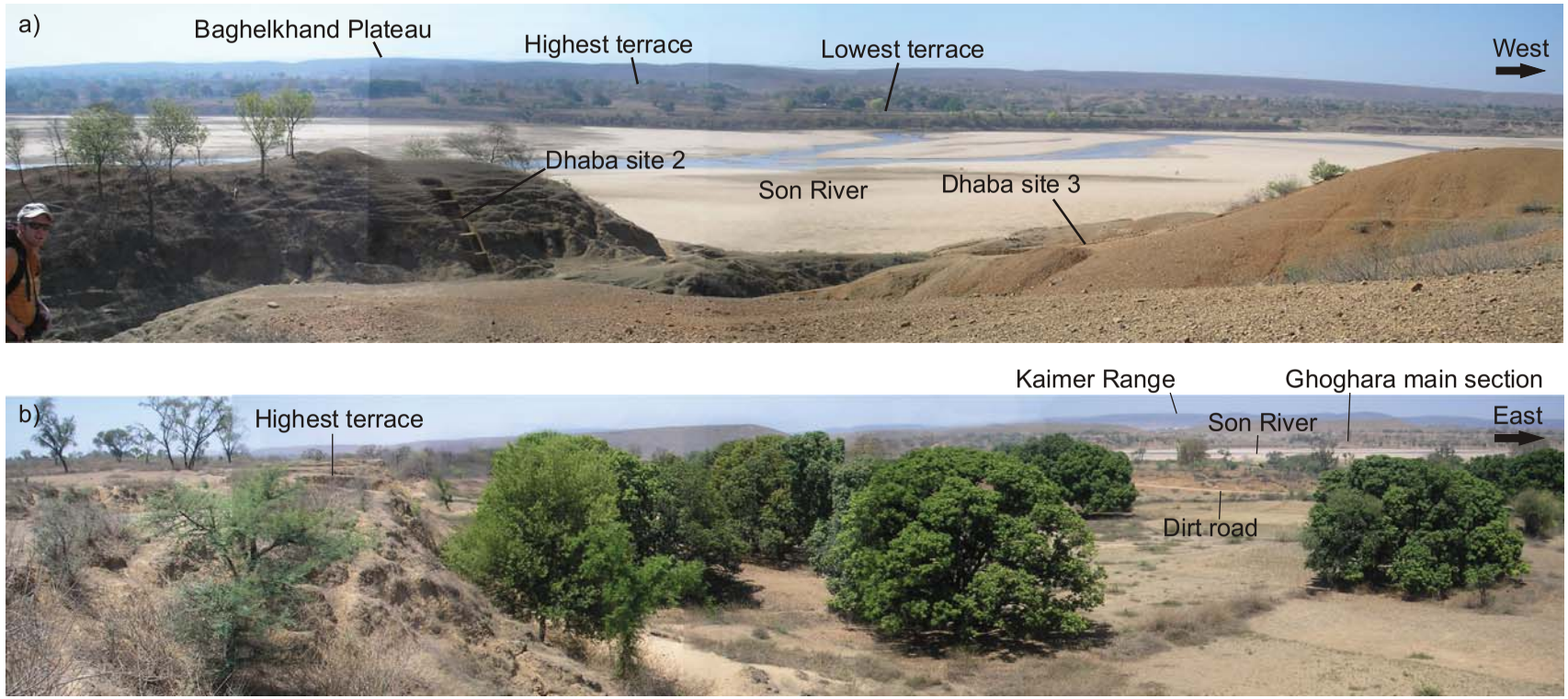

Figure 8-3. a) View south across the Son River from Dhaba sites 2 and 3 (Haslam *et al.* 2012). b) View northwest from the location of IRSL sample 5, which was taken from the highest terrace on the south side of the Son River. The dirt road along which IRSL samples 2, 4 and 6 were collected (Fig. 8-2b) is visible just south of the Son River.

trending bedrock ridges composed of sandstones and shales outcrop along the north bank of the river, as well as ~1 km further north. Archaeological excavations at the site of Dhaba (Haslam *et al.* 2012) were conducted in March, 2009. One trench (site 3) was dug in colluvial sediments on the easternmost flanks of the bedrock ridge, and two trenches (sites 1 and 2) were dug in floodplain silts and sands overlying quartzite and shale bedrock on the north bank of the Son River, closer to the Rehi-Son confluence (Figs 8-2c, 8-3a). These excavations have yielded undated Acheulean, Middle Palaeolithic and microlithic artefacts (Haslam *et al.* 2012). East of the Rehi-Son confluence is the Ghoghara main section, which exposes Youngest Toba Tuff (Williams *et al.* 2009; Gatti *et al.* 2011; Smith *et al.* 2011).

A prominent east-west trending terrace escarpment lies ~500–700 m south of the Son River channel, and, north of this, gently undulating topography slopes toward the river (Figs 8-2b, c, and 8-3b). A slight break in the topography trends east-west, subparallel to the dirt road (Fig. 8-2b, and observed during field surveys on foot); this may mark the edge of another alluvial terrace.

8.3 Methods

8.3.1 Topographic surveys

Topographic profiles were measured across the valley along two traverses near the Rehi-Son confluence (Fig. 8-2c) using a differential global positioning system (DGPS) and electronic total station (ETS). Control points were measured in open (treeless) spaces near each planned traverse using a Trimble R3 Differential DGPS consisting of one reference receiver and 2 rovers. These control points served as benchmarks to which the start and end points of each traverse (measured using the ETS) were tied. Control points were logged in static mode for 1.5 h using horizontal baseline lengths of ~100–150 m to achieve measurement precisions better than 0.01 m and the DGPS data were processed using Trimble Geomatics Office software. A Pentax 326EX ETS was used to measure elevations at 5 m intervals along each traverse. The average estimated measurement error for each elevation measurement was less than 4 mm. The ETS data were imported into an ArcGIS workspace, and superimposed on georeferenced WorldView-1 panchromatic satellite imagery (50 cm horizontal resolution) of the study area (Fig. 8-2c).

8.3.2 Sampling and IRSL measurements

Seven samples for luminescence dating were collected from alluvial sediments on the south side of the Son River (Fig. 8-2c). Two samples (H-1 and H-5) were collected from near the top of the highest terrace, three samples (M-2, M-4 and M-6) were collected from exposed sediments or roadcuts along the dirt road, and two samples (L-3 and L-7) were

collected from gully exposures in the lowest alluvial terrace next to the river channel. The sediments at each sample location were photographed and their texture, colour and sedimentary structures were recorded. Steel tubes, ~5 cm in diameter, were hammered into the face of the exposed alluvial sediments ~60 to ~100 cm below the ground surface, to avoid sampling sediments disturbed by local farming practices (i.e., ploughing). After the tubes were extracted, the sample holes were lengthened and an *in situ* gamma spectrometer detector was inserted for gamma radioactivity measurements. Bagged samples of sediment (~60–200 g) were collected from the walls of the gamma spectrometer detector holes for water content measurements and low-level beta counting in the laboratory. See Chapter 3 for details on sample collection and preparation procedures and equipment.

D_e values were measured using the $IRSL_{50}$ SAR procedure previously tested on KF grains from alluvial sediments in the Middle Son Valley in Chapter 7 (Table 7-3), using consecutive regenerative doses of 46, 68, 91, 114, 0, and 68 Gy. Dose-response curves were fitted with a single saturating exponential function. Fading tests were conducted on all aliquots used for D_e determination using the procedure outlined in Chapter 7 (Table 7-4). As in Chapter 7, the fading rate of each aliquot was quantified using the *g*-value normalised to 2 days (Huntley & Lamothe 2001), and the age of each aliquot was corrected for fading using the correction model of Huntley and Lamothe (2001).

8.3.3 Environmental dose rate determination

The environmental dose rates for all IRSL samples were determined following the procedures outlined in Chapter 3. The water content of the sediments was measured in the laboratory, and the external dose rate was calculated for an estimated long-term, time-averaged water content of 5 ± 2% or 10 ± 2%, depending on the measured water content in the laboratory, which range from 0.3 to 9.1%. These values take into consideration the free-draining nature of the sampled sediments, their collection during the dry season, and the monsoonal climate of the region.

8.4 Results

8.4.1 Alluvial terraces and sediments south of the Son River

The topographic profiles and the elevations of all IRSL sample sites are shown in Figure 8-4. Dhaba site 3 is located ~20 m above river level, and is situated in colluvium derived from the bedrock ridge on the north side of the Son River. The top of the bedrock ridge is more than 40 m above river level. On the south side of the river, the highest alluvial terraces are ~25 to ~30 m above river level, and the lowest terraces are ~10 m above river

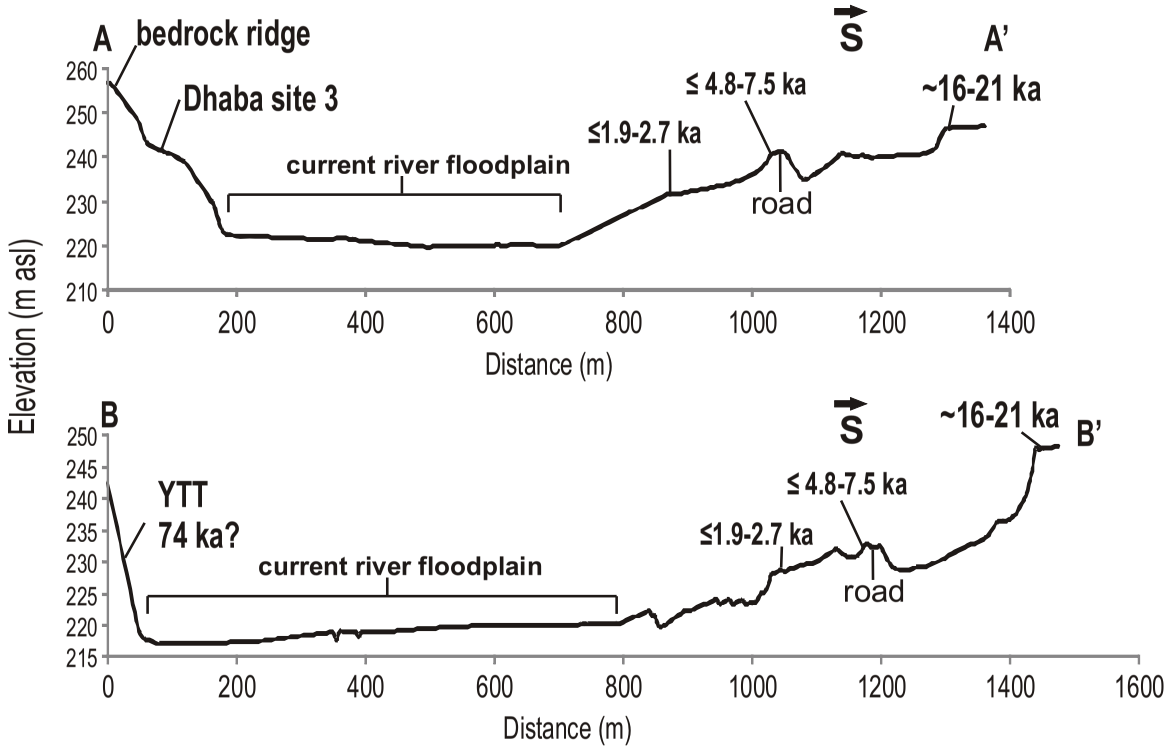

Figure 8-4. Topographic profiles A-A' and B-B'. The current river floodplain, as well as IRSL age estimates of near-surface alluvial sediments are indicated. The depositional age of the YTT is unclear (see Chapter 7). The elevation of YTT as in the Ghoghara main section is shown in B-B'. See Figure 8-2c for a plan view of the traverses and IRSL sample locations.

Figure 8-5. Alluvial sediments sampled for luminescence dating. Samples H-1 and H-5 were taken from the highest terrace south of the Son River. Samples M-2, M-4 and M-6 were taken beside the dirt road ~240-340 m away from the river channel. Samples L-3 and L-7 were taken in gullies near the edge of the lowest terrace. Meter stick for scale. Refer to Figure 8-2c for sample locations.

level. A dip in the topography appears immediately south of the road in both profiles, and this is presumably the result of excavation during road construction.

The sampled sediments on the highest terrace (H-1 and H-5) are dominated by massive, yellowish brown (10 YR 5/6) silt with few calcium carbonate nodules (Fig. 8-5). The sediments located approximately halfway between the highest terrace and the river channel, at ~20 m above river level (M-2, M-4, M-6), are much coarser. At the site of sample M-2, they are characterized by brown (7.5 YR 4/6), matrix-supported coarse sand, pebble-gravel and cobbles. Those at the M-4 sample site are brown (7.5 YR 5/6), crudely-bedded coarse sand, granules and pebbles that are oxidized on the surface, but less so below the surface. The sediments at the site of M-6 are characterised by brown (7.5 YR 5/6) unsorted and massive pebbley coarse sand, overlain by matrix-supported coarse sandy pebble-cobble gravel. The sediments in the lowest terrace (L-3 and L-7) are relatively fine-grained. Sediments at the site of sample L-3 consist of dark yellowish brown (10 YR 4/4), massive silty-fine sand with a rounded cobble-boulder lens. Those at the site of sample L-7 are dominated by yellowish brown (10 YR 5/6) massive silt (Fig. 8-5).

The silts deposited on the highest alluvial terrace, and the silts and silty fine sands deposited on the lowest terrace, are likely low-energy floodplain deposits and are consistent with the sedimentological characteristics of the fine member of the Baghor Formation and of the Khetaunhi Formation, respectively (Table 1-1). The structureless coarse sand and pebble-cobble gravels observed ~20 m above river level likely record high energy flow and rapid deposition within a palaeo-Son River channel dominated by bed-load transport. These deposits could be considered most consistent with the sedimentological characteristics of the Patpara Formation (Table 1-1), but IRSL age estimates reported below suggest that they are much younger than the age assigned by Williams *et al.* (2006).

8.4.2 IRSL age determination

The D_e values, average recycling ratios, recuperation values, fading rates, OD values and fading-corrected age estimates for all samples are listed in Table 8-1. A typical IRSL decay curve and dose-response curve are shown in Figures 8-6 ‘a’ and ‘b’, respectively. Recycling ratios for all aliquots measured are statistically consistent with unity (at 1σ), suggesting that sensitivity correction in the SAR sequence is adequate (Table 8-1). Sample-averaged recuperation values range from ~2 to ~8% of the sensitivity corrected natural signal. The two youngest samples, collected from the lowest terrace adjacent to the Son River (samples L-3 and L-7), exhibit the highest relative recuperation. A typical fading plot is shown in Figure 8-6 ‘c’ and the *g*-value distribution of all aliquots from all samples is shown in Figures 8-6 ‘d’ and ‘e’. The sample-averaged fading rates of all samples range from ~3 to ~4 %/decade and appear to be independent of sample location (Table 8-1).

Table 8-1. D_e values, fading rates, and calculated IRSL age estimates for all samples.

IRSL sample #	Sample location (elevation in m asl)	D_e (CAM)[1] (Gy)	n	Average Recycling Ratio	Average Recup. (%)	Uncorrected CAM[1] age (ka)	*g*-value (%/decade)	OD[2] (%)	Fading-corrected CAM[1] age estimate (ka)[2]	Fading-corrected MAM[1] age estimate (ka)[2]
H-1	highest terrace (~27)	48.2 ± 1.0	24	1.01 ± 0.03	2.0 ± 0.1	12.4 ± 0.4	3.2 ± 0.1	8 ± 2	21.4 ± 0.7	20.9 ± 2.0
M-2	dirt road (~20)	20.5 ± 1.9	24	1.00 ± 0.03	5.0 ± 0.1	7.1 ± 0.7	3.5 ± 0.1	47 ± 7	9.7 ± 1.1	5.6 ± 0.6
L-3	lowest terrace (~10 m)	7.8 ± 1.2	24 (16)	1.00 ± 0.03	8.0 ± 0.3	1.6 ± 0.3	3.6 ± 0.1	76 ± 11 (53 ± 10)	3.9 ± 0.6 (5.1 ± 0.7)	1.9 ± 0.2 (1.9 ± 0.2)
M-4	dirt road (~20 m)	18.9 ± 1.5	24	1.00 ± 0.03	5.0 ± 0.2	7.5 ± 1.6	4.0 ± 0.1	48 ± 7	11.0 ± 1.2	4.8 ± 0.3
H-5	highest terrace (~30 m)	40.5 ± 0.8	24	1.00 ± 0.03	2.0 ± 0.1	12.0 ± 0.4	3.6 ± 0.1	5 ± 2	16.5 ± 0.6	16.5 ± 0.6
M-6	dirt road (~20 m)	28.8 ± 2.7	24	1.00 ± 0.03	4.0 ± 0.1	11.3 ± 1.3	3.6 ± 0.1	45 ± 7	15.3 ± 1.7	7.5 ± 0.9
L-7	lowest terrace (~10 m)	11.2 ± 0.9	24 (23)	1.00 ± 0.03	8.0 ± 0.3	2.8 ± 0.3	3.7 ± 0.1	44 ± 6 (45 ± 7)	3.8 ± 0.3 (3.8 ± 0.4)	2.7 ± 0.2 (2.7 ± 0.2)
GHO-2 (below YTT)	Ghoghara main section	54.6 ± 1.7	24	1.01 ± 0.03	1.18 ± 0.04	22.6 ± 1.0	3.1 ± 0.1	20 ± 4	29.3 ± 1.7	21.3 ± 1.6
GHO-3 (above YTT)	Ghoghara main section	77.7 ± 1.9	24	1.00 ± 0.03	1.28 ± 0.04	25.3 ± 0.9	3.1 ± 0.1	13 ± 2	34.4 ± 1.4	31.2 ± 2.0

[1]Age estimates have been calculated from fading-corrected aliquot ages using the CAM and the MAM. A 0.635 ± 0.003 Gy residual dose (measured from KF aliquots that were bleached in the sun for 2 days, see Chapter 7) was subtracted from all fading-corrected D_e values (and the error propagated into the final D_e value). A possible 2% beta source calibration error has been added in quadrature to the D_e error.

[2]The ages in parantheses were calculated after rejecting aliquots with recuperation values greater than 10%. Eight aliquots were rejected from L-3, but only one from L-7.

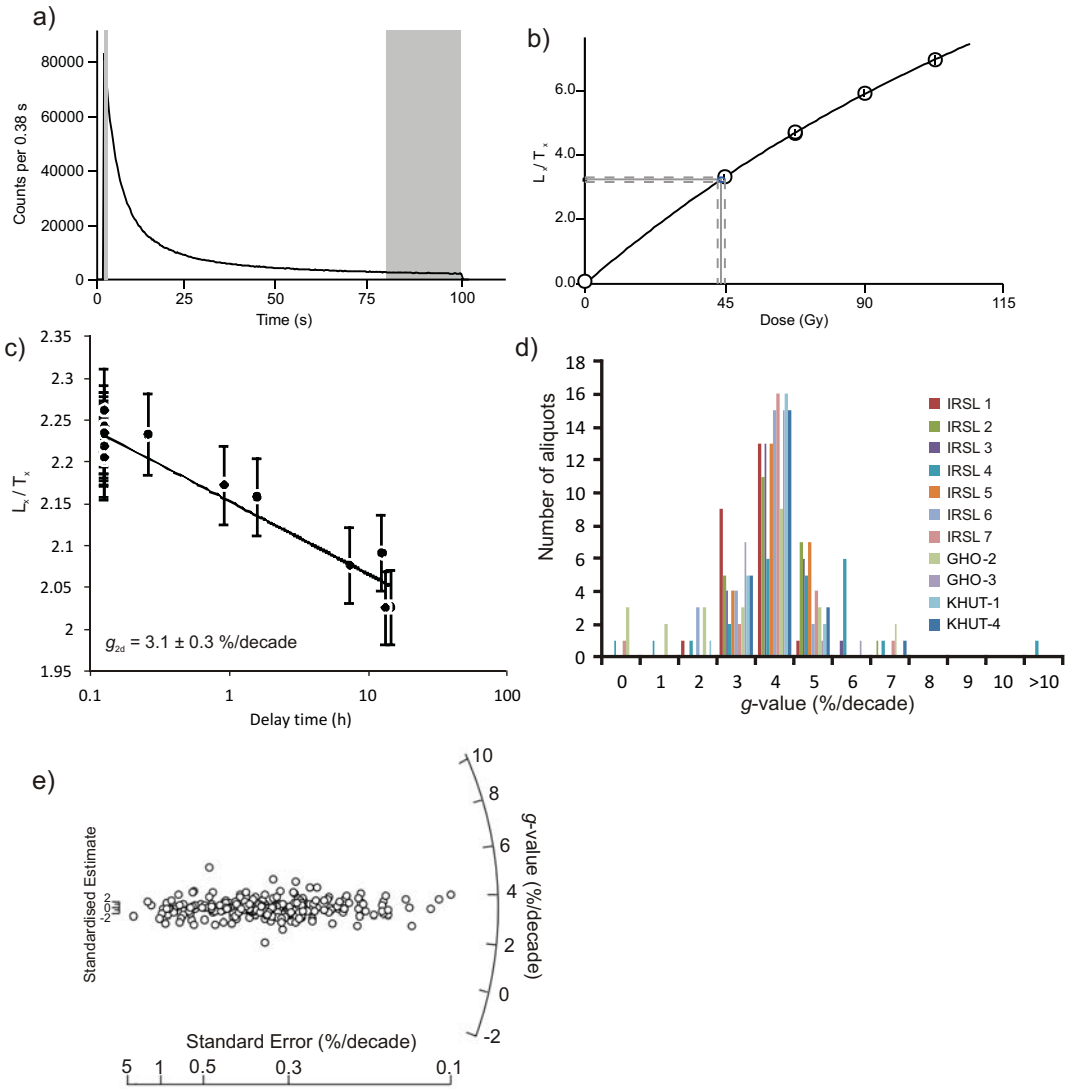

Figure 8-6. Typical IRSL decay curve (a) and dose-response curve (b) for sample H-1. IRSL signal in the first 1 s of stimulation minus the mean background from the last 20 s of stimulation (grey shading in 'a') was used to calculate the D_e values and estimate the fading rates. c) A fading plot for one aliquot from sample H-1. d) Calculated *g*-values for aliquots from all samples in Table 8-1, as well as two samples (KHUT-1 and KHUT-4) collected from above and below YTT ash at the Khunteli Formation type-section (n=264). e) The same *g*-values in 'd' displayed in a radial plot.

Calculated environmental dose rates for all samples collected south of the Son River range from ~2.5 to ~4.8 Gy/ka (Table 8-2).

Fading-corrected aliquot ages for each sample are plotted in radial plots in Figure 8-7. OD values are the lowest for the samples collected from the highest terraces (less than 10%), and highest for samples collected from the dirt road (~45%) and the lowest terrace (up to ~76%) (Table 8-1, Fig. 8-7). Single-grain quartz OSL age distributions from samples GHO-2, GHO-3, KHUT-1 and KHUT-4, and one single-grain KF age distribution from sample GHO-2, have high OD values (~35–45%) and a multi-component structure, while luminescence measurements made on KF grains from a modern sample collected from a sand bar in the Son River channel (KHUT-10) suggest that the source traps for the $IRSL_{50}$ signal in river-transported KF grains are well bleached (Chapter 7). This evidence suggests that overdispersed samples from alluvial deposits in the Middle Son Valley may consist of a mixture of relatively well-bleached fluvial grains and potentially poorly-bleached grains from slumped riverbank deposits (Chapter 7). This may explain a significant proportion of the OD observed in samples M-2, M-4, M-6, L-3 and L-7.

The relatively low OD values associated with the highest terraces (samples H-1 and H-5) may be attributed to: 1) better bleaching conditions on a floodplain surface than within higher-energy depositional environments associated with the medium-coarse sands observed at lower elevations; and/or 2) a negligible contribution of sediment from slumped older riverbank material, due to the absence of any proximal steep (palaeo-) riverbank at the time of sediment deposition. Because the KF aliquots in samples M-2, M-4, M-6, L-3 and L-7 may not consist of completely bleached grains, and/or may contain grains derived from slumping, the MAM was used to estimate the ages of aliquots containing grains that were exposed most recently to sunlight (Table 8-1). Ages have also been calculated using the CAM, for comparison (Table 8-1). As shown in Chapter 7, because of grain-averaging effects, the MAM ages of overdispersed samples (M-2, M-4, M-6, L-3 and L-7) should be considered only as maximum IRSL ages, which may overestimate the time that a significant proportion of grains in each sample were last exposed to sunlight.

Separate age estimates have been calculated for Samples L-3 and L-7 after rejecting all aliquots with recuperation values greater than 10% of the natural signal (ages in parentheses, Table 8-1). This led to a CAM age estimate increase of ~ 1 ka (from ~4 ka to ~5 ka) in L-3, where eight aliquots were rejected, but this change in age is not significant at 2σ. There was no change in the CAM age of IRSL sample L-7, for which only one aliquot was rejected. The MAM ages were not affected for either sample.

Table 8-2. Environmental dose rates for all samples.

		Water (%)[1]		Dose Rates (Gy/ka)			
IRSL sample #	**Sample location**	**Field**	**Used**	**Beta**	**Gamma**	**Cosmic**	**Total[2]**
H-1	highest terrace	2.5	5 ± 2	1.54 ± 0.08	1.18 ± 0.04	0.19 ± 0.02	3.91 ± 0.10
M-2	dirt road	3.6	5 ± 2	1.08 ± 0.09	0.65 ± 0.02	0.18 ± 0.02	2.91 ± 0.11
L-3	lowest terrace	4.6	10 ± 2	2.10 ± 0.09	1.51 ± 0.05	0.17 ± 0.02	4.79 ± 0.11
M-4	dirt road	0.8	5 ± 2	0.76 ± 0.08	0.60 ± 0.02	0.19 ± 0.02	2.55 ± 0.10
H-5	highest terrace	8.9	10 ± 2	1.38 ± 0.07	0.90 ± 0.03	0.17 ± 0.02	3.45 ± 0.09
M-6	dirt road	1.6	5 ± 2	0.81 ± 0.16	0.57 ± 0.02	0.18 ± 0.02	2.56 ± 0.17
L-7	lowest terrace	9.1	10 ± 2	1.75 ± 0.15	1.17 ± 0.04	0.18 ± 0.02	4.10 ± 0.16
GHO-2 (below YTT)	Ghoghara main section	0.3	5 ± 2	0.72 ± 0.05	0.61 ± 0.03	0.09 ± 0.01	2.42 ± 0.08
GHO-3 (above YTT)	Ghoghara main section	0.9	5 ± 2	1.05 ± 0.05	0.91 ± 0.05	0.11 ± 0.01	3.07 ± 0.09

[1]Measured water contents are shown as 'field', and long-term averaged water contents are shown as 'used'. Uncertainties are assigned to accommodate (at 2σ) the field values and any likely variation in water content since sample deposition.

[2]Total dose rate includes environmental beta, gamma, and cosmic ray dose rates, as well as an internal dose rate of 1.00 ± 0.05 Gy/ka derived from U, Th, ^{40}K, and ^{87}Rb inside the K-feldspar grains.

a) H-1 (highest terrace)
OD = 8 ± 2%

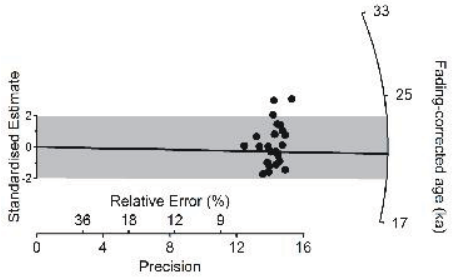

b) Sample M-2 (dirt road)
OD = 47 ± 7%

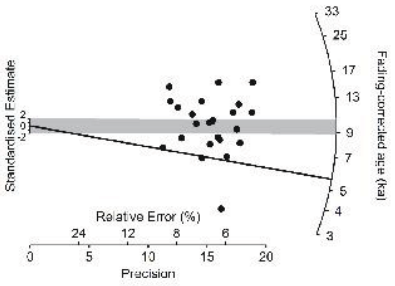

c) Sample L-3 (lowest terrace)
OD = 76 ± 11%

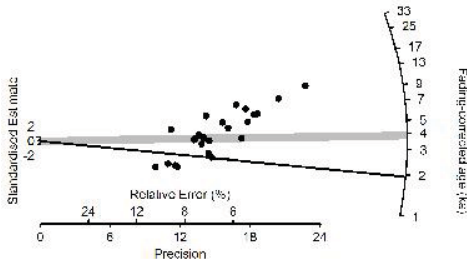

d) Sample M-4 (dirt road)
OD = 48 ± 7%

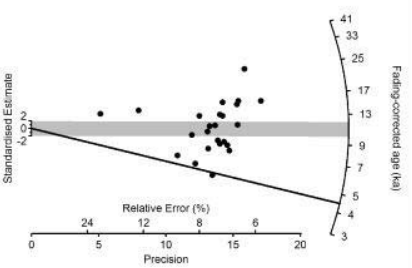

e) Sample H-5 (highest terrace)
OD = 5 ± 2%

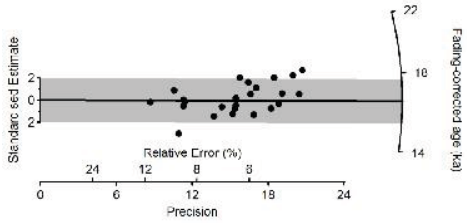

f) Sample M-6 (dirt road)
OD = 45 ± 7%

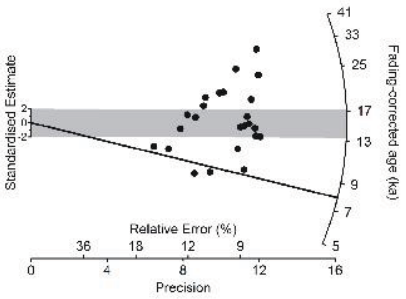

g) Sample L-7 (lowest terrace)
OD = 44 ± 6%

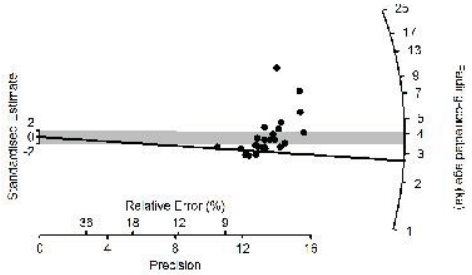

Figure 8-7. $IRSL_{50}$ fading-corrected aliquot ages for each sample, displayed on a radial plot. The grey shaded area is centered on the CAM age estimate and should capture 95% of the points if they were statistically consistent with each other (Galbraith *et al.* 1999). The black line is centered on the MAM age estimate.

8.5 Discussion

8.5.1 Consistencies with previously reported age estimates

IRSL age estimates in this study suggest that the uppermost floodplain silts in the highest alluvial terrace on the south side of the river are ~16 to 21 ka (Fig. 8-4, Table 8-1). The partially oxidized coarse sands and gravels exposed ~5–10 m below this yield maximum age estimates of ~4.8–7.5 ka, and the silts and silty sands exposed near the top of the lowermost terrace, adjacent to the Son River, yield maximum age estimates of ~1.9 ka and ~2.7 ka (Fig. 8-4, Table 8-1). Pal *et al.* (2005) reported IRSL ages from samples BN-1, BN-2, and BN-3 from the Baghore Nala, which is the type-section for the Baghor Formation (Fig. 1-1a). BN-3 was collected from the lower part of the coarse member and dates to ~39 ± 9 ka, BN-2 was collected from the middle part of the coarse member and dates to ~24 ± 3 ka, and BN-1 was collected from the upper fine member and dates to ~19 ± 2 ka (Chapter 1, Table 1-2). Though these ages were not corrected for fading and thus should be interpreted as minimum ages, the IRSL age of BN-1 is comparable to the IRSL ages from the uppermost silts in the highest alluvial terrace in the study area (samples H-1 and H-5, Table 8-1), suggesting that these silts are correlative with the fine member of the Baghor Formation. According to the Williams *et al.* (2006) model, fluvial incision of the Middle Son Valley alluvium commenced ~16 ka after a period of aggradation between ~39 and ~16 ka. Luminescence ages of the highest terrace reported here are consistent with the termination of accumulation of Baghor fine member silts, and the beginning of fluvial incision of the valley alluvium ~16 ka. The two maximum age estimates of the lowest terrace in the study area are slightly lower than previously reported radiocarbon age estimates of 3.215 ± 0.07 ka and 4.74 ± 0.08 ka from shell and a radiocarbon age estimate of 4.13 ± 0.11 ka from charcoal associated with the Khetaunhi Formation (Table 1-2) (Williams & Clarke 1984).

8.5.2 Inconsistencies with the Williams *et al.* (2006) model

Contrary to the predictions of the Williams *et al.* (2006) model (Fig. 8-1), IRSL age estimates suggest that the near-surface alluvial sands and gravels ~20 m above river level are at least ~33 ka younger than the proposed age of the Patpara Formation, and at least ~9 ka younger than the proposed age of the Baghor Formation and the uppermost floodplain silts in the highest alluvial terrace (Table 8-1, Fig. 8-1). These results suggest that the alluvial surface ~20 m above river level is not an erosional feature exposing sediments correlative with the Patpara Formation, but rather a depositional feature consisting of high-energy sands and gravels that were deposited during a brief aggradational phase between ~5 and ~16 ka. However, because only near-surface sediments were sampled in this study, we cannot

exclude the possibility that sediments of Patpara-age or older exist at some depth below the surface.

8.5.3 Chronological evidence for northward migration of the Son River

Maximum age estimates from samples collected above and below YTT ash units at the Ghoghara main section are ~31 and ~21 ka, respectively (Chapter 7, Table 7-5, Fig. 8-4). The main quartz FMM component ages for these samples (which are assumed to approximate the burial age of the sample and not ages of intrusive grains derived from plant roots) are ~44 and ~36 ka, respectively, and are considered more accurate age estimates (Table 7-5, Chapter 7). As discussed in Chapter 7, the YTT ash at the Ghoghara main section may be *in situ* and mark a chronostratigraphic horizon of ~74 ka, and the underlying sands may be younger inset fluvial sediments; or the YTT ash could have been reworked and re-deposited long after the YTT event, between ~36 and ~44 ka ago. In either case, the YTT ash and sediments are thought here to be older than ~16 ka, suggesting that while young (post-~16 ka) inset alluvial sediments have been deposited on the south side of the Son River near the Rehi-Son confluence, similar deposits appear to be absent on the north side (Fig. 8-4). This indicates a general northward migration of the Son River channel after ~16 ka, which may still be continuing today.

8.5.4 Modifications to the Williams *et al.* (2006) model

In light of the new IRSL ages reported in this study, modifications to the model of Williams *et al.* (2006) near the Rehi-Son River confluence are introduced (Fig. 8-8). IRSL age estimates from the topmost terrace mark the termination of deposition of the Baghor Formation fine member silts ~16 to ~21 ka ago. Maximum IRSL age estimates of ~1.9–2.7 ka mark the termination of deposition of the Khetaunhi Formation silts and the sands on the lowest terrace. Maximum IRSL age estimates of ~5–7 ka mark the termination of deposition of a mantle of coarse sands and gravels of unknown thickness between the highest and lowest terraces that was deposited by high energy flow in a palaeo-Son River channel dominated by bed-load transport. Because the luminescence samples reported here were collected from near-surface sediments, additional excavations, ideally including deep sediment cores, detailed logging of sediments, in conjunction with additional numerical ages will be needed to determine if there are any deposits with sedimentological characteristics and ages that are consistent with the Patpara, Khunteli and Sihawal Formations of the stratigraphic model of Williams *et al.* (2006).

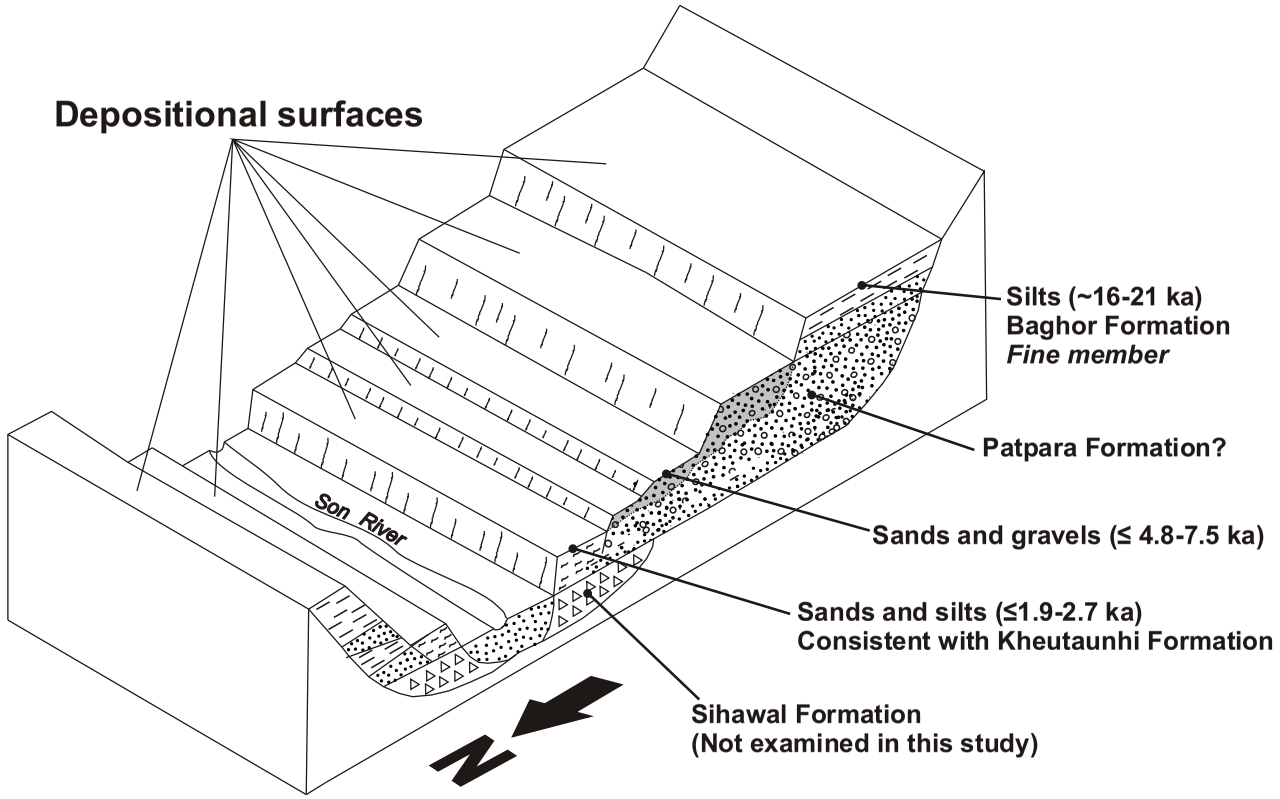

Figure 8-8. Schematic cross-section of the Middle Son Valley looking east from the Rehi-Son confluence, modified after Williams and Royce (1983). Proposed ages of near-surface sediments on the south side of the Son River are based on IRSL age estimates from this study. Sediments consistent in age and sedimentology of the Patpara Formation of Williams *et al.* (2006) may exist at some depth below the surface (see text for explanation). See Figure 8-1 for a specific definition of "depositional surface".

8.5.5 The palaeo-Son River response to past changes in SW Indian monsoon intensity – multiproxy records spanning the last 150,000 years

The climate of the Middle Son Valley (as well as the Belan Valley) is influenced by the Southern Oscillation, the NE (winter) monsoon, and to a large extent, the SW (summer) monsoon (Prasad & Enzel 2006; Williams *et al.* 2006). Prell and Kutzbach (1987) compared a range of palaeoclimate records of the Indian-African monsoon in order to identify the common patterns of SW monsoon variability over the past 150,000 years. These included the SPECMAP composite $\delta^{18}O$ record from Imbrie *et al.* (1984), the record of African aridity based upon *Melorsira* abundance in aeolian sedimentary records (Pokras & Mix 1985), the tropical lake level record, indicating the percentage of lakes in the intertropical zone that are at high or intermediate levels (Street-Perrott & Harrison 1984), the Mediterranean sapropel index, indicating presence or absence of sapropels associated with high tropical African monsoon runoff that reaches the Mediterranean via the Nile River (Rossignol-Strick 1983), the record of monsoon-related pollen in the Gulf of Aden (van Campo *et al.* 1982), the faunal record of monsoon-related upwelling off Arabia (Prell 1984), and the faunal record of salinity and the sea surface temperature of the western Indian Ocean (Prell & Kutzbach 1987). Most palaeoclimate records show four strong SW monsoon-related events that roughly coincide with the four major maxima of northern hemisphere summer radiation at about 10, 82, 104, and 126 ka (Fig. 8-9). The palaeoclimate records are most consistent with the solar radiation record during the last interglacial stage (~125–75 ka) and show less coherent variability from about 75 to 15 ka when the radiation maxima were not as pronounced and when the extent of the ice sheets (inferred from large values of the $\delta^{18}O$ index) was largest.

Patterns of past changes in monsoon intensity for the last 20,000 years are reflected in marine records from the Arabian Sea and palaeoclimate data compiled from terrestrial records from 26 sites in NE Africa, Arabia and India (Overpeck *et al.* 1996, and references therein). These show that the SW Indian monsoon was significantly weaker than present during glacial times (~18 ka). Abrupt increases in monsoon strength appear at ~14.5 ka and 11.4 ka and monsoon intensity reaches a maximum between ~11.5 and 5.0 ka (Overpeck *et al.* 1996).

Clemens and Prell (2003) examined five summer-monsoon proxies (comprised of chemical, biological, and physical indicators) obtained from cores from the Arabian Sea. Each proxy is linked to summer-monsoon variability through independent origins within the oceanographic and atmospheric systems. Visual comparison of the records show that the timing of climatic events is similar, but differences exist in the relative amplitudes of monsoon events in each proxy due to differing impacts of dissolution, preservation, and source area changes. To extract a clearer monsoon-related signal from the time-series data,

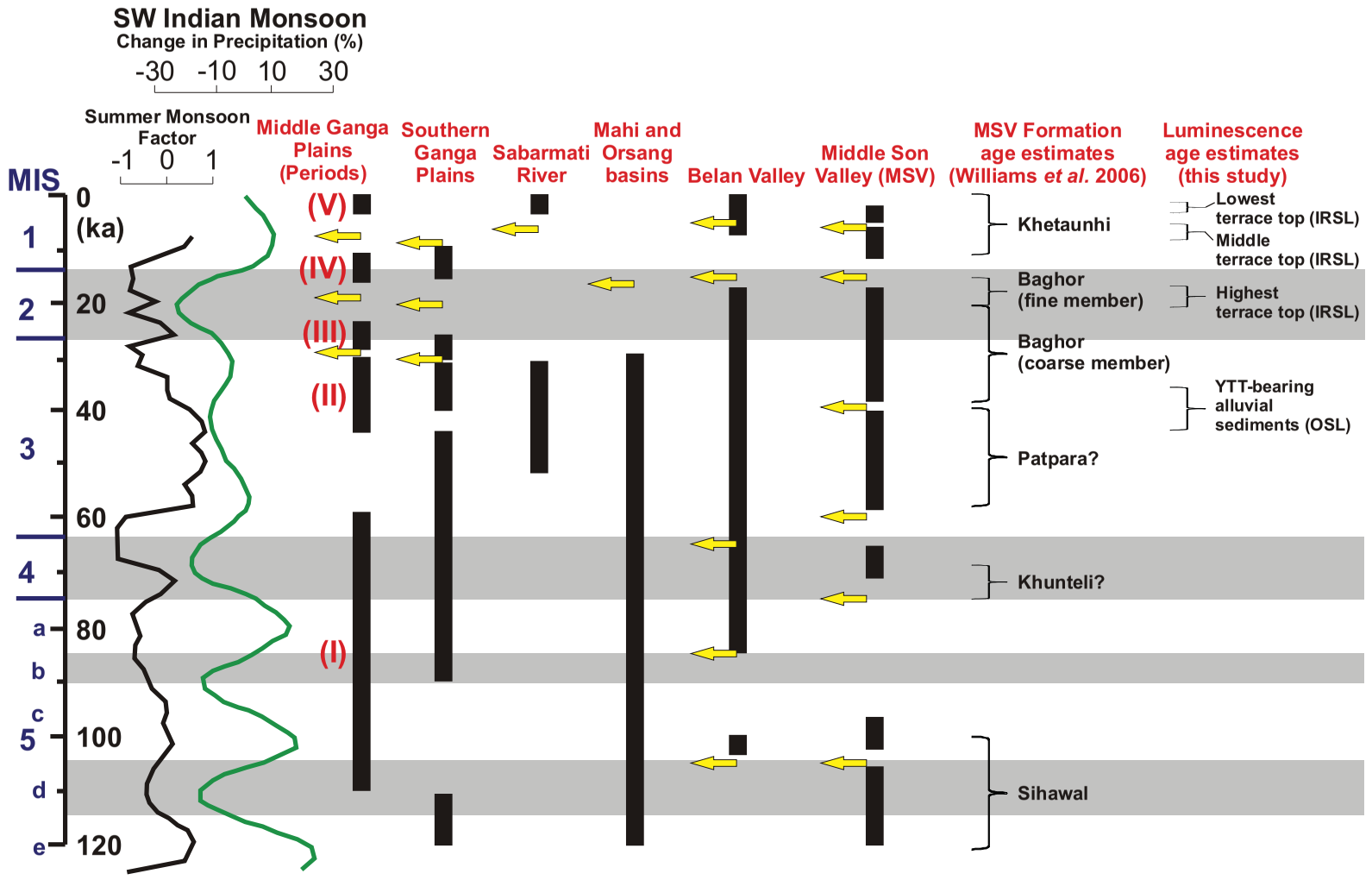

Figure 8-9. The Summer Monsoon Factor of Clemens and Prell (2003) based on stacked Arabian Sea core records and the modelled SW Indian monsoon record is from Prell and Kutzbach (1987). The boundaries between marine isotope stages (MIS) are from Waelbroeck *et al.* (2002). Periods of alluvial aggradation and incision for the Middle Ganga Plains (Roy *et al.* 2011), the southern Ganga Plains (Gibling *et al.* 2005), the Sabarmati River (Srivastava *et al.* 2001) the Belan Valley (Gibling *et al.* 2008) and the Middle Son Valley (Williams *et al.* 2006) are indicated by black bars. Yellow arrows mark incision events. The timing of alluviation and incision is approximate. The Middle Son Valley formation age estimates are from Williams *et al.* (2006) and the luminescence age estimates are from this study (Tables 7-5 and 8-1).

statistical analyses (stacking and principal component analysis) were used to average out the non-monsoon variance. Principal component analyses yielded a plot (called the Summer Monsoon Factor, Fig 8-9) that is considered the most robust representation of relative amplitude through time. This plot shows that strong monsoon signals appear in non-glacial intervals MIS 3, 5a, c and e. Figure 8-9 suggests that strong monsoon signals occur between the present and ~13 ka, at around 25 ka, between ~30 and 60 ka, around ~70 ka, between ~80 and 110 ka, and between ~110 and ~150 ka (Clemens & Prell 2003). The post-LGM increase in monsoon intensities detected by multiproxy records may be responsible for an increase in the palaeo-Son River discharge and incision of the Middle Son Valley floodplain after ~16–21 ka (Fig. 8-9).

8.5.6 Lacustrine records of monsoon intensity in north India during the Holocene

Palaeoclimate records from lakes in north India including pollen, sedimentology, geochemistry, and mineralogy proxies shed some light on the regional Holocene climate history (Sharma *et al.* 2004; Prasad & Enzel 2006) (Fig. 8-10). The most rigorous record from Lake Didwana (NW India) shows a shift from arid steppe vegetation to shrub savanna grassland at ~12.8 ka. This is followed by savanna grassland vegetation from ~7.4 to ~6.0 ka and a sub-humid phase from ~6.0 to 4.1 ka. Semi-arid savanna grassland is present from ~4.1 ka to the present (Prasad & Enzel 2006). Lake level indicators of the same lake suggest that the lake fluctuated between dry/saline to moderate-deep freshwater conditions as a result of increased monsoon precipitation between ~12.8 ka and ~7.5 ka. Subsequently, freshwater conditions became more frequent with dry hyper-saline conditions ~7.6–6.7 ka followed by freshwater conditions from ~6.7 to 5.9 ka. The lake continued to remain fresh until ~4.7 ka when it briefly dried out with mudcracks and subsequently, except for a short period ~1.3–0.8 ka when the lake level was relatively deep, the lake has remained ephemeral to the present day (Prasad & Enzel 2006) (Fig. 8-10). There are some discrepencies between the pollen and sedimentological/mineralogical data and these are attributed to the fact that lake level reflects precipitation transfer directly into the lake hydrology and is less dependent on additional ecological factors or complicating physical factors related to pollen transport and deposition (Prasad & Enzel 2006).

Lake levels influenced by monsoon precipitation have been inferred from the sedimentology, mineralogy and isotopic composition of organic material and carbonates from Lake Lunkaransar (NW India) (Prasad & Enzel 2006) (Fig. 8-10). Sustained high lake levels appear to occur only between 7.2 and 5.3 ka, with a maximum level at ~6.0 ka. The final drop of the water table to below the surface occurred ~5.3 ka and the climate is thought to have remained very similar up until the present (Fig. 8-10). Lake levels inferred from C/N

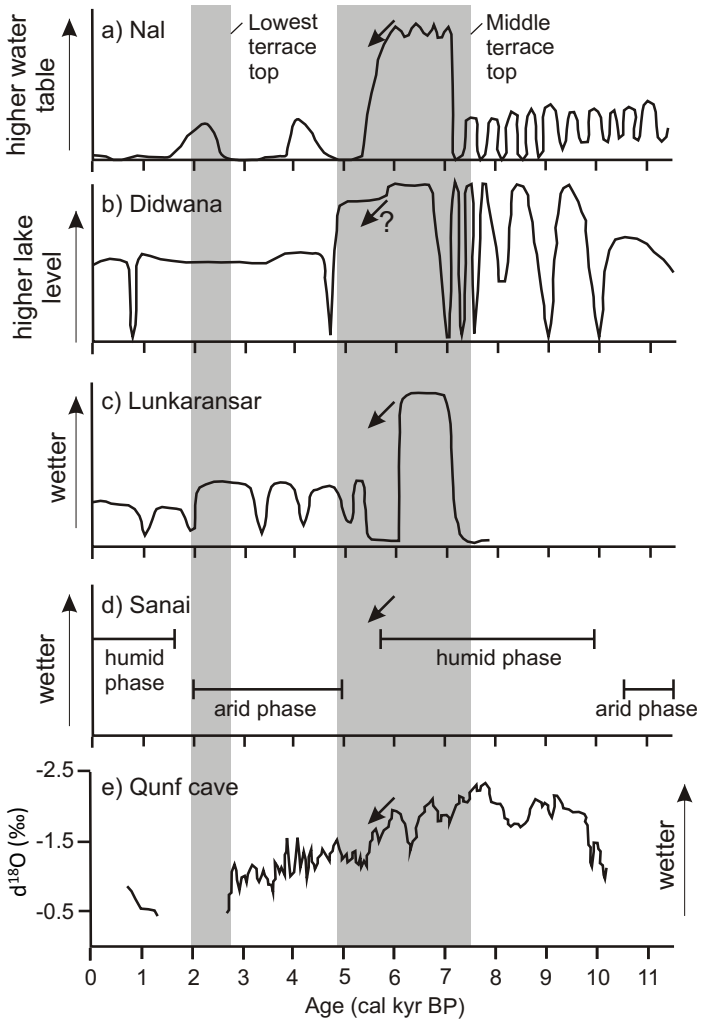

Figure 8-10. NW Indian lacustrine records from Prasad *et al.* (1997) (a), Wasson *et al.* (1984) (b), and Enzel *et al.* (1999) (c) as interpreted by Prasad and Enzel (2006), and the lacustrine record from Sharma *et al.* (2004) (d) as interpreted in this study. e) The speleothem isotope record from Oman (Fleitmann *et al.* 2003). The interpretation of the NW India lacustrine records is presented only in relative wetness terms for the different basins; the absolute water levels of lake or ground water or their transfer to values of precipitation are still problematic (Prasad and Enzel 2006). The Oman cave record was proposed to represent variations in SW monsoon rainfall. The arrow indicates the time when the trend towards aridity began as inferred by Prasad and Enzel (2006). The grey shaded areas represent the luminescence age estimates of the tops of the lowest (~10 m) and middle (~20 m) terraces across from the Rehi-Son confluence in the Middle Son Valley (this study).

ratios and $\delta^{13}C$ of organic matter from Lake Nal Sarovar (NW India) suggest an arid phase from ~7.8 to 7.2 ka followed by amelioration of the climate from ~7.2 to 6.1 ka. A particularly dry phase exists between ~6.1 and ~5.4 ka and this is followed by alternating periods of moderately wet to dry periods from 5.4 ka to the present day (Prasad & Enzel 2006) (Fig. 8-10).

An 18 ka pollen and isotope record from Sanai Tal Lake, on the Ganga Plain in NE India suggests that the lake expanded due to increased monsoon precipitation at about 15 ka, then contracted between ~12.2 and 13.4 ka (Sharma *et al.* 2004). At about 11.5 ka, the lake expanded again, reaching its maximum size at about 6.7 ka (Sharma *et al.* 2004) (Fig. 8-10). Arid phases were inferred from the isotope record at 15–13 ka, 11.5–10.5 ka and 5–2 ka (Sharma *et al.* 2004) (Fig. 8-10).

Lakes in north India show no persistent high lake levels as a result of SW monsoon precipitation during the early Holocene (~10–7 ka) (Fig. 8-10). This is in contrast to well-dated records of Holocene palaeoclimate from Arabian Sea cores (Sirocko *et al.* 1993; Prasad & Enzel 2006, Fig. 4) and speleothem isotope records from Oman (Fleitmann *et al.* 2003; Fleitmann *et al.* 2007) (Fig. 8-10) which generally show intensification of the monsoon from ~11.5 ka to ~5.5 ka before it weakens before the present day.

The IRSL age estimates from the tops of the second lowest (~20 m high) and lowest (~10 m high) terraces across from the Rehi-Son confluence provide age estimates for the termination of aggradation events during the Holocene in this reach of the Son River. Age estimates for the top of the second lowest terrace (M-2, M-4 and M-6) coincide with a "wet-to-dry" transition in all proxies that likely represent rapid decreases in monsoonal precipitation (Fig. 8-10). The recorded wet conditions may have been responsible for high river discharges and the transport and deposition of the coarse sand, pebble-gravel and cobbles observed in the middle terrace under a high-energy depositional environment. Subsequent northward channel migration and incision of the valley alluvium may have begun during a time when the intensity of the SW monsoon was decreasing (Fig. 8-10). The estimated age of the lowest terrace top coincides with the latter part of an arid phase recorded in the Lake Sanai and speleothem isotope records (Fig. 8-10). Therefore aggradation of this late Holocene terrace likely occurred during relatively arid conditions.

8.5.7 Fluvial sequences – The Gangetic Plains, the Belan Valley, and the southern margin of the Thar Desert

Fluvial sedimentary sequences tend to be complex, containing records of palaeoclimate that are patchy and/or of lower resolution than their lacustrine and marine counterparts. River planforms, bedloads and rates of incision and deposition are inherently linked to local tectonics, channel form history, sediment supply, climate, and, in areas

proximal to the coast, changes in sea level. Precipitation associated with the SW monsoon is thought to have had a prominent influence on river discharge and depositional processes in India throughout the late Pleistocene. Estimated periods of aggradation and incision are summarized for a series of Indian river stratigraphic records in Figure 8-9. This figure suggests that intensification of the SW Indian monsoon can lead to river incision or aggradation, depending on the local circumstances. The intensification of the SW monsoon is thought to have been responsible for changes in channel planforms, increases in sediment flux leading to net aggradation, and/or increases in stream power leading to channel incision (e.g., Srivastava *et al.* 2001; Gibling *et al.* 2005; Williams *et al.* 2006; Roy *et al.* 2011).

Fluvial and aeolian sequences from the southern margin of the Thar Desert, India have been used to infer the variability of the SW Indian monsoon over the past 130 ka (Juyal *et al.* 2006). The discharge, channel form and sediment budget of rivers in the Mahi and Orsang basins are thought to have responded to changes in monsoon intensity. Meandering river channel and floodplain sediments dated to 130–120 ka, 100–70 ka, and ~60–30 ka were inferred to represent periods of enhanced monsoon intensity. Braided channel sediments dated to ~120–100 ka and 70–60 ka, and widespread aeolian sediments dated to ~20–11 ka were inferred to represent periods of weak monsoon intensity (Juyal *et al.* 2006). These periods of weak monsoon intensity roughly correlate with the proposed time of deposition of the Sihawal Formation (MIS 5d) and the fine member of the Baghor Formation (MIS 2) (Fig. 8-9) (Williams *et al.* 2006). It is not clear whether or not the alluvial stratigraphy in the southern margin of the Thar Desert records river base level changes as a result of sea-level fluctuations.

Strata recording fluvial activity over the last 100 ka in the middle Ganga Plains record major periods of fluvial aggradation that occurred 111–59 ka (Period I), 45–30 ka (Period II), 30–23 ka (Period III), 16–11 ka (Period IV) and 2.7 ka to present (Period V) (Roy *et al.* 2011) (Fig. 8-9). Period I sediments record prolonged channel activity and some interfluve flooding, followed by floodplain deposition and pedogenesis. A similar period of persistent channel activity was recorded in the southern margin of the Ganga Plains (Gibling *et al.* 2008) (Fig. 8-9). Period II sediments include minor channel fills, aeolian and marsh sediments that are thought to record reduced monsoonal activity. Period III sediments record high-energy channel activity at ~28 ka and levee deposition at 34 and 26 ka, possibly associated with increased monsoon precipitation. These sediments are roughly correlative with the proposed time of deposition of the coarse member of the Baghor Formation and the time of deposition of the sediments bracketing YTT ash at Ghoghara and Khunteli (Fig. 8-10). The Baghor Formation is thought to represent a major phase of aggradation during a period of aridity leading up to and encompassing the LGM (Williams *et al.* 2006). No channel deposits that date between 28 and 15 ka have been found in the middle Ganga

Plains. Aeolian, floodplain and lacustrine deposits in the middle Ganga Plains suggest a cooler and drier climate towards the LGM. Period IV records channel aggradation and channel switching in a braided depositional environment with a high sediment supply. This may reflect landscape instability during monsoon intensification and may be correlative with the time of aggradation of the middle (~20 m high) terrace in the Middle Son Valley. A period of reduced discharged occurs between 13 and 11 ka in the middle Ganga Plains. Period V records late Holocene aggradation that may be associated with monsoon intensification (Roy *et al.* 2011) (Fig. 8-9).

Late Quaternary sequences in the southern Gangetic Plains (Himalayan Foreland Basin) are also thought to reflect floodplain aggradation and degradation in response to fluctuations in SW Indian monsoon intensities (Gibling *et al.* 2005). Fluvial/floodplain sedimentary sequences preserved within interfluves between major Himalayan and cratonic rivers record periodic aggradation between 90 and 27 ka (MIS 5–3) (Fig. 8-9). This was followed by a decrease in aggradation and the formation of underfit streams as a result of a decrease in precipitation during MIS 2. A subsequent increase in precipitation from 15 ka to 5 ka is thought to have promoted incision and widespread badland formation (Gibling *et al.* 2005). The start of this incision event roughly correlates with that proposed for the Middle Son Valley after ~16–21 ka (Fig. 8-9).

Alluvial sequences in the Belan River valley, like those of the Middle Son Valley, have been used as a source of palaeoclimatic information for north India (Gibling *et al.* 2008). The headwaters of the Belan River are in the Kaimur Hills and within 50 km northeast of the village of Sihawal. The main channel drains NW into the Tons, which in turn drains NE into the Ganga River. Sedimentary sections along the Belan River reveal channel-based calcretes above the bedrock that are overlain by mixed-load meandering river channel/floodplain sediments and soils (Gibling *et al.* 2008). Net aggradation of fluvial deposits occurred between ~85 and 16 ka (MIS 5–2) (Fig. 8-9). Channel deposition occurred predominantly from ~85 to 72 ka and was followed by floodplain buildup through to ~16 ka. This fining upward stratigraphic sequence that terminates around 16 ka is reminiscent of the coarse and fine members of the Baghor Formation in the Middle Son Valley, which are thought to record a trend toward aridification during MIS 2 (Williams *et al.* 2006). A prolonged period of fluvial activity in the Belan Valley is in accord with generally high precipitation levels in MIS 5–3. Some evidence for floodplain gullying and erosion at ~21–31 ka exists in the form of reworked gravel lenses in floodplain muds that may record reduced monsoonal precipitation around the LGM. Evidence for climatic instability is present in the form of fluvial and aeolian deposits at the Mahagara and Deoghat localities that range in age from 14 to 7 ka. Incision through terraced sediments as young as ~9 ka at the Mahagara locality has been interpreted to represent monsoon intensification and

increased fluvial energy post-9 ka. This period of wet climatic conditions leading to incision in the Belan Valley roughly correlates with the time of aggradation of the coarse sands and gravels in the middle terrace (~20 m above river level) in the Middle Son Valley (Table 8-1, Fig. 8-10). Decreasing monsoonal activity since ~6 ka is thought to be responsible for local inset terrace aggradation at Mahagara (Gibling *et al.* 2008). This aggradational event in the Belan Valley occurred at a similar time as the aggradational event in the Middle Son Valley that led to the creation of the lowest (~10 m high) terrace (Fig. 8-10).

8.6 Conclusions

In this chapter, the Williams *et al.* (2006) model of alluvial deposition for the Middle Son Valley was tested near the Rehi-Son confluence using cross-valley topographic profiles, field observations, and IRSL age estimates from terraced alluvial sediments. The age estimates for the highest terrace on the south side of the Son River are consistent with a previous IRSL age estimate of the fine member of the Baghore Formation (Pal *et al.* 2005), and the beginning of incision of the Middle Son Valley alluvium ~16 ka as predicted by the Williams *et al.* (2006) model. Maximum age estimates from the lowest terrace are ~1.9 and 2.7 ka, and are slightly younger than previously reported radiocarbon ages ranging from ~3 to ~5 ka associated with the Khetaunhi Formation (Williams and Clarke 1984).

The age estimates for the coarse sands and gravels that lie at intermediate elevations (~20 m above river level) between these two terraces contradict what is predicted by the model. According to the model, these sediments should be between ~40 and 58 ka in age and form part of the Patpara Formation, which has been exposed by fluvial erosion of the overlying Baghor Formation (Fig. 8-1). By contrast, maximum IRSL age estimates presented here suggest that these deposits are only up to ~5–7 ka in age and form inset sediments that were deposited during a brief aggradational phase, sometime after incision of the highest alluvial surface ~16 ka ago. Similar inset sediments appear to be absent on the north side of the Son River and this is indicative of a general northward migration of the river channel. Incision of the Middle Son Valley alluvium across from the Rehi-Son confluence began shortly after ~16–21 ka, probably as a result of SW monsoon intensification. The inset coarse sand and gravel at ~20 m above river level likely aggraded under wet conditions in the early Holocene, and the lowest (~10 m high) inset terrace probably aggraded under more arid conditions during the late Holocene.

Proposed modifications for the Williams *et al.* (2006) model have been made for terraced sediments near the Rehi-Son confluence. These data provide insights into the fluvial history of the Son River and will inform future archaeological surveys by constraining the geomorphic context of surficial and excavated artefacts in the area.

Chapter 9 – Summary, conclusions and recommendations for future research

The aims of this research were to: 1) to explore the luminescence dating potential of KF grains using individual grains and multi-grain aliquots from alluvial sediments in the Middle Son Valley using SAR dating techniques, fading measurements and corrections; 2) assess the time of final deposition of YTT ash-bearing deposits at the Ghoghara main section and the Khunteli type-section using luminescence dating techniques; and 3) test a model of alluvial deposition in the Middle Son Valley (Williams *et al.* 2006) using new IRSL ages and field observations. The main findings and their implications are summarized below.

9.1 The luminescence dating potential of KF grains using SAR dating techniques, fading measurements and corrections

9.1.1 Main findings

Dose recovery experiments in the laboratory suggest that KF grains in the Middle Son Valley are generally suitable for SAR procedures when measured at the multi-grain aliquot and single-grain level. Elemental analyses showed that contaminating quartz grains in KF-rich extracts can be identified by their decay curve characteristics and rejected from further analyses in single-grain studies and that grain-to-grain variations in internal K content will contribute little to the OD in KF single-grain fading-corrected age distributions for sediments examined in this study. The observed spread in individual KF grain fading-corrected ages from one sample (GHO-2) is attributed largely to sediment mixing. Comparisons between single-grain and multi-grain aliquot data from the same sample suggest that $IRSL_{50}$ KF aliquot ages can only serve as maximum age estimates, possibly producing ages within ~5–6 ka of the true burial age of a significant number of grains in a sample. Fading rates for KF grains in the Middle Son Valley average ~3 to 4 %/decade and grain-to-grain variations in fading rates are large (spanning a range of 0 to over 20 %/decade) compared to those of ~25 grain aliquots, which typically range from ~2 to 6 %/decade.

Post-IR IRSL signals have been shown to be less susceptible to fading (e.g., Thomsen *et al.* 2008; Buylaert *et al.* 2009; Thiel *et al.* 2011). However, for samples bracketing YTT ash, fading-corrected $pIRIR_{225}$ ages are ~1.5 to ~2 times those obtained from the $IRSL_{50}$ signal, even after subtraction of residual doses measured from aliquots that have been sun-bleached for 2 days. $IRSL_{50}$ and $pIRIR_{225}$ D_e values measured from a modern sample from a sand bar in the river channel suggest that the source traps of the $pIRIR_{225}$ signal are less susceptible to bleaching in the Son River than are those of the $IRSL_{50}$ signal. Thus, $pIRIR_{225}$ ages for alluvial sediments in the Middle Son Valley are considered less

reliable than $IRSL_{50}$ ages, despite the fact that they are less dependent on fading-correction models.

9.1.2 Implications and future research directions

Previously reported IRSL ages for alluvial sediments in the Middle Son Valley were determined using multiple-aliquot additive-dose methods and were not corrected for fading (Table 1-2) (Pal *et al.* 2005; Williams *et al.* 2006). In this study, KF grains are shown to be suited to the more robust SAR measurement procedure; when the IRSL signal was measured at 50°C, fading rates of ~2 to ~6 %/decade were measured from small aliquots and fading rates of 0 to more than 20 %/decade were measured from single grains. Thus, future luminescence studies that make use of $IRSL_{50}$ signals in KF grains from the Middle Son Valley should apply SAR measurement procedures. The inter-aliquot and inter-grain variability in fading rates observed in this study suggests that fading measurements and corrections should be made on each aliquot or grain used for D_e determination. Future luminescence investigations that attempt to overcome the problems of fading by measuring signals with low or negligible fading rates (including post-IR IR signals or MET-pIRIR signals) should also investigate the bleachability of these signals in waterlain sediments (e.g., Lowick *et al.* 2012).

9.2 Assessing the time of final deposition of YTT ash-bearing deposits at the Ghoghara main section and the Khunteli type-section using luminescence dating techniques

9.2.1 Main findings

Investigations into the time of final deposition of YTT ash deposits in the Middle Son Valley have yielded ambiguous results. All KF and quartz ages from the Ghoghara main section and the Khunteli type-section suggest that final deposition of the sediments bracketing the YTT ash occurred sometime (possibly up to a few tens of thousands of years) after the Toba volcanic super-eruption (Table 7-4). If we take the main quartz FMM component OSL ages, which range from ~36 to ~44 ka, to be the most accurate estimate of the depositional age of these samples in this study, then alluvial sediments above and below the YTT ash would be correlative with either the lower coarse member of the Baghor Formation or the uppermost sediments of the Patpara Formation of the Williams *et al.* (2006) model, as previously hypothesized by Achyrra and Basu (1993), Williams and Royce (1982), Williams and Clarke (1995), Jones and Pal (2005), and Jones (2010).

The luminescence ages in this thesis imply one of two things: 1) the YTT ash at Ghoghara and Khunteli has been reworked by fluvial processes and re-deposited either as fluvial silts, or as mobile, cohesive blocks, several thousand years after the Toba event, or 2)

the YTT ash was deposited soon after the volcanic event ~74 ka ago, but the underlying sediments have since been eroded and replaced by younger, inset fluvial sediments. There are no sedimentological features within the ash units, such as inclined bedding, or sharp irregular contacts with the surrounding sediment that might suggest that the ash has been remobilized as a cohesive block before deposition. It is possible that coarser sediment underlying the YTT ash units has been preferentially eroded and replaced by younger, inset fluvial sediments, however sedimentological evidence for this is lacking. All field observations suggest that the ash has been reworked by fluvial processes and re-deposited as fluvial silts.

9.2.2 Implications and future research directions

YTT occurrences across peninsular India have been considered by some to be an isochronous marker, allowing the use of overlying and underlying soils and carbonates as environmental proxies (Williams *et al.* 2006; Williams *et al.* 2009; Williams 2012b). The Khunteli Formation was introduced by Williams *et al.* (2006) to account for YTT ash-bearing sediments in the Middle Son Valley at the Ghoghara main section and at the Khunteli type-section. However, few aliquot or single-grain luminescence ages produced in this study approximate the age of the YTT event, casting doubt over the existence of the Khunteli Formation and the assumption that all YTT deposits in India can be used as a reliable chronostratigraphic marker (Acharyya & Basu 1993; Acharya & Basu 1994; Westgate *et al.* 1998; Williams *et al.* 2009). The impact of the ~74 ka (or ~73 ka according to Williams 2012a, b) Toba volcanic super-eruption on humans and ecosystems is still hotly debated (e.g., Oppenheimer 2002; Ambrose 2003; Gathorne-Hardy & Harcourt-Smith 2003; Louys 2007; Petraglia *et al.* 2007; Haslam & Petraglia 2010; Williams *et al.* 2010; Petraglia *et al.* 2012; Jones 2012; Williams 2012a), and this has been attributed to (among other reasons) the lack of precise and accurate chronologies for marine and terrestrial proxy records (Williams 2012b). The field observations and luminescence ages presented in this study suggest that, so far the Middle Son Valley is no exception. The previously proposed hypothesis that C_3 forest was replaced by wooded to open C_4 grassland in north-central India after the Toba eruption (Williams *et al.* 2009) is not supported by the data presented in this study. Luminescence investigations in this thesis suggest that sediments above and below YTT ash units at the Rehi-Son confluence and at the Khunteli Formation type-section were last deposited tens of thousands of years after the YTT event. Any soils, pedogenic carbonate nodules, and rootcasts associated with these deposits would have formed even later after sediment deposition, and thus should not be considered reliable proxies for palaeoenvironmental reconstruction before and after the Toba eruption.

Future research into the burial age of the YTT ash units at the Ghoghara main section and the Khunteli Formation type-section should include investigations of the luminescence dating potential of non-volcanic quartz and/or feldspar in the re-worked YTT layers mixed with fluvial silt and sand (e.g., the YTT ash-rich silt unit at the Khunteli Formation type-section, or the reworked layers above the ~4 cm so-called 'primary' ash at the Ghoghara main section (Jones 2010; Gatti *et al.* 2011)). Luminescence ages for the YTT ash itself could help resolve the issue of whether or not it was emplaced before or after the underlying sand units dated in this study. Such investigations could focus on the possibility of determining the burial age of the glass shards in the YTT ash, directly. These could include luminescence investigations of the possibility of isolating an OSL 'fast' component in glass shards (e.g., Berger & Huntley 1994; Tsukamoto *et al.* 2003) or a datable IRSL signal in volcanic plagioclase (e.g., Tsukamoto *et al.* 2010). TL ages from the glass shards could determine the most recent heating event and help resolve any uncertainties as to whether or not the ash is indeed YTT (and not MTT or OTT).

9.3 Testing and refining a model of alluvial deposition in the Middle Son Valley

9.3.1 Main findings

In this study, the Williams *et al.* (2006) model of alluvial deposition for the Middle Son Valley was tested near the Rehi-Son confluence using cross-valley topographic profiles, field observations, and IRSL age estimates from terraced alluvial sediments. IRSL age estimates from the topmost terrace, ~30 m above river level, mark the termination of deposition of the Baghor Formation fine member silts ~16 to ~21 ka ago. Maximum IRSL age estimates of ~1.9–2.7 ka, ~10 m above river level, mark the termination of deposition of the Khetaunhi Formation silts and the sands on the lowest terrace. Maximum IRSL age estimates of ~5–7 ka mark the termination of deposition of a mantle of coarse sands and gravels of unknown thickness ~20 m above river level that was deposited by high energy flow in a palaeo-Son River channel dominated by bed-load transport. The age estimates for the highest terrace on the south side of the Son River are consistent with a previous IRSL age estimate of the fine member of the Baghore Formation (Pal *et al.* 2005), and the beginning of incision of the Middle Son Valley alluvium ~16 ka as predicted by the Williams *et al.* (2006) model. Incision of the Middle Son Valley alluvium across from the Rehi-Son confluence began shortly after ~16–21 ka, probably as a result of SW monsoon intensification. The inset coarse sand and gravel at ~20 m above river level likely aggraded under wet conditions in the early Holocene, and the lowest (~10 m high) inset terrace probably aggraded under more arid conditions during the late Holocene.

9.3.2 Implications and future research directions

The IRSL ages and field observations made near the Rehi-Son confluence showed that the age of terraced alluvial sediments may not conform to the predictions of the Williams *et al.* (2006) stratigraphic model in all reaches of the Son River, and that oxidized fluvial sands and gravels found at intermediate (~15–20 m) elevations above river level should not be assigned to the Patpara Formation without independent chronological control. As pointed out by Haslam *et al.* (2011), the type locality for the Patpara Formation is separated from the main river system by a medial bedrock ridge, so the preserved sediments at Patpara were likely not deposited by a palaeo-Son River, but rather by more localized processes. Sediments near the base of an exposed sequence at the Patpara type locality have been dated to ~137 and ~140 ka using single-grain OSL techniques, suggesting that their deposition occurred at about the same time as sediments associated with the Sihawal Formation at Bamburi and Nakhjar Khurd (Section 1.2.2) (Haslam *et al.* 2011) rather than ~40–58 ka ago, as suggested by the Williams *et al.* (2006) model. More detailed mapping of sediments adjacent to the Son River, and more numerical ages from units that can be laterally traced over longer distances, should help to resolve these inconsistencies and constrain the timing of alluvial deposition and terrace formation in the Middle Son Valley. Both this valley, and its neighbour, the Belan Valley, record major phases in regional climate and human occupation of northern India (Sharma & Clark 1983; Williams *et al.* 2006; Sinha *et al.* 2007; Gibling *et al.* 2008). Improved chronological control on the stratigraphies of these valleys therefore has implications for enhancing our understanding the history of climate change and human occupation in India.

References

Acharyya, S. K. & Basu, P. K. 1993: Toba Ash on the Indian Subcontinent and its implications for correlation of Late Pleistocene alluvium. *Quaternary Research 40*, 10-19.

Acharyya, S. K. & Basu, P. K. 1994: Reply to Comments by S. Mishra and S. N. Rajaguru and by G. L. Badam and S. N. Rajaguru on "Toba Ash on the Indian Subcontinent and Its Implication for the Correlation of Late Pleistocene Alluvium". *Quaternary Research 41*, 400-402.

Adamiec, G. & Aitken, M. J. 1998: Dose-rate conversion factors: update. *Ancient TL 16*, 37-50.

Aitken, M. J. 1998: *An introduction to optical dating: The dating of Quaternary sediments by the use of photon-stimulated luminescence* 267 pp. Oxford University Press, Oxford, New York.

Aitken, M. J. & Smith, B. W. 1988: Optical dating: Recuperation after bleaching. *Quaternary Science Reviews 7*, 387-393.

Ambrose, S. H. 1998: Late Pleistocene human population bottlenecks, volcanic winter, and differentiation of modern humans. *Journal of Human Evolution 34*, 623-651.

Ambrose, S. H. 2003: Did the super-eruption of Toba cause a human population bottleneck? Reply to Gathorne-Hardy and Harcourt-Smith. *Journal of Human Evolution 45*, 231-237.

Anonymous 2007: Guide to "The Risø Single grain laser OSL system". Risø National Laboratory, Roskilde, Denmark.

Arnold, L. J., Bailey, R. M. & Tucker, G. E. 2007: Statistical treatment of fluvial dose distributions from southern Colorado arroyo deposits. *Quaternary Geochronology 2*, 162-167.

Arnold, L. J. & Roberts, R. G. 2009: Stochastic modelling of multi-grain equivalent dose (De) distributions: Implications for OSL dating of sediment mixtures. *Quaternary Geochronology 4*, 204-230.

Auclair, M., Lamothe, M. & Huot, S. 2003: Measurement of anomalous fading for feldspar IRSL using SAR. *Radiation Measurements 37*, 487-492.

Bailey, R. M. 1998: Depletion of the quartz OSL signal using low photon energy stimulation. *Ancient TL 16*, 33-36.

Bailey, R. M. 2010: Direct measurement of the fast component of quartz optically stimulated luminescence and implications for the accuracy of optical dating. *Quaternary Geochronology 5*, 559-568.

Bailey, R. M., Smith, B. W. & Rhodes, E. J. 1997: Partial bleaching and the decay form characteristics of quartz OSL. *Radiation Measurements 27*, 123-136.

Balter, M. 2010: Of two minds about Toba's impact. *Science 327*, 1187-1188.

Banerjee, D., Murray, A. S., Bøtter -Jensen, L. & Lang, A. 2001: Equivalent dose estimation using a single aliquot of polymineral fine grains. *Radiation Measurements 33*, 73-94.

Baril, M. R. 2004: CCD imaging of the infra-red stimulated luminescence of feldspars. *Radiation Measurements 38*, 81-86.

Baril, M. R. & Huntley, D. J. 2003: Infrared stimulated luminescence and phosphorescence spectra of irradiated feldspars. *Journal of Physics: Condensed Matter 15*, 8029.

Berger, G. W. & Huntley, D. J. 1994: Tests for optically stimulated luminescence from tephra glass. *Quaternary Geochronology 13*, 509-511.

Blair, M. W., Yukihara, E. G. & McKeever, S. W. S. 2005: Experiences with single-aliquot OSL procedures using coarse-grain feldspars. *Radiation Measurements 39*, 361-374.

Blumenschine, R. J., Brandt, S. A. & Clark, J. D. 1983: Excavations and Analysis of Middle Palaeolithic Artefacts from Patpara, Madhya Pradesh. *In* Sharma, G. R. & Clark, J. D. (eds.): *Palaeoenvironments and Prehistory in the Middle Son Valley, Madhya Pradesh, North-Central India*, 39-100 pp. A.H. Wheeler and Co, Private Limited, Allahabad.

Bøtter-Jensen, L., Andersen, C. E., Duller, G. A. T. & Murray, A. S. 2003: Developments in radiation, stimulation and observation facilities in luminescence measurements. *Radiation Measurements 37*, 535-541.

Bøtter-Jensen, L., Bulur, E., Duller, G. A. T. & Murray, A. S. 2000: Advances in luminescence instrument systems. *Radiation Measurements 32*, 523-528.

Bøtter-Jensen, L. & Mejdahl, V. 1985: Determination of potassium in feldspars by beta counting using a GM Multicounter System. *Nuclear Tracks and Radiation Measurements 10*, 663-666.

Bøtter-Jensen, L. & Mejdahl, V. 1988: Assessment of beta dose-rate using a GM multicounter system. *Nuclear Tracks and Radiation Measurements 14*, 187-191.

Brennan, B. J. 2003: Beta doses to spherical grains. *Radiation Measurements 37*, 299-303.

Bulur, E. 1996: An alternative technique for optically stimulated luminescence (OSL) experiment. *Radiation Measurements 26*, 701-709.

Bulur, E., Bøtter-Jensen, L. & Murray, A. S. 2000: Optically stimulated luminescence from quartz measured using the linear modulation technique. *Radiation Measurements 32*, 407-411.

Buylaert, J. P., Murray, A. S. & Huot, S. 2008: Optical dating of an Eemian site in Northern Russia using K-feldspar. *Radiation Measurements 43*, 715-720.

Buylaert, J. P., Murray, A. S., Thomsen, K. J. & Jain, M. 2009: Testing the potential of an elevated temperature IRSL signal from K-feldspar. *Radiation Measurements 44*, 560-565.

Buylaert, J. P., Thiel, C., Murray, A. S., Vandenberghe, D., Yi, S. & Lu, H. 2011: IRSL and post-IR IRSL residual doses recorded in modern dust samples from the Chinese Loess Plateau. *Geochronometria 38*, 432-440.

Chauhan, N., Anand, S., Palani Selvam, T., Mayya, Y. S. & Singhvi, A. K. 2009: Extending the maximum age achievable in the luminescence dating of sediments using large quartz grains: A feasibility study. *Radiation Measurements 44*, 629-633.

Chesner, C. A., Rose, W. I., Drake, N. A. & Westgate, J. A. 1991: Eruptive history of Earth's largest Quaternary caldera (Toba, Indonesia) clarified. *Geology 19*, 200-203.

Chivas, A. 2010: Sedimentology and geochemistry of some Indian stratigraphic profiles. *The Toba Super-Eruption: A critical moment in human evolution? Leverhulme Toba Conference*, Centre for Asian Archaeology, Art & Culture, University of Oxford. Feb. 20-21, 2010.

Choi, J. H., Duller, G. A. T. & Wintle, A. G. 2006: Analysis of quartz LM-OSL curves. *Ancient TL 24*, 9-20.

Clark, J. D. & Williams, F. M. 1987: Palaeoenvironments and prehistory in North Central India: a preliminary report. *In* Jacobsen, J. (ed.): *Studies in the Archaeology of India and Pakistan*, 19-41 pp. Aris and Phillips, Ltd., Warminster.

Clemens, S. C. & Prell, W. L. 1991: Late Quaternary forcing of Indian Ocean summer-monsoon winds: A comparison of fourier model and general circulation model results. *Journal of Geophysical Research 96*, 22683-22700.

Clemens, S. C. & Prell, W. L. 2003: A 350,000 year summer-monsoon multi-proxy stack from the Owen Ridge, Northern Arabian Sea. *Marine Geology 201*, 35-51.

Clemens, S. C., Prell, W. L., Murray, D., Shimmield, G. & Weedon, G. 1991: Forcing mechanisms of the Indian Ocean monsoon. *Nature 353*, 720-725.

Cunningham, A. C. & Wallinga, J. 2010: Selection of integration time intervals for quartz OSL decay curves. *Quaternary Geochronology 5*, 657-666.

Davids, F., Duller, G. A. T. & Roberts, H. M. 2010: Testing the use of feldspars for optical dating of hurricane overwash deposits. *Quaternary Geochronology 5*, 125-130.

Demuro, M. 2009: Optical stimulated luminescence dating of tephra-bearing deposits from eastern Beringia. PhD thesis, University of Wollongong, Australia. 449 pp.

Dennen, W. H., Blackburn, W. H. & Quesada, A. 1970: Aluminum in quartz as a geothermometer. *Contributions to Mineralogy and Petrology 27*, 332-342.

Duller, G. A. T. 1991: Equivalent dose determination using single aliquots. *Nuclear Tracks and Radiation Measurements 18*, 371-378.

Duller, G. A. T. 1992: Luminescence chronology of raised marine terraces, south-west North Island, New Zealand. *Institute of Earth Studies.* University of Wales, Aberystwyth.

Duller, G. A. T. 1997: Behavioural studies of stimulated luminescence from feldspars. *Radiation Measurements 27*, 663-694.

Duller, G. A. T. 2003: Distinguishing quartz and feldspar in single grain luminescence measurements. *Radiation Measurements 37*, 161-165.

Duller, G. A. T. 2006: Single grain optical dating of glacigenic deposits. *Quaternary Geochronology 1*, 296-304.

Duller, G. A. T. 2007: Assessing the error on equivalent dose estimates derived from single aliquot regenerative dose measurements. *Ancient TL 25*, 15-24.

Duller, G. A. T. 2008: Single-grain optical dating of Quaternary sediments: why aliquot size matters in luminescence dating. *Boreas 37*, 589–612.

Duller, G. A. T., Bøtter-Jensen, L. & Murray, A. S. 2000: Optical dating of single sand-sized grains of quartz: sources of variability. *Radiation Measurements 32*, 453-457.

Duller, G. A. T., Bøtter-Jensen, L. & Murray, A. S. 2003: Combining infrared- and green-laser stimulation sources in single-grain luminescence measurements of feldspar and quartz. *Radiation Measurements 37*, 543-550.

Duller, G. A. T. & Wintle, A. G. 2012: A review of the thermally transferred optically stimulated luminescence signal from quartz for dating sediments. *Quaternary Geochronology 7*, 6-20.

Enzel, Y., Ely, L.L., Mishra, S., Ramesh, R., Amit, R., Lazar, B., Rajaguru, S.N., Baker, V.R., Sandler, A. 1999: High-resolution Holocene environmental changes in the Thar Desert, northwestern India. *Science 284*, 125-128.

Feathers, J. K. & Tunnicliffe, J. 2011: Effect of single-grain versus multi-grain aliquots in determining age for K-feldspars from southwestern British Columbia. *Ancient TL 29*, 53-58.

Fleitmann, D., Burns, S. J., Mangini, A., Mudelsee, M., Kramers, J., Villa, I., Neff, U., Al-Subbary, A. A., Buettner, A., Hippler, D. & Matter, A. 2007: Holocene ITCZ and

Indian monsoon dynamics recorded in stalagmites from Oman and Yemen (Socotra). *Quaternary Science Reviews 26*, 170-188.

Fleitmann, D., Burns, S. J., Mudelsee, M., Neff, U., Kramers, J., Mangini, A. & Matter, A. 2003: Holocene forcing of the Indian monsoon recorded in a stalagmite from southern Oman. *Science 300*, 1737-1739.

Fu, X., Li, B. & Li, S.-H. 2012: Testing a multi-step post-IR IRSL dating method using polymineral fine grains from Chinese loess. *Quaternary Geochronology In press,* xxx-xxx.

Galbraith, R. F., Roberts, R. G., Laslett, G. M., Yoshida, H. & Olley, J. M. 1999: Optical dating of single and multiple grains of quartz from Jinmium rock shelter, northern Australia: Part I, experimental design and statistical models. *Archaeometry 41*, 339-364.

Galbraith, R. F. 2005: *Statistics for Fission Track Analysis*. 229 pp. Chapman and Hall, London.

Gathorne-Hardy, F. J. & Harcourt-Smith, W. E. H. 2003: The super-eruption of Toba, did it cause a human bottleneck? *Journal of Human Evolution 45*, 227-230.

Gatti, E., Durant, A. J., Gibbard, P. L. & Oppenheimer, C. 2011: Youngest Toba Tuff in the Son Valley, India: a weak and discontinuous stratigraphic marker. *Quaternary Science Reviews 30*, 3925-3934.

Gibling, M. R., Sinha, R., Roy, N. G., Tandon, S. K. & Jain, M. 2008: Quaternary fluvial and eolian deposits on the Belan River, India: paleoclimatic setting of Paleolithic to Neolithic archeological sites over the past 85,000 years. *Quaternary Science Reviews 27*, 391-410.

Gibling, M. R., Tandon, S. K., Sinha, R. & Jain, M. 2005: Discontinuity-Bounded Alluvial Sequences of the Southern Gangetic Plains, India: Aggradation and Degradation in Response to Monsoonal Strength. *Journal of Sedimentary Research 75*, 369-385.

Haslam, M., Clarkson, C., Petraglia, M., Korisettar, R., Jones, S., Shipton, C., Ditchfield, P. & Ambrose, S. H. 2010: The ~74 ka Toba super-eruption and southern Indian hominins: archaeology, lithic technology and environments at Jwalapuram Locality 3. *Journal of Archaeological Science 37*, 3370-3384.

Haslam, M., Harris, C., Clarkson, C., Pal, J. N., Shipton, C., Crowther, A., Koshy, J., Bora, J., Ditchfield, P., Ram, H. P., Price, K., Dubey, A. K. & Petraglia, M. 2012: Dhaba: An initial report on an Acheulean, Middle Palaeolithic and microlithic locality in the Middle Son Valley, north-central India. *Quaternary International In press,* xxx-xxx.

Haslam, M. & Petraglia, M. 2010: Comment on "Environmental impact of the 73 ka Toba super-eruption in South Asia" by M.A.J. Williams, S.H. Ambrose, S. van der Kaars, C. Ruehlemann, U. Chattopadhyaya, J. Pal and P.R. Chauhan [Palaeogeography, Palaeoclimatology, Palaeoecology 284 (2009) 295-314]. *Palaeogeography, Palaeoclimatology, Palaeoecology 296*, 199-203.

Haslam, M., Roberts, R. G., Shipton, C., Pal, J. N., Fenwick, J. L., Ditchfield, P., Boivin, N., Dubey, A. K., Gupta, M. C. & Petraglia, M. 2011: Late Acheulean hominins at the Marine Isotope Stage 6/5e transition in north-central India. *Quaternary Research 75*, 670-682.

Huntley, D. J. 2006: An explanation of the power-law decay of luminescence. *Journal of Physics: Condensed Matter 18*, 1359-1365.

Huntley, D. J. & Baril, M. R. 1997: The K content of the K-feldspars being measured in optical dating or in thermoluminescence dating. *Ancient TL 15*, 11-13.

Huntley, D. J. & Clague, J. J. 1996: Optical Dating of Tsunami-Laid Sands. *Quaternary Research 46*, 127-140.

Huntley, D. J., Godfrey-Smith, D. I. & Haskell, E. H. 1991: Light-induced emission spectra from some quartz and feldspars. *Nuclear Tracks and Radiation Measurements 18*, 127-131.

Huntley, D. J., Godfrey-Smith, D. I. & Thewalt, M. L. W. 1985: Optical dating of sediments. *Nature 313*, 105-107.

Huntley, D. J., Godfrey-Smith, D. I., Thewalt, M. L. W. & Berger, G. W. 1988: Thermoluminescence spectra of some mineral samples relevant to thermoluminescence dating. *Journal of Luminescence 39*, 123-136.

Huntley, D. J. & Hancock, R. G. V. 2001: The Rb contents of the K-feldspar grains being measured in optical dating. *Ancient TL 19*, 43-46.

Huntley, D. J. & Lamothe, M. 2001: Ubiquity of anomalous fading in K-feldspars and the measurement and correction for it in optical dating. *Canadian Journal of Earth Sciences 38*, 1093-1106.

Huntley, D. J. & Lian, O. B. 2006: Some observations on tunnelling of trapped electrons in feldspars and their implications for optical dating. *Quaternary Science Reviews 25*, 2503-2512.

Huot, S. & Lamothe, M. 2003: Variability of infrared stimulated luminescence properties from fractured feldspar grains. *Radiation Measurements 37*, 499-503.

Huot, S. & Lamothe, M. 2011: A detailed luminescence dating investigation of feldspar and quartz single grains from a Late Holocene fluvial sediment. *Geohydro 2011.* Québec.

Imbrie, J., Hayes, J. D., Martinson, D. G., McIntyre, A., Mix, A. C., Morley, J. J., Pisias, N. G., Prell, W. L. & Shackleton, N. J. 1984: The orbital theory of Pleistocene climate; Support from a revised chronology of the marine δ^{18} record. *In* Berger, A., Imbrie, J., Hayes, J., Kukla, G. & Saltzman, B. (eds.): *Milankovitch and Climate*, 269-305 pp. D. Reidel, Hingham.

Jacobs, Z. 2004: Development of luminescence dating techniques for dating Middle Stone Age sites in South Africa. University of Wales, Aberwystwyth.

Jacobs, Z. 2006: Extending the chronology of deposits at Blombos Cave, South Africa, back to 140 ka using optical dating of single and multiple grains of quartz. *Journal of Human Evolution 51*, 255-273.

Jacobs, Z. 2008: Equivalent dose distributions from single grains of quartz at Sibudu, South Africa: context, causes and consequences for optical dating of archaeological deposits. *Journal of Archaeological Science 35*, 1808-1820.

Jacobs, Z., Duller, G. A. T. & Wintle, A. G. 2003: Optical dating of dune sand from Blombos Cave, South Africa: II - single grain data. *Journal of Human Evolution 44*, 613-625.

Jacobs, Z., Duller, G. A. T. & Wintle, A. G. 2006a: Interpretation of single grain De distributions and calculation of De. *Radiation Measurements 41*, 264-277.

Jacobs, Z., Duller, G. A. T., Wintle, A. G., Henshilwood, C. S. 2006b: Extending the chronology of deposits at Blombos Cave, South Africa, back to 140 ka using optical dating of single and multiple grains of quartz. *Journal of Human Evolution 51*, 255-273.

Jacobs, Z. & Roberts, R. G. 2007: Advances in optically stimulated luminescence dating of individual grains of quartz from archeological deposits. *Evolutionary Anthropology 16*, 210-223.

Jacobs, Z., Wintle, A. G. & Duller, G. A. T. 2006c: Evaluation of SAR procedures for De determination using single aliquots of quartz from two archaeological sites in South Africa. *Radiation Measurements 41*, 520-533.

Jacobs, Z., Wintle, A. G., Duller, G. A. T., Roberts, R. G. & Wadley, L. 2008: New ages for the post-Howiesons Poort, late and final Middle Stone Age at Sibudu, South Africa. *Journal of Archaeological Science 35*, 1790-1807.

Jain, M. 2009: Extending the dose range: Probing deep traps in quartz with 3.06 eV photons. *Radiation Measurements 44*, 445-452.

Jain, M. & Ankjærgaard, C. 2011: Towards a non-fading signal in feldspar: Insight into charge transport and tunnelling from time-resolved optically stimulated luminescence. *Radiation Measurements 46*, 292-309.

Jain, M., Murray, A. S. & Bøtter-Jensen, L. 2003: Characterisation of blue-light stimulated luminescence components in different quartz samples: implications for dose measurement. *Radiation Measurements 37*, 441-449.

James, H. V. A. & Petraglia, M. D. 2005: Modern human origins and the evolution of behavior in the later Pleistocene record of South Asia. *Current Anthropology 46*, S3-S27.

Jones, S. C. 2010: Palaeoenvironmental response to the ~74 ka Toba ash-fall in the Jurreru and Middle Son valleys in southern and north-central India. *Quaternary Research 73*, 336-350.

Jones, S. C. 2012: Local- and regional-scale impacts of the ~74 ka Toba supervolcanic eruption on hominin populations and habitats in India. *Quaternary International In press,* xxx-xxx.

Jones, S. C. & Pal, J. N. 2005: The Middle Son Valley and the Toba supervolcanic eruption of ~74 kyr BP: Youngest Toba Tuff deposits and Palaeolithic associations. *Journal of Interdisciplinary Studies in History and Archaeology 2*, 47-62.

Jones, S. C. & Pal, J. N. 2009: The Palaeolithic of the Middle Son valley, north-central India: Changes in hominin lithic technology and behaviour during the Upper Pleistocene. *Journal of Anthropological Archaeology 28*, 323-341.

Juyal, N., Chamyal, L. S., Bhandari, S., Bhushan, R. & Singhvi, A. K. 2006: Continental record of the southwest monsoon during the last 130 ka: evidence from the southern margin of the Thar Desert, India. *Quaternary Science Reviews 25*, 2632-2650.

Kars, R. H. & Wallinga, J. 2009: IRSL dating of K-feldspars: Modelling natural dose response curves to deal with anomalous fading and trap competition. *Radiation Measurements 44*, 594-599.

Kars, R. H., Wallinga, J. & Cohen, K. M. 2008: A new approach towards anomalous fading correction for feldspar IRSL dating tests on samples in field saturation. *Radiation Measurements 43*, 786-790.

Kim, J. C., Roberts, H. M., Duller, G. A. T., Lee, Y. I. & Yi, S. B. 2009: Assessment of diagnostic tests for evaluating the reliability of SAR De values from polymineral and quartz fine grains. *Radiation Measurements 44*, 149-157.

Korisettar, R. 2007: Toward developing a basin model for Paleolithic settlement of the Indian subcontinent: Geodynamics, monsoon dynamics, habitat diversity and dispersal routes. *In* Petraglia, M. & Allchin, B. (eds.): *The Evolution and History of Human Populations in South Asia: Interdisciplinary Studies in Archaeology,*

Biological Anthropology, Linguistics and Genetics, 69-96 pp. Springer, The Netherlands.

Lamothe, M. & Auclair, M. 1997: Assessing the datability of young sediments by IRSL using an intrinsic laboratory protocol. *Radiation Measurements 27*, 107-117.

Lamothe, M. & Auclair, M. 1999: A solution to anomalous fading and age shortfalls in optical dating of feldspar minerals. *Earth and Planetary Science Letters 171*, 319-323.

Lamothe, M. & Auclair, M. 2000: The *fadia* method: a new approach in luminescence dating using the analysis of single feldspar grains. *Radiation Measurements 32*, 433-438.

Lamothe, M., Auclair, M., Hamzaoui, C. & Huot, S. 2003: Towards a prediction of long-term anomalous fading of feldspar IRSL. *Radiation Measurements 37*, 493-498.

Lamothe, M., Balescu, S. & Auclair, M. 1994: Natural IRSL intensities and apparent luminescence ages of single feldspar grains extracted from partially bleached sediments. *Radiation Measurements 23*, 555-561.

Lang, A., Hatté, C., Rousseau, D. -D., Antoine, P., Fontugne, M., Zöller, L. & Hambach, U. 2003: High-resolution chronologies for loess: comparing AMS ^{14}C and optical dating results. *Quaternary Science Reviews 22*, 953-959.

Lang, A. & Wagner, G. A. 1997: Infrared stimulated luminescence dating of Holocene colluvial sediments using the 410 nm emission. *Quaternary Science Reviews 16*, 393-396.

Li, B. & Li, S.-H. 2011: Luminescence dating of K-feldspar from sediments: A protocol without anomalous fading correction. *Quaternary Geochronology 6*, 468-479.

Li, B., Li, S.-H., Duller, G. A. T. & Wintle, A. G. 2011: Infrared stimulated luminescence measurements of single grains of K-rich feldspar for isochron dating. *Quaternary Geochronology 6*, 71-81.

Lian, O. B. 2007a. Optical dating. *In* Scott, E. (ed.): *Encyclopedia of Quaternary Science*, 1491-1505 pp. Elsevier Amsterdam, Netherlands.

Lian, O. B. 2007b: Thermoluminescence dating. *In* Scott, E. (ed.): *Encyclopedia of Quaternary Science*, 1480-1491 pp. Elsevier Amsterdam, Netherlands.

Lian, O. B., Hu, J., Huntley, D. J. & Hicock, S. R. 1995: Optical dating studies of Quaternary organic-rich sediments from southwestern British Columbia and northwestern Washington State. *Canadian Journal of Earth Sciences = Journal Canadien des Sciences de la Terre 32*, 1194-1207.

Lian, O. B. & Huntley, D. J. 1999: Optical dating studies of postglacial aeolian deposits from the south-central interior of British Columbia, Canada. *Quaternary Science Reviews 18*, 1453-1456.

Lian, O. B. & Roberts, R. G. 2006: Dating the Quaternary: progress in luminescence dating of sediments. *Quaternary Science Reviews 25*, 2449-2468.

Louys, J. 2007: Limited effect of the Quaternary's largest super-eruption (Toba) on land mammals from Southeast Asia. *Quaternary Science Reviews 26*, 3108-3117.

Lowick, S. E., Trauerstein, M. & Preusser, F. 2012: Testing the application of post IR-IRSL dating to fine grain waterlain sediments. *Quaternary Geochronology 8*, 33-40.

Mandal, D. 1983: A note on the radiocarbon dates from the Middle Son Valley. *In* Sharma, G. R., Clark, J.D. (eds.): *Palaeoenvironments and Prehistory in the Middle Son Valley*, 185-289 pp. A. H. Wheeler & Co, Private Limited, Allahabad.

Matthews, N. E., Smith, V. C., Costa, A., Durant, A. J., Pyle, D. M. & Pearce, N. J. G. 2012: Ultra-distal tephra deposits from super-eruptions: Examples from Toba, Indonesia and Taupo Volcanic Zone, New Zealand. *Quaternary International In press,* xxx-xxx.

McKeever, S. W. S., Bøtter-Jensen, L., Agersnap Larsen, N. & Duller, G. A. T. 1997: Temperature dependence of OSL decay curves: Experimental and theoretical aspects. *Radiation Measurements 27*, 161-170.

Mejdahl, V. 1979: Thermoluminescence dating: beta-dose attenuation in quartz grains. *Archaeometry 21*, 61-72.

Mejdahl, V. 1983: Feldspar inclusion dating of ceramics and burnt stones. *PACT 9*, 351-364.

Mejdahl, V. 1985: Thermoluminescence dating based on feldspars. *Nuclear Tracks and Radiation Measurements 10*, 133-136.

Mejdahl, V. 1987: Internal radioactivity in quartz and feldspar grains. *Ancient TL 5*, 10-17.

Miall, A. D. 2006: *The Geology of Fluvial Deposits*. 582 pp. Springer, Berlin.

Misra, V. N. 1989: Human adaptations to the changing landscape of the Indian Arid Zone during the Quaternary period. *In* Kenoyer, J. M. (ed.): *Old Problems and New Perspectives in the Archaeology of South Asia*, 3-20 pp. Department of Anthropology, University of Wisconsin, Madison.

Misra, V. N. 2001: Prehistoric human colonization of India. *Journal of Biosciences 26*, 491-531.

Misra, V.D. & Pal, J.N. 2002: *Mesolithic India*. 549 pp. Pushp Prakashan, Allahabad.

Murray, A. S., Buylaert, J. P., Thomsen, K. J. & Jain, M. 2009: The effect of preheating on the IRSL signal from feldspar. *Radiation Measurements 44*, 554-559.

Murray, A. S. & Mejdahl, V. 1999: Comparison of regenerative-dose single-aliquot and multiple-aliquot (SARA) protocols using heated quartz from archaeological sites. *Quaternary Science Reviews 18*, 223-229.

Murray, A. S. & Roberts, R. G. 1997: Determining the burial time of single grains of quartz using optically stimulated luminescence. *Earth and Planetary Science Letters 152*, 163-180.

Murray, A. S. & Roberts, R. G. 1998: Measurement of the equivalent dose in quartz using a regenerative-dose single-aliquot protocol. *Radiation Measurements 29*, 503-515.

Murray, A. S. & Wintle, A. G. 2000: Luminescence dating of quartz using an improved single-aliquot regenerative-dose protocol. *Radiation Measurements 32*, 57-73.

Murray, A. S. & Wintle, A. G. 2003: The single aliquot regenerative dose protocol: potential for improvements in reliability. *Radiation Measurements 37*, 377-381.

Nathan, R. P. & Mauz, B. 2008: On the dose-rate estimate of carbonate-rich sediments for trapped charge dating. *Radiation Measurements 43*, 14-25.

Neudorf, C. M., Roberts, R. G. & Jacobs, Z. 2012: Sources of overdispersion in a K-rich feldspar sample from north-central India: insights from De, K content and IRSL age distributions for individual grains. *Radiation Measurements In press*, xxx-xxx.

Olley, J. M., Caitcheon, G. G. & Roberts, R. G. 1999: The origin of dose distributions in fluvial sediments, and the prospect of dating single grains from fluvial deposits using optically stimulated luminescence. *Radiation Measurements 30*, 207-217.

Olley, J. M., Murray, A. & Roberts, R. G. 1996: The effects of disequilibria in the uranium and thorium decay chains on burial dose rates in fluvial sediments. *Quaternary Science Reviews 15*, 751-760.

Olley, J. M., Pietsch, T. & Roberts, R. G. 2004: Optical dating of Holocene sediments from a variety of geomorphic settings using single grains of quartz. *Geomorphology 60*, 337-358.

Olley, J. M., Roberts, R. G., Yoshida, H. & Bowler, J. M. 2006: Single-grain optical dating of grave-infill associated with human burials at Lake Mungo, Australia. *Quaternary Science Reviews 25*, 2469-2474.

Oppenheimer, C. 2002: Limited global change due to the largest known Quaternary eruption, Toba ~74 kyr BP? *Quaternary Science Reviews 21*, 1593-1609.

Overpeck, J., Anderson, D., Trumbore, S. & Prell, W. L. 1996: The southwest Indian Monsoon over the last 18,000 years. *Climate Dynamics 12*, 213-225.

Pal, J. N., Williams, M. A. J., Jaiswal, M. & Singhvi, A. K. 2005: Infra red stimulated luminescence ages for prehistoric cultures in the Son and Belan Valleys, North Central India. *Journal of Interdisciplinary Studies in History and Archaeology 1*, 51-62.

Petraglia, M. D. 2007: Mind the Gap: Factoring the Arabian Peninsula and the Indian Subcontinent into Out of Africa Models. *In* Mellars, P., Bar-Yosef, O., Boyle, K. & Stringer, C. (eds.): *The Human Revolution Revisited*, 383-394 pp. McDonald Institute Archaeological Publications, Cambridge.

Petraglia, M. D., Ditchfield, P., Jones, S., Korisettar, R. & Pal, J. N. 2012: The Toba volcanic super-eruption, environmental change, and hominin occupation history in India over the last 140,000 years. *Quaternary International In press,* xxx-xxx.

Petraglia, M., Korisettar, R., Boivin, N., Clarkson, C., Ditchfield, P., Jones, S., Koshy, J., Lahr, M. M., Oppenheimer, C., Pyle, D., Roberts, R., Schwenninger, J.-L., Arnold, L. & White, K. 2007: Middle Paleolithic assemblages from the Indian Subcontinent before and after the Toba super-eruption. *Science 317*, 114-116.

Petraglia, M., Korisettar, R., Kasturi Bai, M., Boivin, N., Bora, J., Clarkson, C., Cunningham, K., Ditchfield, P., Oppenheimer, C., Roberts, R. G. & White, K. 2009: Human occupation, adaptation and behavorial change in the Pleistocene and Holocene of south India: recent investigations in the Kurnool District, Andhrah Pradesh. *Eurasian Prehistory 6*, 119-166.

Pokras, E. M. & Mix, A. C. 1985: Eolian evidence for spatial variability of late Quaternary climates in tropical Africa. *Quaternary Research, N.Y 24*, 137-149.

Poolton, N. R. J., Ozanyan, K. B., Wallinga, J., Murray, A. S. & Bøtter-Jensen, L. 2002a: Electrons in feldspar II: a consideration of the influence of conduction band-tail states on luminescence processes. *Physics and Chemistry of Minerals 29*, 217-225.

Poolton, N. R. J., Wallinga, J., Murray, A. S., Bulur, E. & Bøtter-Jensen, L. 2002b: Electrons in feldspar I: on the wavefunction of electrons trapped at simple lattice defects. *Physics and Chemistry of Minerals 29*, 210-216.

Prasad, S. & Enzel, Y. 2006: Holocene paleoclimates of India. *Quaternary Research 66*, 442-453.

Prasad, S. Kusumgar, S., Gupta, S.K. 1997: A mid-late Holocene record of palaeoclimatic changes from Nal Sarovar—A palaeodesert margin lake in western India. *Journal of Quaternary Science 12(2)*, 153-159.

Prell, W. L. 1984: Monsoonal climate of the Arabian Sea during the late Quaternary: A response to changing solar radiation. *In* Berger, A., Imbrie, J., Hayes, J., Kukla, G. & Saltzman, B. (eds.): *Milankovitch and Climate*, 349-366 pp. D. Reidel, Hingham.

Prell, W. L. & Kutzbach, J. E. 1987: Monsoon variability over the past 150,000 years. *Journal of Geophysical Research 92*, 8411-8425.

Prescott, J. R. & Fox, P. J. 1993: Three-dimensional thermoluminescence spectra of feldspars. *Journal of Physics D: Applied Physics 26*, 2245-2254.

Prescott, J. R. & Hutton, J. T. 1994: Cosmic ray contributions to dose rates for luminescence and ESR dating: large depths and long-term time variations. *Radiation Measurements 23*, 497-500.

Rampino, M. R. & Ambrose, S. H. 2000: Volcanic winter in the Garden of Eden; the Toba supereruption and the late Pleistocene human population crash. *Geological Society of America Special Paper 345*, 71.

Rampino, M. R. & Self, S. 1993: Bottleneck in human evolution and the Toba eruption *Science 262*, 1955.

Readhead, M. L. 1987: Thermoluminescence dose rate data and dating equations for the case of disequillibrium in the decay series. *Nuclear Tracks and Radiation Measurements 13*, 197-207.

Readhead, M. L. 2002: Absorbed dose fraction for ^{87}Rb β particles. *Ancient TL 20*, 25-28.

Reed, S. J. B. 1995: Electron probe microanalysis. *In* Potts, P. J., Bowles, J., F.W., Reed, S. J. B. & Cave, M. R. (eds.): *Microprobe Techniques in the Earth Sciences*, 419 pp. The Mineralogical Society, Cambridge.

Rees-Jones, J. 1995: Optical dating of young sediments using fine-grain quartz. *Ancient TL 13*, 9-14.

Reimann, T., Tsukamoto, S., Naumann, M. & Frechen, M. 2011: The potential of using K-rich feldspars for optical dating of young coastal sediments A test case from Darss-Zingst peninsula (southern Baltic Sea coast). *Quaternary Geochronology 6*, 207-222.

Rhodes, E. J. 1990. Optical dating of quartz from sediments. Unpublished PhD thesis. Oxford University.

Rossignol-Strick, M. 1983: African monsoons, an immediate climate response to orbital insolation. *Nature 304*, 46-49.

Rittenour, T. M. 2008: Luminescence dating of fluvial deposits: applications to geomorphic, palaeoseismic and archaeological research. *Boreas 37*, 613-635.

Roberts, H. M. 2007: Assessing the effectiveness of the double-SAR protocol in isolating a luminescence signal dominated by quartz. *Radiation Measurements 42*, 1627-1636.

Roberts, H. M. & Wintle, A. G. 2001: Equivalent dose determinations for polymineralic fine-grains using the SAR protocol: application to a Holocene sequence of the Chinese Loess Plateau. *Quaternary Science Reviews 20*, 859-863.

Roberts, R., Bird, M., Olley, J., Galbraith, R., Lawson, E., Laslett, G., Yoshida, H., Jones, R., Fullagar, R., Jacobsen, G. & Hua, Q. 1998: Optical and radiocarbon dating at Jinmium rock shelter in northern Australia. *Nature 393*, 358-362.

Roberts, R., Walsh, G., Murray, A., Olley, J. M., Jones, R., Morwood, M., Tuniz, C., Lawson, E., Macphail, M., Bowdery, D. & Naumann, I. 1997: Luminescence dating of rock art and past environments using mud-wasp nests in northern Australia. *Nature 387*, 696-699.

Roberts, R. G. 1997: Luminescence dating in archaeology: From origins to optical. *Radiation Measurements 27*, 819-892.

Roberts, R. G., Fenwick, J. L., Arnold, L. J., Jacobs, Z. & Jafari, Y. 2010: Numerical dating of sediments associated with volcanic ash and stone artefacts in southern and northeastern India. *The Leverhulme Toba Conference,* University of Oxford.

Roberts, R. G. & Jacobs, Z. 2008: Dating in Landscape Archaeology. *In* Thomas, J. & David, B. (eds.): *Handbook of Landscape Archaeology*, 347-364 pp. Left Coast Press, Walnut Creek.

Roberts, R. G., Galbraith, R. F., Olley, J. M., Yoshida, H. & Laslett, G. M. 1999: Optical dating of single and multiple grains of quartz from Jinmium Rock shelter, northern Australia: Part II, Results and implications. *Archaeometry 41*, 365-395.

Roberts, R. G., Galbraith, R. F., Yoshida, H., Laslett, G. M. & Olley, J. M. 2000: Distinguishing dose populations in sediment mixtures: a test of single-grain optical dating procedures using mixtures of laboratory-dosed quartz. *Radiation Measurements 32*, 459-465.

Rose, W. I. & Chesner, C. A. 1987: Dispersal of ash in the great Toba eruption, 75 ka. *Geology 15*, 913-917.

Roy, N. G., Sinha, R. & Gibling, M. R. 2011: Aggradation, incision and interfluve flooding in the Ganga Valley over the past 100,000 years: Testing the influence of monsoonal precipitation. *Palaeogeography, Palaeoclimatology, Palaeoecology In press*, xxx-xxx.

Shane, P., Westgate, J., Williams, M. & Korisettar, R. 1995: New geochemical evidence for the Youngest Toba Tuff in India. *Quaternary Research 44*, 200-204.

Sharma, G.R. 1973: Stone Age in the Vindhyas and The Ganga Valley. *In* Agrawal, D.P. & Ghosh, A. (eds.): *Radiocarbon and Indian Archaeology*. 106-110 pp. TIFR, Bombay.

Sharma, G. R. & Clark, J. D. 1982: Palaeo-environments and prehistory in the Middle Son Valley, northern Madhya Pradesh. *Man and the Environment 6*, 56-62.

Sharma, G. R. & Clark, J. D. 1983: *Palaeoenvironments and Prehistory in the Middle Son Valley, Madhya Pradesh, North-Central India*. 320 pp. A. H. Wheeler and Co. Private Limited, Allahabad.

Sharma, S., Joachimski, M., Sharma, M., Tobschall, H. J., Singh, I. B., Sharma, C., Chauhan, M. S. & Morgenroth, G. 2004: Lateglacial and Holocene environmental changes in Ganga plain, Northern India. *Quaternary Science Reviews 23*, 145-159.

Sharma, G.R., Misra, V.D., Mandal, D., Misra, B.B. & Pal, J.N., 1980: *Beginnings of Agriculture*. 200 pp. Abinash Prakashan, Allahabad.

Singarayer, J. S. & Bailey, R. M. 2003: Further investigations of the quartz optically stimulated luminescence components using linear modulation. *Radiation Measurements 37*, 451-458.

Singhvi, A. K., Chauhan, N., Nagar, Y. C. & Jaiswal, M. 2009: Luminescence dating: new improvements in SAR protocol. *In* Murari, M. K., Morthekai, P., Chauhan, N., Biswas, R. H., Shinde, D. P. & Nag, K. (eds.): *Second Asia Pacific Conference on Luminescence and Electron Spin Resonance Dating.* Physical Research Laboratory, Ahmedabad.

Sinha, R., Kumar, R., Sinha, S., Tandon, S. K. & Gibling, M. R. 2007: Late Cenozoic fluvial successions in northern and western India: an overview and synthesis. *Quaternary Science Reviews 26*, 2801-2822.

Smedley, R. K., Duller, G. A. T., Pearce, N. J. G. & Roberts, H. M. 2012: Determining the K-content of single-grains of feldspar for luminescence dating. *Radiation Measurements In press,* xxx-xxx.

Smith, V. C., Pearce, N. J. G., Matthews, N. E., Westgate, J. A., Petraglia, M. D., Haslam, M., Lane, C. S., Korisettar, R. & Pal, J. N. 2011: Geochemical fingerprinting of the

widespread Toba tephra using biotite compositions. *Quaternary International 246*, 97-104.

Sirocko, F., Sarnthein, M., Erlenkeuser, H., Lang, H., Arnold, M. & Duplessy, J. C. 1993: Century-scale events in monsoonal climate over the past 24000 years. *Nature 364*, 322-324.

Sohbati, R., Murray, A. S., Buylaert, J. P., Ortuño, M., Cuhna, P. P. & Masana, E. 2012: Luminescence dating of Pleistocene alluvial sediments affected by the Alhama de Murcia fault (eastern Betics, Spain) – a comparison between OSL, IRSL and post-IR IRSL ages. *Boreas 41*, 250-262.

Spooner, N. A. 1992: Optical dating: Preliminary results on the anomalous fading of luminescence from feldspars. *Quaternary Science Reviews 11*, 139-145.

Spooner, N. A. 1994a: The anomalous fading of infrared-stimulated luminescence from feldspars. *Radiation Measurements 23*, 625-632.

Spooner, N. A. 1994b: On the optical dating signal from quartz. *Radiation Measurements 23*, 593-600.

Srivastava, P., Juyal, N., Singhvi, A. K., Wasson, R. J. & Bateman, M. D. 2001: Luminescence chronology of river adjustment and incision of Quaternary sediments in the alluvial plain of the Sabarmati River, north Gujarat, India. *Geomorphology 36*, 217-229.

Stevens, T., Marković, S. B., Zech, M., Hambach, U. & Sümegi, P. 2011: Dust deposition and climate in the Carpathian Basin over an independently dated last glacial–interglacial cycle. *Quaternary Science Reviews 30*, 662-681.

Street-Perrott, F. A. & Harrison, S. P. 1984: Temporal variations in lake levels since 30,000 yr BP - an index of the global hydrological cycle. *In* Hansen, J. E. & Takahashi, T. (eds.): *Climate Processes and Climate Sensitivity, Geophys. Monogr. Ser.*, 118-129 pp. AGU, Washington, D.C.

Thiel, C., Buylaert, J.-P., Murray, A., Terhorst, B., Hofer, I., Tsukamoto, S. & Frechen, M. 2011: Luminescence dating of the Stratzing loess profile (Austria) - Testing the potential of an elevated temperature post-IR IRSL protocol. *Quaternary International 234*, 23-31.

Thiel, C., Coltorti, M., Tsukamoto, S. & Frechen, M. 2010: Geochronology for some key sites along the coast of Sardinia (Italy). *Quaternary International 222*, 36-47.

Thiel, C., Buylaert, J.-P., Murray, A., Terhorst, B., Hofer, I., Tsukamoto, S. & Frechen, M. 2011: Luminescence dating of the Stratzing loess profile (Austria) - Testing the potential of an elevated temperature post-IR IRSL protocol. *Quaternary International 234*, 23-31.

Thomsen, K. J., Murray, A. S. & Jain, M. 2011: Stability of IRSL signals from sedimentary K-feldspar samples. *Geochronometria 38*, 1-13.

Thomsen, K. J., Murray, A. S., Jain, M. & Bøtter-Jensen, L. 2008: Laboratory fading rates of various luminescence signals from feldspar-rich sediment extracts. *Radiation Measurements 43*, 1474-1486.

Trauerstein, M., Lowick, S., Preusser, F., Rufer, D. & Schlunegger, F. 2012: Exploring fading in single-grain feldspar IRSL measurements. *Quaternary Geochronology In press,* xxx-xxx.

Tso, M. Y. W., Wong, N. W. L. & Li, S. H. 1996: Determination of Lifetime of Infrared Stimulated Signals from Potassium and Sodium Feldspars. *Radiation Protection Dosimetry 66*, 387-389.

Tsukamoto, S. & Duller, G. A. T. 2008: Anomalous fading of various luminescence signals from terrestrial basaltic samples as Martian analogues. *Radiation Measurements 43*, 721-725.

Tsukamoto, S., Duller, G. A. T., Wintle, A. G. & Frechen, M. 2010: Optical dating of a Japanese marker tephra using plagioclase. *Quaternary Geochronology 5*, 274-278.

Tsukamoto, S., Rink, W. J. & Watanuki, T. 2003: OSL of tephric loess and volcanic quartz in Japan and an alternative procedure for estimating De from a fast OSL component. *Radiation Measurements 37*, 459-465.

van Campo, E., Duplessy, J. C. & Rossignol-Strick, M. 1982: Climatic conditions deduced from a 150-kyr oxygen isotope-pollen record from the Arabian Sea. *Nature 296*, 56-59.

Visocekas, R. 1985: Tunnelling radiative recombination in laboradorite: its association with anomalous fading of thermoluminescence *Nuclear Tracks and Radiation Measurements 10*, 521-529.

Visocekas, R. 2000: Monitoring anomalous fading of TL of feldspars by using far-red emission as a gauge. *Radiation Measurements 32*, 499-504.

Visocekas, R. 2002: Tunnelling in Afterglow: its Coexistence and Interweaving with Thermally Stimulated Luminescence. *Radiation Protection Dosimetry 100*, 45-53.

Visocekas, R. & Guérin, G. 2006: TL dating of feldspars using their far-red emission to deal with anomalous fading. *Radiation Measurements 41*, 942-947.

Visocekas, R., Spooner, N. A., Zink, A. & Blanc, P. 1994: Tunnel afterglow, fading and infrared emission in thermoluminescence of feldspars. *Radiation Measurements 23*, 377-385.

Vita-Finzi, C. 2004: Buckle-controlled seismogenic faulting in peninsular India. *Quaternary Science Reviews 23*, 2405-2412.

Waelbroeck, C., Labeyrie, L., Michel, E., Duplessy, J.C., McManus, J.F., Lambeck, K., Balbon, E., Labracherie, M. 2002: Seal-level and deep water temperature changes derived from benthic foraminifera isotopic records. *Quaternary Science Reviews 21*, 295-305.

Wallinga, J., Bos, A. J. J., Dorenbos, P., Murray, A. S. & Schokker, J. 2007: A test case for anomalous fading correction in IRSL dating. *Quaternary Geochronology 2*, 216-221.

Wallinga, J., Murray, A. & Wintle, A. 2000: The single-aliquot regenerative-dose (SAR) protocol applied to coarse-grain feldspar. *Radiation Measurements 32*, 529-533.

Wasson, R.J., Rajaguru, S.N., Misra, V.N., Agrawal, D.P., Dhir, R.P., Singhvi, A.K., Kameswara Rao, K. 1983: Geomorphology, late Quaternary stratigraphy and palaeoclimatology of the Thar dunefield. *Zeitschrift für Geomorphologie N.F. 45*, 117-151.

Welton, J. E. 1984: *SEM Petrology Atlas*. 237 pp. American Association of Petroleum Geologists, Tulsa, OK

Westgate, J. A., Shane, P. A. R., Pearce, N. J. G., Perkins, W. T., Korisettar, R., Chesner, C. A., Williams, M. A. J. & Acharyya, S. K. 1998: All Toba tephra occurrences across Peninsular India belong to the 75,000 yr B.P. eruption. *Quaternary Research 50*, 107-112.

Williams, M. 2012a: The ~73 ka Toba super-eruption and its impact: History of a debate. *Quaternary International In press,* xxx-xxx.

Williams, M. 2012b: Did the 73 ka Toba super-eruption have an enduring effect? Insights from genetics, prehistoric archaeology, pollen analysis, stable isotope geochemistry, geomorphology, ice cores, and climate models. *Quaternary International In press,* xxx-xxx.

Williams, M. A. J., Ambrose, S. H., van der Kaars, S., Ruehlemann, C., Chattopadhyaya, U., Pal, J. & Chauhan, P. R. 2010: Reply to the comment on "Environmental impact of the 73 ka Toba super-eruption in South Asia" by M. A. J. Williams, S. H. Ambrose, S. van der Kaars, C. Ruehlemann, U. Chattopadhyaya, J. Pal, P. R. Chauhan [Palaeogeography, Palaeoclimatology, Palaeoecology 284 (2009) 295-314]. *Palaeogeography, Palaeoclimatology, Palaeoecology 296*, 204-211.

Williams, M. A. J., Ambrose, S. H., van der Kaars, S., Ruehlemann, C., Chattopadhyaya, U., Pal, J. & Chauhan, P. R. 2009: Environmental impact of the 73 ka Toba super-eruption in South Asia. *Palaeogeography, Palaeoclimatology, Palaeoecology 284*, 295-314.

Williams, M. A. J. & Clarke, M. F. 1984: Late Quaternary environments in north-central India. *Nature 308*, 633-635.

Williams, M. A. J. & Clarke, M. F. 1995: Quaternary geology and prehistoric environments in the Son and Belan Valleys, North Central India. *Memoir - Geological Society of India 32*, 282-308.

Williams, M. A. J., Pal, J. N., Jaiswal, M. & Singhvi, A. K. 2006: River response to Quaternary climatic fluctuations: evidence from the Son and Belan valleys, north-central India. *Quaternary Science Reviews 25*, 2619-2631.

Williams, M. A. J. & Royce, K. 1982: Quaternary geology of the Middle Son Valley, North Central India: Implications for prehistoric archaeology. *Palaeogeography, Palaeoclimatology, Palaeoecology 38*, 139-162.

Williams, M. A. J. & Royce, K. 1983: Alluvial History of the Middle Son Valley, North Central India. *In* Sharma, G. R. & Clark, J. D. (eds.): *Palaeoenvironments and Prehistory in the Middle Son Valley, Madhya Pradesh, North-Central India*, 9-21 pp. A. H. Wheeler & Co, Allahabad.

Wintle, A. G. 1973: Anomalous fading of thermoluminescence in mineral samples. *Nature 245*, 143-144.

Wintle, A. G. 1997: Luminescence dating: laboratory procedures and protocols. *Radiation Measurements 27*, 769-817.

Wintle, A. G. & Duller, G. A. T. 1991: The effect of optical absorption on luminescence dating. *Ancient TL 9*, 37-39.

Wintle, A. G. & Murray, A. S. 2006: A review of quartz optically stimulated luminescence characteristics and their relevance in single-aliquot regeneration dating protocols. *Radiation Measurements 41*, 369-391.

Yakowitz, H. 1975: Methods of quantitative x-ray analysis used in electron probe microanalysis and scanning electron microscopy. *In* Goldstein, J. I. & Yakowitz, H. (eds.): *Practical Scanning Electron Microscopy*, 327-372 pp. Plenum Press, New York.

Yakowitz, H. & Goldstein, J. I. 1975: Practical aspects of X-ray microanalysis. *In* Goldstein, J. I. & Yakowitz, H. (eds.): *Practical Scanning Electron Microscopy*, 401-434 pp. Plenum Press, New York.

Yoshida, H., Roberts, R. G., Olley, J. M., Laslett, G. M. & Galbraith, R. F. 2000: Extending the age range of optical dating using single 'supergrains' of quartz. *Radiation Measurements 32*, 439-446.

Zhang, J. F. & Zhou, L. P. 2007: Optimization of the `double SAR' procedure for polymineral fine grains. *Radiation Measurements 42*, 1475-1482.

Zhao, H. & Li, S.-H. 2005: Internal dose rate to K-feldspar grains from radioactive elements other than potassium. *Radiation Measurements 40*, 84-93.

Zimmerman, D. W. 1971: Thermoluminescent dating using fine grains from pottery. *Archaeometry 13*, 29-52.